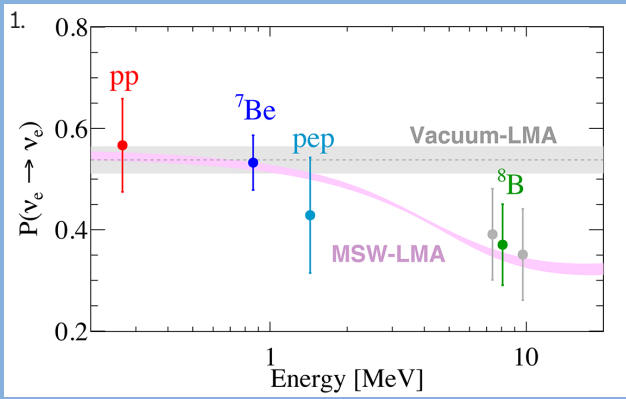

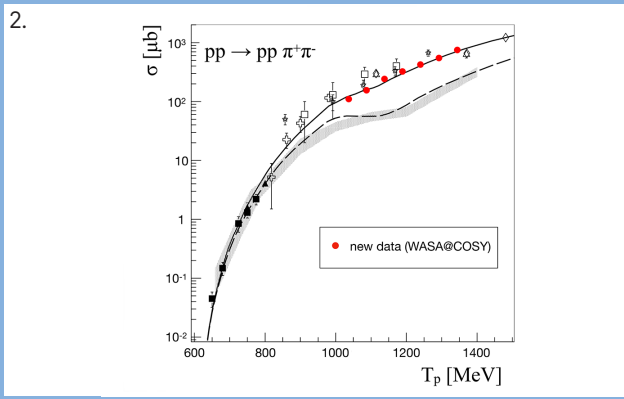

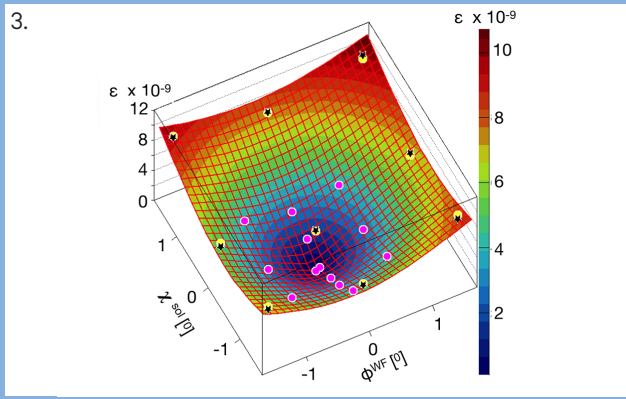

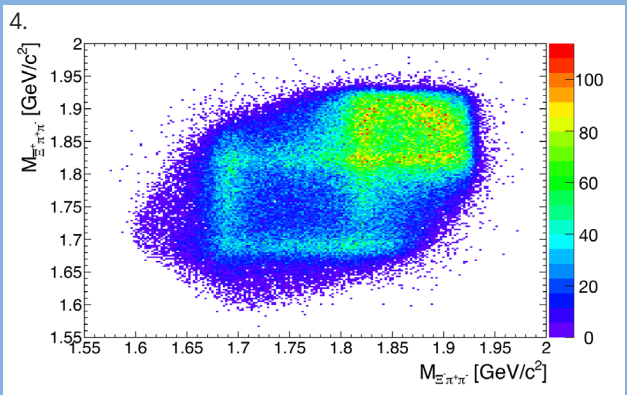

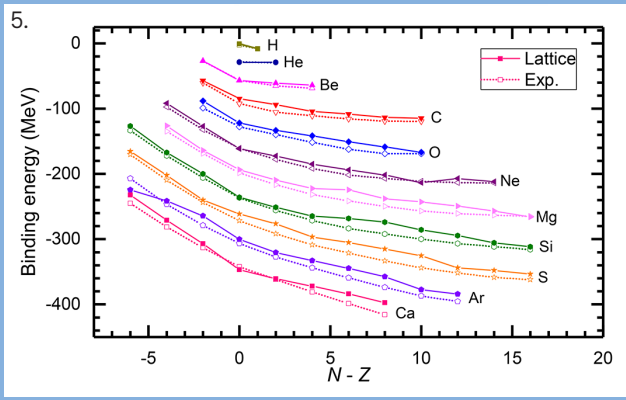

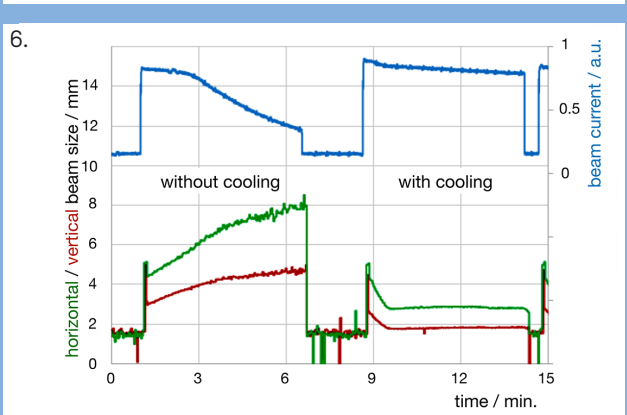

ANNUAL REPORT 2018

Institut für Kernphysik · COSY

Jül-4418

Mitglied der Helmholtz-Gemeinschaft

JÜLICH Forschungszentrum

Annual Report 2018

Institut für Kernphysik / COSY

Cover picture:

1. Borexino results on pp, ^{7}Be (862 + 384 keV), pep, and CNO solar ν's: interaction rates and fluxes, inferred assuming the MSW-LMA oscillation parameters (section 2.4).

2. Exclusive measurements of the quasi-free $pp \to pp\pi^+\pi^-$ reaction measured at WASA@COSY with a deuteron target covering the energy region of the $N^+(1440)$ and $\Delta(1232)\Delta(1232)$ resonance excitations. Calculations describing these excitations by t-channel meson exchange (dashed line) underpredict substantially the experimental total cross section. The shaded band shows isospin based predictions. The solid line results by adding the production of a D_{21} resonance with a strength fitted to the data. For details see the corresponding publication (Phys.Rev.Lett. 121, 052001).

3. The picture shows the measured EDM resonance strength ε of polarized deuterons with momenta of 970 MeV/c as function of the physical rotation of the RF Wien filter ϕ^{WF} around the beam axis and spin rotations in the snake χ^{sol} (section 2.3).

4. Reconstruction of Ξ^* decay channel $\Xi^{+/-}\pi^+\pi^-$ from a Monte Carlo generated event sample showing clear signatures of the resonant states $\Xi(1690)$ and $\Xi(1820)$ (section 2.2).

5. The calculated binding energies from ^{3}H to ^{48}Ca. The solid symbols denote the lattice results and the open symbols denote the experimental values (section 2.5).

6. Compensation of beam loss and size increase due to passing through a cluster-target consistent with densities expected at PANDA by stochastic cooling (section 2.1).

Contents

Preface

After three years into the strategy discussion of Forschungszentrum Jülich (FZJ) and the uncertainties coming along with the conclusion to discontinue the Institute für Kernphysik (IKP) within FZJ for the staff and students of IKP, the year 2018 turned out to be a time of decisions: The Supervisory Boards (Aufsichtsrat) of FZJ and of GSI Darmstadt decided to transfer IKP-1, IKP-2, IKP-4 and IKP-TA from FZJ to GSI as of January 1, 2021. This is to secure the IKP expertise – in our view: accelerator physics (i. p. for storage rings), hadron physics with antiprotons, precision physics for symmetry investigations, neutrino physics and polarization technologies – for the German physics community. The implementation, which was given the project name “TransFAIR", turns out to be a major administrative and regulatory effort, and it remains to be seen if the sought date can be met.
Scientifically, the year 2018 was again a very successful one:

- The JEDI collaboration has conducted a first precursor experiment to study the electric dipole moment (EDM) of the deuteron in COSY, after installation and commissioning of an RF Wien filter. This has been one principal goals of the ERC Advanced Grant “srEDM" and can be considered a major milestone towards EDM searches for charged particles in storage rings.

- The CPEDM collaboration, with major contributions from the JEDI collaboration, submitted a paper to the “European Strategy for Particle Physics" (ESPP) update, outlining the strategy for a search for electric dipole moments (EDM) of charged particles in storage rings with unprecedented sensitivity.

- The Borexino collaboration, with major input from the Jülich group, has recently published the first comprehensive measurement of solar neutrinos produced along the pp-chain, a sequence of nuclear fusion reactions responsible for about 99 percent of solar energy. In particular, Borexino measured the rates of pp, pep, ^{7}Be, and ^{8}B neutrinos and provided limits both on the so called hep neutrinos as well as on neutrino contributions from the CNO-cycle.

Preparations for FAIR are also on track:

- As a major step towards commencement of the FAIR experiments, components of the FAIR experiments have been extensively tested to perform physics measurements at existing facilities. IKP has now completed all STS1 Straw Tube modules needed to enable spectroscopy studies of hyperons at the combined HADES/PANDA FAIR-Phase 0 experiment.

- COSY once again proved to be an invaluable tool for investigating hardware developments intended for later use at the FAIR facility. The full sized stochastic cooling system developed for HESR reached the design parameters running with the newest generation of the PANDA target provided by Münster University.

- Pre-assembly of HESR components is a considerable effort alongside the COSY operation / maintenance and HESR design / production tracking. 75% of the dipole magnets are presently in the storage hall close to FAIR. Two assembly lines for the girders between the dipole magnets are being set up.

In 2018, we celebrated the 70th birthday of Rudolf Maier, long-term director of IKP-4, who retired in early 2014, with a scientific colloquium at IKP.
Finally, I would like to take this opportunity to thank everyone for his/her contributions to our scientific and strategic ventures – most important, that we all have stuck together until now: let’s see, whether IKP will have a future that we are hoping for.

Jülich, May 2019

Hans Ströher

1 White Paper on "Scientific Opportunities of IKP in PoF-IV and Beyond"

The Institute for Nuclear Physics (Institut für Kernphysik, IKP) conducts fundamental research in the fields of nuclear and elementary particle physics. The physics program addresses two big questions of modern physics, namely the matter-antimatter asymmetry of our universe ("Fate of antimatter?" – this is also the motif of JARA-FAME) and a basic understanding of the building blocks matter is comprised of ("How does nature make hadrons and nuclei?"). Both issues are tied together by the quest to understand "Why do we exist at all?" The IKP science has been scrutinized recently in the "Evaluation on the Helmholtz Center Forschungszentrum Jülich – Research Field Matter" with the overall grade "outstanding". (Quote from the report: *In each of the IKP institutes, there are activities that are forefront, crucial and excellent. They all strongly depend on the critical mass of people with great expertise in accelerator science and technology as well as in fundamental nuclear and particle physics. (...) In the opinion of the committee, it is of great importance to keep the relevant competencies together in order not to risk their participation in ongoing programs, especially for HESR, PANDA and the storage ring EDM (srEDM) effort, but especially also for future developments that build on expert knowledge in nuclear and accelerator science and technology (e.g. HBS, JuSPARC, isotope production) and on cutting edge high performance data handling (as e.g. available for PANDA).*) As a result of strategy discussions and decisions of Forschungszentrum Jülich, IKP (i.e. IKP-1 (Experimental Hadron Structure), IKP-2 (Experimental Hadron Dynamics) and IKP-4 (Large Scale Nuclear Physics Equipment)) is planned be transferred to the GSI Helmholtzzentrum für Schwerionenforschung – keeping the competences and activities of IKP-1, IKP-2 and IKP-4 (Quote from draft of "Forschungsbereichsspezifische Ziele": *Die Kompetenzen und Aktivitäten der Institutsbereiche IKP-1, IKP-2 und IKP-4 des FZJ im Bereich der Kernphysik sowie deren Finanzierung sollen ungeachtet ihrer organisatorischen Zuordnung im FB Materie erhalten bleiben.*) In the following, we describe the background of IKP and the scientific opportunities that lie ahead for the institute, based on our history, our experience, the existing hardware and the scientific questions to be answered and the challenges to be met. Unique items, which we bring in, are:

- The COSY facility: a cooler storage ring for (polarized) proton and deuteron beams, including equipment (stochastic cooling, 2 electron coolers, spin manipulators).
- Experience with polarized particles (protons, deuterons): sources, beams and targets, polarimeter, applications.
- Construction and utilization of various types of small- to large-scale detector facilities.
- Know-how in scintillator-based neutrino physics: solar- and geo-neutrinos.
- Large-scale simulations of (polarized) particle beams in storage rings.

1.1 Fundamentals

1.1.1 Expertise

Accelerator/Storage Rings The Institut für Kernphysik (IKP) has a decade-long experience to design, to build and operate as well as to further develop accelerators: foremost the Juelich Light Ion Cyclotron JULIC and Cooler Synchrotron COSY, but also the polarized and unpolarized ion sources for protons and deuterons. IKP has also contributed significantly to the various versions of linear accelerators for spallation neutron sources and it has designed a superconducting linac, which was planned to replace JULIC as the injector for COSY. Recently, it has delivered the proton source for commissioning of the ELENA antiproton ring at CERN. Unique experience is available to produce and accelerate polarized beams without polarization loss and to manipulate them in COSY, to select polarization states and to determine the degree of polarization by the use of nuclear reactions with polarimeters, based on scintillator detectors. A huge expertise has been accumulated over the years to cool and store beams, to accelerate and decelerate them and to use them during energy ramping or at a fixed energy at internal target stations with thin solid, gas or pellet targets. It is also possible to provide (slow (resonant and stochastic) or fast) extracted beams to external target stations – this option was previously used for the TOF- spectrometer and is now exploited for all kinds of detector tests (see below). Electron cooling at low momenta (up to 600 MeV/c) has been used in COSY early on; more recently a high energy electron cooler ($E_e < 2$MeV) has been installed and commissioned in the ring. Stochastic cooling is also used routinely in COSY (momentum range from 1.5 to 3.3 GeV/c); here new pick-up and kicker-devices have been developed at and implemented in COSY.

Experiments For many years, the institutes of IKP have, together with international partners, conducted hadron physics experiments at internal target stations of COSY (using the detectors systems ANKE (magnetic forward spectrometer plus multiple detector systems), COSY-11 (scintillator-based forward detectors using one COSY dipole), EDDA (plastic-scintillator based forward detector), PAX (solid-state detectors in vacuum) and WASA (4π γ-detector plus plastic- scintillator and gas-based forward detectors) - they are thus a most experienced group of scientists to run the HESR internal

detectors like KOALA and PANDA. Their experience also comprises the use of internal solid state, cluster jet and pellet targets as well as polarized (ABS-driven) targets including storage cells; for the latter, deep know-how is available for polarimetry (Lamb- shift, Breit-Rabi and nuclear reaction-based).
Currently, one of the most important measurements at COSY is the so called precursor experiment for a deuteron EDM search, prepared and soon to be executed with the help of an RF Wien-filter by the JEDI (Jülich Electric Dipole moment Investigations) collaboration: for this project, many of the techniques developed over the years (longitudinal polarized beam, long spin coherence time, multiple feedback loops, ...) are required and implemented.

Neutrino Physics Since about 3 years, IKP, together with RWTH Aachen, is involved in neutrino physics, using scintillator-based detector systems: currently Borexino (LNGS, Italy) and in future JUNO (Jiangmen, China). A main focus is on solar and geo-neutrinos and on the neutrino mass hirerachy.

Antiproton Physics For many years, IKP has played an important role in the physics with antiprotons at CERN/AD (ATRAP detector); more recently a small IKP-group is involved in experiments at CERN to investigate how polarized antiprotons can be obtained. As outlined below, this is also a long-term goal of PAX. The PANDA experimental program is of course based on the provision of antiprotons at FAIR, and IKP is pursuing multiple preparations to be ready for the physics start.

Detectors IKP is responsible for the tracking detectors (Straw Tube Trackers (STT) and Microvertex Detectors (MVD)) for HADES and PANDA – the corresponding detector laboratories have been set up at the institute. Together with the general detector laboratory of the institute (see below), it is setting up thick, highly segmented solid-state detectors to measure recoil protons for the PANDA experiment. Together with the University of Ferrara, IKP has constructed and built a Silicon Tracking Telescope for use in the PAX and TRIC experiments, again with the IKP detector lab. A polarimeter based on LYSO scintillator crystals is being built for use in the precursor experiment of the JEDI collaboration to precisely measure the possible polarization change of a deuteron beam circulating in COSY.

Infrastructure (Mechanical, Electronics Workshops, Detector Lab) IKP runs a mechanical workshop at the institute and it has access to the central engineering institute (ZEA-1) for support in the design, construction and implementation of new and complex research infrastructure into COSY (and elsewhere); a recent example is a RF-Wien filter (together with the RWTH Aachen University). The electronics workshop – together with ZEA-2 – has equipped experiments at COSY, CERN, and other facilities with tailored data readout systems mainly based on foreign (RAL, CERN, GSI) developments. Slow control and power supply systems (HV and LV) have been adapted to the dedicated requirements of experiments. Currently, the HV supply and detector signal connection to the FPGA based readout electronics (ZEA-2) for the PANDA STT is under development. Future activities include the low voltage supply and temperature management of the PANDA MVD front end electronics. In addition design, assembly, and commissioning of special electronic circuits for JEDI, beam diagnostics, the radiation protection group and others is accomplished. The IKP detector laboratory has developed and manufactured semiconductor detectors for decades. Normally these detectors are thick, planar detectors made of silicon and germanium up to a maximum diameter of 4". All these detectors are not commercially available and are designed and built specifically for each application. The lab has a unique know-how in the segmentation of the detector contacts. Therefore, the detectors can be segmented either on one side or on both sides. In addition to individual detectors also complete detector systems, consisting of the sensor itself, the cryostat and the preamplifier electronics, are developed and manufactured. Applications of these segmented detectors (systems) are, e.g., atomic and nuclear physics and synchrotron radiation experiments.

Simulation of Beam and Spin Motion A special area of expertise at IKP is the application and further development of beam and spin dynamics simulation codes. Several codes (COSY Infinity, MODE, Bmad) have been extended to properly simulate the spin motion in the presence of a particle EDM in a collaboration between RWTH Aachen University, the Centre National de la Recherche Scientifique (CNRS) Grenoble and Michigan State University. Benchmarking experiments are conducted at the Cooler Synchrotron COSY to validate and further improve these simulation tools. In recent years, simulations of beam and spin dynamics have focused on studies of systematic effects for the “precursor experiment" at COSY as well as for dedicated EDM storage rings. To simulate the beam stability in the HESR High-Energy Storage Ring, the PTC-module of MAD-X is used for beam tracking. The beam simulations are based on measured field distributions from the HESR magnet test bench in order to ensure realistic dynamic aperture simulations for the HESR. IKP is also active in the field of laser-plasma acceleration. Simulations are performed on the FZJ supercomputers in close cooperation with PGI-6, the Jülich Supercomputing Centre (JSC) and HHU Düsseldorf. The exploration of novel laser-driven compact X-ray sources is also carried out through the use of high-resolution particle-in-cell (PIC) simulation codes (e.g., EPOCH). The simulation developments will be complemented by experimental campaigns, e.g., at the PHELIX laser facility at GSI.

1.1.2 Hardware

JULIC JULIC (Juelich Light Ion Cyclotron) is currently used as injector for COSY, providing beams of protons and deuterons via stripping injection of 45 MeV H- or 76 MeV D-, respectively. It is also used for radioisotope production inside the cyclotron hall and, more recently, a dedicated beamline has been built to serve an external target station with direct p- and d-beams – this is used, e.g., for research for the HBS (High Brillance neutron Source) project of JCNS (Jülich Center for Neutron Science).

COSY The COoler SYnchrotron (COSY) is a worldwide unique facility for polarized and phase-space cooled hadron beams, which was utilized for hadron physics experiments until the end of 2014, and since then has been used as a test and exploration facility for accelerator and detector development as well as for the preparation and execution of precision experiments (PAX, JEDI, TRIC). The COSY facility comprises sources for polarized and unpolarized protons and deuterons, the injector cyclotron JULIC (see above), the synchrotron to accelerate, store and cool beams, and internal and external target stations for experimental set-ups. H- (D-)-ions are pre-accelerated up to 0.3 (0.55) GeV/c in JULIC, injected into COSY via stripping injection and subsequently accelerated to the desired momentum below 3.7 GeV/c. Three installations for phase-space cooling can be used: (i) a low-energy electron cooler (between 0.3 and 0.6 GeV/c), installed in one of the straight sections, (ii) stochastic cooling above 1.5 GeV/c, and (iii) a new high-energy electron cooler in the opposite straight section, which can be operated between 0.3 and 3.7 GeV/c.

Polarization Equipment Well-established methods are used to preserve polarization during acceleration. A fast tune jumping system, consisting of one air-core quadrupole, has been developed to overcome depolarizing resonances. Preservation of polarization across imperfection resonances is achieved by the excitation of the vertical orbit using correcting dipoles to induce total spin flips. A superconducting solenoid enables spin manipulation as partial or full snake. The polarization can be continuously monitored by an internal polarimeter (EDDA); an additional polarimeter, making use of the WASA forward detectors, has recently been set up, and a further new polarimeter, based on LYSO- scintillators, is under development. For protons, a beam polarization of 75% up to the highest momentum has been achieved. Vector and tensor polarized deuterons are also routinely accelerated with a degree of polarization of up to 60%. Dedicated tools have been developed to manipulate the stored polarized beam and to precisely determine the beam energy.

Detectors

Straw Tracker Stations (STS) Based on the experience with straw-tube trackers for PANDA, IKP is building one STS for HADES, comprising 704 straws (length about 76 cm) in 4 double layers, including the readout system, for the FAIR Phase-0 program with a pion and a proton beam. The straw modules will later be used in the PANDA Forward-Straw-Tracker.

KOALA The luminosity determination at PANDA for absolute cross section determination will be achieved by measuring this antiproton-proton elastic scattering rate in the Coulomb-nuclear interference region. In order to measure the recoil proton, high precision silicon strip detectors of 1 mm thickness and germanium strip detectors of 5 and 11 mm thickness have been developed. With a pitch of 1.2 mm these measure both recoil angle and deposited energy in order to cleanly identify this process down to a four momentum transfer below $|t| = 0.001$ (GeV/c)2.

LYSO Polarimeter The polarimeter currently consists of 52 individual modules, arranged in 4 segments (up, down, left, right), which can be changed according to requirements. The modules are made from Lutetium-yttrium-oxyorthosilicate (LYSO), an inorganic scintillator crystal, which have a size of 30x30x80 (mm)3. They are read out by silicon multipliers (SiPM). Their time resolution is well below 1ns, the energy resolution for deuterons at 200 MeV is roughly 4%.

WASA Detector After an initial operating phase at the TSL in Uppsala, the WASA detector has been in operation at COSY from 2006 to 2014, producing numerous published physics results. Currently, components of the forward detector systems are being used as a polarimeter for the JEDI measurements, and most of the central calorimeter and tracking detectors have been/will be transferred to GSI where they are planned to be used in Phase-0 experiments for NuSTAR.

1.2 Cooperations

IKP cooperates with numerous national and international universities and research institutes via individual research projects or as a partner in international collaborations. The following list includes the major collaborations during the PoF-III period.

1.2.1 National

German universities and research institutes: GSI Helmholzzentrum für Schwerionenforschung GmbH (including the Helmholtz Institute Mainz (HIM) and Helmholtz Institut Jena (HIJ), Westfälische Wilhelms-Universität Münster, Forschungszentrum Dresden-Rossendorf, Heinrich-Heine Universität Düsseldorf, TU Dortmund, Rheinische Friedrich-Wilhelms-Universität Bonn, Friedrich-Alexander-Universität Erlangen-Nürnberg, Eberhard Karls Universität Tübingen, Justus-Liebig-Universität Giessen, Universität Regensburg, Ruhr-Universität Bochum, RWTH Aachen University, DESY, TU München, Goethe-Universität Frankfurt and TH Darmstadt. JARA-Fame has been founded by IKP and RWTH Aachen University in 2013 in order to coordinate the research in the field of antimatter. More specifically, the scientific focus is on the “fate of anti-matter": baryo- and leptogenesis.

1.2.2 International

Agrarian University (Tbilisi, Georgia), BINP (Novosibirsk, Russia), CERN (Geneva, Switzerland), Georgian Technical University (Tbilisi, Georgia), PNPI (Gatchina, Russia), Tbilisi State University (Tbilisi, Georgia), Polish Academy of Sciences (Poland), Uppsala University (Uppsala, Sweden), Duke University (USA), Jagiellonian University (Krakow, Poland), Institute of Nuclear Physics PAN (Krakow, Poland), Jefferson Laboratory (Newport News, USA), Indian Institute of Technology (Indore, India), L.D. Landau Institute (Moscow, Russia), University of Groningen and Kernfysisch Versneller Instituut (The Netherlands), ITEP (Moscow, Russia), Universitá degli Studi di Ferrara and INFN (Ferrara, Italy), IMP Chinese Academy of Sciences (Lanzhou, China), Southwest University, School of Physical Science and Technology (China), JINR Dubna (Moscow Region, Russia), Michigan State University (USA), Brookhaven National Laboratory (USA), Laboratoire de Physique Subatomique & Cosmologie (LPSC) (Grenoble, France), CAPP/IBS (Daejeon, South Korea), Department of Physics of Cornell University (USA)

1.2.3 Collaborations

ANKE (COSY), bERLinPro (HZB), Borexino (LNGS, Italy), CLAS (JLab, USA), PANDA (FAIR), JEDI (COSY) and CPEDM (CERN), ELENA (CERN), FCC (CERN), JUNO (Jiangmen, China), PAX (COSY), SOX (LNGS, Italy), TOF (COSY), TRIC (COSY), WASA (COSY) and WASA (FRS)

1.3 Current Uses

1.3.1 JULIC as Test and Development Machine for HBS

The dedicated beamline from the cyclotron to the nearest experimental area is currently used by the JCNS (Jülich Center for Neutron Science) group, which intends to build a High Brilliance neutron Source (HBS). After basic investigations like, e.g., measurements of neutron production cross sections by low-energy proton and deuteron beams, JULIC can in future also serve as test and development machine for HBS prototypes.

1.3.2 JULIC as Radioisotope Production Research Facility

JULIC, the injector of COSY, provides beams for ongoing radionuclide development of INM-5. The wide range of beam energy and its flexible operation mode are quite unique in the landscape of available facilities in Europe. Together with INMs on-site very experienced radiochemistry group with an impressive track record in the measurement of excitation functions and development of radionuclides. Currently, irradiations exploiting 45 MeV protons of JULIC are used to explore the production of ^{73}Se as the basis of a new tracer development. The deuteron beams of up to 76 MeV are also planned to be used for radionuclide production like, e.g., ^{72}As, ^{47}Sc and ^{67}Cu.

1.3.3 COSY as Test and Development Platform for FAIR

A significant fraction of the COSY operating time is devoted to test measurements of accelerator and detector systems under development for FAIR. Investigations of various setups of straw tube detectors and their readout electronics have been essential for the STT and FTS systems at PANDA, as well as for the STS1 chambers for the PANDA-Phase-0 experiments

at HADES. Similarly, a significant amount of beam time has been made available to enable critical developments of silicon tracking detectors for CBM and PANDA. Tests of particle identification detectors (e.g. RICH, SiTil, FToF for CBM or PANDA) and calorimeters (PWO for PANDA) are completed or ongoing. Experience since 1993 with e.g. complementary cooling methods, slow extraction, polarized beams and development of beam instrumentation enables tests and benchmarking of state-of-art tools. Especially for beam instrumentation prototype testing, calibration and studies with a broad range of beam qualities are possible at COSY. To guarantee smooth commissioning and operation of the HESR the ion-optical design has been optimized with beam-dynamics simulations. IKP-4 with ZEA-1 operates test equipment for qualification of magnet, radio frequency, instrumentation and vacuum systems. Ongoing measurements of the magnetic fields of the already produced bending dipoles and quadrupoles deliver a more precise insight to the harmonic content of these elements. Dynamic aperture calculations are updated by including new measurement results. Benchmarking the complex software codes with measurements at COSY is mandatory. Without the originally planned RESR (Recuperated Experimental Storage Ring) – which was intended as an accumulator for antiprotons before injection into the HESR, the required redesign of the acceleration system of HESR has been successfully completed. Using a scheme of longitudinal stacking, HESR capabilities were extended to cover the accumulation function previously assigned to RESR. One highlight of the developments of FZJ for HESR is the use of newly invented antennas for the stochastic cooling pick-ups and kickers, which avoid movable electrodes. This cooling method is needed for HESR to deliver particle beams with highest phase space density to the experiments. In-house manufactured systems are tested at COSY routinely until delivery of the last components.

1.3.4 COSY as Test and Development Machine for EDM

The search for Electric Dipole Moments (EDM) of charged particles (foremost protons and deuterons) in storage rings at sensitivities higher than current or future aims for neutrons requires the design and construction of new rings (all electric for protons, combined E-B for deuterons; counter-rotating beams). The necessary technologies (high E-fields, shielding of external B-fields, polarimetry etc.) need to be developed and tested. COSY – although being a conventional storage ring with magnetic deflectors – is the only but still ideal test facility worldwide. It needs to be maintained not only for the proof-of-principle measurement (precursor experiment) but most probably also as injector for a demonstrator ring.

1.3.5 COSY as Education Facility for Accelerator Science

A significant fraction of the beam time at COSY is devoted to beam development and equipment tests. This is frequently also used to train young accelerator scientists in order to gain experience in operating COSY, including the injector, the transfer beam line to the storage ring and the extraction out of the ring to external target stations. We also provide practices for students, e.g. from RWTH Aachen university, where one of our staff is professor of physics, teaching accelerator science.

1.4 Future Program Opportunities

Based on the expertise and science projects mentioned above, the following sections outline possible future contributions to the Helmholtz research fields.

1.4.1 Projects with FZJ

HBS With the expected fading of currently operational reactor facilities, it is expected that a regional neutron source with competitive brilliance and flux can be a significant complement to the upcoming powerful European Spallation Source. To define the design of HBS, it is highly valuable for the HBS team to continue conducting neutron production measurements, target and moderator studies with both proton and deuteron beams at various energies to benchmark their simulations for optimization accordingly.

ATHENA IKP-2/4, together with PGI-6, are participating in the ATHENA project (Accelerator Technology HElmholtz iNfrAstructure). ATHENA is a multi- center project within the Helmholtz Association, which aims to develop compact and cost-effective laser plasma accelerators with applications in science and medicine. IKP-4 will bring in its expertise on the production of polarized hadron beams. Among the scientific goals of ATHENA is to generate such beams worldwide for the first time as well as to produce neutron bunches with laser-plasma technology. These activities include Monte-Carlo simulations on the FZJ supercomputers in the Supercomputing Centre (JSC). Within ATHENA the JuSPARC laser system at Jülich will also be upgraded. The two FZJ institutes are also associated partners of EUPRAXIA (European Plasma Research Accelerator with eXcellence in Applications). Its aim is to provide a conceptual design report for the first 5 GeV plasma-based accelerator in the world with industrial beam quality and user areas.

Radioisotope Production Research Facility At the external beamline of COSY, a new irradiation facility to study reaction cross sections for radioisotope production has been constructed, which allows high-precision measurements with protons up to about 150 MeV. First experiments have started and further studies, e.g. for terbium isotopes, are planned.

1.4.2 Projects with GSI/FAIR

HESR The HESR is a central part of the upcoming FAIR at GSI (Darmstadt) and was designed originally to accelerate and store antiprotons in the momentum range between 1.5 GeV/c and 15 GeV/c, but it will now also be possible to provide heavy ion beams with momenta between 0.6 and 5.8 GeV/c. IKP-4 is leading all activities to build the High Energy Storage Ring for FAIR (except for the building with its infrastructure). After completing the design of the High Energy Storage Ring (HESR), the accelerator group is currently carrying out the realization of all HESR core components together with colleagues in the central workshops of FZJ (ZEA) as well as the collaborators from HESR international consortium. IKP-4 maintain key components and systems as well monitors and interact in the process of civil construction to make sure all details for installation are followed up. For accelerator physics, including operations, IKP-4 continues to study details on accelerator control and beam dynamics, beam control and the required instrumentation. Carrying out HESR or other FAIR related tests and developments at COSY, beam time needs to be available upon request.

PANDA Members of IKP have been making major contributions to the collaboration since its inception. Straw tube technology developed at IKP is the basis for the STT and FTS systems and IKP has taken over the project management to construct the STT. Furthermore, IKP is responsible for the mechanical structures as well as main aspects of the strip detectors for the MVD. Software developments, in particular (but not limited to) track reconstruction are important contributions of IKP to the experiment. Another major activity is the preparation of KOALA, which will provide the normalization needed to that the luminosity detector can attain the necessary absolute precision.

HADES In order to gain operational experience of the PANDA detectors before the full facility is online, some of the systems will temporarily be added to the HADES experiment to investigate pion and proton induced reactions. These systems will cover the small polar angle region where HADES has no acceptance for charged particles, and will dramatically increase the efficiency for hyperon reconstruction in elementary reactions near threshold. IKP will use these data to investigate (virtual) photon transitions in the hyperon spectrum.

PAX The provision of an intense beam of polarized antiprotons would be a great asset and could be a far-future option for a possible HESR-upgrade into a (double) polarized proton-antiproton collider. Based on our experience with protons at COSY to exploit spin-filtering as the method to produce polarization, we could take the tests up again at FAIR, once antiprotons will be available.

NuSTAR After a decade of intense use, WASA-at-COSY ceased operation at the end of 2014. Since then individual components have been used for dedicated studies, such as the forward detectors as a polarimeter and the pellet target to study beam target interactions. Now, the detector systems surrounding the interaction region are being transferred to GSI to be used for FAIR-Phase-0 experiments at the FRS.

1.4.3 Other Projects

CPEDM (Demonstrator, possibly at COSY; final Ring, probably at CERN) The charged-particle EDM search (CPEDM) is a long-term project, which must proceed in stages: currently, essentially all of the experimental work in this field is going on at COSY (see above). The ultimate goal will be a dedicated all-electric storage ring for protons at frozen-spin momentum (0.7 GeV/c) and with clock-wise and counter-clock-wise beams, aiming at a sensitivity of the order of 10^{-29} ecm. As an inevitable intermediate step, a demonstrator all-electric ring at much lower energy (around 30 MeV) is required to demonstrate the fundamental operation principles and to scrutinize/ mitigate the risks. Possible host institutions for this demonstrator are IKP/ COSY (because of the available polarization equipment) and CERN. Recently, it has become clear that all srEDM rings – including COSY in its current set-up – can be used to search for axions (a possible dark-matter candidate) in yet unexplored mass ranges, which also are not (easily) accessible by any other running or proposed measurement.

Neutrino Physics at Borexino and JUNO After data taking with Borexino will be finished in 2020/21, the analysis of data to study CNO- and geo-neutrinos will continue. Emphasis will then shift towards commissioning and data taking with JUNO to study the neutrino mass hierarchy and leptonic CP violation. It is also considered to join a new neutrino project (like, e.g., THEIA, a proposed multi-purpose large-scale neutrino detector in its very early design stages, which aims to utilize water-based liquid scintillator).

Polarized Molecules The polarized Atomic Beam Source (ABS) of COSY-ANKE is now in use in the laboratory to produce nuclear polarized molecules from hydrogen and its isotopes. It is planned to freeze these molecules to produce polarized ice, in which the spins of the protons and deuterons can be adjusted by the ABS separately. Such polarized ice-targets can be employed in nuclear reactions and fusion.

Polarized Fusion The increase of the energy output or the reduction of costs of a fusion reactor by the use of polarized fuel has been discussed for many years. At IKP, a group is exploiting their experience in polarized sources and targets to solve the outstanding problems (e.g. unknown cross sections) and develop the required techniques.

CLAS12 Given the extended time frame until the PANDA experiment is in the data and physics production phase, IKP is making significant contributions to the CLAS12 experiment at JLab. The activities focus on software developments for the tracking detectors and analysis of mesonic transition form factors.

1.5 Summary

The above brief outline of the scientific infrastructure and the know-how of the personnel of the Institute for Nuclear Physics in conjunction with the outstanding scientific program undoubtedly warrant a continuation of the institute in spite of the strategic decision of Forschungszentrum Jülich to withdraw from particle and nuclear physics by the end of PoF-III (Dec. 31, 2020). It is expected that this can be achieved in PoF-IV and beyond with the new administrative home of IKP, GSI Helmholtzzentrum für Schwerionenforschung in Darmstadt, via the ongoing transition project “TransFAIR".

2 Scientific results

2.1 Accelerator research

2.1.1 HESR

IKP is leading the international consortium which is dedicated to build the HESR. It is strongly supported by colleagues from the Central Institutes for Engineering and Analytics (ZEA) of the Research Center Jülich. About 60% of the total project investment money could be either spent or is bound by contract. IKP aims to have as many components ready for delivery to Darmstadt as possible until end of 2020. That is the scheduled date for moving the most of the IKP institutes to FAIR, at least administratively. A new schedule has shifted the ground breaking for the HESR tunnel to 2020, the release of the buildings to users (e.g. HESR) to the end of 2021, and the start of the commissioning of the facility to the end of 2022. This schedule depends upon the progress of the buildings construction: HESR is one of the last buildings that will be built on the FAIR campus.

Magnets All 46 dipole and 84 quadrupole magnets are manufactured and delivered to Jülich. The most important magnetic properties are measured, more detailed measurements are done on random samples. Preassembly of 33 of 46 dipole magnets is completed and those magnets are already at the storage place in Darmstadt. 4 of the dipole magnets need a dedicated vacuum chamber as they are located in the vicinity of the SPARC experimental stations. The chambers will be equipped with inlet and outlet for a LASER beam. These chambers are being produced. Corrector magnets as sextupoles, horizontal and vertical steerers are still in production at our Romanian partners. These magnets are routinely delivered to Jülich. Further magnets such as septum, injection dipole, chicane dipoles are in production at the respective companies. Last delivery to Jülich for these devices is expected in 2019.

Power Converters The start of the acquisition of the main dipole power converters has been scheduled for summer 2019. This will allow the acceptance test at the original load. The power converters for the quadrupole magnets are on site in Jülich and are regularly powered to avoid early aging of the capacitors. The power converters for the correction magnets are part of the Romanian in-kind contribution and are in production. First devices arrived in Jülich and are being subject to the acceptance tests. The power converters for the remaining magnets are either close to completion or already in site in Jülich. Some dedicated devices needed to ease the connection between the coaxial load cables and the magnets are in production, and some of them could already be stored close to Darmstadt.

RF system The air cooled high harmonics cavities are in mechanical design. Mock-ups have shown the feasibility of the design. Ferrite cores as well as solid state power amplifiers are on site. Mechanical work is expected to be close to completion in 2019. 2020 will be needed for control design and realization.

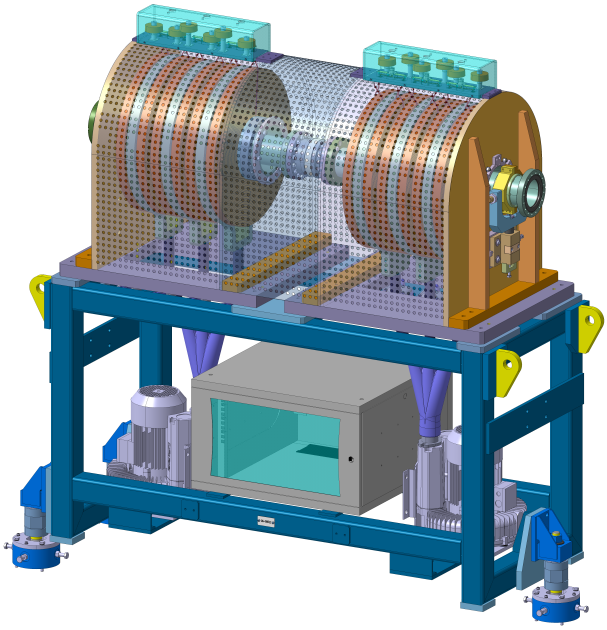

Fig. 1: Final design of the HESR cavity shown with transparent cover. This cavity will be operated also in barrier bucket mode. Using air cooling is favourable for the operation with low noise semiconductor amplifiers. The fans directly below the resonator are blowing the air via dedicated carbon fibre disk with special cooling channels between the ferrite disks. On top of the resonator there are 'tuning' capacitors for each ferrite disk to ensure a broad range of 50 Ohm operation.

Injection Each 10 seconds 10^8 antiprotons will be available for injection into the HESR. After 100 injections acceleration to the final energy with subsequent data taking will start. 4 kicker magnets will be enough to generate a deflection of 6.4 mrad at 3 GeV injection energy. Each magnet will be powered by a pulser power supply which will allow a rise time (and fall time) of 200 ns with a flat top time of 500 ns. With these parameters the HESR can be operated as an accumulator. A test tank for the first magnet has been produced and sent to the contractor building the complete system. Exploiting the Blumlein topology, the power supply can be built relying on semiconductor switches (40 kV, 4000 A). The required pulse shape has been proven with a dummy water line equivalent to the finally used cables. The manufacturer now is testing the specially designed HV coaxial cable. The production of the magnets is waiting for the delivery of the ferrite blocks.

Beam Diagnostics The beam position monitors (BPMs) are in production. The test bench is awaiting the first deliveries. 4 types of differing mechanical length of the attached beam pipes have been defined. The hardware for the beam loss monitors (BLMs) has been bought. The BLMs will be assembled with a joint effort of Jülich and Darmstadt beam diagnostics colleagues. Viewers and scrapers are close to production. Some devices needed only in low number (1 - 2 pieces) still need to be designed mechanically or need to be bought. In the case of mechanical designing, resizing COSY type equipment will be sufficient. E.g. strip line unit, beam profile monitor, nonresonant Schottky pickup, wall current monitor, tune meter. HESR operation with antiprotons requires special attention to the ions originating from the residual gas present in the vacuum pipes. These ions will give rise to an electric potential disturbing the antiproton motion. The ions will be removed using rather small electrostatic fields generated in the ion clearing chambers. They have been designed in Jülich and are presently in production at a company. Wherever possible they will be installed at regular intervals to remove the disturbing ions.

Vacuum, Mechanical Design, Space Management According to the detailed physics design of the individual components comprising the HESR, the required mechanical design of the vacuum vessels , the design of the vacuum system, the tracking of the production at the different companies etc. have been carried out. In many cases own test procedures have been worked out and scenarios have been evaluated. All components are stored electronically to set up the 3D space management. The shape and the built-in details of the building (tunnel and PANDA hall) is regularly updated in co-operation with the Darmstadt colleagues. Equipment which does not allow full baking (250 deg.) has been identified. Thus nearly the complete HESR will be equipped with a baking system. In the arc sections it will also allow activating the NEG coating of the dipole chambers. The heating procedure will be controlled locally on-site. 33 dipole magnets are equipped (by the end of 2018) with vacuum chamber and heating jackets. For each magnet the position of the fiducials is recorded. These magnets are al- ready at the storage area in Darmstadt waiting for the instal- lation. Preassembly of the remaining dipole magnets is expected to be finished during Q2/2019. The preassembly of the 50 quadrupole groups in the arc sections is being set up. One group consists of the quadrupole magnet, typically with a sextupole in combination with a BPM, a steering magnet with an ion clearing chamber, and two pumping chambers. All these components are installed on a common girder. If BPMs and ion clearing chambers together with their heating jackets arrive in time, and if the personnel presently being engaged will be continuously available, the units will be ready for installation by the end of 2019. In parallel the girders for the straight sections will be designed to get them ready for preassembly by the end of 2019. Altogether about 200 units need to be preassembled and transported to Darmstadt.

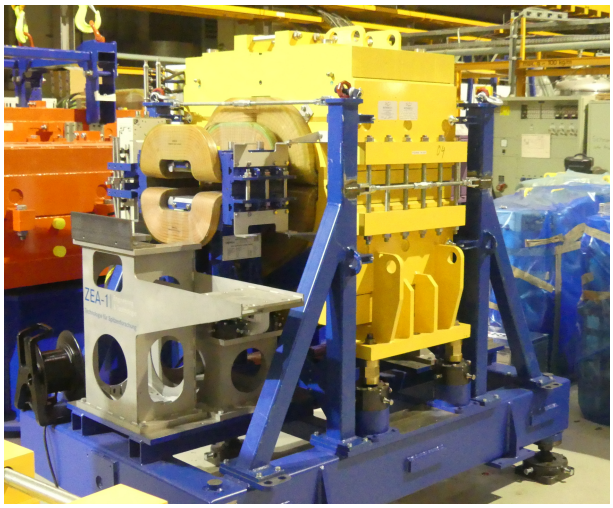

Fig. 2: Quadrupole assembly as used for tests whether the magnets stay in position after road transport. The quadrupole magnet (5.2 t) is positioned in the middle of the frame. To the left side of the quadrupole magnet there is placed a horizontal steering magnet (350 kg) on a dedicated small supporting table. The bearer with the label “ZEA-1" will carry the pumping chamber. 50 of these units are needed in the arc sections of the HESR. Pre-assembly will start in 2019.

Stochastic Cooling Work meanwhile is focused on (i) the assembly of pick-up and kicker tanks in the clean room and (ii) the control circuits. In experiments at COSY the powerful cooling has been validated in various tests. The 2-4 GHz power amplifiers are continuously being delivered. End of assembly is expected in early 2020. Imminent construction works (installation of fire protection doors etc.) in the clean room building might require moving the clean room to a different building. That activity might put the assembly on the critical path.

Experiment Integration Right from the beginning the PANDA experiment and the SPARC experiment will be installed in the HESR. The PANDA analyzing dipole magnet requires to be accompanied by 2 chicane dipole magnets to keep the particle trajectories in HESR closed. In the PANDA hall the floor will be lowered to allow the large diameter equipment of PANDA to be installed at the proper beam height. PANDA installation will happen in 3 stages: Initially, HESR will be commissioned without the PANDA chicane. The chicane magnets (but not the PANDA dipole) will be in place but operated with zero current. The vacuum pipe will be straight. In a second stage the PANDA dipole will be installed in the beam path, but not the PANDA detectors. From that time

on, the chicane magnets together with the PANDA dipole magnet will be operated at their nominal field required by the chicane geometry. In phase 3 the PANDA detectors will be moved into the beam line. HESR is fully planning stage 1 taking into account as much as reasonably possible all details that become known for stages 2 and 3. This includes connecting the vacuum pipe crossing the PANDA detector to the HESR vacuum pipes. Interfaces to the PANDA target etc. have been defined. SPARC requested two experiment stations, one in the northern arc and one in the southern arc of the HESR. The available space for the installations in the vicinity of the interaction point has been defined. Further places for small detectors have been agreed upon. Measures to protect the HESR against failures of gas filled detectors inside the HESR vacuum system have been taken.

2.1.2 Beam cooling

Introduction One of the key systems in HESR is the stochastic cooling system. It is not only essential for enhancing the beam quality for the experiments but is also indispensable for the accumulation of anti-protons in HESR. First longitudinal and vertical cooling was already achieved in 2017, but so far no simultaneous cooling in all three planes.
One of the required targets of the PANDA experiment is being built by scientists at the Münster University. This cluster-jet target has been installed and successfully commissioned in COSY during summer 2018. Electron cooling is the method of choice in achieving the smallest possible momentum spread and transverse emittance. An electron cooler is envisaged for the HESR beyond the modularized start version. Furthermore, it has been shown, that electron cooling at injection energy can benefit the heavy ion operation of the HESR significantly. Beam studies dedicated to high energy electron cooling were carried out at COSY to pave the way for the best possible momentum resolution in the HESR.

First 3D cooling with original HESR Pickup and Kicker The system was extended with an additional hollow fiber line and optical delay-lines. Two high power amplifiers for the vertical plane, two for the horizontal and one for longitudinal cooling were installed. Two groups of the HESR kicker were used for both transverse planes and one halve group for longitudinal cooling. Even with this 'light' stochastic cooling version a full 3D cooling was achieved. New measurement systems and improved software reduced the system set-up time significantly.

PANDA Target meets HESR Stochastic Cooling System in COSY The Münsteran target nearly reached the design value. With 10^{15} atoms/cm^2 it is the thickest cluster target ever installed at COSY. Figure 3 shows the Schottky signal of the 1500$^{\text{th}}$ harmonics without stochastic cooling and barrier-bucket operation. The slip-factor was measured to $\eta = -0.035$. Thus the energy loss due to the thick target is reflected in a shift to higher frequencies of the Schottky signal.
Without cooling and barrier-bucket the circulating beam is broadened and its intensity decreases as particles are lost by hitting the vacuum chamber walls. At some point

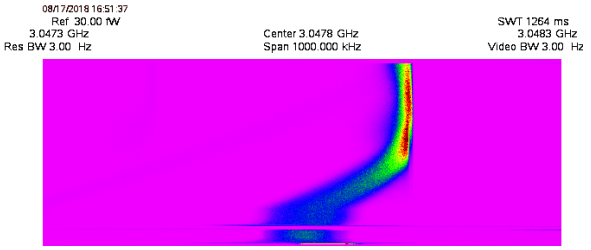

Fig. 3: A spectrogram of a Schottky signal of 1500$^{\text{th}}$ harmonics (only target). The horizontal axis shows frequencies from 3.0473 to 3.0483 GHz. The vertical axis represents time from bottom to top. Schottky signal power is coded by color. Two machine cycles are shown. The duration of the longer one amounts to 320 s.

the local slip-factor changes the sign. Further energy loss now results in a negative frequency change while particles are still loosing energy. Almost all particles were lost during the 5-minute cycle.
The COSY Barrier-Bucket cavity allows barrier-voltages up to $\pm 200V$. With the small eta-value at the momentum of 2.425 GeV/c, the barrier-voltage is to small to capture all particles. Particles outside the bucket get lost in the same way as without barrier-bucket(see figure 4). But also particles inside the barrier leave the bucket after some minutes.

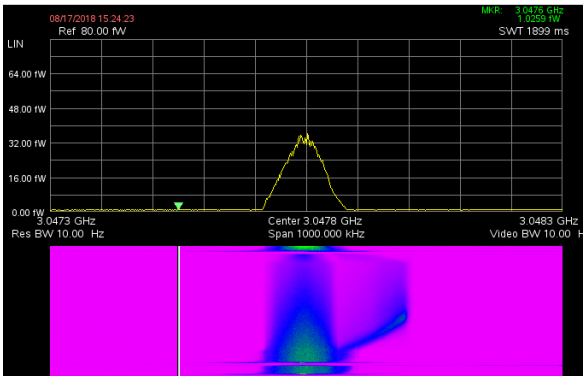

Fig. 4: A spectrogram (lower plot) and a frequency spectrum (upper plot) of a Schottky signal of 1500$^{\text{th}}$ harmonics with barrier-bucket and target. The upper plot corresponds to the top trace shown in the lower plot. See Fig. 3 caption for more details.

With longitudinal cooling a fast cooling was observed at the beginning of the cycle. The momentum spread was decreased by a factor of 2 and a very stable equilibrium was observed for the rest of the 5-minute cycle. Beam

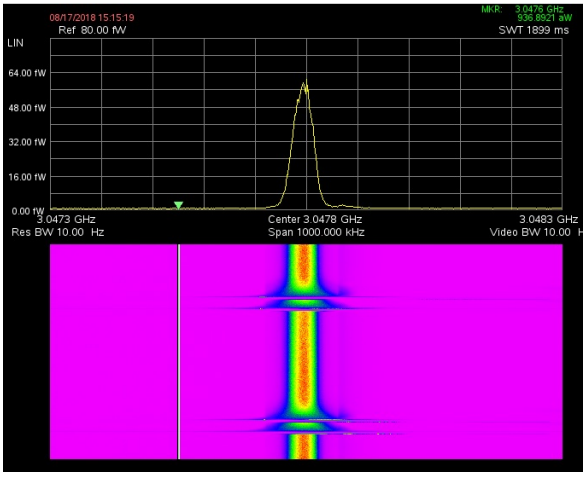

Fig. 5: Schottky signal of 1500th harmonics with stochastic cooling, barrier-bucket and target. See Fig. 4 caption for more details.

losses were significantly reduced. Transverse cooling not only compensates for beam size growth by the target, it was able to reduce the equilibrium emittance even by factor 2 in both planes (see figure 6).

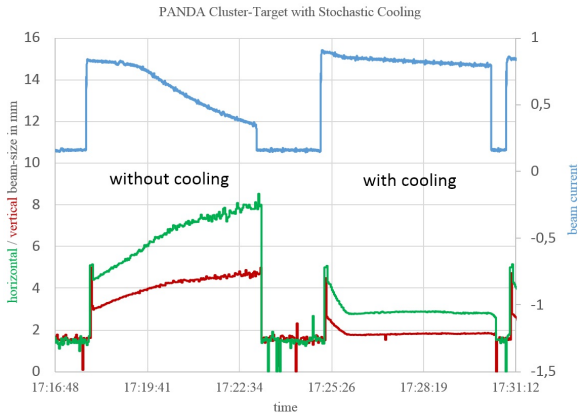

Fig. 6: Beam current and beam size with (right) and without stochastic cooling (left)

Combined application of stochastic and electron cooling Figure 7 shows the benefits of both cooling methods. Transverse stochastic cooling was applied during the first 200 seconds. This quickly led to a significant reduction of transverse emittance. After the stochastic cooling was turned off electron cooling was applied. The electron cooling clearly benefited from the transverse stochastic pre-cooling leading to fast longitudinal electron cooling accompanied by further reduction of the emittance. The joint action of the transverse stochastic and electron cooling as well as an internal cluster-jet target is illustrated in figure 8. The target density was reduced by an order of magnitude for this measurement in order to reduce the emittance growth as the current electron cooling setup could not compensate the fast emittance blowup due to the thick target. The transverse stochastic cooling was

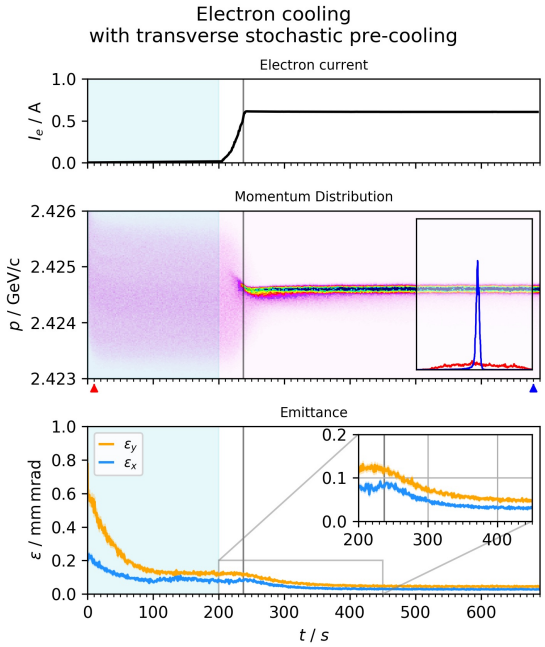

Fig. 7: Transverse stochastic cooling (0-200 s) followed by electron cooling. Shown are the electron current (upper plot), the momentum spread and the evolution of transverse emittance (lower plot).

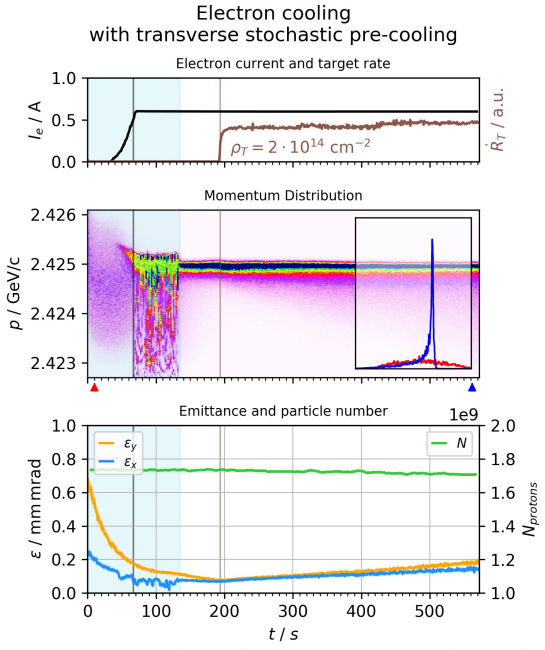

Fig. 8: Compensation of momentum spread growth due to $2 \cdot 10^{14}$ atoms/cm^2 thick target by electron cooling. Shown are the electron beam current and the detector count rate (upper plot), evolution of momentum distribution (center), evolution of transverse emittance and beam current (lower plot). Transverse stochastic cooling was applied during the first 140 seconds of the machine cycle.

very helpful in quickly reducing the proton beam emittance so that electron cooling became more effective. The detector rate does not represent all the events that oc-

curred due to the interaction of the beam with the target. This rate can only be used for qualitative comparison as only a part of the detector was active. We have shown, that electron cooling was able to keep the core of the beam well cooled during the operation of an $2 \cdot 10^{14}$ atoms/cm^2 thick internal cluster-jet target.

2.2 FAIR Experiments

2.2.1 PANDA

In the recent years substantial effort was invested in studying the nucleon and Δ spectrum in photon induced reactions at various laboratories worldwide. In contrast, only marginal progress has been made in the last three decades in improving our knowledge of the excitation spectrum of the multistrange baryons Ξ and Ω. If SU(3) flavor symmetry approximately holds, each of the know $N^\star$ and Δ states should have a corresponding partner state in the Ξ spectrum. However, so far only very few Ξ states have been assigned, mostly on a tentative basis. Improving the data base for both Ξ and Ω states would be very important to understand the relevant degrees of freedom determining the baryon excitation pattern and to scrutinize the theoretical models developed mostly based on data in the non-strange sector. Thanks to the $\bar{p}p$ entrance channel and the large acceptance for both charged and neutral particles, $\overline{\text{P}}$ANDA is the ideal instrument for studying multi-strange baryon spectra. The expected cross sections are relatively large ($\sigma(\bar{p}p \to \bar{\Xi}^+\Xi^-) \simeq 2\,\mu$b), and the detector allows to study a large variety of decay modes of the resonant Ξ states, the knowledge of which is relevant for understanding their structure.

PandaRoot Simulations Full PandaRoot simulation studies have been performed for three final states sensitive to different $\Xi^\star$ decay modes, the study of a forth channel has been started. Details on the status of the simulation studies are shown in Table 1.
In all cases, the Monte Carlo event generator EvtGenhas been used to generate the signal events at incident antiproton momentum of 4.6 GeV/c. This momentum corresponds to a center-of-mass energy about 100 MeV above the $\Xi(1820)$ resonance, being the state with the highest mass of the states listed by the particle data group that can be populated at the selected momentum. In addition, single pion decay is energetically possible for the decuplet ground state $\Xi(1530)$ and for the $\Xi(1690)$ state whereas the decay modes ΛK^- and $\Xi^-\pi^+\pi^-$ are kinematically only allowed for the two higher-mass states $\Xi(1690)$ and $\Xi(1820)$. All states which may kinematically contribute to the decay modes listed in Table 1 have been included in the generation of signal events with EvtGen in simulation and analysis of the respective reaction channel. A continuum contribution to the given final state was also taken into account. The one-star state $\Xi(1620)$which was recently confirmed by Bellewas not included in the generation of signal events.

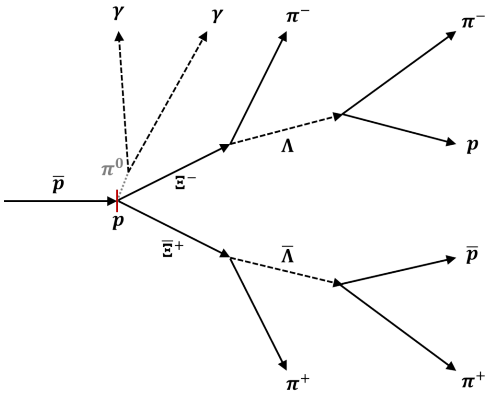

Fig. 9: Decay tree of the generated $\bar{\Xi}^+\Xi^-\pi^0$ final state.

The considered reaction channels have complex decay trees with three ($\bar{p}p \to \bar{\Xi}^+\Lambda K^-$ & c.c.) or four ($\bar{p}p \to \bar{\Xi}^+\Xi^-\pi^+\pi^-$, $\bar{\Xi}^+\Xi^-\pi^0$) displaced decay vertices of Λ and Ξ hyperons, and at least six charged quasi-stable particles in the final state, as shown in Fig. 9. Two different methods of reconstructing the decay tree have been used. As first approach, the decay tree was reconstructed step by step for each decay, starting form the $\Lambda \to p\pi^-$ ($\bar{\Lambda} \to \bar{p}\pi^+$) decay with a geometrical vertex fit. The vertex fitted candidates then passed a kinematical fit with a constraint to the parent Λ mass. This procedure was repeated for the $\Xi^- \to \Lambda\pi^-$ ($\bar{\Xi}^+ \to \bar{\Lambda}\pi^+$) decay. In the last step the daughter particle system of the $\bar{p}p$ system was reconstructed with a vertex fit and a subsequent four-constraint fit to the initial four-momentum vector. Alternatively, in the second approach, the whole decay tree was fitted in a single step with a "decay tree fitter", having the advantage that it results in a consistent set of four-momenta of the particles across all generations within the decay tree.
For all considered reaction reaction channels the achievable ratio of signal to hadronic background events was evaluated by using the event generator DPM based on the Dual Parton Modelrepresenting the total inelastic $\bar{p}p$ cross section. In all cases, no background event survived the applied selection criteria, resulting in a lower limit for the signal-to-background ratio.

Analysis Results *Analysis of $\bar{\Xi}^+\Lambda K^-$ & c.c.*: About 10 million signal events with a 2:2:1 ratio of contributions of the resonant states $\Xi(1690)$ and $\Xi(1820)$, and a non-resonant continuum, respectively, were simulated and analyzed for the two charge conjugated final states. Fig. 10 shows the $\bar{\Xi}^+\Lambda K^-$ Dalitz plot and the ΛK^- invariant mass distribution of the reconstructed final event sample as obtained in a tree fit analysis, not using Monte Carlo information on the particle species. Within statistical fluctuations the corresponding distributions of the charge conjugate final state are identical.
Total reconstruction efficiencies of 5.4% and 5.5% were obtained for the $\bar{\Xi}^+\Lambda K^-$ and for the $\Xi^-\bar{\Lambda}K^+$ final state,

Table 1: Unless self-conjugate, decay modes and final state implicitly include the charge conjugate case as well, "conventional" denotes a step-by-step reconstruction of the decay tree, as explained in the text, "tree fit" is for a full fit of the complete decay tree in a single step, "PID" indicates that the analysis does *not* use Monte Carlo information on the particle species, "version" specifies which PandaRoot version has been used (either more than one year old or up-to-date).

decay mode	final state	conventional	tree fit	PID	version
$\Xi^{\star-} \to \Lambda K^-$	$\bar{\Xi}^+\Lambda K^-$	done	done	done	new
$\Xi^{\star-} \to \Xi^-\pi^+\pi^-$, $\Xi^{\star 0} \to \Xi^-\pi^+$	$\bar{\Xi}^+\Xi^-\pi^+\pi^-$	done	done	started	$> 1\,y$
$\Xi^{\star-} \to \Xi^-\pi^0$	$\bar{\Xi}^+\Xi^-\pi^0$	done	started	started	$> 1\,y$
$\Xi^{\star-} \to \Xi^-\eta$	$\bar{\Xi}^+\Xi^-\eta$	–	started	planned	new

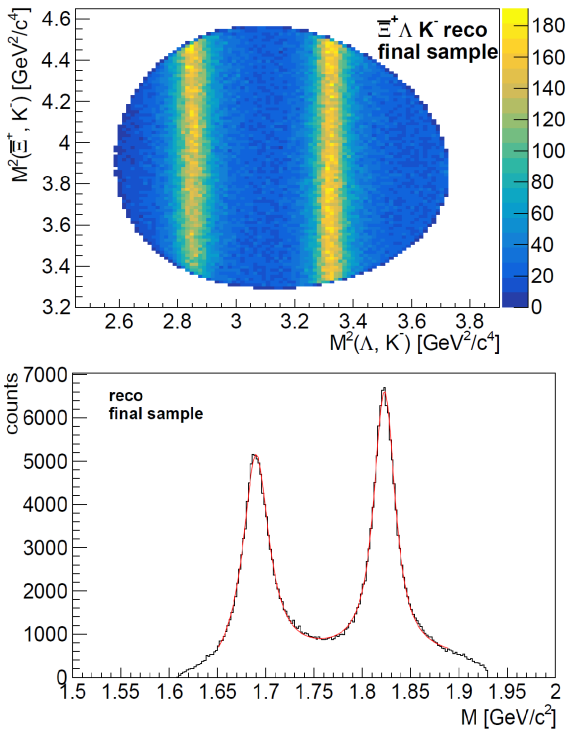

Fig. 10: Reconstructed Dalitz plot of the $\bar{\Xi}^+\Lambda K^-$ final state (upper panel) and ΛK^- invariant mass distribution (lower panel).

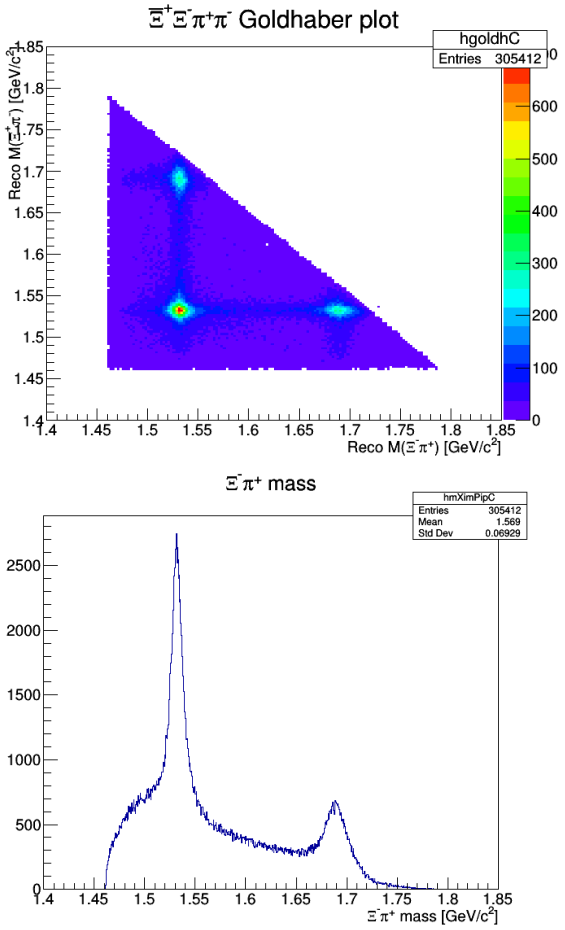

Fig. 11: Reconstructed 'Goldhaber' plot of the $\bar{\Xi}^+\pi^-$ mass versus the $\Xi^-\pi^+$ invariant mass sensitive to the single charged pion decay of the neutral resonant states $\Xi(1530)^0$ and $\Xi(1690)^0$ (& c.c.) (upper panel) and the projection on the $\Xi^-\pi^+$ mass distribution (lower panel).

respectively. In both cases the true signal purity is 97.7%, i.e. the combinatorial background only contributed 2.3% although no cuts on the particle identity were applied. The signal-to-background ratio was evaluated in the analysis of a DPM sample of 10^8 events using the identical selection criteria as for the signal sample. As a result not a single event survived, and a lower signal-to-background limit of 18.9 was deduced.

Analysis of $\bar{\Xi}^+\Xi^-\pi^+\pi^-$: 5.6 million events were simulated and analyzed. The decay of the $\bar{p}p$ system was specified to include the charged and neutral three resonant states $\Xi(1530)$, $\Xi(1690)$, and $\Xi(1820)$ in all combinations with the charge conjugate of these resonances or the Ξ^- ($\bar{\Xi}^+$) ground state, which are kinematically allowed to populate the considered $\bar{\Xi}^+\Xi^-\pi^+\pi^-$ (strong interaction) final state. Specifically this means that the two charged higher mass states contribute to double pion decay, whereas the two neutral lower mass states contribute to single pion emission. In addition, a direct non-resonant decay mode of the $\bar{p}p$ parent system to the $\bar{\Xi}^+\Xi^-\pi^+\pi^-$ final state was included.

The corresponding decay tree has eight charged particles in the final state of quasi-stable particles. The analysis

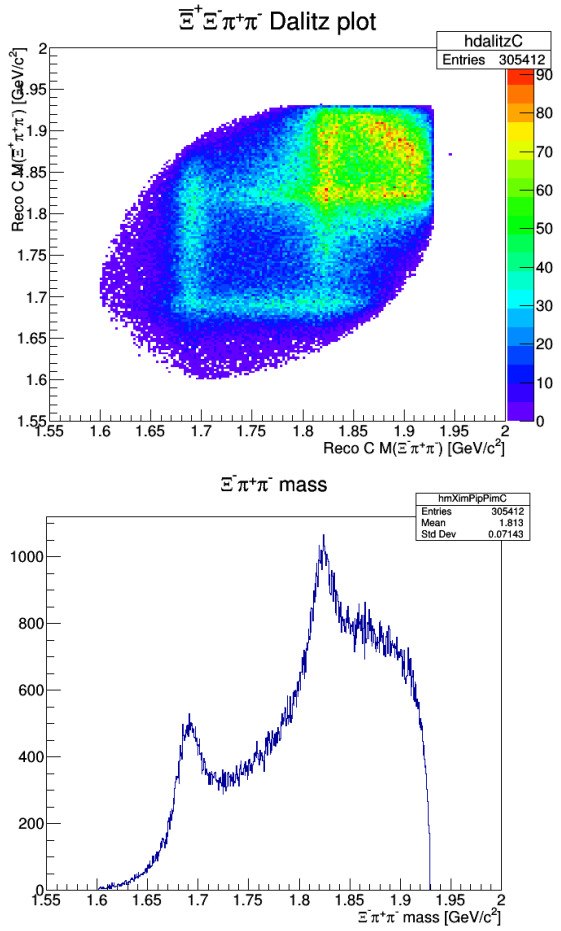

Fig. 12: Reconstructed modified Dalitz plot with the $\pi^+\pi^-$ pair as a pseudoparticle, showing the mass of the $\bar{\Xi}^+\pi^+\pi^-$ system versus the mass of the $\Xi^-\pi^+\pi^-$ system, sensitive to the double pion decay of the charged resonant states $\Xi(1690)^-$ and $\Xi(1820)^-$ (& c.c.) (upper panel) and the projection on the $\Xi^-\pi^+\pi^-$ mass distribution (lower panel).

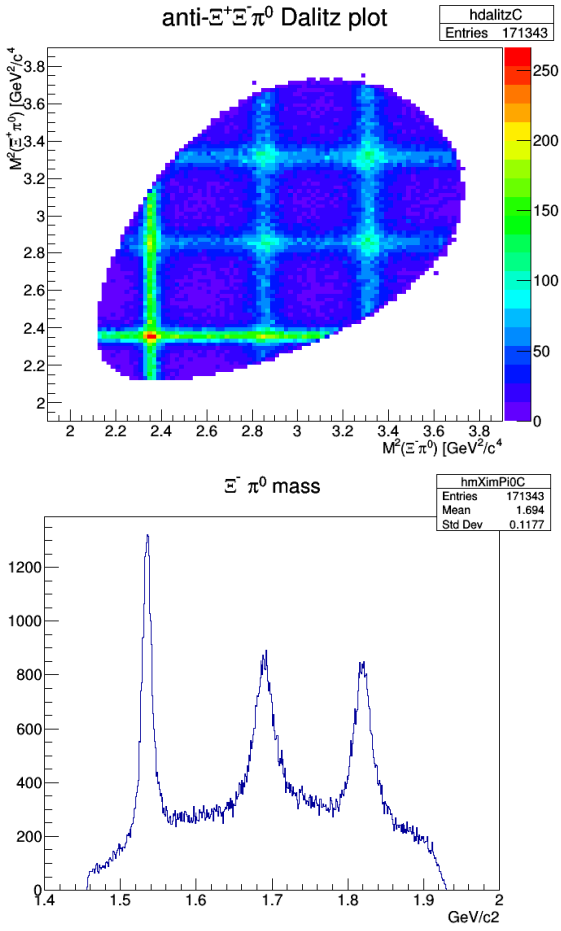

Fig. 13: Reconstructed Dalitz plot of the $\bar{\Xi}^+\Xi^-\pi^0$ final state (upper panel) and $\Xi^-\pi^0$ invariant mass distribution (lower panel).

was based on 'ideal PID', i.e. the Monte Carlo information ('proton' or 'pion') was used for assigning the particle type to the reconstructed charged particle tracks while the sign of the charge was determined from the track curvature. As the first step a vertex fit was applied to all found $\pi^+\pi^-$ combinations in order to remove the prompt $\pi^+\pi^-$ pair from the list of charged pion candidates and to reduce the combinatorial background in reconstructing the decay tree.

Both the conventional step by step reconstruction and the full decay tree fit were used in the analysis. Fig. 11 and Fig. 12 show the reconstructed events obtained in the tree fit analysis in representations sensitive to single and double pion decay, respectively. A total reconstruction efficiency of 5.5% at 99.1% purity has been obtained. A signal-to-background ratio > 3.9 was deduced from a comparative analysis of 22 million DPM events.

Analysis of $\bar{\Xi}^+\Xi^-\pi^0$: 4.4 million $\bar{\Xi}^+\Xi^-\pi^0$ non-resonant continuum events and 5 million events containing the three resonant states $\Xi(1530)^-$, $\Xi(1690)^-$, $\Xi(1820)^-$, each of their antiparticles and $\bar{\Xi}^+\Xi^-\pi^0$ continuum part at equal weight of $1/7$ each have been analyzed with the conventional step by step reconstruction of the decay tree, using 'ideal PID' for the charged particle candidates. In order to reduce the combinatorial background in combining the two neutral candidates originating from other particles than photons, e.g. neutrons, which are wrongly interpreted as photon candidates, the photon time information in the electromagnetic calorimeter (EMC) has been used.

Fig. 13 shows the reconstructed $\bar{\Xi}^+\Xi^-\pi^0$ final state in the analysis of the event sample containing the resonant states. 3.9% reconstruction efficiency at 97.2% purity was obtained. The impurity is mostly due to a wrong selection of photon candidates, accidentally having a pair mass close to the nominal π^0 mass. A current study based an a tree fit without using MC information on the particle species indicates that the reconstruction efficiency is only

marginally reduced, but the impurity due to combinatorial background increases roughly by a factor two. The signal-to-background ratio was evaluated based on the identical analysis of 22 million DPM events and found to be > 4.6.

Rate Estimates: The simulation studies described confirm the feasibility of a comprehensive Ξ baryon spectroscopy program at $\overline{\text{P}}$ANDA, which can already be started at an early stage of the experiment with redueced luminosity. With production cross sections around $1\,\mu$b and reconstruction efficiencies $\sim 5\%$ nearly 20000 signal events can be reconstructed per day. Clean and high-statistics event samples of size similar to those presented in the simulation studies can be collected in a run time of about two weeks.

2.2.2 KOALA

The goal of KOALA is to measure the antiproton-proton elastic scattering differential cross section at HESR, which is crucial for the PANDA luminosity detector to be able to achieve an absolute precision of 3% for the cross-section normalization. KOALA consists of 3 main components including the recoil detector, the forward detector as well as the hydrogen cluster jet target. The recoil detector is a position sensitive energy detector, which includes 2 thick, high purity germanium strip sensors and 2 silicon strip sensors. A two-layer scintillator telescope is implemented as the forward detector to measure the elastically scattered beam particles close to the beam axis. A thin hydrogen cluster jet target is implemented for KOALA measurement.

The KOALA recoil detector was built and then commissioned at COSY by measuring proton-proton elastic scattering. The commissioning results of the recoil detector show the full feasibility of the experiment proposal. The recoil detector by itself has precisely measured recoil protons down to a kinetic energy of 600 keV. In order to measure even lower kinetic energies, e.g. 400 keV, the background from produced pions near a polar angle of 90° must be suppressed by demanding a coincidence with the forward detector. To verify this concept, a fast plastic scintillator detector has been built and is currently being installed near the beam axis. For the full measurement, the PANDA luminosity monitor detector will serve as the forward detector and is being prepared for the measurement at COSY. The hydrogen cluster jet target has been renewed and tested by the Muenster group. A special collimator has been built for the KOALA measurement to ensure that the target material has a maximum extent of 1 mm along the beam axis. The full target has been installed at COSY. A sketch of the KOALA setup for commissioning at COSY is shown in the figure 14 (top). So far, all of the required components have been installed at COSY as shown in figure 14 (bottom). The commissioning of the full setup of KOALA at COSY will take place in the first quarter of 2019.

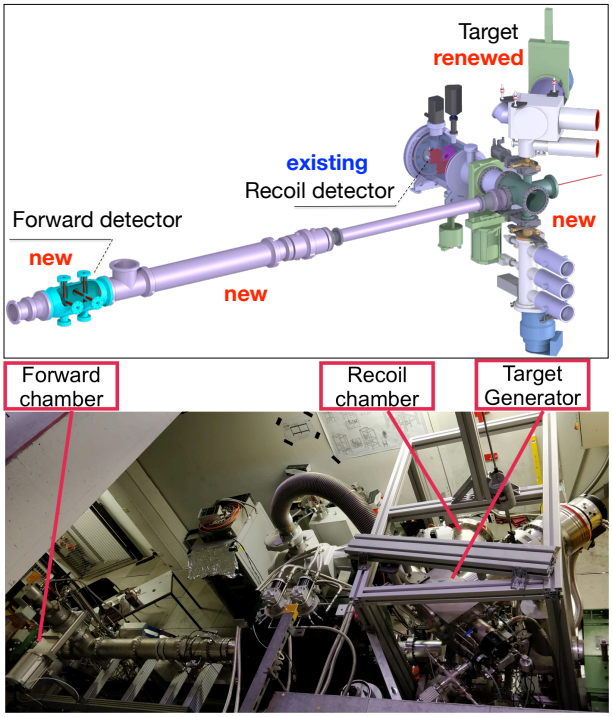

Fig. 14: Sketch of the KOALA setup (top) and a photograph of the KOALA installation at COSY (bottom).

2.3 EDM

From JEDI to CPEDM: a Prototype EDM Storage Ring

Introduction The Standard Model (SM) of particle physics is not capable to account for the apparent matter-antimatter asymmetry of our Universe. Physics beyond the SM is required and is either probed by employing highest energies (e.g., at LHC), or by striving for ultimate precision and sensitivity (e.g., in the search for electric dipole moments). Permanent electric dipole moments (EDMs) of particles violate both time reversal (T) and parity (P) invariance, and are via the CPT-theorem also CP-violating. Finding an EDM would be a strong indication for physics beyond the SM, and pushing upper limits further provides crucial tests for any corresponding theoretical model, e.g., SUSY.

Up to now, EDM searches focused on neutral systems (neutron, atoms, and molecules). The current bound of the neutron EDM is $|d_{\text{n}}| < 3.0 \times 10^{-26} e \cdot cm$. Storage rings offer the possibility to measure EDMs of charged particles by observing the influence of the EDM on the

spin motion in the ring. Direct searches of proton and deuteron EDMs, however, bear the potential to reach sensitivities beyond $10^{-29} e \cdot cm$.
If an EDM exists, the spin vector will experience an additional torque in the electromagnetic fields of the storage ring resulting in a change of the original spin direction. If the bending fields in a storage ring are adjusted according to the particle momentum in such a way that the longitudinally polarized spins of the particle beam are kept aligned ("frozen") with their momenta, electric fields in the rest frame of the particles will precess the spin via the EDM into the vertical direction. This change of the vertical component of the beam polarization from early to late storage times is the signature of the EDM signal, which can be determined with the help of a polarimeter.
Triggered by the workshop “Physics Beyond Colliders" (PBC) organized by CERN, a new collaboration (CPEDM for “Charged Particle EDM") was formed with the aim of preparing a feasibility study for a dedicated EDM storage ring at CERN as input for the update of the “European Strategy for Particle Physics" (ESPP). The ultimate goal of the CPEDM collaboration is to design, build, and operate a proton all-electric ring with frozen spins at the magic momentum of about 0.7 GeV/c (233 MeV). For this purpose a roughly 500 m long storage ring is required, capable to inject and simultaneously store counter-rotating beams to reach a desired sensitivity for the EDM measurement in the order of $10^{-29} e \cdot cm$.
A step-wise approach is pursued, starting with ongoing technical feasibility studies at the Cooler Synchrotron COSY in Jülich, followed by a first direct EDM measurement of a charged particle at COSY. It is foreseen to construct an intermediate prototype proton EDM ring, and finally, on a longer time scale, design and build the high precision proton EDM storage ring.
Here, in the first section, we present a starting point lattice for the prototype EDM ring in terms of geometry, type and strength of the elements. The storage ring should be small and simple, and as inexpensive as possible. The second section describes the results of commissioning experiment at COSY with the RF Wien filter, including Lorentz force measurements, driven oscillations and the resonant build-up of vertical polarization.

Prototype EDM Ring Layout

Design Requirements and Considerations Before designing a final EDM ring with ultimate precision, a smaller-scale prototype ring (PT EDM ring) must be constructed first to prove critical features and capabilities required for EDM measurements. The proposed ring is designed to be capable of achieving its claimed goals:

- Storage of high intensity beams for a sufficiently long time;
- Beam injection with multiple polarization states (longitudinal and sideways) in both clockwise (CW) and counter-clockwise (CCW) beams;
- Simultaneously circulating CW and CCW beams with frozen spin capability;
- Magnetic shielding to reduce the ambient radial magnetic field components;
- Polarization measurements for both CW and CCW beams using the same target;
- Phase-space beam cooling (electron cooling) before injection, or stochastic cooling.

The PT EDM ring will have a circumference of about 100 m and will be operated in two modes. The first mode would work with all-electric bending (at 30 MeV proton energy). This would show that such a concept works and the feasibility of the ring with simultaneous counter-rotation beams. The second mode would expand the operating range of proton energies to 45 MeV with the addition of magnetic bends (air core). With this combination, "frozen" spin operation could be demonstrated for a proton beam, other spin manipulation tools developed, and a reduced-precision proton EDM value measured. Alternating fills in counter-rotating directions would allow cancellation of the average radial magnetic field that is the leading cause of systematic error. The systematic error will strongly be associated with the needed magnetic field reversal.

Ring Design The present ring design for the prototype is a fourfold symmetry "squared" ring with 8 m long straight sections as shown in Fig. 15. This is the result of studies discussing different lattices like round and racetrack type shapes. The basic beam parameters are given in Table 2.

Table 2: Basic beam parameters for the PT ring

	E only	E,B	unit
kinetic energy	30	45	MeV
$\beta = v/c$	0.247	0.299	
momentum	239	294	MeV/c
γ (kinetic)	1.032	1.048	
magnetic rigidity $B\rho$		0.981	T·m
electric field E only	6.67		MV/m
E-field (frozen spin)		7.00	MV/m
B-field (frozen spin)		0.0327	T

The lattice consists of 4 unit cells each of them bending 90° in the arcs. Each of them compromises the following focusing structure: QF - B - QD - B - QF, with QF is a focusing quadrupole, QD a defocusing quadrupole and B an electric/magnetic bending unit. The bend elements consist of electric and magnetic bending. The pure electric bending provides to required rigidity for 30 MeV protons. For a proton energy of 45 MeV magnetic bending has to be applied in addition. The straight sections must house two injection regions for clockwise (CW) and counter-clockwise (CCW) operation. There will as well

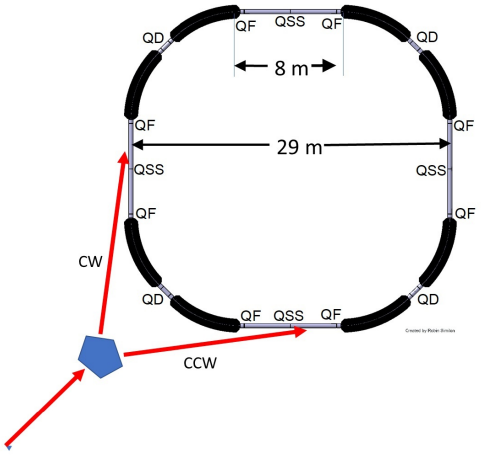

Fig. 15: The basic layout of the PT EDM ring, consisting of eight dual, superimposed electric and magnetic bends; three families of quadrupoles (focusing: QF, defocusing: QD, and straight section: QSS); and four 8 m long straight sections. The total circumference is about 100 m. Injection lines for injecting counter-circulating beam are represented just as stubs.

be a quadrupole QSS in the center of each of the straight section to gain additional tuning possibilities.

The performance of the PT ring has to be discussed in terms of systematic errors, beam lifetime, spin coherence time, instabilities and beam dynamic limits like intra-beam scattering, multiple rest gas scattering, and wake field effects. The basic parameters for the PT EDM ring elements are given in Tables 3 and 4.

Beam injection: Injection into the PT ring will closely resemble injection into a nominal all-electric ring. In particular there will be an even number of bunches in each beam, with alternating sign polarizations, whether in single beam or counter-circulating beam operation. The injector for the PT ring could be the electron-cooled beam from COSY or make use of equipment at CERN. The beams will be protons in the 30 to 45 MeV range, in a cooled phase space of 1 π mm·mrad, with the beams bunched into 2, 4, 6 or 8 bunches to be fed into counter-circulating beams in the PT ring. Injection into the prototype ring will be done using switching magnets distributing the beams into clockwise (CW) or counter-clockwise (CCW) direction as sketched in Fig. 15. All beam bunches are transferred with vertical polarization, either up or down.

Electric bends: The electrostatic deflectors consist of two cylindrically-shaped parallel metal plates with equal potential and opposite sign. With the zero voltage contour of electric potential defined to be the center line of the deflector, the ideal orbit of the design particle stays on the center line. The electrical potential vanishes on the center line of the bends, as well as in drift sections

Table 3: Number of elements and geometry

		units
# B-E deflectors	8	
# arc D quads	4	
# arc F quads	8	
# straigh quads	4	
quad length	0.400	m
straight length	8.000	m
bending radius	8.861	m
electric plate length	6.959	m
arc length (45°)	15.718	m
circumference total	102.000	m

Table 4: Parameter of bend elements

		units
Electric		
gap between plates	60	mm
plate length	6.959	m
total bending length	55.673	m
total straight length	44.800	m
bend angle per unit	45°	m
Magnetic		
magnetic field	0.0327	T
current density	5.000	A/mm^2
windings/element	60	

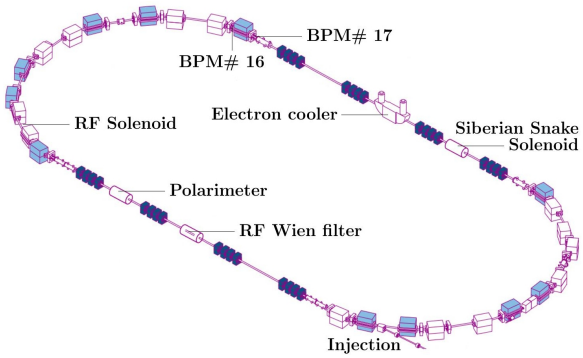

Fig. 16: Sketch of COSY with the positions of the relevant elements.

well outside the bends. Therefore, the electric potential vanishes everywhere on the ideal particle orbit. With the electric potential seen by the ideal particle continuous at the entrance and exit of the deflector, its total momentum is constant everywhere (even through the RF cavity). The designed ring lattice requires electric gradients in the range from 5 to 10 MV/m. This is more than the standard values for most accelerator deflectors separated by a few centimeters. Assuming 60 mm distance between the plates, to achieve such high electric fields we have to use high voltage power supplies.

Magnetic bends: The experiments require periodic reversals of the magnetic bending field to use symmetry to suppress systematic deviations. The reversal of the magnetic field should be done with best possible repro-

ducibility. This is why the magnetic field production will be iron-free.

Summary The reference energy for the PT EDM ring will be 45 MeV protons for frozen spin experiments using combined magnetic and electric bending and 30 MeV protons for the pure electric bending and simultaneous clockwise and counter-clockwise mode of operation. Performing the first direct, precision measurement of the proton EDM strong physics motivation requires frozen spin experiments using protons, deuterons, and eventually electrons. Further studies have to be carried out to prove, that the required beam lifetime and spin-coherence time can be reached. Handling systematic error signals remains to be the main challenge for a charged-particle EDM ring. In addition, the ability to store a sufficient number of polarized protons (10^{10} particles) in a phase space of 10 mm·mrad has to be demonstrated in a necessarily predominantly electric storage ring. Up to now, all existing relativistic rings are magnetic systems. The key issues will be addressed by the construction and operation of a small-scale prototype ring before designing the ultimate proton all-electric ring for the highest EDM sensitivity.

Proof of Principle EDM (*precursor*) Experiment Using COSY Highest EDM sensitivity shall be achieved with a new type of machine, namely with an *electrostatic* circular storage ring, where the centripetal force is produced by electric fields. This E field couples to the EDM of the orbiting particles and provides the desired sensitivity ($< 10^{-28} e \cdot cm$). The idea behind such a proof-of-principle experiment (so-called precursor experiment) is to use a novel $\vec{E} \times \vec{B}$ RF Wien filter to accumulate the EDM related spin rotation in order to make them measurable. In a magnetic machine, the particle spins precess about the local stable spin axis. In an ideal machine, this axis corresponds to the vertical (y) direction of the magnetic fields $\vec{B}_{\text{dipole}} \propto \vec{e}_y$ in dipole magnets. In this situation, an RF device that is operating on some harmonic of the spin-precession frequency can be used to accumulate the EDM effect as function of time in the cycle, provided the particle ensemble is coherently precessing in the horizontal plane.
In order for the RF system of the Wien filter to stay tuned precisely on a harmonic of the spin-precession frequency, a phase-lock between the spin-precession of the particle ensemble in the ring and the RF of the Wien filter is needed. The horizontally precessing polarization serves as a co-magnetometer for the buildup of the vertical polarization (EDM) signal. The goal of the experiment is to show that a conventional *magnetic* storage ring can be employed to obtain a first direct EDM measurement of the deuteron (or proton).

Commissioning of the RF Wien Filter A novel high precision waveguide RF Wien filter (see IKP Annual Report 2017) was constructed and installed at COSY for that purpose. In the following the commissioning of that device will be described. In this experiment polarized deuterons was used with a momentum of 970 MeV/c. After beam preparation (injection, acceleration, bunching, electron cooling) the originally vertical polarization of the particles is flipped into the horizontal plane by means of an RF solenoid. The spins of the particles precess now with a frequency of $f_S = \gamma G f_{\text{rev}} = 120.765\,\text{kHz}$, where $\gamma = 1.126$ is the relativistic factor, $G = -0.143$ the deuteron's magnetic anomaly and f_{rev} the revolution frequency. The polarization has been measured with the forward part of the former WASA detector.
The RF Wien filter was installed in the center of one of the straight sections of the COSY accelerator (Fig. 16). Here, a so-called low-β section is available which allows one to change the β-function of the machine and therefore the beam diameter.
In order for the RF Wien filter to act solely on the particle spin without disturbing the beam itself, the ratio between the total electric to the magnetic field, must be set to 173 Ω for 970 MeV/c particles. Fulfiling this condition leads to a vanishing Lorenz force. In this case, the RF Wien filter is referred to, as matched. Matching the device is realized by terminating it with a load impedance. It is a form of an impedance matching network composed of a fixed high-power water cooled resistor, a fixed air core coil and 4 variable high power capacitors. Only two capacitors C_L and C_T were used. Varying these capacitors changes the impedance of the network and therefore introduces fields reflections back into the device.
The driving circuit of the RF Wien filter allows one to run at four different harmonics of the spin precession frequency ($f_{WF} = k f_{\text{rev}} \pm f_S$ with $k = \pm 1, \pm 2$). Adjustable capacitive elements are used to match the system in order to fulfill the Wien filter condition, i.e., induce no Lorentz force onto the circulating beam. To ensure this, the beam position is measured at the RF Wien filter frequency with a suitable beam position monitor (BPM #17) at some other place in the accelerator.

Measurements of EDM-like polarization buildup The first measurements were performed in January/February 2018 using a beam of unpolarized deuterons with a momentum of 970 MeV/c. The response of BPM #17 on the settings of the matching elements C_L and C_T at a frequency of 871 kHz and an input power of 600 W (integrated electric field of 1700 V) can be seen in the top two panels of Fig. 17. An additional measurement delivers the phase between the electric and magnetic field (E/B phase). This phase should also be zero to ensure a proper perfomance of the device. With this additional information the matching point can be define to be at $C_L = 6800$ and $C_T = 4950$. The lower two panels of Fig. 17 show the response of BPM #17 with the low-β section powered up. It can be seen that the induced beam oscillations are higher for the respective settings of C_L and C_T. Powering the low-β section on reduces the size of the deuteron beam inside the RF Wien

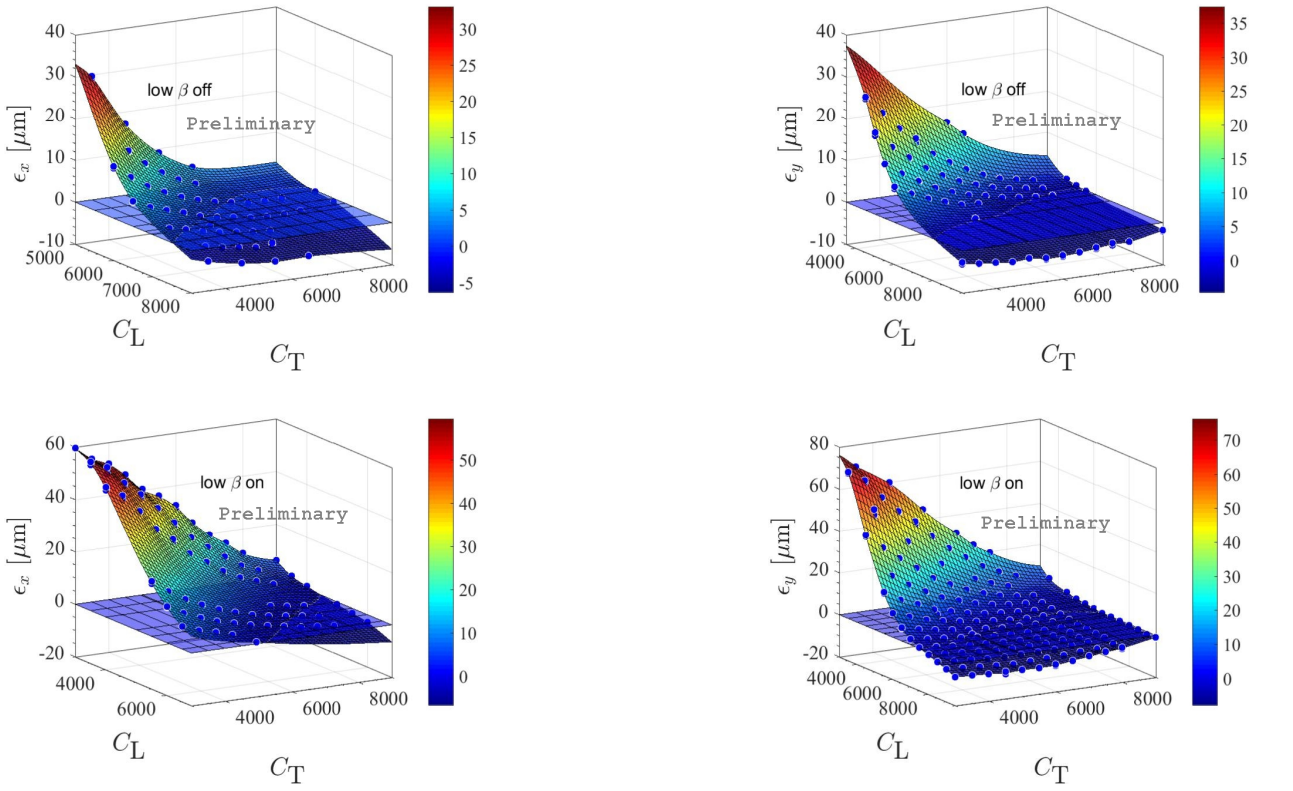

Fig. 17: Horizontal (left panels) and vertical (right panels) beam oscillation amplitude ε of the beam position measured at the BPM #17 of COSY depending on the settings of the matching elements C_L and C_T at a frequency of 871 kHz and an RF power of 600 W. The low-β magnets were powered during the measurements shown in the lower panels. The matching point is at $C_L = 6800$ and $C_T = 4950$.

filter at the cost of larger angles between the trajectories of the passing deuterons with respect to the axis of the RF Wien filter. The next step in the commissioning of the matched RF Wien filter was the observation of the effect on the polarization of the deuterons. The following measurements were conducted during a measurement period in May 2018 with polarized deuterons. The RF Wien filter is rotatable around the COSY beam axis in order to align the magnetic field in a desired way. The device was now rotated so that the magnetic field is in the horizontal plane (radial to the circulation deuteron beam, x-axis). This RF field induces now small spin kicks which rotate the spin of the particles in the plane spanned by the beam direction (z-axis) and the originally vertical spin (y-axis). Oscillations of the vertical spin component can be observed (Fig. 18). The period length of the damped oscillations depends on the power fed into the RF Wien filter. Rotating the RF Wien filter into a position where the magnetic field is in the vertical plane the oscillations of the spin should vanish. In an ideal ring only an oscillation (or build-up) of the vertical polarization caused by the EDM should remain. EDM induced vertical polarization oscillations in an experimental situation with an RF Wien filter can generally be described by $p_y(t) = a \sin(\Omega^{p_y} t + \phi_{RF})$. The associated EDM resonance strength ε^{EDM} can be defined as the ratio of angular frequency Ω^{p_y} relative to the orbital angular frequency Ω^{rev} in the machine, $\varepsilon^{EDM} = \frac{\Omega^{p_y}}{\Omega^{rev}}$. The term "EDM" applies to the case that only the EDM contributes to Ω^{p_y}.

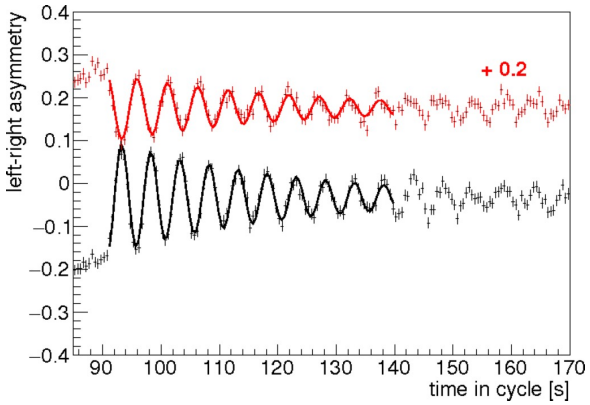

Fig. 18: Oscillations of the vertical spin component of two different spin states driven by the RF Wien filter with an RF power of 15 W rotated into a position where the magnetic field points into the radial (horizontal) direction. The red curve is shifted for better visibility.

In practice, the resonance strength will receive contributions from other sources, such as rotations of the RF Wien filter and solenoidal fields in the ring that generate unwanted spin kicks. This build-up was measured depending on the relative phase between the Wien filter RF and the spin direction (Fig. 19). The upper panel shows the

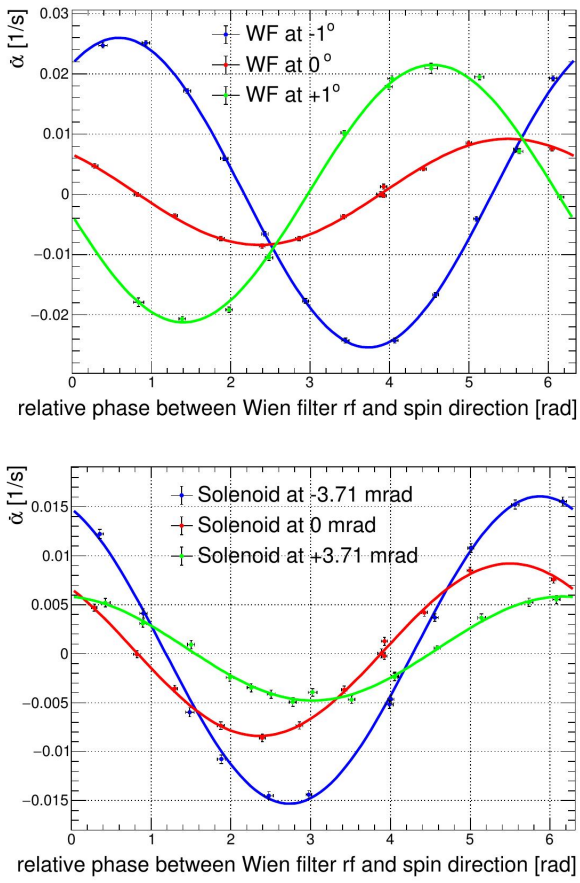

Fig. 19: Build-up rates $d\alpha/dt$ of the vertical spin as a function of the relative phase between the Wien filter radio frequency and the spin direction depending on the rotation of the RF Wien filter magnetic field out of the vertical direction (upper) and the rotation angle introduced by the Siberian snake solenoid (lower). The RF Wien filter was powered at 1 kW.

dependence on the RF Wien filter rotation angle, where 0° is the direction vertical to the COSY plane. The non-vanishing build-up at 0° originates from magnetic imperfections in the COSY accelerator. These imperfections rotate the stable spin axis away from the ideal direction. To compensate for this effect in the yz-plane a Siberian Snake solenoid is used on the other side of the COSY accelerator. The dependence of the vertical spin build-up ($d\alpha/dt, \alpha = P_V/P_H$) on the rotation angle caused by this solenoid is shown in the lower panel of Fig. 19.

To achieve a measurement of the EDM of deuterons in COSY the measured build-up rates of the vertical polarization component have to be compared with simulations of the real machine. First simulations of an **ideal** machine (Fig. 20) show that the EDM manifests in a minumum of the build-up rates at some rotation angle of the RF Wien filter at a solenoid strenght of zero. Simulations of the

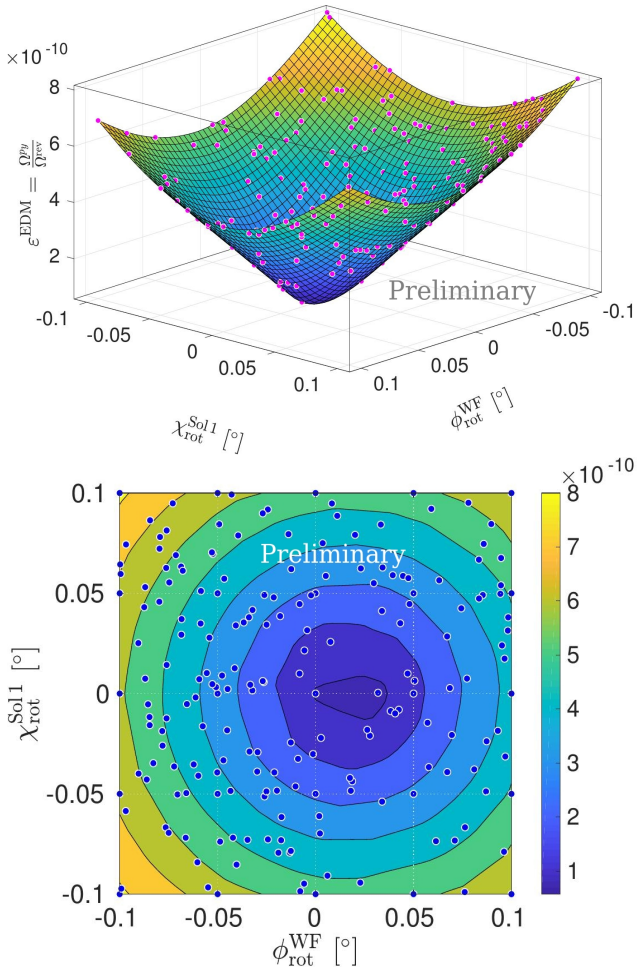

Fig. 20: Resonance strength expectation $\varepsilon^{\mathrm{EDM}} = \Omega^{\mathrm{py}}/\Omega^{\mathrm{rev}}$ for an EDM of $d = 10^{-18}$ e·cm, where Ω^{py} is the angular frequency of the vertical polarization oscillation and Ω^{rev} is the orbital angular frequency.

real machine including the positions of all magnets and the circulating deuteron beam together with a measurement of the dependence shown in Fig. 20 will lead to a first EDM measurement of the deuteron at COSY.

Summary The first direct measurement of the deuteron EDM at COSY is well underway. A second run shall take place at the end of 2019. The anticipated deuteron EDM sensitivity of the measurements is about 10^{-18} to $10^{-20} e \cdot cm$.

There is a strong interest of the high-energy physics community in storage ring searches for the EDM of protons and light nuclei as part of physics program of the post-LHC era. In the framework of the recently formed CPEDM Collaboration that evolved out of JEDI, the design of a 30 MeV all-electric EDM prototype storage ring is being prepared. Possible hosts are CERN or COSY.

2.4 Neutrino Physics

2.4.1 Comprehensive measurement of pp-chain solar neutrinos with Borexino

The weak interactive nature of neutrinos makes them very challenging to detect, however, it also makes them a valuable source of information from the most extreme environments of our universe. Neutrinos are the sole messengers from the dense core of the Sun that we can use as a handle to study the solar energy production. Even photons require around 100,000 years to reach the surface of the Sun, from where they are free to reach the Earth in about 8 minutes. The Sun and the stars with similar masses produce most of their energy ($\approx 99\%$) in the proton-proton (pp) fusion chain, a sequence of nuclear reactions converting hydrogen into helium (see upper-left scheme on Fig. 21). The neutrinos emitted by five of these reactions are referred in the following as pp, pep, ^{7}Be, ^{8}B, and hep-neutrinos. Alternatively, the stars heavier than the Sun are hypothesised to be fueled mainly by the alternative CNO catalytic cycle (see upper-right scheme on Fig. 21). The measurement of all neutrino components is the most direct way to test our understanding of the solar energy production and the predictions of the Standard Solar Model (SSM).One of the most important unanswered questions about the Sun is the solar metallicity, that is, the abundances of elements heavier than He, even though it is a fundamental parameter for the determination of the physical properties of the Sun. A precise measurement of the solar neutrino fluxes comprising the pp-chain and the CNO cycle would provide stringent boundary conditions to the SSMs or could event directly settle the controversy between high-metallicity (HZ) and low-metallicity (LZ) SSMs.

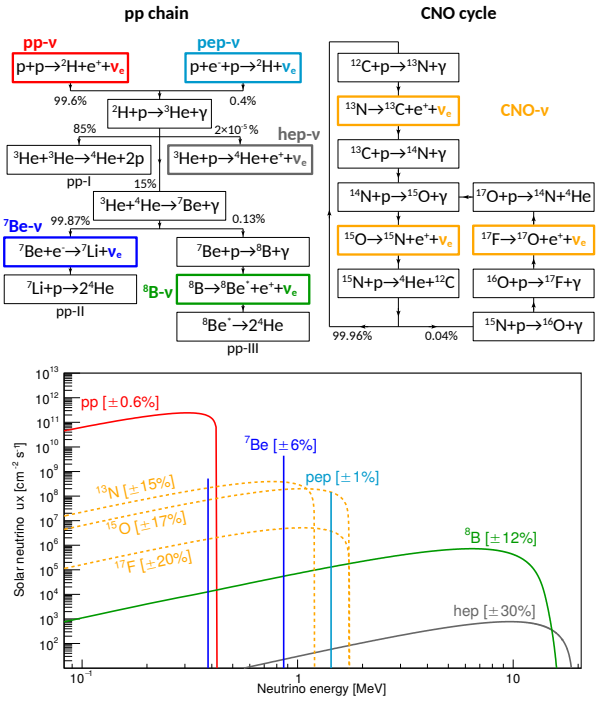

Fig. 21: Top: schematic view of the pp and CNO nuclear fusion sequences. Bottom: expected energy spectrum of solar neutrinos. The numbers show the errors on the flux predicted by the SSM.

Moreover, an enormous flux of the solar neutrinos on the surface of the Earth ($\approx 10^{11}$cm^{-2} s^{-1}) allows for studying the properties of these elusive particles themselves. Solar neutrinos reach the Earth as a mixture of all neutrino flavours (electronic, muonic, and tauonic) owing to the oscillation mechanism enhanced by the Mikheyev-Smirnov-Wolfenstein (MSW) effect.The different fusion reactions produce neutrinos at different energy ranges, providing optimal experimental configuration to study the resonance character of the neutrino flavour conversion in matter.

The Borexino detector, located at Laboratori Nazionali del Gran Sasso in Italy, has been designed with the primary goal to observe only ^{7}Be solar neutrinos. However, in the most recent publication, the measurement of all components of pp-chain neutrinos has been presented (hep only upper limit). Borexino detects neutrinos by means of their weak elastic scattering off electrons. A fraction of the incoming neutrino energy E_ν is transferred to one electron, which deposits it in the liquid scintillator. The scintillator light is detected by about 2,000 photomultiplier tubes, which ensure high detection efficiency. For mono-energetic ^{7}Be ($E_\nu = 0.384$ and 0.862 MeV) and pep (E_ν= 1.44 MeV) neutrinos, the induced electron recoil end-points are at 0.230 MeV, 0.665 MeV, and 1.22 MeV, respectively. For the continuous pp and ^{8}B spectra, they are 0.261 MeV and 15.2 MeV, respectively. The analysis proceeds in two steps: (1) the event selection, with a different set of cuts in the three energy regions to optimize the final sensitivity, and (2) the extraction of the neutrino and residual background rates with a combined fit of distributions of global quantities built for the events surviving the cuts. Fits were performed (significantly reliant on Jülich Supercomputing Centre (JSC) resources with several hundred configurations, yielding results whose spread is incorporated in the systematic uncertainties.

In the low-energy multivariate fit, performed to extract the pp, pep, and ^{7}Be neutrino rates, we first constrain the CNO neutrino interaction rate to the value predicted by the HZ-SSM assuming the MSW-LMA scenario (4.92 ± 0.55 counts per day per 100 t), and then, separately, to the LZ-SSM predictions (3.52 ± 0.37 counts per day per 100 t). Only the pep neutrino rate is slightly influenced by

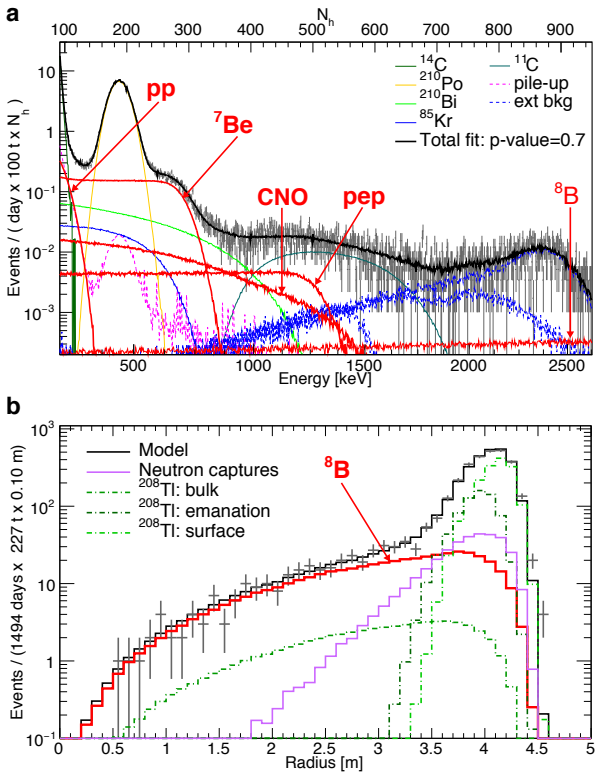

Fig. 22: Distributions of events after selection cuts and best fits with neutrino and background components. a) Low-energy region: energy spectrum with suppressed ^{11}C cosmogenic background. The horizontal upper scale is in units of N_h, that is, the total number of photons collected for each event. b) High-energy region: radial distribution of events.

this constraint and thus two results for it are shown in Table 5. In both cases, the absence of the *pep* reaction in the Sun is rejected with $> 5\sigma$ significance, enough to definitively claim the discovery of solar *pep* neutrinos. The ^{7}Be solar-neutrino flux is determined with a total uncertainty of 2.7%, a factor of 1.8 improvement with respect to the previous Borexino resultand a factor of two smaller than the theoretical uncertainty. The *pp* interaction rate is consistent with our previous resultand has an uncertainty of 9.5%.

The measurements reported in the Table 5 represent a complete study of the solar *pp*-chain and of its different terminations by means of neutrino detection in a single detector and with a uniform data analysis procedure. These measurements can be used either to test the MSW-LMA paradigm assuming SSM flux predictions or, alternatively, to probe our understanding of solar physics assuming the validity of the neutrino oscillation mechanism.

The interaction rates of *pp*, *pep*, ^{7}Be, and ^{8}B neutrinos reported in Table 5 can be used to deduce the electron neutrino survival probability P_{ee} at different energies. Assuming the HZ-SSM fluxes and neutrino-electron cross-sections, we obtain P_{ee} for each solar-neutrino component: $P_{ee}(pp,\ 0.267\ \text{MeV}) = 0.57 \pm 0.09$, $P_{ee}(^{7}\text{Be},\ 0.862\ \text{MeV}) = 0.53 \pm 0.05$, $P_{ee}(pep,\ 1.44\ \text{MeV}) = 0.43 \pm 0.11$, and $P_{ee}(^{8}\text{B},\ 8.1\ \text{MeV}) = 0.37 \pm 0.08$. In the low-energy region, Borexino results are the most precise measurement of the electron neutrino survival probability. In the high-energy region, $P_{ee}(^{8}\text{B})$ is in agreement with higer-precision measurements provided by water-based Cherenkov detectors SuperKamiokande (Japan) and SNO (Canada). Borexino is the only experiment that can simultaneously test neutrino flavour conversion both in the vacuum (low-energy region) and in the matter-dominated (high-energy region) regimes. The Borexino data is in the excellent agreement with the expectations from the MSW-LMA (large mixing angle) paradigm and rejects the vacuum-LMA hypothesis at 98.2% C.L.

Since solar neutrinos are detected on Earth only about 8 min after being produced, they provide a real-time picture of the core of the Sun. In particular, the neutrino fluxes determined experimentally can be used to derive the total power generated by nuclear reactions in the Sun's core. By using exclusively the new Borexino results, we find $L = (3.89^{+0.35}_{-0.42})$ erg s^{-1}, in agreement with the luminosity calculated using the well measured photon output $L = (3.846 \pm 0.015)$ erg s^{-1}. This confirms experimentally the nuclear origin of the solar power with the best precision obtained by a single solar-neutrino experiment. Considering that it takes around 10^5 years for radiation to flow from the energy-producing region to the surface of the Sun, this comparison proves also that the Sun has been in thermodynamic equilibrium over this timescale.

The Borexino results are compatible with the temperature profiles predicted by both HZ- and LZ-SSMs. However, the ^{7}Be and ^{8}B solar-neutrino fluxes measured by Borexino provide an interesting hint in favour of the HZ-SSM prediction. Assuming HZ to be true, in the frequentist hypothesis test, our data disfavour LZ at 96.6% C.L. In the Bayesian approach, comparing the two models assuming that they have the same probability a priori (50% for the HZ hypothesis and 50% for LZ hypothesis), the data show a mild preference for HZ with respect to LZ. The odds are 5:1 or, equivalently, the Bayes factor is 4.9.

Furthermore, we derive the ratio $R_{\text{I/II}}$ between the ^{3}He-^{4}He and the ^{3}He-^{3}He fusion rates, which quantifies the relative intensity of the two primary terminations of the *pp* chain (*pp*-II and *pp*-I; see Fig. 21), a critical probe of solar fusion. Neglecting the ^{8}B neutrino contribution, this ratio can be extracted from the measured *pp* and ^{7}Be neutrino fluxes by the relation, $R_{\text{I/II}} = 2\Phi(^{7}\text{Be})/[\Phi(pp) - \Phi(^{7}\text{Be})]$. We find $R_{\text{I/II}} = 0.1780^{+0027}_{-0.023}$, in agreement with the most up-to-date predicted values of $R_{\text{I/II}} = 0.180 \pm 0.011$ (HZ) and 0.161 ± 0.010 (LZ).

In summary, this study confirms the nuclear origin of the solar power and provides the most complete real-time insight into the core of our Sun so far.

	Rate [cpd/100 ton]	Flux [$cm^{-2}s^{-1}$]
pp	$134 \pm 10\ ^{+6}_{-10}$	$(6.1 \pm 0.5\ ^{+0.3}_{-0.5}) \times 10^{10}$
^{7}Be	$48.3 \pm 1.1\ ^{+0.4}_{-0.7}$	$(4.99 \pm 0.13\ ^{+0.07}_{-0.10}) \times 10^{9}$
pep (HZ)	$2.43 \pm 0.36\ ^{+0.15}_{-0.22}$	$(1.27 \pm 0.19\ ^{+0.08}_{-0.12}) \times 10^{8}$
pep (LZ)	$2.65 \pm 0.36\ ^{+0.15}_{-0.24}$	$(1.39 \pm 0.19\ ^{+0.08}_{-0.13}) \times 10^{8}$
^{8}B	$0.223^{+0.015+0.006}_{-0.016-0.006}$	$(5.68^{+0.39+0.03}_{-0.41-0.03}) \times 10^{9}$
CNO	< 8.1 (95% C.L.)	$< 7.9 \times 10^{8}$ (95% C.L.)

Table 5: Borexino results on pp, ^{7}Be (862 + 384 keV), pep, and CNO solar ν's: interaction rates and fluxes, inferred assuming the MSW-LMA oscillation parameters. The first error is statistical only. The second error is the systematic uncertainty.

2.4.2 Borexino and JUNO

Borexino, located at the Laboratori Nazionali del Gran Sasso in Italy, is the liquid-scintillator experiment that has tackled an extensive physics program for more than ten years. Its distinctive technical feature, the ultra-low radioactive background of the inner scintillating core, has exceeded all expectations and became the basis of the outstanding achievements obtained so far. The Borexino collaboration has recently published the first comprehensive measurement of solar neutrinos produced along the pp-chain, a sequence of nuclear reactions responsible for about 99 percent of solar energy. In particular, Borexino measured the interaction rates of pp, pep, ^{7}Be, and ^{8}B neutrinos and provided limits on hep neutrinos, as well as on the CNO-cycle contributions. In addition, Borexino succeeded to measure geo-neutrinos, neutrinos from the radioactive decays inside the Earth. The neutrino group of IKP-2 gives fundamental contributions at all levels: from low level analyses (data quality control, detector stability, effective quantum efficiency of PMTs), through higher level analysis (sensitivity studies, spectral fits for solar and geo-neutrinos), up to the global physics coordination of the collaboration and paper preparation.

The Jiangmen Underground Neutrino Observatory (JUNO), a next generation multi-purpose antineutrino detector currently under construction in Jiangmen in China, plans to start data taking in 2021. The central detector will contain 20 kton of liquid scintillator and will be equipped with 18,000 20 inch and 25,000 3 inch PMTs. Measuring reactor antineutrinos of two powerplants at a baseline of 53 km, the unprecedented design energy resolution is 3% at 1 MeV. The main physics goal is to determine the neutrino mass hierarchy within six years of run time with a significance of 3-4 sigma. Additional physics goals are the precision measurement of the solar neutrinos, geo-neutrinos, supernova burst neutrinos, the diffuse supernova neutrino background as well as the search for proton decays. The involvement of the IKP-2 neutrino group is mosly in the area of analyses (waveform, muon track, energy, and position reconstructions, reconstruction methods with neural networks, suppression of pile-up events, systematics on the neutrino mass hierarchy measurement). Recently, the group has taken the responsibility to develop the system of calibration of the 20 ton liquid scintillator detector OSIRIS, that will be monitoring the radio-purity of the liquid scintillator during the filling of JUNO.

2.5 Theoretical Investigations in IKP-3/IAS-4

2.5.1 Introduction

The IKP theory group studies the strong interactions in their various settings — spanning topics in hadron structure and dynamics, the nuclear many-body problem, symmetry tests in Quantum Chromodynamics (QCD), physics beyond the Standard Model and strongly correlated electronic systems. The first focus of the theory group is the formulation and application of effective field theories for precision hadron and nuclear physics based on the symmetries of QCD. The second focus is related to high performance computing in nuclear and hadronic physics, spear-headed by the work on nuclear lattice simulations. Since July 2012, the group is heavily involved in the activities of the collaborative research center "Symmetries and the emergence of structure in QCD" (CRC 110) together with researchers from Bonn University, TU München, Ruhr-Universität Bochum, IHEP/CAS (Beijing, China), ITP/CAS (Beijing, China) and Peking University (China). This CRC is presently in its second funding period (until 06/2020). Some of the high-lights of these activities are discussed in the following.

2.5.2 Essential elements of nuclear binding

A first principles approach to nuclear forces is provided by chiral effective field theory (χEFT), where interactions are arranged as a low-energy expansion in powers of momentum and pion mass. The nucleon-nucleon (NN) and three-nucleon (3N) interactions are determined by fitting to experimental data on NN scattering and 3N observables. χEFT has been combined with state-of-the-art computational algorithms and powerful supercomputers to produce a wealth of new predictions and insights into nuclear structure and reactions. While many calculations establish the reliability of χEFT in light nuclei, some problems have been found for the binding energies and charge radii of medium-mass nuclei. The core issue is that χEFT many-body calculations do not yet give reliable and accurate predictions at higher nuclear densities. If one reaches high enough orders in the χEFT expansion, then the problems are expected to be resolved. Many-nucleon forces start contributing at higher orders and can tame the problems appearing at higher

nuclear densities. However, the number and complexity of these many-nucleon interactions are enormous, and a systematic treatment of such effects is not yet practical. One pragmatic approach is to further constrain the nuclear force using nuclear structure data from medium-mass nuclei or the saturation properties of nuclear matter. A rather different line of investigation has looked at the microscopic origins of the problem. Using nuclear lattice EFT (NLEFT) we had shown earlier that nuclear matter sits near a quantum phase transition between a Bose gas of alpha particles and the nuclear liquid. It is argued that local SU(4)-invariant forces play an increasingly important role at higher nuclear densities, and this could explain why some χEFT many-body calculations are successful while others are not. The term local refers to velocity-independent interactions, and the SU(4) is Wigner's approximate symmetry of the nuclear interactions where nucleons can be regarding as four components of an SU(4) multiplet. We have followed this idea further, taking a constructive reductionist approach and deduce the minimal nuclear interaction that can reproduce the ground state properties of light nuclei, medium-mass nuclei, and neutron matter simultaneously with no more than a few percent error in the energies and charge radii. It can be shown that this can be achieved with a leading order approach that features SU(4)-invariant two- and three-nucleon interactions, a non-local smearing of the nucleon operators as well as a parameter that controls the degree of locality of the interaction. One can show that within such a minimal approach, the ground state properties of light nuclei, medium-mass nuclei, and neutron matter can be described, see Fig. 23 for the binding energies of 86 even-even isotopes. We expect that these new insights might help design new χEFT calculations with better convergence at higher densities. Aside from the Coulomb interaction, all of the other interactions in this minimal model obey Wigner's SU(4) symmetry. This seems to be an example of emergent universality. The SU(4) interaction resurges at higher densities not because the underlying fundamental interaction is invariant, but because the SU(4) interaction is coherently enhanced in the many-body environment. This is not to minimize the important role of spin-dependent effects such as spin-orbit couplings and tensor forces. However, it does seem to suggest that SU(4) invariance plays a key role in the bulk properties of nuclear matter.

2.5.3 The Tjon band in NLEFT

Most NLEFT calculations so far have been performed at next-to-next-to-leading order (NNLO) in the chiral expansion and using a coarse latting spacing of $a \simeq 2\,\mathrm{fm}$. For such a lattice spacing, even if the three-nucleon force is adjusted to give the proper ^{3}H binding energy, the binding energy of the ^{4}He nucleus is severely overbound, violating the correlation between these two observables already observed by Tjon a long time ago. In pionless EFT, it could be shown that this correlation is a consequence of the fact that the same operator that renormalizes the three-

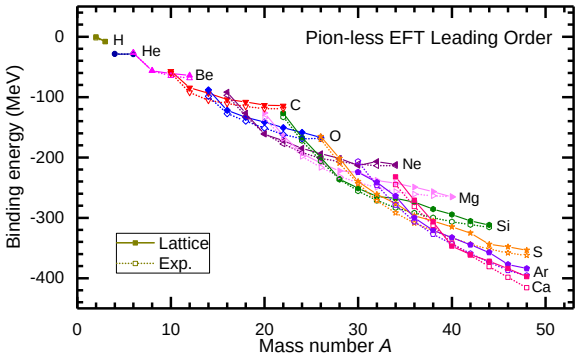

Fig. 23: The calculated binding energies from ^{3}H to ^{48}Ca. The solid symbols denote the lattice results and the open symbols denote the experimental values. Different symbols and colors denote different element. The Coulomb interaction is taken into account perturbatively.

nucleon force (3NF) also renormalizes the four-nucleon force. In chiral NLEFT, this deficiency was overcome by an effective four-nucleon operator for large lattice spacings. To get a better understanding of this phenomenon, we investigated the two-, three-, and four-body sector for lattice spacings from $a = 1.32$ fm to $a = 1.97$ fm up to N2LO and including subleading two-pion-exchange contributions as well as the electromagnetic interaction and the leading 3NFs. There is a general convergence of the phase shifts in the two-body sector by including higher orders as well as shifting to smaller lattice spacings. In the three-body sector we found almost similar results at N2LO for all three-cases. The reason for this is that the three-body bound state is not sensitive to all np-phase shifts in the same way and even though the description of the phase shifts became better in general, some particular phase shifts do not improve leading to the the general underbinding of the system. In the ^{4}He system we recovered the earlier obserbed strong overbinding of about 6 MeV due to lattice effects for the coarse lattice which becomes smaller with decreasing lattice spacings and vanishes finally for sufficiently small a, cf. Fig. 24. By comparing the triton and ^{4}He binding energies for each lattice spacing and each order, one can see a convergence towards the Tjon line with smaller lattice spacing after including N2LO two-nucleon forces, the corresponding electromagnetic corrections and three-nucleon forces, respectively. Finally, at sufficiently small a, the Tjon line is hit, confirming the conjecture that light (and medium mass) nuclei can be described by 2NFs and 3NFs only. The inclusion of 3N forces give a ^{4}He binding energy prediction of $E_B = -28.37(28)(4)$ MeV which is consistent with the experimental value of 28.30 MeV. The residual lattice spacing dependence in np scattering, which is at the heart of the deviation from the Tjon-band, vanishes at N3LO for a in the range from 1 to 2 fm, thus leading to results consistent with the Tjon band and no further need of an effective four-nucleon operator. Still, further investigations of these implicit multi-particle interactions

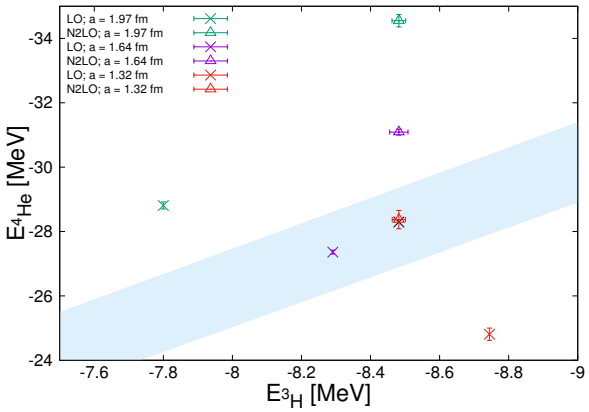

Fig. 24: LO (crosses) and NNLO (triangles) results for the ^{3}H and ^{4}He binding energies for three different lattice spacings $a = 1.97\,\mathrm{fm}$ (green), $a = 1.64\,\mathrm{fm}$ (violet) and $a = 1.32\,\mathrm{fm}$ (orange). The emprical value is given by the black cross. The blue shaded area depicts the Tjon-band.

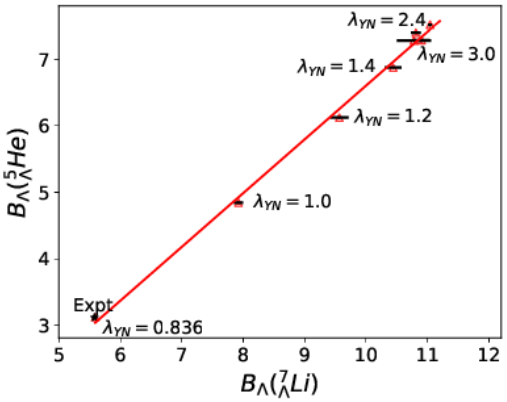

Fig. 25: Correlation of $B_\Lambda({}^7_\Lambda\mathrm{Li};{}^5_\Lambda\mathrm{He})$. The experimental values $B_{\Lambda,\mathrm{Expt}}({}^7_\Lambda\mathrm{Li};{}^5_\Lambda\mathrm{He})$ is marked by a black star.

are necessary as these small lattice spacings require very expensive computational ressources.

2.5.4 Jacobi no-core shell model for hypernuclei

Due to a wealth of data and by using effective field theories, especially chiral perturbation theory, there has been a lot progress in the understanding of nuclear interactions in recent years. Far less is know about so-called hypernuclear interactions of hyperons with nucleons. The difficulty to perform scattering experiments with the short-lived hyperons has only allowed us to collect a very limited set of data. Nevertheless, due to the presence of strange quarks in hyperons, understanding these interactions gives quantitative insight into the effects of explicit chiral symmetry breaking due to the masses of the quarks. Moreover, depending on the strength of these hypernuclear interactions, hyperons might affect the properties of astrophysical objects like neutron stars. Since scattering data are difficult to obtain, hypernuclei, bound states of hyperons and nuclei, will be an important source of information on hypernuclear interactions. Several of these hypernuclei have been experimentally identified starting from the hypertriton ($^3_\Lambda$H), a bound state of a neutron, proton and Λ hyperon, and accurate new measurements can be expected in future from facilities like J-PARC, Jefferson Laboratory, MAMI and FAIR. In order to relate the data to new realizations of hypernuclear interactions, one requires a reliable method to predict the binding energies and properties of several hypernuclei based on realistic interactions. In the past years, we have therefore extended the Jacobi no-core shell model to hypernuclei. To solve the many-body Schrödinger equation for hypernuclei, we represent it in an harmonic oscillator basis. Thereby, we separate off the center-of-mass motion and build basis states with well-defined total angular momentum. This significantly reduces the dimensionality of the resulting set of linear equations allowing us to perform a large number of calculations for different interactions. Still, the preparation of transition matrix elements and the antisymmetrization of the nucleons is computationally demanding. But these ingredients are independent of the interactions and have to be obtained only once. For practical calculations, the interactions have to be evolved using the similarity renormalization group (SRG) to make them soft enough that converged many-body results can be obtained. Thereby, the description of two-baryon data does not change but new few-baryon interactions will be induced. In the first step, we restricted ourselves to interactions on the two-baryon level and found that the effects of these few-baryon interactions are strongly correlated when comparing the results for several hypernuclei depending on the SRG parameter λ_{YN}. As an example, we show in Fig. 25 the correlation of the energy to separate the Λ from the hypernucleus B_Λ for $^7_\Lambda$Li and $^5_\Lambda$He. For the SRG parameter, we performed a series of calculations that allows us to determine B_Λ and the numerical uncertainty due to the limitations of our basis states. The uncertainties for $^7_\Lambda$Li is shown in the figure as black bars, the one for $^5_\Lambda$He is negligible. For the special choice of $\lambda_{YN} = 0.836$ fm^{-1} and for the interactions chosen for this calculation, both of these hypernuclei are predicted in agreement with the experimental values as indicated by the black star. For the same SRG parameter and same interaction, we identified predictions for some hypernuclei that are deviating from experiment. We currently study the dependence of such predictions on the hyperon-nucleon interaction and also for hypernuclei containing two Λ hyperons. The results of these calculations will guide the development of new hypernuclear interactions that are consistent with all the available data and that will allow for a much more reliable prediction of properties of hyperons and neutron stars.

2.5.5 Applying numerical gauge theory algorithms to graphene

The Hybrid Monte Carlo (HMC) algorithm is the numerical workhorse of the lattice gauge field community. The essential aspect of this algorithm is its collective updates of fields during the evolution of a lattice Quantum Monte Carlo calculation. Such updates are essential for capturing physics near second order phase transitions where correlation lengths diverge and therefore all length scales become relevant. This behavior occurs in all gapped lattice gauge theories as the continuum limit is approached. Prior to HMC, lattice gauge theory calculations required exponentially increasing high-performance computing (HPC) resources to perform calculations approaching the continuum limit and physical pion mass M_π. Such "critical slowing down" was detrimental for progress in this field until HMC came along.

Many systems in condensed matter and solid state physics also undergo second order phase transitions at critical couplings. A prominent example is the hexagonal Hubbard model which is used to model various physical systems, one of which is graphene. Here the phase transition corresponds to the formation of an interaction-induced Mott gap, making the system an insulator. Simulations of such systems have been historically done on modest lattice sizes where the use of algorithms based off local updates (i.e. Metropolis) have sufficed, even at critical coupling. However, because of the potential use of graphene in next generation electronics, there has been renewed interest to push simulations to scales approaching macroscopic scales ($\sim 10^{-9}$ m). Not surprisingly these local update algorithms exhibited "critical slowing down".

Recently, we applied a variant of the HMC algorithm, one that employs Hasenbusch preconditioning, to simulate the hexagonal Hubbard model system. An extremely favorable scaling with system size was found, particularly as the continuum limit was approached, see Fig. 26. Here, the speedup compared to traditional calculations without preconditioning could be as large as an order of magnitude. Such speedup allowed us to investigate the largest graphene system to date on a computer, an 102×102 system. Future calculations will push system sizes even larger and pinpoint the critical coupling with unprecedented precision.

We also addressed another critical issue related HMC simulations of such systems, namely, the issue of ergodicity. Because of the geometry of the system, the distribution of generated background fields during an HMC simulation becomes very multi-modal, with each mode largely separated from one another, see the inset of Fig. 26. This requires exponential time for HMC to "tunnel" between the modes, which leads to an *in practice* ergodicity problem. We solved this problem by devising a new form of HMC, one that employs "ergodicity jumps" between the modes, enabling all modes to be sampled with their correct respective weights.

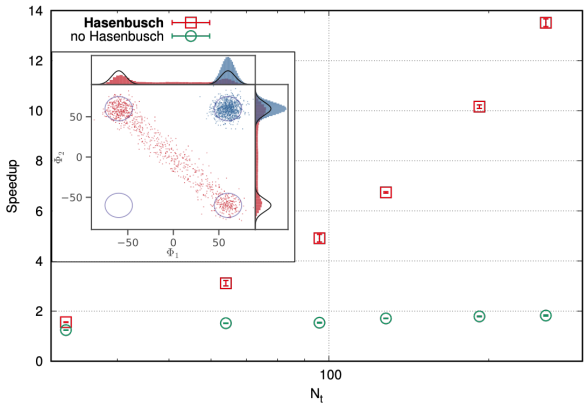

Fig. 26: Speedup of Hasenbusch acceleration algorithm compared to standard HMC as a function of the number of timesteps N_t. The inset figure shows the multi-modal distribution of auxiliary fields that lead to an ergodicity problem.

2.5.6 Is there an $X(1835)$ resonance?

The $X(1835)$ resonance, a state listed by the Particle Data Group, has a long and somewhat erratic history. It was first discovered by the BES Collaboration in 2005 in the decay $J/\psi \to \gamma\eta'\pi^+\pi^-$ and subsequently seen in other reactions such as $J/\psi \to \gamma K_s^0 K_s^0 \eta$. Initially the resonance was associated with the anomalous near-threshold enhancement in the antiproton-proton ($\bar{p}p$) invariant-mass spectum in the reaction $J/\psi \to \gamma\bar{p}p$ which would point to a baryonium-type state (or $\bar{N}N$ quasi-bound state) as possible explanation for its structure. However, with increasing statistics it became clear that the two phenomena are not necessarily connected, not least due to a striking difference in the width of the respective resonances required for describing the invariant mass spectra of the two reactions in question. On top of that, in a recent re-measurement of $J/\psi \to \gamma\eta'\pi^+\pi^-$ by the BESIII Collaboration the initial peak around 1835 MeV was no longer observed. Nonetheless, there is still a pronounced structure in the invariant mass spectrum, but it has moved to higher energies and is now located around 1870 MeV. Interestingly, the structure seen in the new $J/\psi \to \gamma\eta'\pi^+\pi^-$ data is located very close to the $\bar{p}p$ threshold which is at 1877 MeV. This suggests that the dynamics of the $\bar{N}N$ system and, specifically, the opening of the $\bar{N}N$ channel could have something to do with the appearance of this structure. Indeed, this could be the case if the contribution of the two-step process $J/\psi \to \gamma\bar{p}p \to \gamma\eta'\pi^+\pi^-$ to the $J/\psi \to \gamma\eta'\pi^+\pi^-$ reaction amplitude is sizable or even dominant. Since the amplitude for $J/\psi \to \gamma\bar{p}p$ is strongly enhanced near the $\bar{p}p$ threshold due to the $\bar{N}N$ interaction in the final state, this is by no means implausible. We analyzed the origin of the structure associated with the $X(1835)$ resonance, as observed in the reaction $J/\psi \to \gamma\eta'\pi^+\pi^-$, based on the above hypothesis. Specific emphasis was put on the $\eta'\pi^+\pi^-$ in-

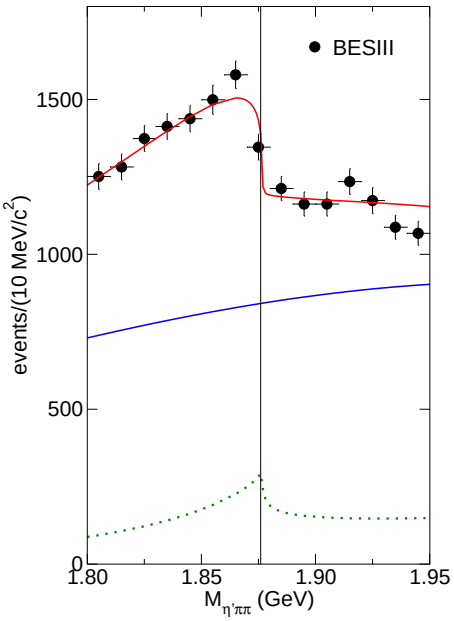

Fig. 27: The $\eta'\pi^+\pi^-$ invariant mass spectrum in the reaction $J/\psi \to \gamma\eta'\pi^+\pi^-$. Results for the contribution from the $J/\psi \to \gamma\bar{N}N \to \gamma\eta'\pi^+\pi^-$ transition (dotted line) and the background term (dashed line) are shown, together with the full results (solid line). The horizontal line indicates the $\bar{p}p$ threshold.

variant mass spectrum around the $\bar{p}p$ threshold. A main ingredient of our calculation is the $\bar{N}N$ interaction. Here we build on our latest $\bar{N}N$ potential, derived in the framework of chiral effective field theory up to next-to-next-to-next-to-leading order. That potential reproduces the amplitudes determined in a partial-wave analysis of $\bar{p}p$ scattering data from the $\bar{N}N$ threshold up to laboratory energies of $T_{lab} \approx 200-250$ MeV. Utilizing that $\bar{N}N$ potential we evaluated the contribution of the two-step process $J/\psi \to \gamma\bar{p}p \to \gamma\eta'\pi^+\pi^-$ to the total reaction amplitude. The amplitude for $J/\psi \to \gamma\bar{p}p$ was constrained from corresponding data by the BESIII Collaboration, while for $\bar{N}N \to \eta'\pi\pi$ we took available branching ratios for $\bar{p}p \to \eta'\pi^+\pi^-$ as guideline. Combining the contribution of this two-step process with a background amplitude, that simulates other transition processes which do not involve an $\gamma\bar{N}N$ intermediate state, allowed us to achieve a quantitative description of the invariant-mass dependence shown by the data near the $\bar{p}p$ threshold, see Fig. 27. In particular, the structure detected in the experiment emerges as a threshold effect. It results dynamically from an interference of the smooth background amplitude with the strongly energy-dependent two-step contribution. Obviously, there is no need for a genuine $X(1835)$ resonance in this scenario.

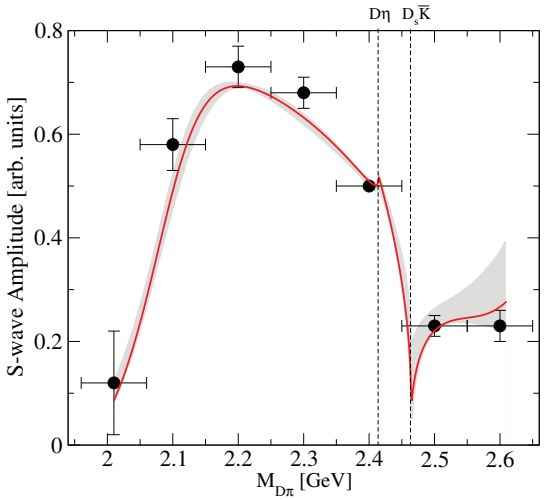

Fig. 28: Comparison of the S-wave amplitude determined in this work to the S-wave anchor points found in the experimental analysis by the LHCb collaboration. The solid red line gives the best fit results and the grey band quantifies the uncertainties that emerged from the fitting procedure. The dashed perpendicular lines indicate the location of the $D\eta$ and $D_s\bar{K}$ threshold, respectively.

2.5.7 Towards a new paradigm for heavy-light meson spectroscopy

In recent years evidence has accumulated that the $D_s(2317)$ and the $D_{s1}(2460)$, both having masses very different from the quark model expectations, are hadronic molecules made of KD and K^*D, respectively. If correct the symmetries of QCD and in particular the flavor SU(3) symmetry allow one to make predictions for sibling states. Experimental confirmation of their existence provides a highly non-trivial check of the assumed nature of the mentioned charm-strange states. Since the SU(3) symmetry is broken in QCD via the non-vanishing quark masses, to pursue the above mentioned program it is necessary to perform dynamical calculations that include in particular the effects of the strange quark mass in order to provide reliable predictions for the physical world. The calculations underlying this work are based on unitarized chiral perturbation theory employing amplitudes evaluated to next–to–leading order and fitted to a set of light–meson-D–meson scattering lengths determined in lattice QCD. A calculation of this kind also allows one to control to the given accuracy the quark mass dependence of the resonance poles. This made it possible to successfully test the mentioned amplitudes also on other lattice data. The underlying SU(3) structure for the scattering of the pseudo-Goldstone bosons off D-mesons generates two multiplets of resonances: An antitriplet, which also emerges in the quark model and to which the $D_s(2317)$ belongs, and an exotic sextet. In addition, there is a 15–plet, but in this the interaction is repulsive and does there-

fore not lead to any poles. The new insight reported in the work described here was the demonstration that the proximity of one of the sextet states to the $D\eta$ and $D_s\bar{K}$ thresholds provides a very natural explanation of an otherwise irritating structure in recent LHCb data for the reaction $B^- \to D^+\pi^-\pi^-$. To be specific: The $\pi^- D^+$ S–wave amplitude extracted from these data by the LHCb collaboration showed a quite unusual energy dependence in the range of the $D\eta$ and $D_s\bar{K}$ thresholds. By fitting a production amplitude derived from the above described scattering amplitude with only two free parameters to the LHCb data, an excellent fit could be achieved. Moreover, as demonstrated in Fig. 28, our study allows one to interpret the energy dependence of the LHCb data as resulting from the mentioned thresholds. Since so pronounced threshold effects are possible only with a nearby singularity, the line shape shown in Fig. 28 is a direct consequence of the sextet pole near by. To further confirm the molecular nature of the mentioned state we are currently performing studies in lattice QCD at quark masses sufficiently high that the sextet state can be reliably extracted from the lattice data. This in combination with a direct experimental test for the molecular nature of $D_s(2317)$, namely the determination of its width which could be done at PANDA, could complete a decade long research to identify hadronic molecules in the heavy–light sector.

2.5.8 Prediction of new negative-parity doubly charmed baryons

The discovery of Ξ_{cc}^{++} by the LHCb Collaboration triggered predictions of more doubly charmed baryons. By taking into account the scattering of light pseudoscalar mesons off the ground state doubly charmed baryons, a set of negative-parity spin-1/2 doubly charmed baryons are predicted already from an unitarized version of leading order chiral perturbation theory. However, the accuracy of the calculation can be improved further: For a doubly-heavy baryon, the distance between the two heavy quarks QQ may be estimated as $r_d \sim 1/(m_Q v_Q)$, with v_Q the heavy quark velocity. For doubly charmed baryons with an S-wave charm diquark one finds $m_c v_c \sim 800$ MeV. On the other hand the distance of the light quark to the QQ-pair is $r_q \sim 1/\Lambda_{\rm QCD}$, with $\Lambda_{\rm QCD} \sim 250$ MeV the scale of nonperturbative QCD. Thus one may expand in $r_d/r_q \sim 0.3$. To leading order (LO) in this expansion the S-wave QQ diquark appears as a point-like color antitriplet source, similar to a heavy antiquark, and this leads to an approximate heavy antiquark-diquark symmetry (HADS). Diquarks with higher partial waves are spatially much more extended, and thus such an approximation is not expected to work for them. This approximate symmetry allows one to relate doubly heavy baryons to singly-heavy mesons. Therefore, one can construct a chiral effective field theory (EFT) describing the Nambu–Goldstone Bosons (NGBs) scattering off the ground state (positive parity) doubly charmed baryons (or antibaryons). The low-energy constants (LECs) in such a theory can be connected with those in the EFT describing NGBs scattering off ground state (negative parity) anticharmed (or charmed) mesons. In particular, the LECs in the next-to-leading-order chiral Lagrangian have been fixed by fitting to the lattice QCD results of several charmed-meson–light-meson S-wave scattering lengths, and the unitarized amplitudes using these inputs have been shown to be in a remarkable agreement with lattice QCD energy levels.

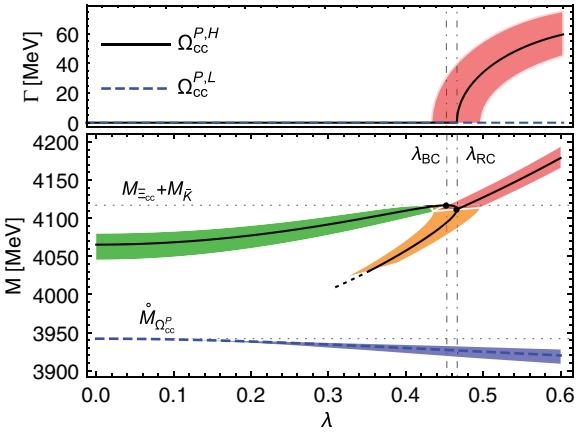

Fig. 29: The widths (upper panel) and the masses of the two lowest $1/2^-$ Ω_{cc}^P states (lower panel) depending on the value of λ with isospin symmetry imposed. The green, orange and red bands correspond to the cases of bound state, virtual states and resonance, respectively. The bands are obtained by taking into account uncertainties of the subtraction constant and the LECs determined from lattice data available for heavy-light mesons.

In doubly heavy baryons there is one phenomenon that is absent in the singly heavy mesons: One can reach the same quantum numbers discussed above also with a ccq baryon, where the cc-pair is in a P–wave. Then the Pauli principle requires the spin of the cc–pair to be zero contrary to the ground states where this spin is one. Thus, transitions from these P–wave states to tow-body states that contain a ground state baryon and an NGB are suppressed by spin symmetry. Accordingly one expects the corresponding coupling constant λ to be $\mathcal{O}(\Lambda_{\rm QCD}/m_c) \ll 1$. In our study we vary λ in a reasonable range to study the sensitivity of the pole locations to this parameter.

Our calculations result in a spectrum richer than that of heavy mesons. We find two very narrow $J^P = 1/2^-$ Ω_{cc}^P, which very likely decay into $\Omega_{cc}\pi^0$ breaking isospin symmetry (see Fig. 29). In the isospin-1/2 Ξ_{cc}^P sector, three states are predicted to exist below 4.2 GeV with the lowest one being narrow and the other two rather broad. We suggest to search for the Ξ_{cc}^P states in the $\Xi_{cc}^{++}\pi^-$ mode. If the HADS is indeed a good symmetry and the assumed dynamics of the NBGs on heavy sources is cor-

rect, then the states reported here must exist. Thus, experimental evidence of their existence as well as unsuccessful searches will in any case teach us a lot about the structure of hadrons.

2.6 Further activities

2.6.1 The CLAS experiment at CEBAF

Experiments at Jefferson Lab (The Thomas Jefferson National Laboratory in Newport News, VA, USA) use the continuous electron beam accelerator facility CEBAF which was recently upgraded from 6 GeV to 12GeV electron beams. The CEBAF Large Acceptance Spectrometer CLAS, is located in Hall-B at Jefferson Lab and has been taking data since February 2018. The physics program of IKP is focused on light meson decays while planning to extend towards time-like forms factors of hyperons. The latter could serve as a pre-study to measurements with the PANDA experiment.

1. Light meson decays from the 6 GeV era are analyzed using CLAS photoproduction data. The results on Dalitz plot analyses with meson decays into three pions will be evaluated in collaboration with Jefferson Physics Analysis Center JPAC. The aim is the modelling of hadron dynamics by observing hadron-hadron correlations. The understanding of the final-state correlations is serving the search for exotic hadron states which will be conducted at heavier meson masses. A paper on the Dalitz analysis of the $\eta \to \pi^0\pi^+\pi^-$ - decay is in preparation and the topic will be continued using 12 GeV data.

2. Dalitz decays of mesons are used to study electromagnetic transition form factors via the decay into an electron-positron pair and a third particle. The form factors are fundamental properties of hadrons which are not sufficiently well known. in addition, renewed interest has arisen due to the theoretical uncertainty of the hadronic contribution to the muon (g-2) anomaly. The largest uncertainty of the SM prediction comes from the hadronic quantum corrections, in particular, hadronic vacuum polarization and hadronic light-by-light scattering. The latter contribution can be accessed by measuring the Dalitz-decay of the light pseudoscalar mesons. The analysis of the light meson Dalitz decays is ongoing for the 6 GeV photoproduction data. (3) IKP has an approved experiment proposal to evaluate the η' meson form factor. The proposed measurement is expected to increase the world statistics by a factor 35 for $\eta' \to \gamma^*\gamma$. Also other light meson decay studies will be extended by analyzing data from the beginning 12 GeV measurement campaign. A first result is the π^0 cross section, determined via the Dalitz decay channel, which provides insight into the pion production mechanisms for photon beam energies up to 5.45 GeV.

3. The 6 GeV CLAS experiment has recently provided information on the properties of Ξ hyperons and the investigations of the $f_0(1500)$ meson resonance as one of several contenders to have significant mixing with a predicted lightest glueball.

2.6.2 BaBar / Belle

The B-factories BaBar and Belle were very performant e^+e^- asymmetric colliders, located in Stanford (the first) and in Tsukuba (the second), built for studying CP-violation effects in the B-meson system. They both started to collect data in 1999, and ended in 2008 (BaBar) and 2010 (Belle). They mostly had run at the enegy in the center of mass of $\Upsilon(4S)$, but in the last period of data taking they collected small data samples at the energy in the center of mass of $\Upsilon(2S)$ and $\Upsilon(3S)$; the Belle experiment only collected small data sets at the energy of $\Upsilon(1S)$ and $\Upsilon(5S)$ before the last shut-down in 2010. The total integrated luminosity of the BaBar experiment reaches 517 fb^{-1}, while for Belle this number rises to 1026 fb^{-1}. BaBar and Belle are a triumph in the history of B-factories, since they reached luminosities well beyond the project desinged, producing high-quality and outstanding results, which allowed for example to verify the theory of Kobayashi-Maskawa (Nobel Price for the discovery of the mechanism of spontaneous broken symmetry in subatomic physics, 2008). Thanks to the collected high luminosity, the investigation of rare processes and the study charmonium and bottomonium spectra has been possible. Although their data taking is over since a decade, still physicists work on the extremely and valuable huge data sets collected by these B-factories. In particular, for charmonium spectroscopy and the search for new exotic states, Belle and BaBar demonstrated that these resonant states enhance in very rare processes, therefore a huge statistics is needed for further investigation, even more than what was collected by each of these experiments.
The Belle II experiment, a major upgrade of the former Belle experiment, will be located at the same facility than Belle in Japan, and just started its Phase 3 of data taking. Belle II plans to collect an integrated luminosity up to 50 ab^{-1} by 2026. While waiting that this enormous data set will be available, the idea to bind together the data set of the BaBar and Belle experiment was brought up for searching for exotics with charm- and strange- quark content, and looking for hexaquark states. The idea was presented at the DFG and approved on December 21, 2017. The project started as an individual DFG fellowship in 2018 at the IKP1 Institute, with the analysis of the following physics processes:

- $B \to J/\psi\phi K$;
- $B_s^0 \to D_s^- D_{s0}^*(2317)^+\pi^0$;
- $e^+e^- \to J/\psi\phi X$ in the continuum;
- $e^+e^- \to D_s^- D_{s0}^*(2317)^+ X$ in the continuum;

- $e^+e^- \rightarrow X(3872)\bar{D}^0X$ in continuum, with $X(3872) \rightarrow D^0\bar{D}^{0*}$.

The feasibility study of the latter channel, $e^+e^- \rightarrow X(3872)\bar{D}^0X$, represents a preliminary study based on a theoretical idea brought up by Canham and Hammer in 2009 to search for hexaquark states with *ccc*-quark content. If we obtain a reasonable reconstruction efficiency (expected in any case less than 1%), the other channel that we want to analyze in this project is $e^+e^- \rightarrow D_s^+D_{s0}^*(2317)^+\bar{D}^0X$, if a signal if found in the invariant mass system of $D_s^-D_{s0}^*(2317)^+$ compatible with the X(4140) or the X(4274). The X(4140) and the X(4274) have been observed up to now only through B decays, in the invariant mass system of $J/\psi\phi$. In case of success, the results of these analyses will have an important impact in understanding the nature of resonant states with $c\bar{c}s\bar{s}$ quark content, whose nature is still unknown. The LHCb experiment analyzed the $B^+ \rightarrow J/\psi\phi K^+$ channel; but it is difficult for LHCb to analyze the invariant mass system of $D_s^-D_{s0}^*(2317)^+$, due to clear limitation in the low-energy photon reconstruction. BaBar and Belle do not have this problem, since they can reconstruct photon with E>50 MeV. Therefore, 4 of the 5 pillars on which the approved DFG project is based on, are unique physics cases. About the analysis of $B \rightarrow J/\psi\phi K$, BaBar and Belle can perform the analysis of the neutral channel, $B^0 \rightarrow J/\psi\phi K_s^0$, which is very difficult in other experiments for which this analysis could be feasible, due to the correct reconstruction of the K_s^0.
The plan in Belle II is also to analyze the invariant mass system of $J/\psi\phi$ in every possible decay mechanism, due to the high potential discovery. Until Belle II will not reach the needed luminosity to perform such analysis, combining the Belle and the BaBar full datasets offers the possibity to perform analysis with unique potential discovery.

2.6.3 Polarized molecules

The recombination of polarized hydrogen atoms into molecules inside a storage cell like at ANKE or PAX is one option to loose nuclear polarization of such a polarized gas target. If the nuclear polarization is preserved during the recombination process, the figure of merit can be increased due to the lower velocity of the molecules compared to the atoms, which will increase the target density. In order to investigate and to maximize the preservation of the polarization during the recombination process a dedicated setup with a storage cell was built and used within a collaboration of the PNPI (Petersburg Nuclear Physics Institute, Gatchina, Russia), the PGI-6 (Peter-Grünberg Institut, FZJ) and the IKP. In the meantime, highly polarized H_2, D_2, and even HD molecules were successfully produced on surface coatings like gold ($0.25 < P < 0.45$) or Fomblin ($P > 0.8$). Even polarized H_3^+ ions are observed, which are mainly produced by the interaction of a polarized H_2^+ ion with a polarized H_2 molecule. Within the measurement precision the H_3^+ polarization of $P = -0.23$ was equal to the H_2 polarization of $P = -0.25$. In recent experiments a nickel coating was tested that in general should destroy the polarization of the hydrogen atoms by wall collisions due to the magnetic field gradients between the different domains at the nickel surface. The application of an external magnetic field results in an increased reduction of the polarization losses and at $0.7\,T$, the saturation field of nickel, the polarization loss was minimized like expected.

2.6.4 HBS developments

Comparison of neutron yields produced by proton and deuteron beams on a thick Be target Within the scope of the Jülich High Brilliance Source (HBS) project, that aims to develop a Compact Accelerator-based Neutron Source (CANS) based on nuclear reactions of light ions with a metal target, the IKP-4 and JCNS-2 institutes collaborate in order to define parameters of the HBS facility at an early stage. For the development on the corresponding target and accelerator design, it is necessary to set the particle species, i.e. protons or deuterons, for the neutron production. Since the according databases (TENDL 2017) didn't provide sufficient certainty in the cross sections at low MeV energies, the neutron yields of proton and deuteron beams impinging on a thick Be target have been measured. The measurement was carried out at the NESP (Niederenergiestrahlplatz) in the BigKarl area with proton and deuteron beams degraded to 10, 20, 30 and 40 MeV energy. The neutron yield was measured via prompt gammas produced in a polyethylene (PE) moderator. Neutron capture of hydrogen in the PE volume results in the emission of 2.2 MeV gamma rays that have been recorded by a Ge gamma detector. The detector efficiency of this setup was determined by a calibration AmBe-source. Figure 30 shows the results of the neutron yield measurements for protons and deuterons as well as the ratio of neutron yields of deuterons over protons. Due to the modest increase in neutron yield for deuterons and less challenging efforts in terms of radiation safety for protons than for deuterons the measurements clearly indicate to focus on protons for HBS.

Moderation of neutrons to cryogenic temperatures The neutrons produced inside a metal target have an energy in the MeV range which is not suitable for most neutron experiments. They require a moderation of the neutrons to thermal energies (10 meV - 500 meV) with typically a polyethylene moderator or cold hydrogeneous matter (1 meV - 10 meV). The cryogenic moderator is being cooled with helium or nitrogen and requires a moderator material which has a high neutron scattering cross section at these temperatures. For this different materials are being used like methane, hydrogen or mesitylene. The cross sections for neutron scattering for these materials come with a high uncertainty and experimental validation is required.

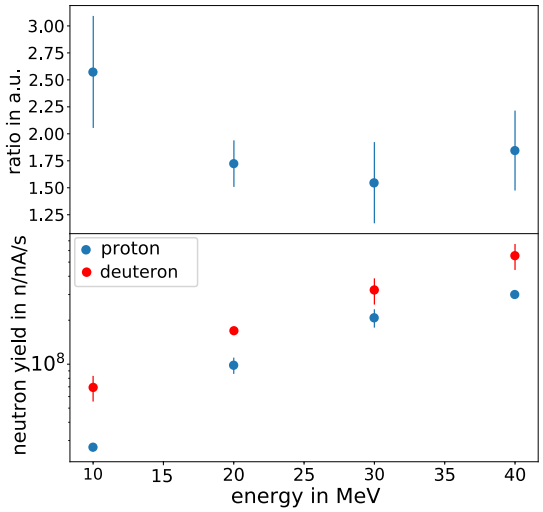

Fig. 30: Deuteron and proton induced neutron yield and ratio of deuteron neutron yield over proton neutron yield

We performed an experiment to measure the moderation performance of mesitylene at 77 K (Fig. 31 The neutrons were produced by a pulsed proton beam impinging on a solid aluminum target. They were moderated to thermal energies by a surrounding polyethylene moderator with an extraction channel in proximity to the target. Into this extraction channel, a cryogenic mesitylene moderator was inserted moderating the neutrons to $\approx$ 6.9 meV and directing them into a 7 m long neutron guide. With the 7 m long flight path and a trigger signal synchronised with pulse structure of the proton beam, a time-of-light spectrum could be measured.

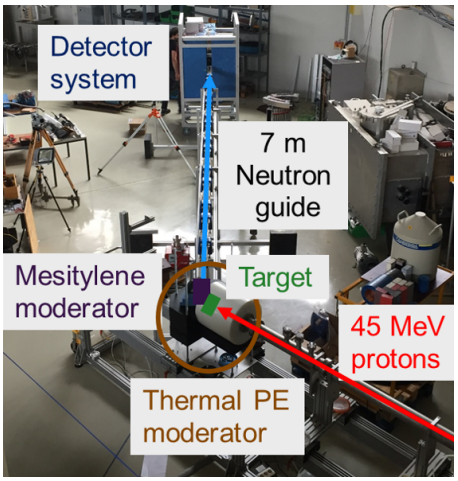

Fig. 31: Moderation experiment at COSY facility

The measured neutron energy spectrum for a mesitylene moderator at a temperature of 77 K shows a shift to lower

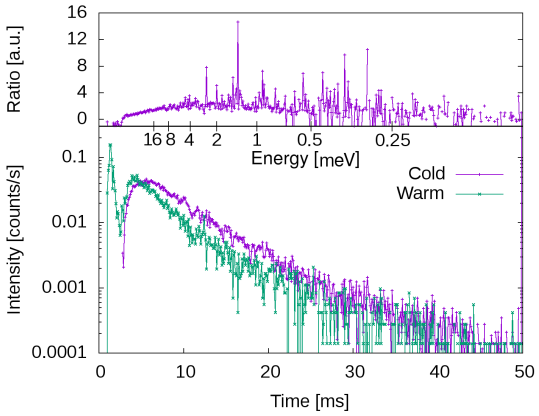

Fig. 32: Moderation of neutron energy spectrum to cryogenic temperatures for a mesithylene moderator.

energies in comparison to a measurement at room temperature, see Fig. 32. This leads to an intensity gain of $\sim$ 3 at these energies. Further experiments are planed with an improved setup and with temperatures down to 10 K where we expect an intensity gain of around 10.

2.6.5 Polarized Particle Acceleration from Laser-Plasma Interaction

Introduction FZJ is very active in the field of laser-plasma interaction with matter accommodating local and regional research teams from a wide range of disciplines including condensed matter physics, materials science, structural biology, accelerator technology, plasma and nuclear physics. The Short-Pulsed Particle and Radiation Center (JuSPARC) will become an interdisciplinary center for collaborative research using ultra-short pulsed photons in the first and second stage with ultra-high repetition rate and later on with higher energies. In a later stage, the production and handling of polarized hadron beams is planned and preparatory work is already performed based on the long-term experience of IKP. The proposed JuSPARC Ti:Sapphire laser system has a modular architecture allowing amplification stages to be added consecutively and ranging from peak power below Terawatt with repetition rates up to MHz, which is presently in the realization phase, up to Petawatt peak power in the final stage of JuSPARC. Most recently FZ Jülich extended its plans in this field under the umbrella of the new research and development platform for accelerator technology ATHENA (Accelerator Technology HElmholtz iNfrAstructure), whose funding was approved by the Helmholtz Association (HGF) mid of the year 2018. Expertise in the field of beam and spin simulation with PIC codes, production and handling of polarized beams (polarized sources and targets, polarimeter) and experience with experiments at conventional storage rings as well as at laser system at IKP is added to the already existing expertise at PGI-6 in these research fields.

Hadron Acceleration and Polarized Beam Production One unexplored field of particle acceleration is the motion of particle spins in huge magnetic fields inherently present in relativistic plasmas. In the framework of the JuSPARC facility and the ATHENA consortium, the laser-driven generation of polarized proton and ^{3}He-ion beams in combination with the development of advanced target technologies is being pursued. Another goal of these investigations is to demonstrate experimentally that the nuclear spin alignment in a fusion plasma survives for periods at least comparable to the energy confinement time. Novel target technologies will be employed at different laser facilities. Experiments are in preparation for the ten Petawatt laser system SULF at SIOM in Shanghai and the Petawatt Laser Facility at GSI in Darmstadt. Finally, these targets can be utilized in the future stages of JuSPARC with laser intensities from the roughly hundred Terawatt up to the Petawatt level. This development is strongly connected to ATHENA$_{hadron}$: Development of polarized targets for proton and ion acceleration. Besides the FZJ cooperation partner: PGI-6, JSC, IKP-2 and 4, also HHU Düsseldorf (Institut für Theoretische Physik) are involved.

Experiments The first and only experiment measuring the polarization of laser-accelerated protons has been performed at the ARCturus laser facility at HHU Düsseldorf. For the measurements a 100 Terawatt Ti:Sa laser system with a typical pulse duration of 25 fs and a repetition rate of 10 Hz has been used producing an intensity of several 1020 Wcm^{-2} when being focused on a thin foil target. The result of this experiment can be summarized as follows: No polarization buildup was observed in the laser-accelerated proton beam. Another conclusion from this experiment is that both a stronger laser pulse with an intensity of about 1023 Wcm^{-2} and a high-density gas target instead of a thin foil target are required to observe proton polarization. Therefore, a crucial prerequisite of the program is the development of targets containing high-density pre-polarized hydrogen nuclei to produce highly polarized relativistic ion beams. The final experiments, aiming at the first observation of a polarized proton beam from laser-generated plasmas, will be carried out at the laser system SULF at SIOM in Shanghai. For the experimental realization, a polarized HCl gas-jet target is under construction at IKP where the degree of hydrogen polarization is measured with a Lamb-shift polarimeter. In parallel, a hyperpolarized ^{3}He gas-jet target is prepared for experiments at the PHELIX Petawatt Laser Facility at GSI in Darmstadt to measure the degree of spin-polarization of laser-accelerated ^{3}He^{2+} ions. The time line for the next steps to produce laser-accelerated polarized protons and ions is to perform the experiment with hyperpolarized ^{3}He gas jet ("static" polarization) at PHELIX in 2019. The experiments with nuclear polarized H atoms from HCl jet ("dynamic" polarization) at SULF will then start in 2020.

Simulation of Beam Acceleration with Polarization In order to predict the degree of beam polarization from a laser-driven plasma accelerator, particle-in-cell simulations including spin effects have been carried out for the first time. For this purpose, the Thomas-BMT equation, describing the spin precession in electromagnetic fields, has been implemented into the VLPL (Virtual Laser Plasma Lab) code. The Monte-Carlo simulations are performed on the supercomputers (close cooperation of IKP-4, PGI-6, JSC and HHU Düsseldorf). By implementing spin effects in a 3D-PIC simulation code, theoretical predictions on the proton spin behavior during laser-driven plasma acceleration can be made.VLPL is the only PIC code with explicit treatment of particle spins worldwide up to now. The simulation developments will be complemented by experimental campaigns at the SULF laser facility in Shanghai, the PHELIX laser facility at GSI, and finally at the future stages of the JuSPARC laser facility.

Production of Polarized Beams For the experimental realization at the SULF laser facility, a polarized gas-jet target is under construction at the FZJ in the framework of ATHENA$_{hadron}$, where the degree of hydrogen polarization is measured with a Lamb-shift polarimeter. An HCl gas jet is injected into the interaction chamber by a standard nozzle with a fast short-pulse piezo valve that can be operated at 5 bar inlet-gas pressure to produce a gas density in the range of roughly 10^{19} cm^{-3}. Few millimeters below the nozzle, the interaction between the gas and two laser beams takes place. The polarizing laser system is a pulsed Ni:YAG laser from EKSPLA. Its peculiarity is the quasi-simultaneous output of the fundamental wavelength at 1064 nm and the fifth harmonic at 213 nm. The repetition rate of the laser system is 5 Hz and the pulses duration is about 170 ps, which is twice shorter than the transfer time of the electron spin polarization to the nucleus due to the hyperfine interaction beat (roughly 0.35 ns). The ultraviolet laser photons excite the HCl into a state with parallel electron spins that will immediately dissociate into separated atoms. Therefore, the electrons of the hydrogen atoms are fully polarized. Due to the hyperfine beat, this electron polarization is transferred into a nuclear polarization after 0.35 ns. If in this moment the SULF laser will ionize the atoms, the nuclear polarization should be preserved in the accelerated protons. The linearly polarized 1064 nm beam with pulse energy of 100 mJ is focused with an intensity of 1011 Wcm^{-2} into the interaction chamber to align the HCl bonds. Thus, the hydrogen atoms after the dissociation with the ultraviolet photons will leave the interaction point in one plane only. This option is very useful to adjust the trajectories of the separated hydrogen atoms, so that there nuclear polarization can be measured with a Lamb-shift polarimeter in the laboratory to optimize the interaction process of gas jet and laser beams.

2.6.6 Detector lab

Compton polarimeters open a unique insight into the dynamics of atomic processes in highly charged heavy ions investigated e.g. by experiments at the accelerator facility GSI. The actual detector systems which allow to determine linear polarization of an x-ray source cover an energy range from 40 keV up to 400- 500 keV. In order to cover an energy range from a few keV to 30 keV a Compton polarimeter prototype has been developed. The concept is based on a passive low-Z scatterer (e.g. Be, SiC, PE) in which the emitted x-rays will undergo Compton scattering and in a subsequent step they will be deposited on a 3.5 mm thick pixelated HPGe detector with a structure of 19 hexagonal pixels. The degree of linear polarization is determined from the asymmetry of the scattering distribution. The detector may be used as a 19-pixel x-ray detector or in combination with a scatterer as Compton polarimeter. The readout stage is split into two parts. The first part is the cryogenically cooled FET input stage and the second stage is built from discrete charge sensitive preamplifiers operating at room temperature.
Another project is a segmented 16 mm thick HPGe-detector realized realized together with GSI, HI- Jena and Friedrich-Schiller-University Jena. The detector is segmented into 64 pixels (3.5 mm x 3.5 mm each) arranged in a 8x8 matrix. For tests with different preamplifiers to optimize the energy resolution, the design of the system allows an easy exchange of the cold FETs without removing the wire-bonds to the pixels.

A Beam Time at COSY in 2018

For 2018 in total 4536 hours of operation were scheduled for experiments, 1512 hours for FAIR related activities, 2408 hours for JEDI, and 616 hours for irradiations for the HBS developments. About 5 % (280 hours) were used for COSY studies and 1256 hours were spent on machine development and experiment setup. The shutdown periods used for maintenance and installations summed up to 2688 hours. The beamtime distribution is given in table 6.

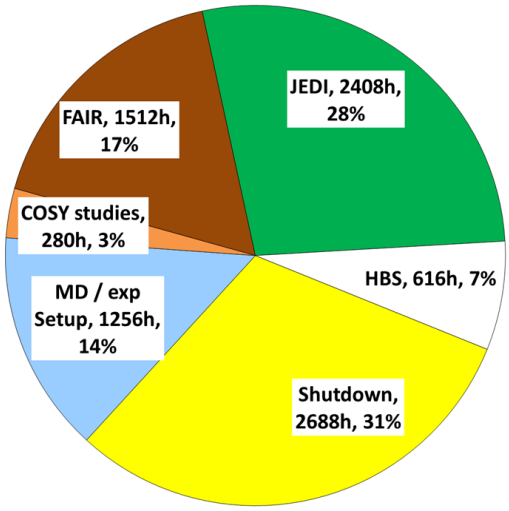

Fig. 33: COSY beam-time statistics in 2018.

Table 6: COSY operation in 2018.

Experiment	hours
Shutdown	2688
MD/exp. Setup	1256
COSY beam studies	280
FAIR beam dynamic studies	736
CBM	208
PANDA	568
JEDI	2408
HBS	616

B Councils

COSY Beam Time Advisory Committee (CBAC)

Prof. K. Aulenbacher	Universität Mainz, Germany
Prof. O. Kester	TRIUMF, Canada
Prof. J. Miller	Boston University, USA
Prof. C.J. Schmidt	GSI Darmstadt, Germany
Prof. M. Weber	KIT, Karlsruhe, Germany (Chairperson)

POF Review Panel

M. C. Aronson	Texas A&M University (Chairperson)	USA
I. Anderson	Oak Ridge National Laboratory	USA
A. Bracco	University of Milano	Italy
T. Forsyth	Institut Laue-Langevin	France
B. D. Gaulin	McMaster University	Canada
D. F. Geesaman	Argonne National Laboratory	USA
B. Jacak	Lawrence Berkeley Laboratory	USA
K. Kirch	Paul Scherrer Institut	Switzerland
K. Mortensen	University of Copenhagen	Denmark
T. Nakada	École polytechnique fédérale de Lausanne	Switzerland
D. A. Neumann	National Institute of Standards and Technology	USA
C. Petrillo	University of Perugia	Italy
A. Tennant	Oak Ridge National Laboratory	USA
F. Willeke	Brookhaven National Laboratory	USA
F. Zimmermann	CERN	Switzerland

C Publications – Journal Articles in 2018

1. **Novel event classification based on spectral analysis of scintillation waveforms in Double Chooz**
   T. Abrahão *et al.* (Double Chooz Collaboration)
   JINST **13**(01) 01031 (2018)

2. **Importance of d -wave contributions in the charge symmetry breaking reaction $dd \to {}^4\mathrm{He}\pi^0$**
   P. Adlarson *et al.*
   Phys. Lett. B **781** 645 - 650 (2018)

3. **An Isotensor Dibaryon in the p p $\to$ p p $\pi^+\pi^-$ Reaction?**
   P. Adlarson *et al.*
   Phys. Rev. Lett. **121** 052001 (2018)

4. **Search for C violation in the decay $\eta \to \pi^0 e^+ e^-$ with WASA-at-COSY**
   P. Adlarson *et al.*
   Phys. Lett. B **784** 378 - 384 (2018)

5. **Total and differential cross sections of η -production in proton-deuteron fusion for excess energies between Q_η =13 MeV and Q_η =81 MeV**
   P. Adlarson *et al.*
   Phys. Lett. B **782** 297 - 304 (2018)

6. **Spin Dependence of η Meson Production in Proton-Proton Collisions Close to Threshold**
   P. Adlarson *et al.*
   Phys. Rev. Lett. **120** 022002 (2018)

7. **Backward single-pion production in the $pd \to {}^3\mathrm{He}\pi^0$ reaction with WASA-at-COSY**
   P. Adlarson *et al.*
   Eur. Phys. J. A **54** 149 (2018)

8. **Measurement of the decay $\eta' \to \pi^0\pi^0\eta$ at MAMI**
   P. Adlarson *et al.*
   Phys. Rev. D **98** 012001 (2018)

9. **Comprehensive measurement of pp-chain solar neutrinos**
   M. Agostini *et al.* (Borexino Collaboration)
   Nature **562** 496 (2018)

10. **The Monte Carlo simulation of the Borexino detector**
    M. Agostini *et al.*
    Astropart. Phys. **97** 136 - 159 (2018)

11. **Spectroscopy of the hidden-charm $[qc][\overline{qc}]$ and $[sc][\overline{sc}]$ tetraquarks in the relativized diquark model**
    M.N. Anwar, J. Ferretti and E. Santopinto
    Phys. Rev. D **98** 094015 (2018)

12. **Performance of a prototype Straw Tube Tracker for the $\overline{\mathrm{P}}$ANDA experiment**
    A. Apostolou *et al.*
    J. Phys.: Conf. Ser. **1024** 012013 - (2018)

13. **Measurement of the analyzing powers in $\vec{p}d$ elastic and $\vec{p}n$ quasi-elastic scattering at small angles**
    S. Barsov *et al.*
    Eur. Phys. J. A **54** 225 (2018)

14. **Gauged and ungauged: a nonperturbative test**
    E. Berkowitz *et al.*
    J. High Energ. Phys. **2018** 124 (2018)

15. **Extracting the Single-Particle Gap in Carbon Nanotubes with Lattice Quantum Monte Carlo**
    E. Berkowitz *et al.*
    Eur. Phys. J. Web of Conferences **175** 03009 (2018)

16. **Few-nucleon and many-nucleon systems with semilocal coordinate-space regularized chiral nucleon-nucleon forces**
S. Binder *et al.*
Phys. Rev. C: Nucl. Phys. **98** 014002 (2018)

17. **Ab initio translationally invariant nonlocal one-body densities from no-core shell-model theory**
M. Burrows *et al.*
Phys. Rev. C: Nucl. Phys. **97** 024325 (2018)

18. **A per-cent-level determination of the nucleon axial coupling from quantum chromodynamics**
C.C. Chang *et al.*
Nature <London>: Phys. Sci. **558** 91 - 94 (2018)

19. **Effective field theory for collective rotations and vibrations of triaxially deformed nuclei**
Q.B. Chen *et al.*
Phys. Rev. C: Nucl. Phys. **97** 064320 (2018)

20. **The high-speed after-pulse measurement system for PMT**
Y. Cheng *et al.*
J. Instrum. **13** P05014 - P05014 (2018)

21. **Line shape analysis of the Kβ transition in muonic hydrogen**
D.S. Covita *et al.*
Eur. Phys. J. D **72** 72 (2018)

22. **$J/\psi \to \gamma\eta'\pi^+\pi^-$ and the structure observed around the $\overline{p}p$ threshold**
L. Dai, J. Haidenbauer and U. Meißner
Phys. Rev. D **98** 014005 (2018)

23. **A new method to study the number of colors in the final-state interactions of hadrons**
L. Dai and U. Meißner
Phys. Lett. B **783** 294 - 300 (2018)

24. **Amplitude analysis of the anomalous decay $\eta' \to \pi^+\pi^-\gamma$**
L. Dai *et al.*
Phys. Rev. D **97** 036012 (2018)

25. **Test of semilocal duality in a large N C framework**
L. Dai, X. Kang and U. Meißner
Phys. Rev. D **98** 074033 (2018)

26. **Photoproduction of π^0 mesons off protons and neutrons in the second and third nucleon resonance regions**
M. Dieterle *et al.*
Phys. Rev. C: Nucl. Phys. **97** 065205 (2018)

27. **Derivation of spontaneously broken gauge symmetry from the consistency of effective field theory I: Massive vector bosons coupled to a scalar field**
D. Djukanovic, J. Gegelia and U. Meißner
Phys. Lett. B **785** 543 - 550 (2018)

28. **Triviality of Quantum Electrodynamics Revisited**
D. Djukanovic, J. Gegelia and U. Meißner
Commun. Theor. Phys. **69** 263 - (2018)

29. **Electric Dipole Moment Results from lattice QCD**
J. Dragos *et al.*
Eur. Phys. J. Web of Conferences **175** 06018 - (2018)

30. **Towards a new paradigm for heavy-light meson spectroscopy**
M. Du *et al.*
Phys. Rev. D **98** 094018 (2018)

31. **Interactions between vector mesons and dynamically generated resonances**
M. Du *et al.*
Eur. Phys. J. C **78** 988 (2018)

32. **Extracting the σ -term from low-energy pion-nucleon scattering**
J.R.d. Elvira *et al.*
J. Phys. G **45** 024001 - (2018)

33. **Advantages of nuclear fusion with polarized fuel**
R. Engels *et al.*
Proc. Sci., SISSA PSTP2017, 10 (2018)

34. **Production and storage of polarized H_2, D_2, and HD molecules**
R. Engels *et al.*
Proc. Sci., SISSA PSTP2017, 9 (2018)

35. **How (not) to renormalize integral equations with singular potentials in effective field theory**
E. Epelbaum *et al.*
Eur. Phys. J. A **54** 186 (2018)

36. **Wilsonian Renormalization Group and the Lippmann-Schwinger Equation with a Multitude of Cutoff Parameters**
E. Epelbaum, J. Gegelia and U. Meißner
Commun. Theor. Phys. **69** 303 - (2018)

37. **Microscopic clustering in light nuclei**
M. Freer *et al.*
Rev. Mod. Phys. **90** 035004 (2018)

38. **Experimental and theoretical study of deuteron-proton elastic scattering for proton kinetic energies between T = 882.2 MeV and T = 918.3 MeVI**
C. Fritzsch *et al.*
Phys. Lett. B **784** 277 - 283 (2018)

39. **Observation of $\Upsilon(2S) \to \gamma\eta_b(1S)$ Decay**
B.G. Fulsom *et al.*
Phys. Rev. Lett. **121** 232001 (2018)

40. **Lyman-α source for laser cooling antihydrogen**
G. Gabrielse *et al.*
Opt. Lett. **43** 2905 - 2908 (2018)

41. **Once more on the Higgs decay into two photons**
J. Gegelia and U. Meißner
Nucl. Phys. B **934** 1 - 6 (2018)

42. **Muon reconstruction with a geometrical model in JUNO**
C. Genster *et al.*
J. Instrum. **13** T03003 (2018)

43. **Radiative pion capture in ^2H , ^3He , and ^3H**
J. Golak *et al.*
Phys. Rev. C: Nucl. Phys. **98** 054001 (2018)

44. **Connection between zero chromaticity and long in-plane polarization lifetime in a magnetic storage ring**
G. Guidoboni *et al.*
Phys. Rev. Accel. Beams **21** 024201 (2018)

45. **Hadronic molecules**
F. Guo *et al.*
Rev. Mod. Phys. **90** 015004 (2018)

46. **Antinucleon-nucleon interaction in chiral effective field theory**
J. Haidenbauer
Eur. Phys. J. Web of Conferences **181** 01028 (2018)

47. **Scattering of charmed baryons on nucleons**
J. Haidenbauer and G. Krein
Z. Phys. A-Hadron Nucl. **54** 199 (2018)

48. **Phase measurement for driven spin oscillations in a storage ring**
N. Hempelmann *et al.*
Phys. Rev. Accel. Beams **21** 042002 (2018)

49. **Development of a Field Mapper for the Determination of the Multipole Components of the Curved HESR Dipole Magnets**
J.H. Hetzel *et al.*
IEEE T. Appl. Supercon. **28** 9001104 (2018)

50. **Simulation of proton-proton elastic scattering for the KOALA recoil detector**
Q. Hu *et al.*
Nucl. Instr. Meth. Phys. Res. A **898** 133 - 138 (2018)

51. **First measurement of helicity-dependent cross sections in $\pi^0\eta$ photoproduction from quasi-free nucleons**
A. Käser *et al.*
Phys. Lett. B **786** 305 - 312 (2018)

52. **Effect of electron beam cooling on transversal and longitudinal emittance of an external proton beam**
K. Kilian *et al.*
Nucl. Instr. Meth. Phys. Res. A **880** 15-21 (2018)

53. **The Tjon band in Nuclear Lattice Effective Field Theory**
N. Klein *et al.*
Eur. Phys. J. A **54** 121 (2018)

54. **Lattice improvement in lattice effective field theory**
N. Klein, D. Lee and U. Meißner
Eur. Phys. J. A **54** 233 (2018)

55. **Resonance-like coherent production of a pion pair in the reaction $pd \to pd\pi\pi$ in the GeV region**
V.I. Komarov *et al.*
Eur. Phys. J. A **54** 206 (2018)

56. **A primer to numerical simulations: the perihelion motion of Mercury**
C. Körber *et al.*
Phys. Educ. **53** 055007 - (2018)

57. **Hubbard-Stratonovich-like Transformations for Few-Body Inter-actions**
C. Körber, E. Berkowitz and T. Luu
Eur. Phys. J. Web of Conferences **175** 11012 - (2018)

58. **Exclusive photoproduction of π^0 up to large values of Mandelstam variables s , t , and u with CLAS**
M.C. Kunkel *et al.*
Phys. Rev. C **98** 015207 (2018)

59. **Theoretical study of the $\Delta^{++} - \Delta^-$ configuration in the deuteron using an antiproton beam**
A.B. Larionov *et al.*
Phys. Rev. C: Nucl. Phys. **98** 054611 (2018)

60. **Few-body universality in the deuteron- α system**
J. Lei *et al.*
Phys. Rev. C: Nucl. Phys. **98** 051001 (2018)

61. **Neutron-proton scattering with lattice chiral effective field theory at next-to-next-to-next-to-leading order**
N. Li *et al.*
Phys. Rev. C: Nucl. Phys. **98** 044002 (2018)

62. **Excitation spectra of exotic nuclei in a self-consistent phonon-coupling model**
N. Lyutorovich *et al.*
Phys. Rev. C: Nucl. Phys. **98** 054304 (2018)

63. **Deuteron analysing powers in deuteron-proton elastic scattering at 1.2 and 2.27 GeV**
D. Mchedlishvili *et al.*
Nucl. Phys. A **977** 14 - 22 (2018)

64. **Three-particle bound states in a finite volume: Unequal masses and higher partial waves**
Y. Meng *et al.*
Phys. Rev. D **98** 014508 (2018)

65. **Solar Neutrinos Spectroscopy with Borexino Phase-II**
L. Miramonti *et al.*
Universe **4** 118 - (2018)

66. **Faddeev approach to the reaction $K^- \to \pi\Sigma n$ at p_K = 1 GeV/c**
K. Miyagawa, J. Haidenbauer and H. Kamada
Phys. Rev. C: Nucl. Phys. **97** 055209 (2018)

67. **Determination of N^* amplitudes from associated strangeness production in p+p collisions**
R. Münzer *et al.*
Phys. Lett. B **785** 574 - 580 (2018)

68. **The $\eta'\eta$-carbon potential at low meson momenta**
M. Nanova *et al.*
Eur. Phys. J. A **54** 182 (2018)

69. **Track propagation methods for the correlation of charged tracks with clusters in the calorimeter of the $\overline{\text{P}}$ANDA experiment**
T. Nasawasd *et al.*
J. Instrum. **13** T02008 - T02008 (2018)

70. **Heavy Physics Contributions to Neutrinoless Double Beta Decay from QCD**
A. Nicholson *et al.*
Phys. Rev. Lett. **121** 172501 (2018)

71. **Λ N $\to$ NN EFT potentials and hypertriton non-mesonic weak decay**
A. Pérez-Obiol, D.R. Entem and A. Nogga
J. Phys.: Conf. Ser. **1024** 012033 (2018)

72. **Exotics at Belle and Perspectives at Belle II**
E. Prencipe
Act. Phys. Pol. B / Proc. Suppl. **11** 447 (2018)

73. **High-statistics measurement of the $\eta \to 3\,\pi^0$ decay at the Mainz Microtron**
S. Prakhov *et al.*
Phys. Rev. C: Nucl. Phys. **97** 065203 (2018)

74. **Solar neutrino analysis with the Borexino detector**
M. Redchuk
J. Phys.: Conf. Ser. **1056** 012050 - (2018)

75. **The impact of $K^+\Lambda$ photoproduction on the resonance spectrum**
D. Rönchen, M. Döring and U. Meißner
Eur. Phys. J. A **54** 110 (2018)

76. **Dispersive analysis of pion-nucleon scattering and the pion-nucleon sigma term**
J. Ruiz de Elvira *et al.*
PoS Hadron2017 141 (2018)

77. **Search for the lepton-flavor-violating decay $B^0 \to K^{*0}\mu^{\pm}e^{\mp}$**
S. Sandilya *et al.*
Phys. Rev. D **98** 071101 (2018)

78. **Exploratory study of possible resonances in heavy meson - heavy baryon coupled-channel interactions**
C. Shen *et al.*
Chinese Phys. C **42** 023106 - (2018)

79. **The predictive power of spallation models for isotopic cross sections**
U. Singh *et al.*
Eur. Phys. J. A **54** 109 (2018)

80. **Pressure stabilized straw tube modules for the PANDA Forward Tracker**
J. Smyrski *et al.*
J. Instrum. **13** P06009 - P06009 (2018)

81. **Experimental study of the $\gamma p \to \pi^0 \eta p$ reaction with the A2 setup at the Mainz Microtron**
V. Sokhoyan *et al.*
Phys. Rev. C: Nucl. Phys. **97** 055212 (2018)

82. **Recent results of HESR original stochastic cooling tanks at COSY**
R. Stassen, B. Breitkreutz and N. Shurkhno
J. Phys.: Conf. Ser. **1067** 052013 (2018)

83. **Breaking and restoration of rotational symmetry in the low energy spectrum of light $\alpha\alpha$-conjugate nuclei on the lattice I: ^{8}Be and ^{12}C**
G. Stellin, S. Elhatisari and U. Meißner
Eur. Phys. J. A **54** 232 (2018)

84. **Behavior of the collective rotor in wobbling motion**
E. Streck *et al.*
Phys. Rev. C: Nucl. Phys. **98** 044314 (2018)

85. **EDM Experiments at Storage Rings**
H. Ströher
Eur. Phys. J. Web of Conferences **181** 01031 (2018)

86. **Review of Particle Physics**
M. Tanabashi *et al.*
Phys. Rev. D **98** 030001 (2018)

87. **Self-consistency in the phonon space of the particle-phonon coupling model**
V. Tselyaev *et al.*
Phys. Rev. C **97** 044308 (2018)

88. **Search for time-reversal-invariance violation in double polarized antiproton-deuteron scattering**
Y. Uzikov and J. Haidenbauer
Eur. Phys. J. Web of Conferences **181** 01015 (2018)

89. **Line shapes of the $Z_b(10610)$ and $Z_b(10650)$ in the elastic and inelastic channels revisited**
Q. Wang *et al.*
Phys. Rev. D **98** 074023 (2018)

90. **Octet baryon magnetic moments at next-to-next-to-leading order in covariant chiral perturbation theory**
Y. Xiao *et al.*
Eur. Phys. J. C **78** 489 (2018)

91. **New spectrum of negative-parity doubly charmed baryons: Possibility of two quasistable states**
M. Yan *et al.*
Phys. Rev. D **98** 091502 (2018)

92. **Observation of $e^+e^- \to \pi^+\pi^-\pi^0\chi_{b1,1}(1P)$ and search for $e^+e^- \to \phi\chi_{b1,1}(1P)$ at $\sqrt{s} = 10.96 - 11.05$ GeV**
J.H. Yin *et al.*
Phys. Rev. D **98** 091102 (2018)

93. **Charge Symmetry Breaking in the reaction $dd \to {}^4\mathrm{He}\pi^0$ with WASA-at-COSY**
M. Zurek
PoS Hadron2017 157 (2018)

D Talks and Colloquia in 2018

1. F. Abusaif
   Development of compact highly sensitive beam position monitors for storage rings
   7th International Symposium on Symmetries in Subatomic Physics, Aachen, Germany: 2018-06-10 - 2018-06-15

2. D. Alfs and D. Grzonka
   Design of a detector for studies of s=-2 baryon interaction induced by stopped antiproton annihilation
   15th International Workshop on Meson Physics, Krakow, Poland: 2018-06-07 - 2018-06-12

3. D. Alfs, D. Grzonka and M. Zielinski
   Drift chamber calibration and track reconstruction in the P-349 antiproton polarization experiment
   15th International Workshop on Meson Physics, Krakow, Poland: 2018-06-07 - 2018-06-12

4. D. Alfs
   Search for polarization in the antiproton production process
   DPG-Frühjahrstagung, Bochum, Germany: 2018-02-26 - 2018-03-02

5. D. Alfs
   Liquid target-based antiproton detectors
   AVA Topical Workshop Detectors & Diagnostics for low energy ion and antiproton beam, Vienna, Austria: 2018-10-15 - 2018-10-17

6. Z. Bagdasarian
   Neutrino hunters around the world
   Georgian-German School and Workshop in Basic Science, Tbilisi, Georgia: 2018-08-20 - 2018-08-24

7. Z. Bagdasarian
   Core-collapse supernova detection with Borexino and friends
   Workshop on Core-collapse Supernova Neutrino Detection, Orsay, France: 2018-07.04 - 2018-07-05

8. Z. Bagdasarian
   Everything you want to know about the Borexino new results - Group report
   Deutsche Physikalische Gesellschaft (DPG) Spring Meeting, Bochum, Germany: 2018-02-26 - 2018-03.-02

9. Z. Bagdasarian
   Catch me if you can: the latest Borexino investigations on neutrinos
   Aachen, Germany: 2018-05-18

10. Z. Bagdasarian
    Everything you need to know about the Borexino new results
    Oak Ridge, USA: 2018-05-03

11. Z. Bagdasarian
    Everything you need to know about the Borexino new results
    New York, USA: 2018-04-25

12. I. Bekman *et al.*
    Experience and Prospects of Real-Time Signal Processing and Representation for the Beam Diagnostics at COSY
    International Conference on Accelerator and Large Experimental Control Systems (16th), Barcelona, Spain: 2017-10-08 - 2017-10-13

13. E. Berkowitz *et al.*
    Extracting the Single-Particle Gap in Carbon Nanotubes with Lattice Quantum Monte Carlo
    35th International Symposium on Lattice Field Theory, Granada, Spain: 2017-06-18 - 2017-06-24

14. E. Berkowitz *et al.*
    Progress in Multibaryon Spectroscopy
    The 36th Annual International Symposium on Lattice Field Theory, East Lansing, MI, USA: 2018-07-22 - 2018-07-28

15. Y. Cheng
    Physics potential and status of JUNO
    Prospects in Neutrino Physics, London, Great Britain: 2018-12-19 - 2018-12-21

16. Y. Cheng *et al.*
Impact of energy response of liquid scintillator detector on JUNO Mass Hierarchy Sensitivity
Deutsche Physikalische Gesellschaft, Würzburg, Germany: 2018-03-19 - 2018-03-23

17. Y. Cheng and L. Ludhova
GNA fitter and Detector response impact on MH sensitivity study
28th International Conference on Neutrino Physics and Astrophysics, Heidelberg, Germany: 2018-06-04 - 2018-06-09

18. R.W. Engels *et al.*
Production and Storage of Polarized H2, D2 and HD Molecules
The XVII International Workshop on Polarized Sources, Targets and Polarimetry, Daejeon, South Korea: 2017-10-16 - 2017-10-20

19. R.W. Engels *et al.*
Advantages of Nuclear Fusion with Polarized Fuel
The XVII International Workshop on Polarized Sources, Targets and Polarimetry, Daejeon, South Korea: 2017-10-16 - 2017-10-20

20. Ch. Genster
Status of the Jiangmen Underground Neutrino Observatory
New Trends in High Energy Physics, Budva, Becici, Montenegro: 2018-09-24 - 2018-09-30

21. Ch. Genster
The Jiangmen Underground Neutrino Observatory – Group Report
Deutsche Physikalische Gesellschaft (DPG) Spring Meeting, Würzburg, Germany: 2018-03-19 - 2018-03-23

22. K. Grigoryev
Electrostatic deflector development for JEDI collaboration
7th International Symposium on Symmetries in Subatomic Physics, Aachen, Germany: 2018-06-10 - 2018-06-15

23. D. Grzonka
Search for polarized antiproton production
Low Energy Antiproton Conference, Paris, France: 2018-03-12 - 2018-03-16

24. D. Grzonka
Polarization analysis of antiprotons produced in pA collisions
15th International Workshop on Meson Physics, Krakow, Poland: 2018-06-07 - 2018-06-12

25. J. Haidenbauer
Antinucleon-nucleon interaction in chiral effective field theory
6th International Conference on Exotic Atoms and Related Topics, Vienna, Austria: 2017-09-11 - 2017-09-15

26. J. Haidenbauer
Baryon-baryon interaction in chiral effective field theory
XXII International Conference on Few-Body Problems in Physics, Caen, France: 2018-07-09 - 2018-07-13

27. D. Han, L. Ludhova and S. Kumaran
Background study for an updated geoneutrino analysis with Borexino
Deutsche Physikalische Gesellschaft, Würzburg, Germany: 2018-03-19 - 2018-03-23

28. C. Hanhart
Open questions and issues in light meson spectroscopy
International Workshop on Hadron Structure and Spectroscopy, Bonn, Germany: 2018-03-19 - 2018-03-21

29. C. Hanhart
Heavy Exotics:Concepts, Insights and Perspectives
April Meeting of the American Physics Society, Columbus, Ohio, USA: 2018-04-14 - 2018-04-17

30. C. Hanhart
How to master light meson dynamics: From hadron spectroscopy to CP phases
7th International Symposium on Symmetries in Subatomic Physics, Aachen, Germany: 2018-06-10 - 2018-06-15

31. V. Hejny
Measurement of Electric Dipole Moments at Storage Rings
Hadron Physics Summer School 2018, Jülich, Germany: 2018-09-24 - 2018-09-28

32. P. Kampmann *et al.*
Reduction of the 14C background for the neutrino mass-hierarchy measurement of the JUNO experiment
Deutsche Physikalische Gesellschaft, Würzburg, Germany: 2018-03-19 - 2018-03-23

33. P. Kampmann
Reduction of the 14C-Background in JUNO
11th International Neutrino Summer School, Mainz, Germany: 2018-05-21 - 2018-06-01

34. P. Kampmann
Reduction of the 14C-Background in JUNO
7th International Symposium on Symmetries in Subatomic Physics, Aachen, Germany: 2018-06-10 - 2018-06-15

35. I. Keshelashvili *et al.*
Polarimetry - from basics to precision
XVII International Workshop on Polarized Sources, Targets & Polarimetry, Kaist, South Korea: 2017-10-16 - 2017-10-20

36. I. Keshelashvili, D. Mchedlishvili and F. Müller
A new approach to use LYSO scintillators for polarimetry in the storage ring EDM measurements
18th International Conference on Calorimetry in Particle Physics, Eugene, USA: 2018-05-21 - 2018-05-25

37. S. Kumaran
Optimisation of selection cuts for updated geoneutrino analysis with Borexino
Deutsche Physikalische Gesellschaft (DPG) Spring Meeting, Würzburg, Germany: 2018-03-19 - 2018-03-23

38. A. Lehrach
Overview of Compact Proton Accelerators
4rd Int. HBS Meeting, Unkel am Rhein, Germany: 2018-10-04 - 2018-10-05

39. A. Lehrach
Hadron Accelerators - Progress and Plans at FZJ
4th Annual Matter and Technologies Meeting, Berlin, Germany: 2018-07-12 - 2018-07-14

40. A. Lehrach
Lecture on Accelerator Physics
Hadron Physics Summer School, Jülich, Germany: 2018-09-24 - 2018-09-29

41. A. Lehrach
Lattice considerations
CP-EDM Meeting with CERN, EDM workshop, Jülich, Germany: 2018-03-08 - 2018-03-09

42. L. Ludhova
Overview on solar, geo, and reactor neutrino experiments
DISCRETE 2018. 6th Symposium on Prospects in the Physics of Discrete Symmetries, Austrian Academy of Science, Vienna, Austria: 2018-11-26 - 2018-11-30

43. L. Ludhova
Systematic errors in Borexino Solar and Geoneutrino Analyses
The International Workshop on Next Generation Nucleon Decay and Neutrino Detectors (NNN18), Vancouver, Canada: 2018-10-31 - 2018-11-04

44. L. Ludhova
Geoneutrinos
History of the Neutrino, Paris, France. (youtube): 2018-09-05 - 2018-09-07

45. L. Ludhova
Low-energy neutrino physics with Borexino and JUNO
Université Libre de Bruxelles, Brussels, Belgium: 2018-12-14

46. S. Martin, A. Lehrach and R.M. Talman
Design of a Prototype EDM Storage Ring
23rd International Symposium Spin Physics and Related Phenomena, Ferrara, Italien: 2018-09-10 - 2018-09-14

47. A. Nass
Commissioning of the RF Wien filter for a first deuteron EDM measurement at COSY / Jülich
23rd International Spin Symposium, Ferrara, Italy: 2018-09-10 - 2018-09-14

48. A. Nogga
Benchmarks and first applications of SMS 3NFs
The 4th Meeting of the Low Energy Nuclear Physics International Collaboration, Bochum, Germany: 2018-02-19 - 2018-02-20

49. Ö. Penek, S. Marcocci and A. Vishneva
Analytical Multivariate Fit in the Borexino Solar Neutrino Analysis
Deutsche Physikalische Gesellschaft, Würzburg, Germany: 2018-03-19 - 2018-03-23

50. E. Prencipe
Exotics at Belle and Perspectives at Belle II
10th International Winter Workshop "Excited QCD" 2018, Kopaonik, Serbia: 2018-03-11 - 2018-03-15

51. E. Prencipe
Exotics at Belle and perspectives at Belle II
eQCD2018, Kopaonik, Serbia: 2018-03-11 - 2018-03-15

52. E. Prencipe
X, Y, Z states at Belle II
The 9th International Workshop on Charm Physics, Novosibirsk, Russia: 2018-05-21 - 2018-05-25

53. E. Prencipe
Search for exotic states with c- and s- quark content
International Workshop XLVI on Gross Properties of Nuclei and Nuclear Excitations, Hirschegg, Austria: 2018-01-14 - 2018-01-20

54. E. Prencipe
Search for exotic states with c- and s- quark content
BaBar collaboration meeting, Bonn, Germany: 2018-10-18

55. E. Prencipe
yHEP report 2018
KuHK meeting, Bad-Honnef, Germany: 2018-12-06

56. E. Prencipe
Search for exotic states with c- and s- quark content: connecting the dots from e^+e^- to ppbar machines
Seminar at Bonn University, Bonn, Germany: 2018-10-25

57. E. Prencipe
Statistics in HEP: the importance of estimating correct uncertainties
Hadron Physics Summer School 2018, Jülich, Germany: 2018-09-27

58. E. Prencipe
GENFIT2: general track-fitting tool for nuclear and particle physics
PANDA tracking workshop, Darmstadt, Germany: 2018-09-19

59. J. Pretz
Electric Dipole Moment Measurements at Storage Rings
ECT* workshop, Discrete symmetries in particle, nuclear and atomic physics and implications for our universe, Trento, Italy: 2018-10-08 - 2018-10-12

60. F. Rathmann
Electric Dipole Moment Searches using Storage Rings
Colloquium talk, Paul-Scherrer Institut Villigen, Switzerland: 2018-12-06 - 2018-12-06

61. F. Rathmann
Electric Dipole Moment Searches using Storage Rings
23rd International Spin Physics Symposium, Ferrara, Italy: 2018-09-10 - 2018-09-14

62. M. Redchuk
Solar neutrino analysis with the Borexino detector
Deutsche Physikalische Gesellschaft, Würzburg, Germany: 2018-03-19 - 2018-03-23

63. M. Redchuk
Solar neutrino analysis with the Borexino detector
11th International Neutrino Summer School, Mainz, Germany: 2018-05-21 - 2018-06-01

64. J. Ritman
Investigation of the transition form factors of excited hyperons with HADES
668. WE-Heraeus Seminar on Baryon Form Focus: Where do we stand?, Bad Honnef, Germany: 2018-04-23 - 2018-04-27

65. J. Ritman
Straw Tube Systems at Jülich and PANDA Muon Detectors at JINR
International Conference on the Super Tau Charm facility, Novosibirsk, Russia: 2018-05-26 - 2018-05-27

66. J. Ritman
Light Meson Decays: upcoming analysis reports on the decays $\eta \to \pi^0\pi^+\pi^-$ and $\omega \to \pi^0 e^+ e^-$
CLAS Collaboration Meeting, Newport News, USA: 2018-03-06 - 2018-03-09

67. J. Ritman
Physik in der Küche
Saturday Morning Physics, Bochum, Germany: 2018-11-14

68. M. Schever *et al.*
Waveform reconstruction for IBD and Muon Events in JUNO
Deutsche Physikalische Gesellschaft, Würzburg, Germany: 2018-03-19 - 2018-03-23

69. M. Schever
Waveform Reconstruction of IBD and Muon Events in JUNO
28th International Conference on Neutrino Physics and Astrophysics, Heidelberg, Germany: 2018-06-04 - 2018-06-09

70. V. Schmidt
Search for Electric Dipole Moments at COSY in Jülich - Closed-orbit and spin tracking simulations
DPG-Frühjahrstagung 2018, Würzburg, Germany: 2018-03-19 - 2018-03-23

71. R. Shah *et al.*
Studies on trigger configuration for the JUNO experiment
Deutsche Physikalische Gesellschaft, Würzburg, Germany: 2018-03-19 - 2018-03-23

72. H. Smitmanns and A.M. Thompson
OzoneSonde Data Quality Assessment JOSIE 2017-SHADOZ Campaign & ASOPOS Reload & COST Initiative
SPARC-OCTAV Workshop, Mainz, Germany: 2018-11-07 - 2018-11-09

73. R. Stassen, B. Breitkreutz and N. Shurkhno
Recent results of HESR original stochastic cooling tanks at COSY
9th International Particle Accelerator Conference, Vancouver, Canada: 2018-04-29 - 2018-05-04

74. T. Wagner
Beam-based alignment tests at the Cooler Synchrotron (COSY)
7th International Symposium on Symmetries in Subatomic Physics, Aachen, Germany: 2018-06-11 - 2018-06-15
Hyperfine Interact. 239 61

75. Y. Xu *et al.*
e + /e - Discrimination with Deep Learning Method
Deutsche Physikalische Gesellschaft, Würzburg, Germany: 2018-03-19 - 2018-03-23

76. M. Zurek
Recent Progress of the Storage Ring EDM Search with the JEDI Collaboration
DPG-Frühjahrstagung, Bochum, Germany: 2018-02-26 - 2018-03-02

77. M. Zurek
Polarimetry for a Storage-Ring Electric-Dipole-Moment Measurement
15th International Workshop on Meson Physics, Kraków, Poland: 2018-06-07 - 2018-06-12

78. M. Zurek
Searches for electric dipole moments (EDM) at a storage ring with JEDI
20th International Workshop on Neutrinos from Acceleratotors, Blacksburg, VA, United States: 2018-08-13 - 2018-08-18

79. M. Zurek
Probing symmetries in the world of hadrons with COSY
Heavy Ion Tea Seminar, Nuclear Science Division, Lawrence Berkeley National Laboratory, Berkeley, USA: 2018-02-12

E Bachelor, Master and Ph.D. Theses

E.1 Dissertation / PhD Theses

1. A. Apostolou
   Particle-identification capability of the straw tube tracker and feasibility studies for open-charm production with PANDA
   University of Groningen

2. N. Hempelmann
   Polarization Measurement and Manipulation for Electric Dipole Moment Measurements in Storage Rings
   RWTH Aachen University

3. J. Hetzel
   Beam-dynamics calculations including magnetic field measurements for the high-energy storage ring (HESR) at FAIR / Strahldynamikrechnungen unter Berücksichtigung von Magnetfeldmessungen für den Hochenergie-Speicherring (HESR) an FAIR
   RWTH Aachen University

4. A. Saleev
   New aspects of spin dynamics for precision experiments to search for the electric dipole moment of charged particles at storage rings
   Samara University, Russia

5. J. Slim
   A Novel Waveguide RF Wien Filter for Electric Dipole Moment Measurements of Deuterons and Protons at the COoler SYnchrotron (COSY)/Jülich
   RWTH Aachen University

6. F. Trinkel
   Development of a Rogowski coil Beam Position Monitor for Electric Dipole Moment measurements at storage rings
   RWTH Aachen University

7. S. Vejdani
   Particle-Identification capability of the Straw Tube Tracker and Feasibility Studies for the Charmed-Baryon Program with PANDA
   University of Groningen

E.2 Master Theses

1. S. Kumaran
   Updated Geoneutrino Measurement with the Borexino Detector
   RWTH Aachen University.

2. K. Olschewsky
   Systematic study of negative parity hadronic molecules
   Bonn University (FZJ-2019-02372)

3. D. De Rosa
   Software development for Fourier analysis of detector-signal in an EDM experiment
   Ferrara University

4. R. Shah
   Studies on the Trigger Configuration for the JUNO experiment
   RWTH Aachen University.

E.3 Bachelor Theses

1. L. Ebsen
   Study of track direction reconstruction in liquid scintillator detector
   RWTH Aachen University

2. P. Heinen
   Determination of the ρ' and ρ" Pole from the Pion Vector Form Factor with Padé Approximants
   Bonn University (FZJ-2019-02371)

3. A. Krampe
   Entwicklung eines Strahlprofilscanners für JEDI
   RWTH Aachen University

4. C. Schneider
   Generalisation of the Gounaris-Sakurai Parametrisation to overlapping inelastic resonances
   Bonn University (FZJ-2019-02370)

F Awards

- U.-G. Meißner: “Distinguished Scientist Award" of the Chinese Academy of Sciences
- U.-G.Meißner: Honorary Doctorate from the Ivane Iavakhishvili Tbilisi State University (TSU)
- C. Hanhart: Lehrpreis der Universität Bonn
- M. Redchuk : Poster prize at the 11th International Neutrino Summer School - May 21- June 01, 2018 - Mainz, Germany.

G Third Party Funded Projects

Project	**Responsible**	**Funded by**
Untersuchung von exotischen 4-Quark Zuständen	E. Prencipe	DFG
PGSB: Experimental tests of time-reversal	H. Ströher	HGF
(CASCADE) Computational Science for Comp	T. Luu / U. G. Meißner	HGF
SFB/TRR 110 Quantenchromodynamik TP A01	J. Haidenbauer	DFN/SFB, NFSC
SFB/TRR 110 Quantenchromodynamik TP B03	C. Hanhart	DFN/SFB, NFSC
SFB/TRR 110 Quantenchromodynamik TP B06	A. Nogga	DFN/SFB, NFSC
SFB/TRR 110 Quantenchromodynamik TP Z01	U. G. Meißner	DFN/SFB, NFSC
SFB/TRR 110 Quantenchromodynamik TP Z02	C. Hanhart	DFN/SFB, NFSC
SFB/TRR 110 Quantenchromodynamik TP B09	T. Luu / U. G. Meißner	DFN/SFB, NFSC
PANDA/ Straw Tube Tracker	J. Ritman	Industrieprojekt mit der GSI GmbH
PANDA/ Micro Vertex Detector	J. Ritman	Industrieprojekt mit der GSI GmbH
HESR - Dipole und Quadrupole	R. Tölle	Industrieprojekt mit der FAIR GmbH
HESR - sonstige Magnete	U. Bechstedt	Industrieprojekt mit der FAIR GmbH
HESR - Netzgeräte	M. Retzlaff	Industrieprojekt mit der FAIR GmbH
HESR - Hochfrequenz	R. Stassen	Industrieprojekt mit der FAIR GmbH
HESR - Injektion	R. Tölle	Industrieprojekt mit der FAIR GmbH
HESR - Strahldiagnose	V. Kamerdzhiev	Industrieprojekt mit der FAIR GmbH
HESR - Vakuum	F. Esser	Industrieprojekt mit der FAIR GmbH
HESR - Stochastische Kühlung	R. Stassen	Industrieprojekt mit der FAIR GmbH
HESR - Panda-Integration	D. Prasuhn	Industrieprojekt mit der FAIR GmbH
AVA MSCA ITN	D. Grzonka	EU
srEDM ERC Advanced Grant Management	H. Ströher	EU
srEDM ERC Advanced Grant Research	H. Ströher	EU
ATHENA-Hadron	A. Lehrach	HGF
(Accelerator Technology HElmholtz iNfrAstructure)		

H Collaborations

- Belle-II (B(meson) to lepton lepton (v.2))
(https://www.belle2.org)
- bERLinPro (Berlin Energy Recovery Linac Prototype, HZB)
(https://www.helmholtz-berlin.de/zentrum/zukunft/berlinpro/index_de.html)
- Borexino (Boron solar neutrino experiment, LNGS, Italy)
(http://borex.lngs.infn.it)
- CLAS (CEBAF Large Acceptance Spectrometer, JLab, USA)
(https://www.jlab.org/Hall-B/clas-web)
- CPEDM (Electric Dipole Moments, CERN)
(http://pbc.web.cern.ch/edm/edm-org.htm)
- ELENA (CERN) (Extra Low Energy Antiproton ring)
(https://espace.cern.ch/elena-project/SitePages/Home.aspx)
- FCC (CERN) (Future Circular Collider)
(https://home.cern/science/accelerators/future-circular-collider)
- JEDI (Jülich Electric Dipole moment Investigation, COSY)
(http://collaborations.fz-juelich.de/ikp/jedi)
- JUNO (Jiangmen Underground Neutrino Observatory, Jiangmen, China)
(http://juno.ihep.cas.cn)
- JuSPARC (Jülich Short-Pulsed Particle and Radiation Center)
(https://jusparc.fz-juelich.de/)
- PANDA (Anti-Proton Annihilation at Darmstadt, FAIR)
(https://panda.gsi.de)
- PAX (Polarized Antiproton eXperiments, COSY)
(http://collaborations.fz-juelich.de/ikp/pax)
- PDG (Particle Data Group)
(pdg.lbl.gov)
- TRIC (Time Reversal Invariance at Cosy, COSY)
(http://www.fz-juelich.de/ikp/ikp-2/DE/Forschung/TRIC/_node.html)
- WASA (Wide Angle Shower Apparatus, FRS)
(https://www-win.gsi.de/frs/index.htm)

I Conferences (co-)organized by the IKP

I.1 Hadron Physics Summer School (HPSS 2018)

The IXth edition of the bi-annual Hadron Physics Summer School (HPSS) took place in Jülich on September 24-28, 2018. This is a jointly organized physics school by scientists from the IKP and IAS institutes at Forschungszentrum Jülich, the Universities of Aachen, Bonn, Bochum, Düsseldorf and Giessen, financed by IKP, the Helmholtz-Institut für Strahlen und Kernphysik of Bonn, and CRC110.
A total of 65 students were selected by curriculum and reference letters out of 90 applications. Our selected students were bachelor-, master- and early-PhD students from China, Georgia, Germany, India, Poland, Russia, Sweden, Turkey, United Kingdom, Ukraine, United States, in equal part male/female.
The school comprised lectures and 7 working groups (each participant joined one) covering simultaneously theoretical, experimental, and accelerator aspects. The focus was on current issues in hadron physics with emphasis on current and future programs at the accelerators COSY (Jülich), ELSA (Bonn), LHC (CERN), CEBAF (Jefferson Lab), BEPC (Beijing) and FAIR (Darmstadt) featuring experiments like PANDA, Crystal Barrel, LHCb, CLAS, BESIII, Belle II as well as the search for electric dipole moments of charged particles in storage rings (JEDI) and neutrino physics.
As a part of the HPSS, a social event including a visit of the COSY facility and the laboratory where the PANDA components have been tested, with a following-up dinner, was organized. Figure 34 shows the HPSS 2018 students and some of the working group tutors in front of the building hosting the COSY control room, at the Forschungszentrum Jülich. The feedback of the participants provided via feedback sheets filled anonymously was extremely positive.

Fig. 34: Group photo of the HPSS 2018, in front of the building hosting the COSY control room, at the Forschungszentrum Jülich.

We consider the IXth edition of HPSS 2018 a great success consolidating the already proven cooperation among theorists, experimentalists and people woking in hardware of all institutes involved in the HPSS organization, and we are looking forward to the next edition of HPSS in 2020.

I.2 International Workshop on Meson Physics (MESON 2018)

The 15th International Workshop on Meson Physics - MESON 2018 - took place in Cracow, Poland, from 7 to 12 June 2018. We were celebrating the 15th edition of this conference. Therefore the opening of the conference was devoted to the memories of previous editions and during the banquet an anniversary cake was served. At this point, we also wanted to recall briefly the history of this series of conferences. The tradition of MESON conferences dates back to 1991. The main initiator of the first MESON conference was Walter Oelert and it was co-chaired by Eckart Grosse and Andrzej Magiera. The first three meetings were thematically related to the physics program planned for the accelerator COSY and started in GSI. The meetings were attended by many experts in meson physics, and the program was not limited only to low-energy meson physics which the organizers dealt with. Then we realized that meetings of this kind were very useful for the whole community involved in various aspects of meson physics. Therefore we decided to continue our meetings extending their program beyond standard meson physics. Since 1996 our conferences have gained their current name MESON and have become traditional meetings of the meson community. Since the beginning the Jagiellonian University and Forschungszentrum Jülich were the conference organizers, and the third organizer GSI Darmstadt was replaced by LNF-INFN Frascati in 2000 and fourth organizer INP-PAS Cracow has joined in 2010. Over the years also the chairmen have changed. Among them, the largest number of conferences were presided over by Carlo Guaraldo, Hartmut Machner, Lucjan Jarczyk, St. Kistryn, Andrzej Magiera and Hans Stöher. The number of participants from about 70 at the begining increased and stabilized on about 180 in recent conferences. Over 1200 physicists from all over the world participated in all conferences, and more than a thousand contributions were published in the conference proceedings. The recent MESON2018 conference was attended by over 170 participants from 25 countries representing 69 institutions from around the world. In total, there were 38 plenary talks, 69 parallel session talks and 26 posters. Additionaly a special public talk on hadron therapy was given by Paweł Olko. Laura Fabbietti presented an overview of the current status of the physics areas in which mesons play an important role, together with a preview of the planned investigations. The topics of the conference included hadronic and electromagnetic meson production in a broad energy range, meson interaction with mesons and nuclei, structure of hadrons, fundamental symmetry studies with mesons, exotic systems, rare decays. Theoretical talks focused mainly on

the problems of low-energy QCD with use of effective field theory and lattice QCD. Widely presented were diverse approaches to the problems of dynamical chiral symmetry breaking, kaon bound states, mesic atoms and nuclei, and mesons in nuclear matter. The success of the conference was made possible by the extensive work of the Advisory Committee, the Organizing Committee and the Local Organizing Committee. We especially thank our institutions for their financial and generous support. Special thanks go to the scientific secretary Aleksandra Wrońska for her excellent organization of the last few conferences. In subsequent conferences, we will miss her great commitment because she decided to leave our organizing committee. We gratefully acknowledge further financial assistance from our sponsors: European Physical Journal, Nowoczesna Elektronika Ltd., CAEN and the Municipality of Cracow (KRK2B). Last but not least, we thank all the participants for interesting presentations and lively discussions on recent results and expected further discoveries in the fields related to meson physics. We will further continue with the organization of he MESON conferences and hope to have a celebration of the 20th edition in next 10 years. The goal of MESON conferences will remain the same: bring people together and let them inspire each other in the beautiful surrounding and a friendly atmosphere of Cracow.

Fig. 35: Participants of the International Workshop on Meson Physics (MESON 2018) in Kracow.

I.3 7^{th} International Symposium on Symmetries in Subatomic Physics (SSP 2018)

From June 10th-15th 2018 IKP and RWTH jointly organized the 7th symposium on symmetries in subatomic physics (SSP2018). About 80 physicists from around the world attended the conference. The scientific program was devoted to recent accomplishments as well as future developments in a broad area of physics research, exploring fundamental symmetries in theory and experiment in atomic, nuclear and particle physics. Topics covered included neutrino physics, precision experiments, dark matter and energy, cosmology and CP-violation. In total 56 presentations were given and 13 posters were presented.

Fig. 36: Participants of the 7th Symposium on Symmetries in Subatomic Physics (SSP2018) at the Super C building at RWTH Aachen University.

I.4 Georgian-German Science Bridge: 8th GGSWBS Workshop in Tbilisi: "Science at Multidisciplinary SMART|Labs in Georgia"

During August 20 - 25, 2018, Ivane Javakhishvili Tbilisi State University (TSU) hosted the 8th joint bi-annual meeting called Georgian-German School and Workshop in Basic Science (GGSWBS; see: http://collaborations.fz-juelich.de/ikp/cgswhp/cgswhp18/) with the participation of Forschungszentrum Jülich (represented by IKP as well as IEK, INM, IBG, and ZEA) and the Georgian partner universities (AUG, ISU, GTU and TSU). This event is a joint targeted program of Shota Rustaveli National Science Foundation of Georgia (SRNSFG) and Jülich. The subject of this event was "Science at multidisciplinary SMART | Labs in Georgia".
The school and seminar focused on three main topics:

1. Symmetries in Subatomic Physics (related to SMART | EDM_Lab): the major thrust was devoted to arguably one of the most pressing questions in natural sciences - the reason for the dominance of matter over antimatter in the universe, which may be related to our search for Electric Dipole Moments of charged particles.

2. Atmospheric Research and Modelling, related to the SMART | AtmoSim_Lab;

3. Medical Imaging and Biomarkers, related to the SMART | BioMed_Lab.

The meeting was attended by international experts from accelerator groups, particle physics and technology institutes from various international collaborations (for particle physics, these comprised JEDI, Borexino, JUNO and PAX) as well as Bachelor, Master and PhD students from Jülich and the Georgian universities. During the event, the lectures were delivered by Hans Ströher and Ulf-G. Meißner (IKP, IAS), Andreas Wahner and Astrid Kiendler-Scharr (IEK), Jon Shah and Bernd Neumaier (INM), Ghaleb Natour and Stefan van Waasen (ZEA) of Forschungszentrum Jülich. The contents of the lectures fully covered the subjects of the meeting. Thus, the goals of the school and workshop were successfully achieved. As part of the event, eleven excellent students were selected from various scientific fields – Physics, Mathematics, Chemistry, Biology and Engineering Technology, corresponding to the mentioned FZJ institutes – which were granted internships of month each in Forschungszentrum Jülich. Talks of the workshop together with additional information have been published in 2018 as "Schriften des Forschungszentrums Jülich, Reihe Schlüsseltechnologien/Key Technologies, Band/Volume 182 (Eds.: A. Kacharava, K. Kotetishvili, and H. Ströher)".

Fig. 37: Participants of the international meeting "Science at Multidisciplinary SMART | Labs" (GGSWBS'18) in Tbilisi.

J Teaching Positions

Institute	Name	University
IKP-1	PD Dr. A. Gillitzer	Bonn
	Prof. Dr. F. Goldenbaum	Wuppertal
	Prof. J. Ritman Ph.D.	Bochum
	Dr. T. Stockmanns	Bochum
IKP-2	Prof. Dr. D. Gotta	Köln
	PD Dr. F. Rathmann	Aachen
	Prof. Dr. L. Ludhova	Aachen
	Prof. Dr. Dr. h.c. mult. H. Ströher	Köln
	Prof. Dr. J. Pretz	Aachen
IKP-3/IAS-4	Univ. Doz. Dr. J. Haidenbauer	Graz
	Prof. Dr. C. Hanhart	Bonn
	Prof. Dr. T. Luu	Bonn
	Prof. Dr. Dr. h.c. U.-G. Meißner	Bonn
	Dr. A. Nogga	Bonn
	PD Dr. A. Wirzba	Bonn
IKP-4	Prof. Dr. A. Lehrach	Aachen

K Personnel

K. Abuayyash (IKP-2) (1st May until 31st July 2018)
F. Abusaif (IKP-2)
A. Aksentev (IKP-2)
Msc. D. Alfs (IKP-1)
B. Alberdi (IKP-2) (since 15th October 2018)
Dr. M. Anwar (IKP-3/IAS-4) (since 1st September 2018)
Dr. Z. Bagdasarian (IKP-2)
Dr. U. Bechstedt (IKP-4) (until 31st March 2018)
Dr. I. Bekman (IKP-4)
C. Berchem (IKP-TA)
Dr. E. Berkowitz (IKP-3/IAS-4)
M. Beyß (IKP-2) (since 15th October 2018)
DP L. Bianchi (IKP-1) (until 31st January 2018)
Dr. C. Böhme (IKP-4)
M. Böhnke (IKP-4)
Dr. J. Böker (IKP-4)
DI N. Bongers (IKP-4)
Dr. B. Breitkreutz (IKP-4)
P. Brittner (IKP-4)
J. But (IKP-TA)
Dr. Y. Cheng (IKP-2)
W. Classen (IKP-4)
S. Clausen (IKP-2) (1st May until 31st December 2018)
M. Comuth-Werner (IKP-TA)
DI F.U. Dahmen (IKP-4)
Dr. L. Dai (IKP-3/IAS-4) (until 31st August 2018)
DI N. Demary (IKP-TA)
MBA A. Derichs (IKP-1)
C. Deliege (IKP-4)
G. D'Orsaneo (IKP-2)
R. Dosdall (IKP-1)
C. Ehrlich (IKP-4)
Dr. R. Engels (IKP-2)
B. Erkes (IKP-4)
Msc. W. Esmail (IKP-1) (since 15th January 2018)
DI F.-J. Etzkorn (IKP-4)
Dr. O. Felden (IKP-TA)
H.-W. Firmenich (IKP-TA)
N. Fröhlich (IKP-4)
Dr. R. Gebel (IKP-4)
Dr. J. Gegelia (IKP-3/IAS-4) (until 31st December 2018)
Msc. C. Genster (IKP-2)
R. Geppert (IKP-TA) (until 31st August 2018)
PD Dr. A. Gillitzer (IKP-1)
J. Göbbels (IKP-TA)
Prof. Dr. F. Goldenbaum (IKP-1)
Prof. Dr. D. Gotta (IKP-2) (until 31st January 2018)
A. Göttel (IKP-2) (since 1st November 2018)
Dr. K. Grigoryev (IKP-2)
Dr. D. Grzonka (IKP-1)
PD Dr. J. Haidenbauer (IKP-3/IAS-4)
Hamzic, Salun (IKP-4) (since 1st October 2018)
Prof. Dr. C. Hanhart (IKP-3/IAS-4)
D. Han (IKP-2) (until 14th September 2018)
T. Hahnraths-von der Gracht (IKP-TA)
BEng. A. Halama (IKP-4)
Dr. M. Hartmann (IKP-2)
DI R. Hecker (IKP-TA)
Dr. V. Hejny (IKP-2)
Dr. N. Hempelmann (IKP-2) (until 28th February 2018)
Dr. J.-H. Hetzel (IKP-4)
M. Holona (IKP-TA)
Dr. A. Kacharava (IKP-2)
Dr. V. Kamerdzhiev (IKP-4)
Msc. P. Kampmann (IKP-2)
J. Kannika (IKP-1) (since 1st November 2018)
C. Käseberg (IKP-4) (since 15th October 2018)
A. Kelleners (IKP-TA) (until 30th September 2018)
Dr. I. Keshelashvilli (IKP-2)
A. Kieven (IKP-4)
S. Kistemann (IKP-TA)
B. Klimczok (IKP-TA)
J. Knothe (IKP-TA) (since 1st October 2018)
F. König (IKP-2) (9th March 2018 unil 31st October 2018)
Dr. C. Körber (IKP-3/IAS-4) (until 30th June 2018)
M. Kremer (IKP-TA)
DI T. Krings (IKP-TA)
S. Kroon (IKP-2) (since 12th November 2018)
M. Küven (IKP-4)
S. Kumaran (IKP-2)
Dr. M. Kunkel (IKP-1) (until 31st December 2018)
Dr. T. Lähde (IKP-3/IAS-4)
Dr. A. Lai (IKP-1)
K.-G. Langenberg (IKP-4)
Prof. Dr. A. Lehrach (IKP-4)
Dr. D. Lersch (IKP-1) (until 28th February 2018)
C. Li (IKP-4) (until 15th January 2019)
MSc. S. Liebert (IKP-4)
Dr. X.-H. Liu (IKP-3/IAS-4) (until 31st October 2018)
Dr. B. Lorentz (IKP-4)
Prof. Dr. L. Ludhova (IKP-2)
Prof. Dr. Th. Luu (IKP-3/IAS-4)
D. Marschall (IKP-4) (until 31st May 2018)
M. Maubach (IKP-TA)
MSc. I. Matuschek (IKP-3/IAS-4)
DI H.-P. May (IKP-4) (until 5th June 2018)
Prof. Dr. Dr. h.c. U.-G. Meißner (IKP-3/IAS-4)
Dr. S. Merzliakov (IKP-4)
Msc. F. Müller (IKP-2)
S. Müller (IKP-TA)
J. Nadenau (IKP-2) (until 30th September 2018)
Dr. A. Naß (IKP-2)
Dr. A. Nogga (IKP-3/IAS-4)
V. Payak (IKP-2) (until 8th June 2018)
Msc. Ö. Penek (IKP-2)
BSc J. T. Peters (IKP-4)
MSc. V. Poncza (IKP-4)
Dr. D. Prasuhn (IKP-4)
Dr. E. Prencipe (IKP-1)
Prof. Dr. J. Pretz (IKP-2)
D. Prothmann (IKP-TA)
H. Pütz (IKP-4)
DP J. Pütz (IKP-1)

PD Dr. F. Rathmann (IKP-2)
Msc. M. Redchuk (IKP-2)
DI K. Reimers (IKP-4)
DI M. Retzlaff (IKP-4)
Msc. M. Rimmler (IKP-4) (since 1st July 2018)
Prof. J. Ritman (IKP-1)
G. Roes (IKP-TA)
Dr. B. Roy (IKP-1) (since 14th December 2018)
D. Ruhrig (IKP-4)
A. Saleev (IKP-2) (since 1st January 2018)
PD Dr. S. Schadmand (IKP-1)
MSc. M. Schever (IKP-2)
Dr. R. Schleichert (IKP-2)
F. Scheiba (IKP-4)
H. Schiffer (IKP-TA)
M. Schmühl (IKP-4)
Msc. A. Scholl (IKP-1) (since 1st October 2018)
K. Schumacher (IKP-TA)
Dr. Th. Sefzick (IKP-TA)
Prof. Dr. Y. Senichev (IKP-4) (until 31st January 2018)
Dr. V. Serdyuk (IKP-1)
R. Shah (IKP-2) (until 30th September 2018)
MSc. N. Shurkhno (IKP-4)
Siddique, Saad (IKP-4) (since 1st October 2018)
DI M. Simon (IKP-4)
H. Simonsen (IKP-TA)
H. Smitmanns (IKP-2) (since 15th November 2018)
Dr. X. Song (IKP-1) (until 12th January 2018)
D. Spölgen (IKP-2)
Dr. R. Stassen (IKP-4)
G. Sterzenbach (IKP-1)
Dr. T. Stockmanns (IKP-1)
Prof. Dr. Dr. h. c. H. Ströher (IKP-2)
A. Thampi (IKP-1) (since 1st July 2018)
MSc. M. Thelen (IKP-4)
Dr. T. Tolba (IKP-1) (since 13th August 2018)
Dr. R. Tölle (IKP-4)
MSc. F. Trinkel (IKP-2) (until 31st January 2018)
J. Uehlemann (IKP-1)
Dr. Y. Valdau (IKP-4)
DI T. Vashegyi (IKP-4)
Msc. T. Wagner (IKP-2)
Dr. C. Weidemann (IKP-4) (until 3 1st December 2018)
Dr. P. Wintz (IKP-1)
PD Dr. A. Wirzba (IKP-3/IAS-4)
MSc. J.-L. Wynen (IKP-3/IAS-4)
Dr. X. Xiong (IKP-3/IAS-4) (until 30th September 2018)
Dr. H. Xu (IKP-1)
Y. Xu (IKP-2)
Dr. E. Zaplatin (IKP-4) (until 28th February 2018)
H. Zens (IKP-4)
Dr. Y. Zhou (IKP-1)
Dr. M. Zurek (IKP-2) (until 15th July 2018)

IKP-1 = Experimental Hadron Structure
IKP-2 = Experimental Hadron Dynamics
IKP-3/IAS-4 = Theory of the Strong Interactions
IKP-4 = Large-Scale Nuclear Physics Equipment
IKP-TA = Technical Services and Administration

L Further Contributions

Short reports

1. JEDI Polarimetry progress report
2. Search for 4 quark and 6 quark exotic states with charm and strange quark content
3. Testing the $\Delta^{++} - \Delta^{-}$ configuration in the deuteron with antiprotons
4. Feasibility Study to Measure the Reaction $\bar{p}p \to \Xi^{-}\bar{\Xi}^{+}\pi^{+}\pi^{-}$ in PANDA
5. Study of Excited Ξ Baryons in $\bar{p}p$-Collisions with the PANDA Detector
6. Feasibility study of excited hyperon production and decay via electromagnetic modes for the PANDA Phase-0 measurements at HADES
7. Monte Carlo Supported Particle Identification in the P-349 Antiproton Polarization Experiment
8. Machine Learning Approach for Track Reconstruction in Particle Experiments
9. Utilizing Machine Learning Techniques for Charged Particle Identification (PID) at the PANDA experiment
10. Exploration of Machine/Deep Learning Methods for track reconstruction at PANDA and the PANDA@HADES Forward Detector System
11. A PANDA Track Finding Algorithm based on the Apollonius Problem
12. Improvements on the Data Acquisition System of KOALA Experiment at COSY
13. Structural design and realization of the HADES STS1 as a PANDA Phase-0 Experiment
14. The PANDA STT prototype with a sampling ADC readout
15. SiPM Radiation Hardness Study with COSY
16. Simulation study and testing prototypes for FToF detector in PANDA experiment
17. Semiconductor detector development for GSI/FAIR
18. The WASA MDC for experiments at FRS in GSI
19. A Lamb-shift polarimeter for a polarized molecular source in Novosibirsk
20. Status of the polarized H2, D2 and HD molecule production
21. A new type of laser-induced polarized proton source
22. Integration of the COSY 2 MeV Electron Cooler into EPICS
23. Correction of BPM electrical offsets and gain errors
24. Tools for software Development Tools at COSY

Poster prepared for conferences and workshops

1. Track Reconstruction and Particle Identification in the P-349 Antiproton Polarization Experiment
2. Design of a detector for studies of S=-2 baryon interaction induced by stopped antiproton annihilation
3. Drift chamber calibration and track reconstruction in the P-349 Antiproton Polarization Experiment
4. Simulations of Excited Hyperon Production with the PANDA Phase-0 Measurements at HADES
5. The EDM polarimeter development at COSY-Jülich

6. Electrostatic Deflector Development
7. Beam Based Alignment at the Cooler Synchrotron (COSY)
8. First Commissioning Results of the Waveguide RF Wien Filter
9. Spin tune mapping at COSY
10. Development of compact, highly sensitive beam position monitors for storage rings
11. Search for Electric Dipole Moments at COSY in Jülich - Closed Orbit and Spin Tracking Simulations
12. Muon veto in the JUNO detector
13. Solar neutrino analysis with the Borexino detector
14. Waveform reconstruction of IBD and muon events in JUNO
15. Reduction of the ^{14}C-background
16. Reduction of the ^{14}C-background in JUNO
17. Reduction of the ^{14}C-background in JUNO
18. GNA fitter and detector response impact on JUNO mass hierarchy sensitivity
19. Event reconstruction with machine learning in JUNO

JEDI Polarimetry progress report

I. Keshelashvili and D. Mchedlishvili

During last year, significant work have been made for the storage ring EDM dedicated polarimeter project. Improvements were done on LYSO-SiPM modules, its voltage supply system, on readout and simulation (Geant4) software and one week beam time at the beginning of Mai have been performed.

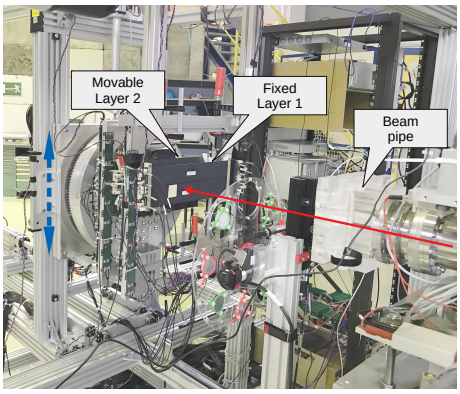

Fig. 1: The experimental setup at the BigKarl experimental hall. In two layers of plastic scintillator bars are shown in front of 52 LYSO-SiPM modules.

Until 2018, we always used one balk plastic scintillator bars in front of each polarimeter arm. During different beam times, we tested 0.5, 1 and 2 cm thick plastic scintillator material. Before the above-mensioned beam time, we designed and simulated dedicated triangular plastic scintillator wall in front of calorimeter. The aim of this system is to act as a ΔE and tracking detector at the same time. The total thickness of overlapping (stacked) plastic scintillator bars will be 2 cm. The base of the triangle will cover two crystals, so the total with would be 6 cm. The amplitude analysis (difference over sum) between neighbor scintillators will deliver information about the position of the track. Two orthogonal layers of such system are forseen. The very first deuteron beam test with two leyers (each 3 scintillator bars) has been performed during the 2018 beam time. See figure 1. The results are very consistent with the Geant4 simulation. With very simple and fast online analysis one can deliver about 1 mm position resolution. This result can be improved over time and is absolutely sufficient for the experiment. Moreover, with such fine resolution, we will face the statistical limits.

Due to the problems of delivering polarized deuteron beam from COSY, the plans [1] for the beam time have been altered.

The time was spent to investigate the elastic peak spreading for particular crystals. We learned that the ultimate energy resolution (less than 1 %) which we achieved with the improvement of LYSO-SiPM modules hits the limits of crystal light output homogeneity. We have scanned all 52 modules as 5×5 matrix with a pencil beam for 3 different energies (meaning different depth). The standard deviation of different areas shows around 1% depending on crystal [2].

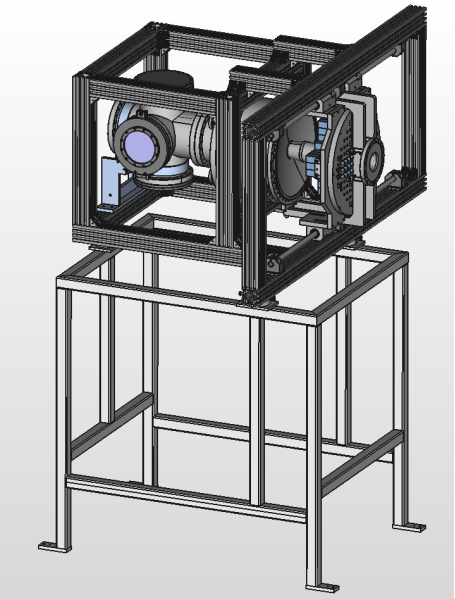

Fig. 2: The JEDI polarimeter assembly is shown for the installation at EDDA plas planned for the year 2019. Currently, the detector is assembled and undergoes the vacuum and other tests in a laboratory environment.

The further development of the Geant4 model for the coming setup is under development (see figure 2). Currently, we are studying the influence on the asymmetry of objects in front of crystals (like beam pipe, exit window, plastic scintillator bars, etc.) The most significant distortion is seen on the asymmetry from a block targets which are approaching the beam from the top or left side. The results show up to 10This is not really disturbing effect since is constant and we can always calibrate by analyzing the unpolarized cycles. And as expected no asymmetries for our symmetric detector design is seen from the MC simulation.

References:

[1] http://collaborations.fz-juelich.de/ikp/jedi/public_files/proposals/JEPO_01.2019.pdf

http://collaborations.fz-juelich.de/ikp/jedi/public_files/usual_event/Iraki_Keshelashvili_GGSWBS18.pdf

[2] I Keshelashvili et al 2017 J. Phys.: Conf. Ser. 928 012018

Search for four and six quark exotic states with charm and strange quark content

Ashish Thampi, Elisabetta Prencipe and James Ritman

The analysis of the $J/\psi\phi$ invariant mass system has been controversial, and it is important to investigate in particular the two enhancements observed at 4140 and 4274 MeV/c^2, and two more peaks at 4500 and 4700 MeV/c^2 by the LHCb experiment in the same invariant mass system through B^+ decays. We propose to perform such analysis using the whole Belle data set of 772 Millions $B\bar{B}$ pairs collected at a center of mass energy corresponding to the $\Upsilon(4S)$ resonance. The experiment Belle was located at the KEK accelerator, an asymmetric e^+e^- collider in Tsukuba (Japan). The experiment Belle ran for 10 years, from 1999 to 2010, and has been replaced by the new generation detector Belle II.

Exotic states are searched for in the $J/\psi\phi$ invariant mass range through $B^{\pm,0} \to J/\psi\phi K^{\pm,0}$. The basic event selection is based on the following criteria: $J/\psi \to l^+l^-$ ($l^\pm = e^\pm, \mu^\pm$), $\phi \to K^+K^-$; $2.95 < m_{e^+e^-} < 3.04$ GeV/c^2, $2.97 < m_{\mu^+\mu^-} < 3.04$ GeV/c^2, $1.004 < m_{K^+K^-} < 1.034$ GeV/c^2.

The following kinematic variables have been defined as Lorentz invariants for better analysis performance: *Beam constrained mass* ($M_{\rm bc}$) and *Energy difference* (ΔE). The $\Upsilon(4S)$ decays into two same-mass particles, B and $\bar{B}$, thus imposing two constraints in the centre of mass (CM) frame. If the B meson is correctly reconstructed, the energy of its decay products has to be equal to half the CM energy or equal to the beam energy in the $\Upsilon(4S)$ rest frame, and its reconstructed mass has to be equal to that of B meson.

$$M_{\rm bc} = \sqrt{E_{beam}^2 - \boldsymbol{p}_B{}^2} \tag{1}$$

$$\Delta E \equiv E_B - E_{beam} \tag{2}$$

E_{beam} is the beam energy in the CM frame and $\boldsymbol{p}_B$ is the CM momentum of the B meson. Ideally ΔE should be zero and $M_{\rm bc}$ should peak around the nominal B mass (which is 5.279 GeV/c^2). We then apply the selection cuts $-0.2 < \Delta E < 0.2$ GeV, $M_{\rm bc} > 5.27$ GeV/c^2.

In order to check how efficiently the proposed selection reconstructs events, we perform a Monte Carlo (MC) study by generating 1 million signal events, using the PHSP model of the MC generator EvtGen. A Dalitz plot study has been performed to check the distribution of the reconstruction efficiency versus $J/\psi\phi$ invariant mass. We performed a bin-wise study, splitting the invariant mass range of the $J\psi\phi$ system in 10 MeV bins. In every bin, we plot the ratio between the selected $J/\psi\phi$ event over the corresponding generated values. Yields are extracted from the Dalitz plot of ${M_{J/\psi\phi}}^2$ vs $M^2_{J/\psi K}$. The result of this study is reported in Fig. 1. The efficiency distribution shows a deep decrease of efficiency at threshold. This is expected due to the poor reconstruction efficiency of low momentum kaons, and leads to an average efficiency of 15%.

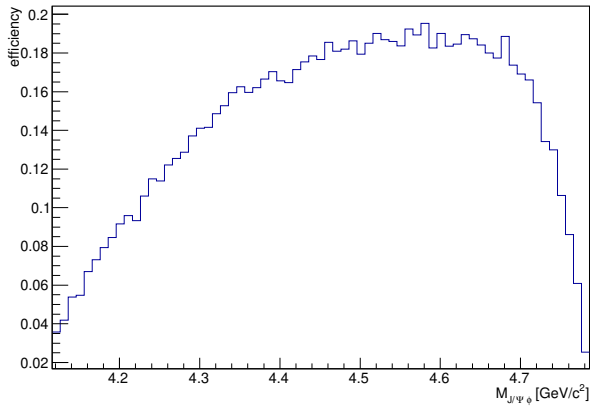

Figure 1: Efficiency profile obtained from the Dalitz plot analysis

We are planning to perform a comprehensive study of all background sources, mostly coming from $q\bar{q}$ combinations ($q = u, s, d, c, b$ quarks), but these are not expected to be significant. Contribution from combinatorial background is in fact expected to be very small, according to the published BaBar study on an equivalent channel. A purity >90% for both, B^0 and $B^\pm$ channels is expected. We will calculate the branching ratio, extract yield by fitting the $M_{\rm bc}$ distribution and then study the invariant mass distribution of the $J/\psi\phi$ system. We expect to collect double the statistics than the BaBar experiment, which will improve the uncertainity in the upper limit estimate.

Testing the $\Delta^{++}-\Delta^{-}$ configuration in the deuteron with antiprotons

Alexei Larionov,* Albrecht Gillitzer, Johann Haidenbauer, and Mark Strikman†

Motivation: The deuteron is the cleanest system allowing to test non-nucleonic degrees-of-freedom in nuclei. The meson-exchange calculations of the deuteron [1, 2, 3, 4] predict that the deuteron has a $\Delta-\Delta$ component with a probability $\sim 0.3-1.4\%$. Due to a large binding energy, the internal motion in the $\Delta-\Delta$ system is relativistic, with a typical momenta $k\sim 0.4-0.5$ GeV/c. This corresponds to the inter-Δ distances $\sim \pi/2k \sim 0.6-0.8$ fm which are much smaller than the inter-nucleon distance in the ordinary deuteron ~ 4 fm. Thus, the wave function of the $\Delta-\Delta$ system has a strong overlap with other non-nucleonic configurations such as e.g. six quark states. Experimental data on the $\Delta-\Delta$ component are quite scarce and strongly divergent, with a $\Delta-\Delta$ probability ranging from $\lesssim 0.4\%$ [5] to 16% [6].

In view of the upcoming $\overline{\text{P}}$ANDA experiment – we theoretically address the reaction channel $\bar{p}d\to\pi^-\pi^-\Delta^{++}$ at $p_{\rm lab}=10-15$ GeV/c for the kinematics with two energetic π^- mesons in the forward lab. hemisphere and a slow Δ^{++}. The "signal" reaction channel is $\bar{p}\Delta^-\to\pi^-\pi^-$ annihilation on the virtual Δ^- leading to a practically instantaneous (on nuclear scale) release of the spectator Δ^{++}. The possible background channels include at least two steps and, thus, are expected to be moderate. We will consider the following two possible background reactions: (i) $\bar{p}n\to\pi^-\pi^0$ followed by the charge exchange (CEX) reaction $\pi^0 p\to\pi^-\Delta^{++}$ and (ii) $\bar{p}n\to\pi^-\pi^-\pi^+$ followed by $\pi^+ p\to\Delta^{++}$. The details of the work can be found in [7].

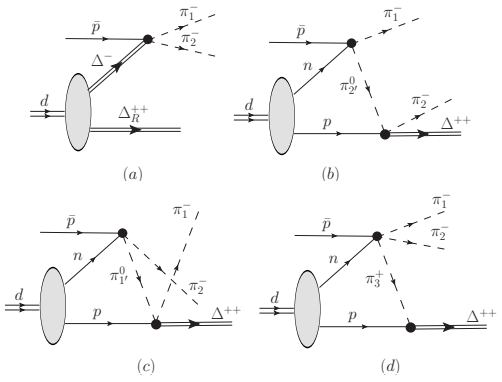

Fig. 1: (a) Impulse approximation diagram showing the production of a pion pair in antiproton annihilation on one of the Δ's of a Δ-Δ configuration in the deuteron. (b) Direct and (c) exchange diagrams of two-pion annihilation with inelastic CEX of π^0. (d) The diagram of three-pion annihilation with π^+ absorption.

Model: The Feynman diagram of the signal process is shown in Fig. 1(a). The nonrelativistic (NR) treatment of the $\Delta-\Delta$ wave function leads to the following expression for the modulus squared of the invariant matrix element:

$$\overline{|M^{(0)}_{\pi_1\pi_2\Delta_R;\bar{p}d}|^2}=\frac{2E_{\Delta_R}m_d}{E_\Delta}(2\pi)^3|\phi_{\Delta-\Delta}(\boldsymbol{k})|^2\,\overline{|M_{\pi_1\pi_2;\bar{p}\Delta}|^2}\,, \quad (1)$$

where $\overline{|M_{\pi_1\pi_2;\bar{p}\Delta}|^2}$ is the modulus squared of the invariant matrix element for the $\bar{p}\Delta\to\pi_1\pi_2$ transition while the overline means averaging over spin projections of the initial particles and summing over those of the final particles. The energy and momentum of the struck Δ in the deuteron rest frame are, respectively, $E_\Delta=m_d-E_{\Delta_R}$ and $\boldsymbol{k}=-\boldsymbol{p}_{\Delta_R}$, m_d is the deuteron mass. The energy and momentum of the residual Δ are $E_{\Delta_R}=\sqrt{m^2_{\Delta_R}+\boldsymbol{p}^2_{\Delta_R}}$ and $\boldsymbol{p}_{\Delta_R}$, respectively, with m_{Δ_R} being the invariant mass of the residual Δ (which can be, in principle, off-shell). The deuteron-spin-averaged modulus squared of the $\Delta-\Delta$ wave function is normalized to the probability $P_{\Delta-\Delta}$ of a Δ-Δ configuration in the deuteron:

$$\int d^3k|\phi_{\Delta-\Delta}(\boldsymbol{k})|^2=P_{\Delta-\Delta}\,. \quad (2)$$

In the light-cone (LC) treatment of the $\Delta-\Delta$ wave function, the graph with the antidelta emitted from the antiproton disappears in the infinite momentum frame which leads to another expression for the the modulus squared of the invariant matrix element:

$$\overline{|M^{(0)}_{\pi_1\pi_2\Delta_R;\bar{p}d}|^2}=\frac{2(m_\Delta^2+\boldsymbol{k}^2)^{1/2}m_d}{(m_d-m_\Delta)(2-\alpha)^2}(2\pi)^3|\phi_{\Delta-\Delta}(\boldsymbol{k})|^2\overline{|M_{\pi_1\pi_2;\bar{p}\Delta}|^2}\,, \quad (3)$$

where m_Δ is the physical (on-shell) mass of the Δ resonance. The LC variable α is defined in the deuteron rest frame as

$$\alpha=\frac{E_{\Delta_R}-p^z_{\Delta_R}}{m_d/2}\,, \quad (4)$$

while the internal momentum $\boldsymbol{k}$ is defined by relations

$$\alpha=1+\frac{k^z}{\sqrt{m_\Delta^2+\boldsymbol{k}^2}}\,,\quad \boldsymbol{k}_t=-\boldsymbol{p}_{\Delta_R t}\,. \quad (5)$$

The diagrams of the possible background processes are shown in Figs. 1(b),(c),(d). The amplitudes of the transitions $\bar{p}\Delta^-\to\pi^-\pi^-$ and $\bar{p}n\to\pi^-\pi^0$ have been calculated within N and Δ exchange model. For the amplitude of the CEX process $\pi^0 p\to\pi^-\Delta^{++}$, we have employed the reggeized ρ-exchange model. The $\bar{p}n\to\pi^-\pi^-\pi^+$ amplitude has been described by a simple s-dependent matrix element extracted from the angle-integrated experimental $\bar{p}n\to\pi^-\pi^-\pi^+$ cross section. The $\Delta-\Delta$ component of the deuteron wave function is a superposition of the $^3S_1$, $^3D_1$, $^7D_1$, and $^7G_1$ states. In calculations, we applied the wave functions of the np and $\Delta-\Delta$ systems according to the coupled-channel folded-diagram potential model of ref. [4] with a $\Delta-\Delta$ probability of 1.35%.

Results: The transition probability for the three-body final state is defined in general by four variables (if one takes into account the energy-momentum conservation and the azimuthal symmetry due to summation over spin projections). As independent variables we choose α, transverse momentum $p_{\Delta t}$ of the residual Δ (lower index "R" is dropped here and below for brevity), the LC momentum fraction of one of the outgoing pions ("1st pion")

$$\beta=\frac{2(E_1+p_1^z)}{E_{\bar{p}}+m_d-E_\Delta+p_{\rm lab}-p^z_\Delta}\,, \quad (6)$$

*Also at the National Research Center "Kurchatov Institute", 123182 Moscow, Russia and Frankfurt Institute for Advanced Studies (FIAS), D-60438 Frankfurt am Main, Germany

†Pennsylvania State University, University Park, PA 16802, USA

and the relative azimuthal angle $\phi_{\pi\Delta} = \phi_\pi - \phi_\Delta$ between the 1st pion and the Δ. Note that in the c.m. frame of the two pions the approximate relation $\beta = 1 + \cos(\Theta_{c.m.})$ holds, with the scattering angle $\Theta_{c.m.}$ of the 1st pion relative to the $\bar{p}$ beam axis. The differential cross section of the process $\bar{p}d \to \pi^-\pi^-\Delta^{++}$ can be expressed as follows:

$$\alpha\beta \frac{d^5\sigma}{d\alpha d\beta d\phi_{\pi\Delta} dp_{\Delta t} dp_{\Delta t} dp_\Delta^2} = \frac{\overline{|M_{\pi_1\pi_2\Delta;\bar{p}d}|^2} p_{1t} \mathcal{A}(p_\Delta^2)}{16(2\pi)^4 p_{\rm lab} m_d \kappa_t} , \quad (7)$$

where the quantity

$$\kappa_t = 2|p_{1t}(E_2 + p_2^z)/(E_1 + p_1^z) + p_{1t} + \mathbf{p}_{\Delta t} \cdot \mathbf{p}_{1t}/p_{1t}| \quad (8)$$

originates from expressing the phase space volume of the outgoing particles in terms of the LC momentum fractions and transverse momenta. The possible off-shellness of the residual Δ is taken into account in Eq.(7) by the spectral function of the Δ-resonance

$$\mathcal{A}(p_\Delta^2) = \frac{\sqrt{p_\Delta^2}\Gamma_\Delta/\pi}{(p_\Delta^2 - m_\Delta^2)^2 + m_\Delta^2\Gamma_\Delta^2} , \quad \int\limits_{(m_\pi+m_N)^2}^{+\infty} \mathcal{A}(M^2) dM^2 = 1 . \quad (9)$$

In numerical calculations we have set the residual Δ^{++} on the physical mass shell.

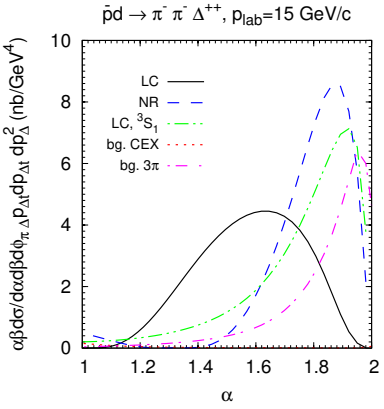

Fig. 2: Differential cross section of the reaction $\bar{p}d \to \pi^-\pi^-\Delta^{++}$ at $p_{\rm lab} = 15$ GeV/c vs α of the residual Δ for $p_{\Delta t} = 0$, $\beta = 1.5$. Solid (dashed) line – signal (Fig. 1(a)) for the LC (NR) wave function. Dotted line – CEX background (Fig. 1(b),(c)). Dot-dashed line – three-pion annihilation background (Fig. 1(d)). Dot-dot-dashed line – LC signal calculated with the large-distance asymptotic form of the $\Delta - \Delta$ wave function.

Fig. 2 shows the differential cross section at $p_{\rm lab} = 15$ GeV/c. The LC and NR calculations produce significantly different α-dependence of the signal. The maxima in the α-distribution of the signal are governed by the dominating $^7D_1$ state in the $\Delta - \Delta$ wave function, so that the deuteron momentum distribution is peaked at $k = 0.41$ GeV/c (at $p_{\Delta t} = 0$ this corresponds to $\alpha = 1.32$ and $\alpha = 0.68$ for LC wave function and to $\alpha = 1.80$ and $\alpha = 0.95$ for the NR one). Due to the presence of the internal-momentum-dependent denominator in Eq.(5) the strength of the α-distribution is extended towards smaller values of α (i.e. larger positive p_Δ^z) in the case of LC calculation as compared to the NR one.

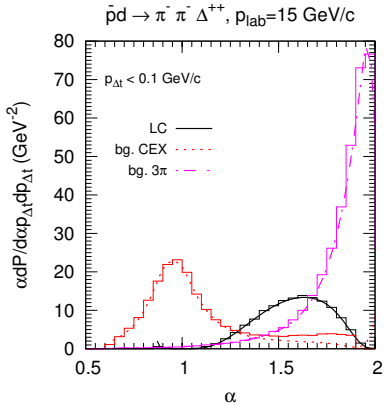

Fig. 3: Histograms: probability distributions of α of the residual Δ^{++} at $p_{\rm lab} = 15$ GeV/c in the kinematics with $p_\Delta^2 = m_\Delta^2$; $p_{\Delta t} < 0.1$ GeV/c; $\beta = 1.4 - 1.6$; $p_1^z, p_2^z > 1$ GeV/c. The sampled distributions are normalized to unity after integration over α and $p_{\Delta t}$. Smooth lines: analytical results of Fig. 2 multiplied by constant factors for appropriate normalization.

Backgrounds have quite different α-dependence from the signal calculated with LC effects. This is well visible in the Monte-Carlo-sampled α-distributions in Fig. 3. The pion CEX background is important for forward production of Δ^{++} (small α). In this case the Δ^{++} may experience large longitudinal momentum transfer from the scattered pion. In other kinematics the CEX background is strongly suppressed relative to the three-pion annihilation background. The latter grows strongly for backward Δ^{++} (large α), because in this case the c.m. energy of the colliding $\bar{p}n$ system is small which leads to a large $\bar{p}n \to \pi^-\pi^-\pi^+$ amplitude.

Conclusions: We have developed the model for the description of the $\bar{p}d \to \pi^-\pi^-\Delta^{++}$ process, including the signal contribution of the $\bar{p}$ annihilation on the $\Delta^- - \Delta^{++}$ component of the deuteron. It is shown that the LC effects lead to clearly distinguishable signal from the background of usual annihilations. The α-distributions of the Δ^{++} at small transverse momenta would allow to extract the signal for the $\Delta - \Delta$ probabilities in the deuteron down to $\sim 0.3\%$.

References:

[1] P. Haapakoski and M. Saarela, Phys. Lett. **B** 53 (1974) 333.
[2] H. Arenhövel, Z. Phys. **A** 275 (1975) 189.
[3] R. Dymarz and F. C. Khanna, Nucl. Phys. **A** 516 (1990) 549.
[4] J. Haidenbauer, K. Holinde, and M. B. Johnson, Phys. Rev. **C** 48 (1993) 2190.
[5] D. Allasia *et al.*, Phys. Lett. **B** 174 (1986) 450.
[6] H. Braun *et al.*, Phys. Rev. Lett. 33 (1974) 312.
[7] A.B. Larionov, A. Gillitzer, J. Haidenbauer, and M. Strikman, Phys. Rev. **C** 98 (2018) 054611.

Feasibility Study to Measure the Reaction $\overline{\mathrm{p}}\mathrm{p} \to \Xi^-\overline{\Xi}^+\pi^+\pi^-$ in PANDA

Alessandra Lai, Tobias Stockmanns, James Ritman

The understanding of the baryon excitation spectrum is one of the main goals of non-perturbative Quantum Chromodinamics (QCD). Most of the efforts have been devoted to studies in the nucleon and Δ sector. So far, the agreement between the observations and the predictions of the quark model is rather poor. Several low-lying states have been observed at energies different from the predicted ones and, on the other hand, several predicted higher lying states have not yet been seen experimentally. This phenomenon is known as the *problem of the missing resonances* [1]. For states with strangeness as an extra degree of freedom (i.e., Λ, Σ, Ξ, Ω baryons), the experimental data quality becomes poorer. Some new states have been observed in the Λ and Σ spectra, but so far confirmation and unambiguous interpretation are missing [2, 3]. Considering double or triple strange baryons, i.e., Ξ and Ω, some excited states have been observed but spin-parity quantum numbers have not been determined. Since the PDG edition of 1988, nothing significant on the Ξ resonances has been added. In $\overline{\mathrm{p}}\mathrm{p}$ collisions at PANDA, a large fraction of the inelastic cross section is associated with channels resulting in a baryon-antibaryon pair in the final state. Moreover, the production of an extra particle (a K or D meson) is not necessary for strangeness conservation. This reduces the energy threshold and thus the number and complexity of the background channels that would affect the reconstruction of such states. The PANDA experiment aims to perform, among others, a comprehensive Ξ spectroscopy program, in order to contribute to the understanding of fundamental questions of QCD.
This document reports on the feasibility study to measure the reaction $\overline{\mathrm{p}}\mathrm{p} \to \Xi^-\overline{\Xi}^+\pi^+\pi^-$.

Signal Generation and Reconstruction

Four million events of the process under study, depicted in Figure 1, are generated. The continuum case as well as all the resonant decay branches involving particles that are known so far (Table 1) are included in the simulation. For all the decays, a uniform phase space distribution is chosen. The momentum of the antiproton beam is chosen to be $4.6\,\mathrm{GeV/c}$, in order to have enough energy to populate the resonant states. The reconstruction of the complete decay tree is carried out backward, starting from the eight charged final state particles (i.e., protons and pions). Combining them appropriately, one can reconstruct the intermediate states Λ and $\overline{\Lambda}$ and then further the Ξ^- and $\overline{\Xi}^+$. Finally including the pair of prompt pions (i.e., directly coming from the primary interaction point), the original $\overline{\mathrm{p}}\mathrm{p}$ system is reconstructed. To aid this procedure, some kinematic fits are employed. A vertex fit is used to select the pair of prompt pions which originate from a common point (i.e., the primry interaction vertex). By means of this selection, the combinatorial background, due to the presence of multiple pions in the decay chain, is reduced. The composite states, Λ and Ξ, are reconstructed by combining their daughter particles ($\mathrm{p}\pi$ for the Λ and $\Lambda\mathrm{p}$ for the Ξ), then applying a vertex fit, to select those with the same origin, and finally a mass fit, to discard accidental combination that do not belong to a decay. For the reconstruction of the $\overline{\mathrm{p}}\mathrm{p}$ system, a constraint on the four-momentum vector of the $\Xi^-\overline{\Xi}^+\pi^+\pi^-$ is applied subsequently to a vertex fit.

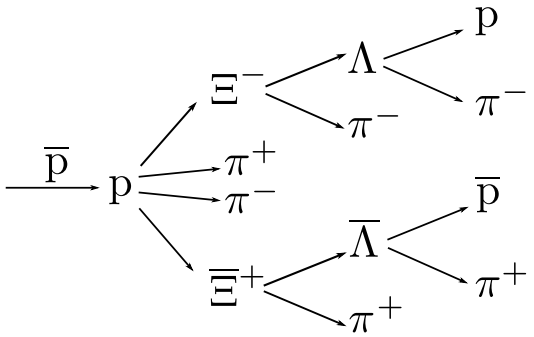

Fig. 1: Pictorial representation of the process under study.

$\overline{\mathrm{p}}\mathrm{p} \to$		$\to \overline{\Xi}^+\Xi^-\pi^+\pi^-$
$\overline{\mathrm{p}}\mathrm{p} \to$	$\Xi^-(1690)^*\overline{\Xi}^+$ (+ c.c.)	$\to \overline{\Xi}^+\Xi^-\pi^+\pi^-$
$\overline{\mathrm{p}}\mathrm{p} \to$	$\Xi^-(1820)^*\overline{\Xi}^+$ (+ c.c.)	$\to \overline{\Xi}^+\Xi^-\pi^+\pi^-$
$\overline{\mathrm{p}}\mathrm{p} \to$	$\Xi^0(1530)^*\overline{\Xi}^+\pi^-$ (+ c.c.)	$\to \overline{\Xi}^+\Xi^-\pi^+\pi^-$
$\overline{\mathrm{p}}\mathrm{p} \to$	$\Xi^0(1690)^*\overline{\Xi}^+\pi^-$ (+ c.c.)	$\to \overline{\Xi}^+\Xi^-\pi^+\pi^-$
$\overline{\mathrm{p}}\mathrm{p} \to$	$\overline{\Xi}^0(1530)^*\Xi^0(1530)^*$	$\to \overline{\Xi}^+\Xi^-\pi^+\pi^-$
$\overline{\mathrm{p}}\mathrm{p} \to$	$\overline{\Xi}^0(1530)^*\Xi^0(1690)^*$	$\to \overline{\Xi}^+\Xi^-\pi^+\pi^-$
$\overline{\mathrm{p}}\mathrm{p} \to$	$\overline{\Xi}^0(1690)^*\Xi^0(1530)^*$	$\to \overline{\Xi}^+\Xi^-\pi^+\pi^-$

Table 1: Decay branches implemented in the simulation of the signal events. *c.c.* stands for charge conjugate.

The main results of the study, in terms of reconstruction efficiency (defined as the fraction of generated events that is reconstructed) and resolution, are summarized in Table 2 and Table 3. The measured values are consistent for particles and their respective antiparticles. The total efficiency for the channel under study is 5 %, mostly limited by the combined acceptance of the eight final state particles. The mass resolution for the composite particles is few MeV. By looking at the invariant mass spectra of the two $\Xi\pi$ subsystems one can clearly identify the reconstructed Ξ resonances that decay according to $\Xi \to \Xi\pi$ (Figure 2). To observe the resonant states that decay according to $\Xi \to \Xi\pi\pi$ instead, one has to consider the two $\Xi\pi\pi$ subsystems (Figure 3).

Background Studies

To study the impact of the presence of background on the reconstruction of the signal of interest, 22 million events are generated using the total inelastic $\overline{\mathrm{p}}\mathrm{p}$ cross section. The analysis of this background sample is carried out with the same algorithm used for the signal data set. The outcome of this study shows that not even a single background event is misidentified as signal. This leads to the conclusion that 2.3 events can be excluded at the 90 % confidence level. Given the obtained results, one calculates that the signal-to-background ratio is at least 3.9 and roughly 18 000 $\overline{\mathrm{p}}\mathrm{p} \to \Xi^-\overline{\Xi}^+\pi^+\pi^-$ events per day are expected during the first phase of PANDA, when a beam luminosity of $1 \times 10^{31}\,\mathrm{cm^{-2}\,s^{-1}}$ will be available. That is to say that the 4 million simulated events would correspond to approximately 10 days of data taking.

	p	π (Λ)	π (Ξ)	π prompt
ε_{reco}	83 %	70 %	75 %	94 %
σ_p/p	1.50 %	1.47 %	1.34 %	1.36 %

Table 2: Reconstruction efficiency and momentum resolutions for the final state particles.

	Λ	Ξ	$\Xi^-\bar{\Xi}^+\pi^+\pi^-$
ε_{reco}	54 %	34 %	5 %
σ_p/p	1.42 %	1.30 %	1.50 %
σ_{xy}	0.1 mm	0.3 mm	0.3 mm
σ_z	0.5 mm	1.3 mm	1.2 mm
σ_M	2 MeV/c^2	3.8 MeV/c^2	

Table 3: Reconstruction efficiency and resolutions (i.e., momentum, spatial, and mass) for the composite states/system.

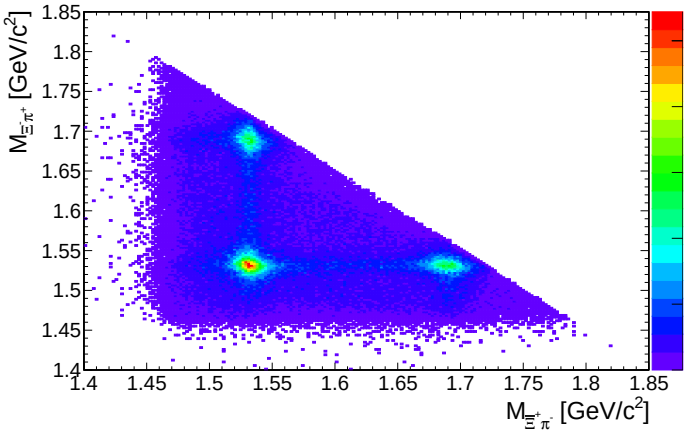

Fig. 2: Goldhaber plot for the $\Xi\pi$ systems. The vertical bands indicate the presence of resonances.

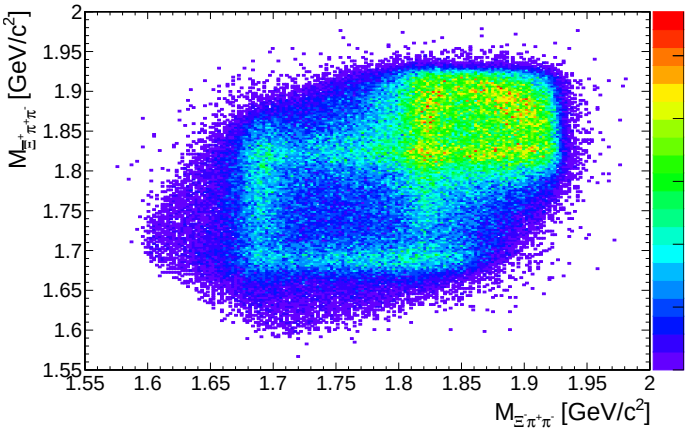

Fig. 3: Two dimensional invariant mass plot for the $\Xi\pi\pi$ systems. The vertical bands indicate the presence of resonances.

Conclusions and Outlook

The feasibility study described so far proves that the reaction $\bar{p}p \to \Xi^-\bar{\Xi}^+\pi^+\pi^-$ can be studied in PANDA with good statistics already in the first phase of the experiment, having reduced beam luminosity. Despite the relatively small total reconstruction efficiency of 5 %, a clean signal can be identified thanks to the decay topology which offers a good intrinsic background suppression. Moreover, it shows that all the interesting resonant states can be succesfully reconstructed by means of the developed analysis algorithm.

This study respresents the first steps towards a comprehensive feasibility study for the process of interest. In the future, the analysis could be optimized to maximize the signal-to-background ratio. In order to do that, more input from background data simulation is necessary. One order of magnitude more statistics would already allow to make more realistic estimations. Furthermore, a future follow up study could include the impact on the reconstruction of a non-uniform angular distribution of the decays.

References:

[1] Klempt, E., *Mass formula for baryon resonances*, 2002, doi: 10.1103/PhysRevC.66.058201

[2] Zychor, I. et al., *Evidence for an Excited Hyperon State in $pp \to pK^+Y^{0*}$*, 2006, doi: 10.1103/PhysRevLett.96.012002

[3] Adamovich, M. I. et al., *Observation of a resonance in the K(s)p decay channel at a mass of* 1765 MeV/c^2, 2007, doi: 10.1140/epjc/s10052-007-0284-9

Study of Excited Ξ Baryons in p̄p-Collisions with the P̄ANDA Detector

Jennifer Pütz

Introduction

Understanding the excitation pattern of baryons is indispensable for a deep insight into the mechanism of non-perturbative QCD. Systematic experimental studies have so far been focused on the nucleon excitation spectrum, while very little is known on excited states of double and triple strange baryons. In p̄p collisions a large fraction of the cross section is associated to final states with a baryon-antibaryon pair together with additional mesons, giving access to excited baryon and antibaryon states. With its large acceptance, the PANDA detector is well-suited for a comprehensive baryon spectroscopy program in the multi-strange sector.
Since the kinematic fit algorithms implemented in PandaRoot – the software framework for PANDA– have shown some critical issues, another procedure that fits the full decay tree at once is implemented in the analysis algorithms to study the reactions $\bar{p}p \to \bar{\Xi}^+ \Lambda K^-$ and $\bar{p}p \to \Xi^- \bar{\Lambda} K^+$.

Event generation

For the study of excited Ξ baryons a total number of 10 million signal events are generated with the event generator EvtGen [1]. The data sample consists of 5 million events each for $\bar{\Xi}^+ \Lambda K^-$ and $\Xi^- \bar{\Lambda} K^+$, also including resonances. A beam momentum of 4.6 GeV/c has been chosen, corresponding to a center-of-mass energy of $\sqrt{s} = 3.25\,\text{GeV}$, which is $\sim 300\,\text{MeV}$ above the $\bar{\Xi}^+ \Lambda K^-$ production threshold. If not otherwise specified, the charge conjugate process is implicitly included in the following. The kinematics of the decay given by the chosen beam momentum allows the population of the two resonance states Ξ(1690) and Ξ(1820). The properties of both resonances used for the event generation are chosen according to [2]. The production cross section is expected to be similar ($\sim \mu$ b) to the production of the ground state Ξ in $\bar{p}p \to \Xi^- \bar{\Xi}^+$ [3]. Figure 1 shows the Dalitz plot for the simulation.

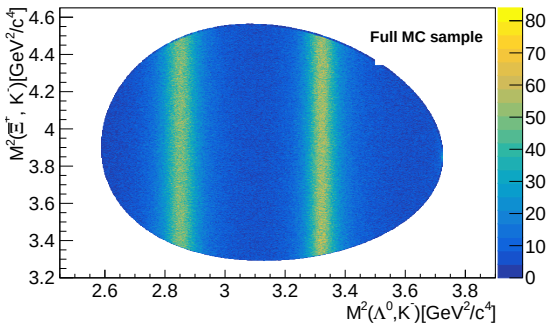

Fig. 1: Dalitz plot for the generated sample. The Ξ resonances are observable as vertical bands.

Reconstruction

To event reconstruct begins with the final state particles and proceeds backwards through the reaction chain. The selected final state particles are proton, anti-proton, π^-, π^+, K^+ and K^- mesons. Since the algorithms for track reconstruction are not able to deal with displaced vertices, an ideal track reconstruction algorithm has to be used for the reconstruction of the final state particles. To make the selection more realistic, only particles with at least 3 hits in any inner tracking detector of PANDA are selected. The reconstruction efficiencies for all final state particles are shown in table 1. The reconstruction efficiency denotes the ratio between the number of true reconstructed and generated candidates.

Table 1: Reconstruction efficiency ϵ for final state particles. The statistical error on the reconstruction efficiency is $\sigma_\epsilon = 0.1\,\%$ for all particles .

particle	ϵ[%]
π^-	71.2
π^+ ($\bar{\Lambda}$)	68.6
π^+ ($\bar{\Xi}^+$)	73.7
K^- (Resonances)	84.9
K^- (Continuum)	85.1
p	88.7
$\bar{p}$	82.3

(a) $\bar{p}p \to \bar{\Xi}^+ \Lambda K^-$

particle	ϵ[%]
π^+	70.6
π^- (Λ)	68.3
π^- (Ξ^-)	73.1
K^+ (Resonances)	86.7
K^+ (Continuum)	86.9
p	86.2
$\bar{p}$	83.4

(b) $\bar{p}p \to \Xi^- \bar{\Lambda} K^+$

For the reconstruction of a Λ hyperon a proton and a π^- meson are combined and analogous the $\bar{\Lambda}$ is reconstructed by combining a $\bar{p}$ and a π^+. On the selected Λ and $\bar{\Lambda}$ candidates a mass cut within a mass window of $0.3\,\text{GeV/c}^2$ symmetric to the nominal Λ mass is performed. This mass window cut rejects those candidates with a reconstructed mass far away from the expected value. Since this analysis uses a full decay tree fit, meaning that the fit is performed on the reconstructed $\bar{\Xi}^+ \Lambda K^-$ and $\Xi^- \bar{\Lambda} K^+$ candidates, no further cuts are applied for the selection of the composite state particles. The reconstruction scheme of the $\bar{\Xi}^+$ is similar to the reconstruction of the Λ and $\bar{\Lambda}$. After combining the $\bar{\Lambda}$ and π^+ to $\bar{\Xi}^+$ and the Λ and π^- to Ξ^- a mass cut within a window of $\pm 0.15\,\text{GeV/c}^2$ symmetric to the nominal Ξ^- mass is performed.
For the reconstruction of the whole decay chain both the $\bar{\Xi}^+ \Lambda K^-$ system and its charge conjugate are combined. On the resulting candidates the full decay tree fit is performed with the DecayTreeFitter implemented in PandaRoot. The fitting routine includes different fitting algorithms. For this analysis the DecayTreeFitter performs vertex fits as well as kinematic fits with mass constraints for Λ, $\bar{\Lambda}$, Ξ^- and $\bar{\Xi}^+$ and a kinematic fit with the constraint to match the 4-momentum vector of the reconstructed candidate to the initial 4-momentum vector of the p̄p entrance channel. The candidates with a fit probability (Fig. 2) less than 0.01% are rejected. In addition to the cut on the fit probability a cut on the fit status is introduced to assure that the fit has converged for the selected candidates. 71.4% of the events survive

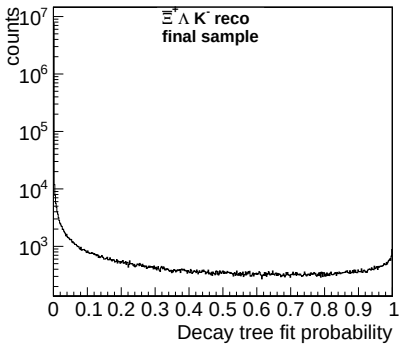

Fig. 2: Probability distribution of the full decay tree fit.

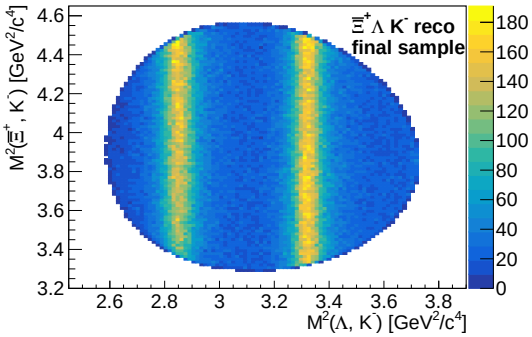

Fig. 3: Dalitz plot for the reconstruction.

the cut on the fit status. After applying all cuts on the selected sample a reconstruction efficiency of 5.4 % for $\bar{\Xi}^+\ \Lambda\ \mathrm{K}^-$ and 5.5 % for $\Xi^-\ \bar{\Lambda}\ \mathrm{K}^+$ is achieved. As an example, figure 3 shows the Dalitz plot for the final reconstructed $\bar{\Xi}^+\ \Lambda\ \mathrm{K}^-$ sample. The result is in good agreement with the input shown in figure 1. To evaluate the mass of the resonances a polynomial function combined with two Voigt functions are fitted to the mass distribution for the final selected $\Lambda\ \mathrm{K}^-$ and $\bar{\Lambda}\ \mathrm{K}^+$ system. The mass distribution for the $\Lambda\ \mathrm{K}^-$ system is shown in

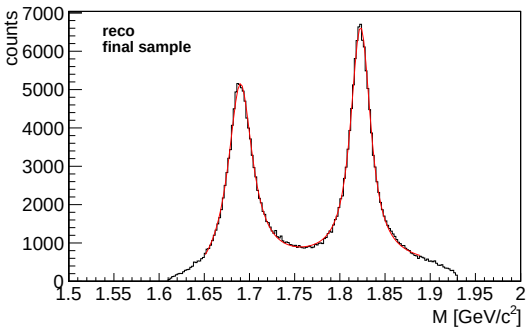

Fig. 4: Invariant mass distribution for the $\Lambda\, K^-$ system.

figure 4. The results for both resonance masses shown in table 2 are consistent with the input values. The error on the fit values is dominated by the systematic error which is estimated by varying the fit parameters. In contrast to the $\Xi\,(1690)^-$ and $\bar{\Xi}\,(1690)^+$ widths, the width for $\Xi\,(1820)^-$ and $\bar{\Xi}\,(1820)^+$ are smaller than the input value $\Gamma_{\mathrm{Gen}}\,(\Xi\,(1820)) = 24\,\mathrm{MeV/c^2}$. The deviation is $2.75\,\sigma$ for $\Xi\,(1820)^-$ and $5\,\sigma$ for $\bar{\Xi}\,(1820)^+$. The source for this discrepancy is still under investigation.

Table 2: Reconstructed resonance masses and widths determined with a fit containing two Voigt functions and a polynomial.

particle	Mass [MeV/c^2]	Width [MeV/c^2]
$\Xi\,(1690)^-$	(1690.0 ± 0.1)	(30.1 ± 0.5)
$\bar{\Xi}\,(1690)^+$	(1690.2 ± 0.1)	(29.5 ± 0.4)
$\Xi\,(1820)^-$	(1823.0 ± 0.1)	(22.9 ± 0.5)
$\bar{\Xi}\,(1820)^+$	(1823.1 ± 0.1)	(22.0 ± 0.4)

Background Studies

For background studies 100 million events have been generated using the Dual Parton Model based generator DPM [4]. All background events are subject to the same reconstruction procedure including identical cuts as for the signal events. Out of 100 million generated events no background event survived the applied cuts. The observation of no background corresponds to a 90% confident level of 2.3 events. Therefore, it is only possible to estimate a lower limit for the signal-to-background ratio and the signal significance. Since the ratio of the number of generated background and signal events does not reflect the ratio of the respective cross section a scaling factor B is needed. B is calculated as

$$B = \frac{N_{\mathrm{sig}}^{\mathrm{gen}}/\sigma_{\mathrm{sig}}}{N_{\mathrm{bg}}^{\mathrm{gen}}/\sigma_{\mathrm{bg}}}, \tag{1}$$

where $N_{\mathrm{sig}}^{\mathrm{gen}}$ is the number of generated signal events and $N_{\mathrm{bg}}^{\mathrm{gen}}$ the number of generated background events. The cross section for the signal is assumed to be $\sigma_{\mathrm{sig}} = 1\,\mu\mathrm{b}$. For $\bar{\mathrm{p}}\mathrm{p}$ reactions at 4.6 GeV/c the inelastic cross section is $\sigma_{\mathrm{bg}} = 50\,\mathrm{mb}$ [2]. The number of reconstructed signal events is 270,867 for $\bar{\Xi}^+\ \Lambda\ \mathrm{K}^-$ and 283,617 for $\Xi^-\ \bar{\Lambda}\ \mathrm{K}^+$, assuming a branching ratio of $BR\,(\Xi^* \to \Lambda\, K^-) = 1$ The significance S is given by

$$S = \frac{N_{\mathrm{sig}}}{\sqrt{N_{\mathrm{sig}} + N_{\mathrm{bg}} \cdot B}} \tag{2}$$

The numbers of reconstructed signal and background events lead to $S > 513$ and a signal-to-background ratio of 19.1:1 for $\bar{\Xi}^+\ \Lambda\ \mathrm{K}^-$ and $S > 507$ and a signal-to-background ratio of 19.5:1 for $\Xi^-\ \bar{\Lambda}\ \mathrm{K}^+$. Assuming the start luminosity $\mathcal{L} = 1 \cdot 10^{31}\,\mathrm{cm^{-2}\,s^{-1}}$ for $\overline{\mathrm{P}}$ANDA, one expects 38,452 events to be reconstructed per day corresponding to about 15 days of data taking to collect a data sample comparable in size to the reconstructed Monte Carlo sample presented in this report.

References:

[1] D.J. Lange, "The EvtGen particle decay simulation package", doi:10.1016/s0168-9002(01)00089-4

[2] C. Patrignani, *et al.*, https://doi.org/10.1103/PhysRevD.98.030001

[3] W. Erni, *et al.*, "Physics performance report for PANDA: Strong interaction studies with antiprotons.", arXiv:0903.3905 (2009)

[4] A. Capella,*et al.*, "Dual parton model",doi:10.1080/01422410108225691

Feasibility study of excited hyperon production and decay via electromagnetic modes for the PANDA Phase-0 measurements at HADES

Waleed Esmail, Tobias Stockmanns, and James Ritman

The electromagnetic (EM) decay of bayrons provides detailed information on their underlying structure. Interactions of real and virtual photons with electric charges of the quark fields provide unique information about the quark structure of hadrons and about phenomenological parameters describing their form factors. The proposed study is the EM decay channels of excited hyperons, in particular Σ(1385) produced in p(4.5GeV)+p reactions using the HADES spectrometer along with the proposed Forward Detector (FD). The FD will extend the acceptance of HADES towards lower polar angles 0.5°-6.5°, which will be of crucial importance to hyperon reconstruction. The FD system consists of two stations, each composed of 8 layers of self-supporting straw tubes. They are based on developments for the PANDA forward tracker. The reaction under investigation is:

$$p(4.5GeV)p \rightarrow K^+ p\, \Sigma(1385)^0 \;\rightarrow\; K^+ p\, \Lambda\, \gamma \;\rightarrow\; K^+ p\, p\, \pi^- \gamma$$

Analysis workflow:

1. Generation of 1 million events of this reaction using the Pluto event generator, which is a phase space generator. To account for the fact that $\Sigma(1385)^0$ has an anisotropic Angular Distribution (AD). The measured AD at beam energy of 3.5 GeV has been parameterized and included in the event generator. See Figure (1).
2. The output from Pluto is passed through the detector simulation of HADES and the FD. The output from this step is the so-called DST (Data Summary Tapes) files, the basic data format for any HADES analysis.
3. DST files contain the reconstructed particle tracks, thus these tracks have to be identified as particle candidates, a process known as charged Particle Identification (PID). The PID of final state particles ($K^+ p\, p\, \pi^-$) is done using an Artificial Neural Network (ANN). The photon is a neutral particle of zero mass, so it is identified as a cluster of energy at the electromagnetic calorimeter with no tracks associated to it and β close to 1.
4. The next step is to reconstruct the decay tree starting from the $p\, \pi^-$ to reconstruct the Λ hyperon. Λ can be reconstructed at HADES by combining the 4-vector of the proton and pion and performing topological cuts (e.g. Λ decay length). Λ also can be reconstructed by the FD by combining pion tracks from HADES and proton tracks from the FD. After reconstructing Λ, exclusive events of the excited hyperon (Σ(1385)) can be reconstructed with efficiency of ~ 3%.

Using this reconstruction efficiency, the production rate of Σ(1385) at the upcoming p(4.5GeV)+p beam time is estimated to be 2800 events per day.

Background estimation:

A study of the background contribution to the signal reaction (1) has been started. Unfortunately not all background reactions were measured at a beam kinetic energy 4.5 GeV. So the cross section of different background sources has to be estimated at 4.5 GeV. For that purpose cross section (for different background sources) at different energies has been collected from the literature and fitted by a phase space parameterization. An example of the fit is shown in Figure (2).

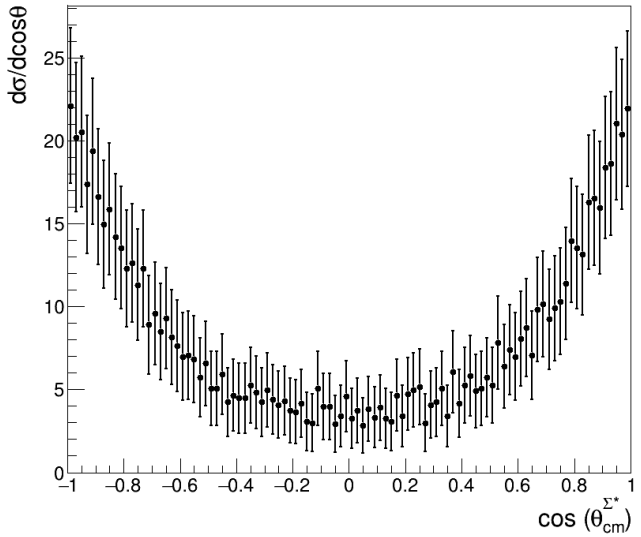

Figure 1 Pluto output, the Angular Distribution of the excited hyperon $\Sigma(1385)$ as implemented by the Monte Carlo code Pluto.

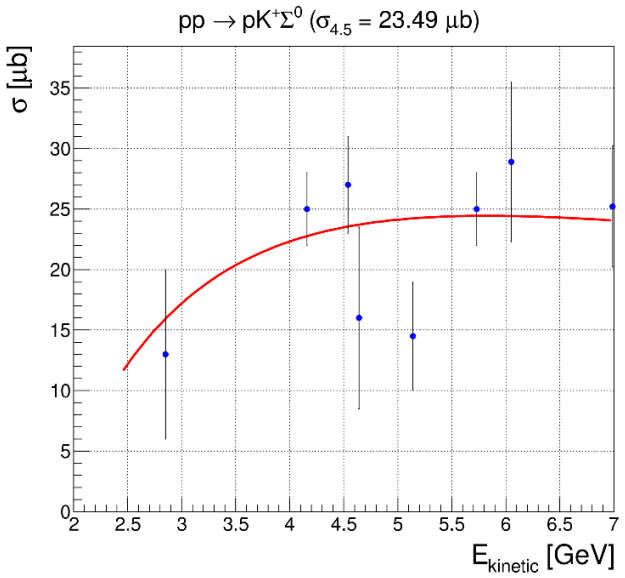

Figure 2 Measured values of cross section of $pp \rightarrow pK^+\Sigma^0$ and a phase space interpolation is shown as a red line. The value at 4.5 GeV is estimated to be 23.5 μb

Monte Carlo Supported Particle Identification in the P-349 Antiproton Polarization Experiment

D. Alfs, D. Grzonka, K. Kilian, T. Sefzick, J. Ritman

P-349 Experiment

The goal of the P-349 experiment is to test whether antiprotons produced in high-energy proton-proton collisions are polarized [1]. Polarization is going to be determined from the left-right asymmetry in the scattering of antiprotons on a liquid hydrogen target in the CNI region.
The measurements took place in 2014, 2015 and 2018 (the latter with an upgraded setup). The details of the experimental method and status of the analysis can be found in [2].
Antiprotons are produced by a 24 GeV/c proton beam bombarding a solid target. There is one antiproton per about 10^6 incident protons expected and the momentum distribution of produced antiprotons is peaked around 3.5 GeV/c.
Negatively charged secondary beam particles of momentum equal to 3.5 GeV/c are delivered to the experimental setup in form of 400 ms long spills. There are about 4000 antiprotons out of $5 \cdot 10^5$ particles expected in a single spill and about 3 antiprotons per spill scattered in an angular range corresponding to the CNI region [3]. The main background comes from negatively charged pions [4].
In this report proposed procedures of particle identification are described and preliminary results for the 2015 measurement are shown.

Particle identification with aerogel and plexiglass Cherenkov detectors

There are two types of Cherenkov detectors used for PID in the experiment: an aerogel Cherenkov detector and a plexiglas DIRC. The refractive index of the former one was equal to n = 1.03 and was chosen so that Cherenkov light is produced by the passage of a 3.5 GeV/c pion but not for an antiproton of the same momentum. It was used as an online veto and allowed for reduction of the number of stored events by a factor of about 30. Furthermore, its performance was verified during measurements with positively charged particles at lower energies, where p/π^+ separation was possible also by a time of flight measurement. For the 2018 setup an upgraded version of the detector was prepared [5] but the Plexiglass DIRC was not changed.
For the offline analysis a plexiglas DIRC was used [6] (see Fig. 1) Two types of photomultipliers were used for readout: R8900-100-M16 (4x4 channels, 26.2×26.2 mm^2) and Hamamatsu H8500C (8x8 channels, 52×52 mm^2). To reduce the number of readout channels, all pairs of neighboring channels in the horizontal direction of the optics were coupled, resulting in matrices shown in Fig. 2. Furthermore, no Cherenkov photons are expected to hit the upper row of photomultipliers, therefore they are not used in the analysis.
In a simplified case, the $\pi^-/\bar{p}$ separation can be performed by fitting a single parabolic function to the hits from both PMT matrices combined together. This is sufficient for an initial $\pi^-/\bar{p}$ separation, however, as the detector response is dependent on the track inclination and hit position, a Monte Carlo supported method is needed for an optimized selection of antiproton events.
Based on an existing CAD geometry a Geant4 model for the DIRC has been developed and optimized by adjusting a generated photon distribution to the experimental data.

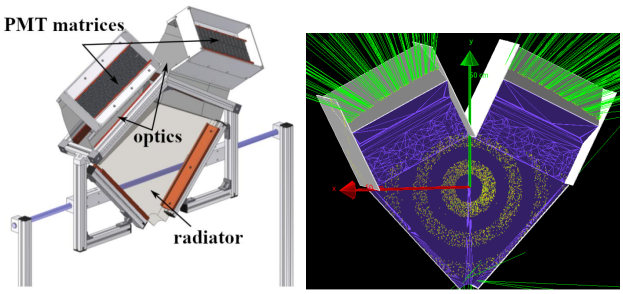

Fig. 1: Plexiglas DIRC - a scheme of the detector (left) and Geant4 simulation of the detector response (right).

Monte Carlo supported particle identification (based on 2014/15 data)

With a preliminary PID a data sample consisting of antiproton candidates was chosen and its mean track parameters were estimated. Then, a corresponding DIRC response was simulated with 3.5 GeV/c pions and antiprotons and reference matrices were created, each based on 10^3 MC events, see Fig. 2. The matrices were normalized to the total number of entries to account for the fact that there are more Cherenkov photons produced for pions.

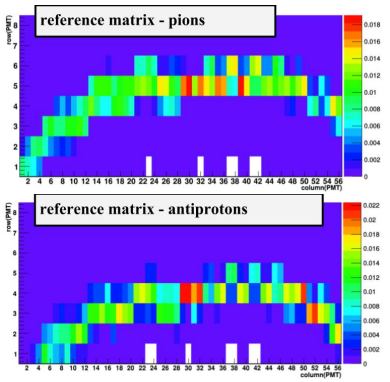

Fig. 2: Reference matrices for π^- (upper histogram) and $\bar{p}$ (lower histogram).

Several methods of $\pi^-/\bar{p}$ separation were tested, here the most promising two are described.
For a single event probability parameters $p_{\bar{p}}$ and p_{π^-} are calculated:

$$p_{\bar{p}/\pi^-} = \Sigma_{ij} R^{ij}_{\bar{p}/\pi^-} a_{ij}, \quad (1)$$

where the sum goes over all non-zero elements of the PMT matrices in the considered event ($a_{ij} = 1$ when there was a hit in a channel ij), $R^{ij}_{\bar{p}/\pi^-}$ is the normalized photon number from the reference matrix for $\bar{p}/\pi^-$.
Method 1: These values are then placed on a 2D histogram as shown in Fig. 3.
Method 2: The values are normalized so that $p_{\bar{p}} + p_{\pi^-} = 1$ and then a new variable $p \in \langle -1, 1 \rangle$ is introduced. p values closer to -1 correspond to antiproton and p values closer to 1

correspond to pion. For a single event:

$$p = -1 + \sqrt{2} \cdot \sqrt{\left(1 - \frac{p_{\bar{p}}}{p_{\bar{p}} + p_{\pi^-}}\right)^2 + \left(\frac{p_{\pi^-}}{p_{\bar{p}} + p_{\pi^-}}\right)^2}. \quad (2)$$

Results for this method are shown in Fig. 5.
A sample of more realistic MC events was generated by introducing a photon registration probability and adding noise hits in order to match the experimental detector response.
Then, the same analysis was performed on a data sample and sample of realistic MC events. The results are shown in Fig. 3 - 5.

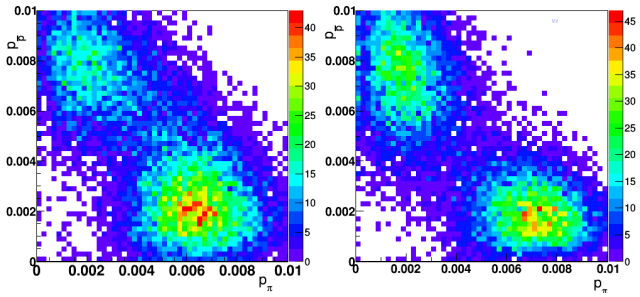

Fig. 3: Antiproton-pion separation using method 1 for a data sample consisting of a group of tracks with similar track parameters (left) and realistic MC events (right).

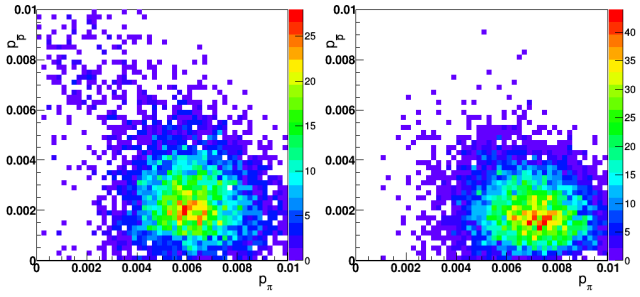

Fig. 4: Results od method 1 for the same group of tracks as in Fig. 3 with additional condition of at least one hit in the aerogel Cherenkov detector (left) and realistic MC pion events (right).

The results for data and simulation are comparable and the discrepancy between the simulation and experimental separation can be caused by:

- usage of a point-like beam with no emittance used for preparation of reference matrices,
- not precise beam parameters in simulation,
- incorrect number of noisy hits, too high/low probability of the photon registration in simulations,
- data sample containing scattered events not belonging to the beam (data sample was chosen based on the preliminary PID with a single parabolic function fit).

In the ideal case, there should be reference matrices generated for each event based on its track parameters. Realistically, for a final PID a set of reference matrices for groups

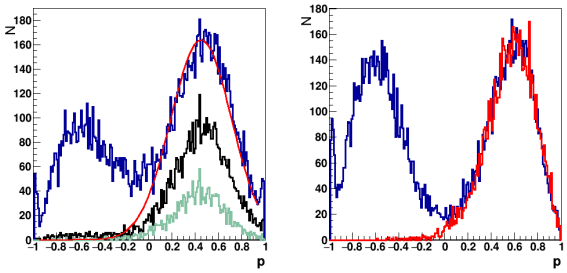

Fig. 5: Results of antiproton-pion separation using method 2. Left: Antiproton-pion separation for a data sample consisting of a group of tracks with similar parameters as in 3 (blue), with at least one (black) or at least two (light green) hits in the aerogel Cherenkov detector. A sum of Gaussian functions was fitted to the distribution without additional cuts and the part corresponding to pions is plotted in red. About 5% of pions are misidentified as antiprotons when a cut at $p = -0.1$ is introduced. Right: Antiproton-pion separation for realistic MC pion events. The result for a pure pion sample is plotted in red.

of tracks with similar parameters will be used. In order to extract a reasonable grid of reference matrices the sensitivity of different track parameters was studied by performing $\pi^-/\bar{p}$ separation for a set of data simulated with track parameters varying from the ones used for a reference matrix. This included rotations around x and y axis, shifts of the track position on a DIRC plane in x and y direction as well as combinations of these parameters.
The results of DIRC simulations are relevant for all measured data and will be used for the final particle identification in the analysis.

References:

[1] D. Grzonka, et al., Acta Phys. Polon. B 46 191 (2015)
[2] D. Alfs et al., EPJ Web of Conferences 199, 05017 (2019)
[3] D. Grzonka, CERN-SPSC-2014-016/SPSC-P349 (2014)
[4] T. Eichten et al., Nucl. Phys. B 44, 333-343 (1972)
[5] D. Grzonka et al., EPJ Web of Conferences 199, 05013 (2019)
[6] A. Zink et al., JINST 9 C04014 (2014)

Machine Learning Approach for Track Reconstruction in Particle Experiments

Jakapat Kannika

Track reconstruction in particle physics experiments is a process in which data are clustered into different groups of tracks according assumptions of trajectories of the particles. In addition to clustering, some physical information of the tracks also have to be extracted during this reconstruction process. The task of this project in the PANDA experiment is to implement a machine learning algorithm to track particles on the straw tube tracker (STT) of the PANDA detector, see Fig.1. Using a machine learning on the track reconstruction task has been studied by some research groups where a variety of machine learning techniques such as convolutional neural network (CNN), recurrent neural network (RNN) and graph neural network (GNN) was used.

As a first step of this project, track finding is being implemented on toy data. The toy data generator is written and used to control environments of the experiment where the number of rows and columns, the fraction of noise hits and a shape of the plane can be specified. The generator is also used for generating a training data simple for a supervised machine learning program. We have designed a track finding algorithm based syntactic pattern recognition using a machine learning technique. This proposed algorithm will be applied to the toy data, see Fig.2.

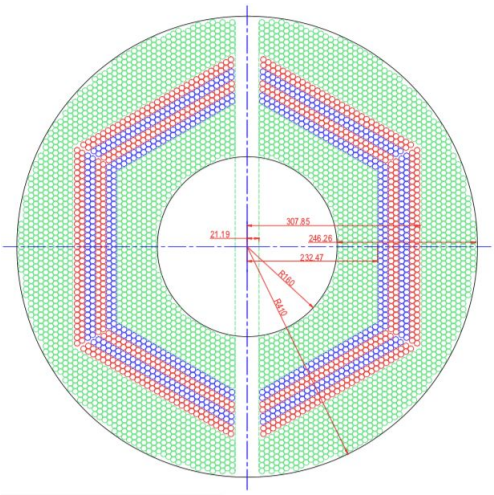

Fig.1 PANDA straw tube tracker (STT) in xy-view.

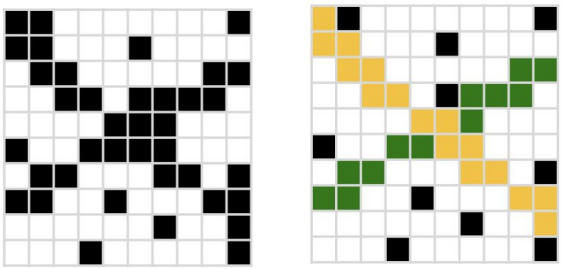

Fig.2 (a) raw data produced by the toy data generator, (b) reconstructed tracks.

The aim of this experiment is to prove that the proposed algorithm can be used to reconstruct tracks from data points in the presence of noise. Performance indicators, such as the speed and accuracy of the algorithm will be measured, and limitations of the method will be investigated.

Utilizing Machine Learning Techniques for Charged Particle Identification (PID) at the PANDA experiment.

Waleed Esmail, Tobias Stockmanns, and James Ritman

Each PID system at PANDA provides information, to discriminate difference particle species. For example, the RICH system provides lepton hadron separation, while the calorimeter provides electron and pion separation. Hence, a combination between different PID systems provides a much more powerful set of PID variables. Thus PANDA combines the PID system information based on the likelihood method, the various likelihoods from the sub-detectors are combined by multiplication:

$$P_{tot,i} = \prod_{detector} P_{detector,i} \qquad i \in (e, \mu, \pi, K, p)$$

Another way of combining the PID information is achieved by using a multivariate method, currently two methods were implemented into PandaRoot:

1. Boosted Decision Trees (BDTs).
2. Artificial Neural Network (ANN).

As a first step toward understanding the performance of both methods data is generated using two different Monte Carlo event generators, the box generator and the EvtGen. The generated data are passed through Geant4 for full simulation of the PANDA detector, and then different particle species are matched to their Monte Carlo truth information to obtain a clean sample for training. 37 variables/observables from all PID systems are used to train both BDT and ANN.

1. BDTs: A single Decision Tree (DT) learn a hierarchy of "if-else" questions, leading finally to a decision. A BDT is an ensemble method i.e. a collection of DTs. The key concept behind boosting is to focus on training samples that are hard to classify. XGBoost is an open-source software library has been used to train two BDT as multiclass classifier, one trained on box generator data, the other on EvtGen data. Several performance metrics were evaluated, of particular interest is the PID output probabilities.

2. ANN: An Artificial Neural Network is an interconnected group of nodes arranged in layers. The basic layout consists of an input layer, one or more hidden layers, and an output layer. All inputs are modified by a weights and summed, and an activation function controls the amplitude of the output. Similar to BDT two classifiers were trained but using Keras package.

Figure 1 provides a comparison between the BDT, the ANN and the likelihood method. As can be seen electrons are the cleanest prediction of both methods (ANN and BDT) above 95% accuracy compared to the likelihood method 93%. The trained algorithms also provides a better pion and kaon identification compared to the likelihood method.

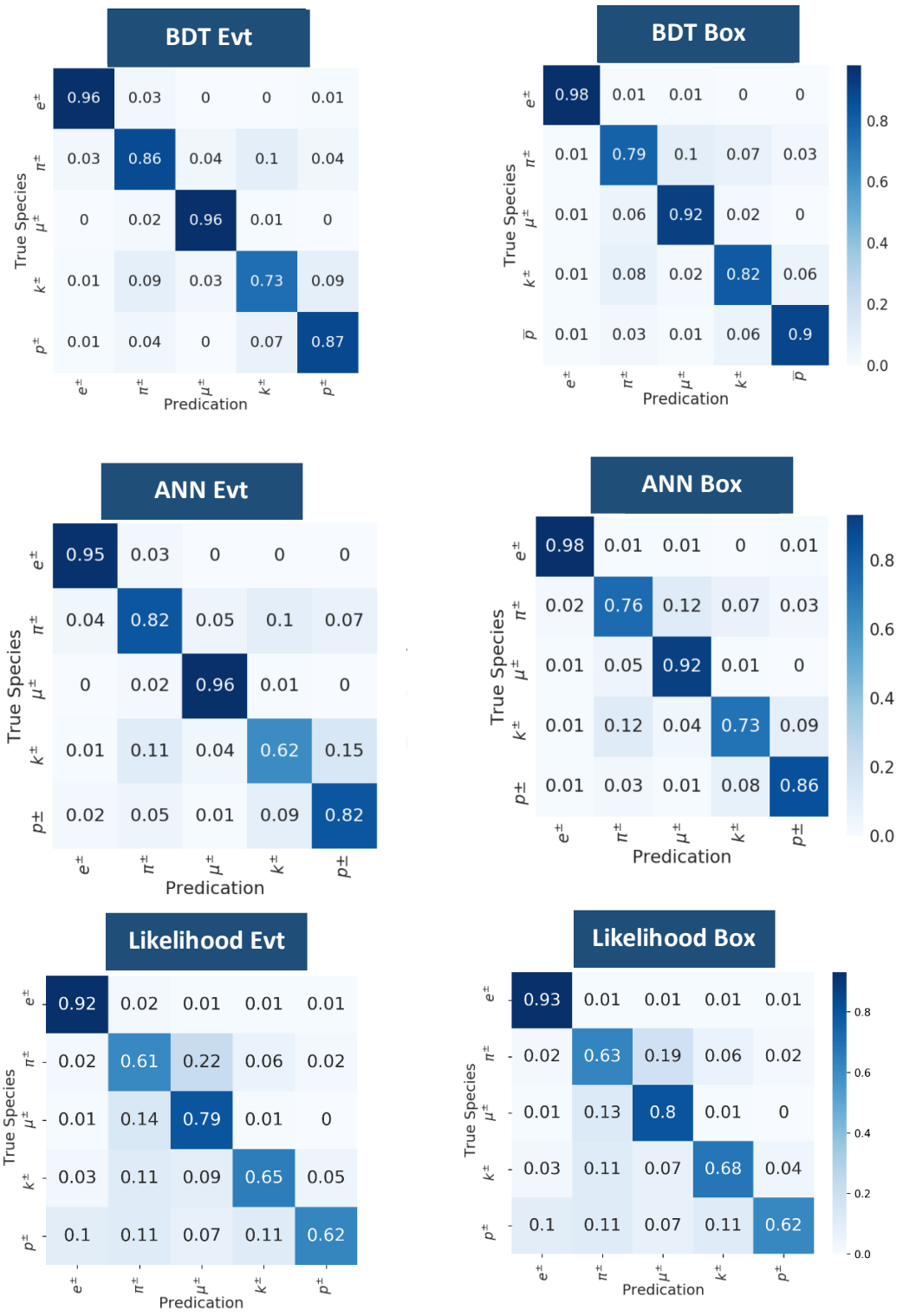

Figure 1 Comparison between the BDT (upper row), and the ANN (middle row), and the likelihood method (bottom row) in the form of a confusion matrix CM. The columns of the CM reports the prediction of the algorithm.

Exploration of Machine/Deep Learning Methods for track reconstruction at PANDA and the PANDA@HADES Forward Detector System

Waleed Esmail, Tobias Stockmanns, and James Ritman

As a fixed target experiment, most of the produced particles at PANDA will have a forward boost. Therefore it is of crucial importance to have an efficient, robust and fast track reconstruction algorithm at the forward part of the experiment (Forward Tracking System FTS). The FTS is located downstream of the interaction region and measures particles at small polar angles, i.e. θ below $5°$ in the vertical and $10°$ in the horizontal plane. The design of the FTS is based on self-supporting straw tubes arranged in three pairs of planar stations. One pair (FT1, FT2) is placed upstream of the FS dipole magnet, the second pair (FT5, FT6) downstream of the magnet, and the third pair (FT3, FT4) is placed inside the gap of the magnet. Each tracking station consists of four double layers of straws: the first and the fourth one are vertical straws and the two intermediate double layers are composed of straws tilted at $+5°$ and $-5°$, respectively. The combinatorial seeding and track building algorithms are inherently serial and scale quadratic or worse with the detector occupancy. It is thus important to investigate new solutions such as methods based on Machine/Deep Learning.

Collision events that happens at the interaction point generate different particles which leave space-points "hits" in the detector. The track reconstruction algorithm should combine the correct hits (coming from the same particle) together in a process also known as pattern recognition or track finding.

Because the problem is far from trivial. It is often better to divide it into steps. My first approach is to divide the algorithm into two steps:

1. The first step is to combine correct hits together in three different regions of the detector (FTS1/FTS2 together, FTS3/FTS4 together, and FTS5/FTS6 together) by using unsupervised learning technique, in particular k-means algorithm. K-means is a simple clustering algorithm that aims to partition a set of observations (in this case hits) into a number of clusters k (in this case tracks). Because the number of clusters k is not known in advance the elbow method is used to fix it, which simply looks at the percentage of variance explained as a function of the number of clusters. By applying this step tracks segments are found in the three different regions of the detector mentioned above.

2. The second step is to connect track segments found by step1 to build a full track. This method uses Recurrent Neural Networks (RNNs) to build the full tracks. In RNN the connections between neurons form a directed graph. This allows it to exhibit temporal behavior for a time sequence (in this case hits in subsequent detector layers), which makes RNN a perfect method for track building. RNN is used in this step as a classification algorithm i.e. it is trained to accept two track segments for different detector regions (e.g. segment in FTS1, FTS2 and segment in FTS3, FTS4) and outputs a number (probability) between 0 and 1. 1 means that both segment form a true track, while 0 means wrong combination between segments (ghost track).

   To test the proposed algorithm, box event generator is used to simulate particle tracks in the PANDA detector for different momentum ranges and polar angles 0^{o}-10^{o}. **Figure [1]** shows a pictorial representation of the output of the RNN.

It has been noticed that the first step crashes if the event contains only one track, the reason behind this is that k-means tries to cluster the track into its hits i.e. each hit becomes a cluster by itself. For this reason step1 is currently being replace by supervised algorithm, namely an Artificial Neural Network (ANN) which trained to accepts the coordinates of hit pairs or triplets and outputs whether the pairs/triplets are on the same track or not. This type of ANN can reach an overall accuracy of 93% on pair/triplet classification. Work is still ongoing to improve the accuracy and to benefit from all available information provided by the detector (e.g. drift radius).

Other methods:

a) Convolution Neural Network (CNN) is difficult to apply for this problem, because CNN must accept an image as an input or in machine learning terminology an array of number (pixels), while the FTS hits provided by the detector are continuous. In order to prepare FTS hits for CNN it must be pixelated first or i.e. histogramming the data, which introduces a lot of difficulties.

b) Graph Neural Network (GNN) in this method hits are viewed as vertices of a graph (in graph theory sense) and tracks are viewed as the edges of the graph. A GNN model can learn on this representation and solve tasks with predictions over the graph nodes, edges, or global state. Work is still ongoing on this part.

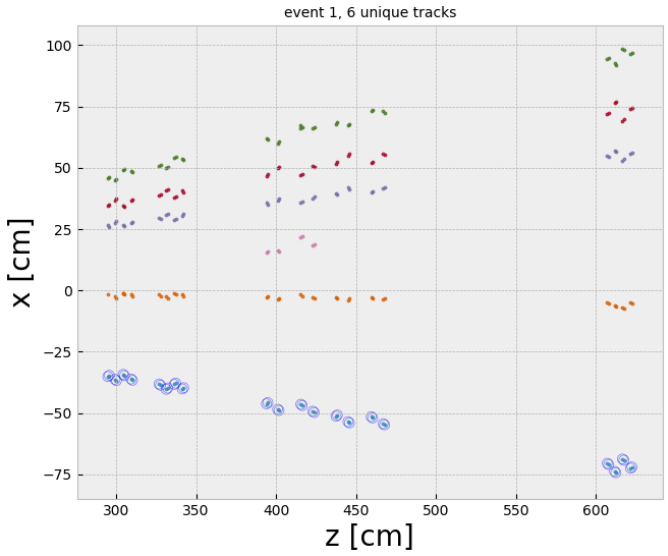

Figure 1 Output of the RNN. The Figure shows the x-z projection of data from PANDA FTS, different colors indicate unique particle tracks, the circles indicate the track found by RNN. For illustration purposes only one found track is shown.

A PANDA Track Finding Algorithm based on the Apollonius Problem

Anna Scholl, Tobias Stockmanns and James Ritman

One of the main components of the PANDA experiment is the Straw Tube Tracker (STT). It consists of over 4200 gas-filled drift tubes. The detector layout consists of layers parallel to the beam axis and skewed layers with an angle, with respect to the beam axis, of about ±3º for a three-dimensional reconstruction. When a charged particle ionizes the gas in one of the drift tubes, the electrons drift to the anode, which is located in the center of each tube. Since only the drift time of the electrons to the anode is known, as well as the position of the anode wire, only the radius around the anode where the ionization must have taken place can be calculated. This results in a cylinder (isochrone) around the anode wire. Simulated isochrone data for a track in the STT are shown in figure 1. The skewed layers are drawn in green and the layers parallel to the beam axis are shown in black. The track of the charged particle must pass tangentially to the isochrones of the layers parallel to the beam axis.

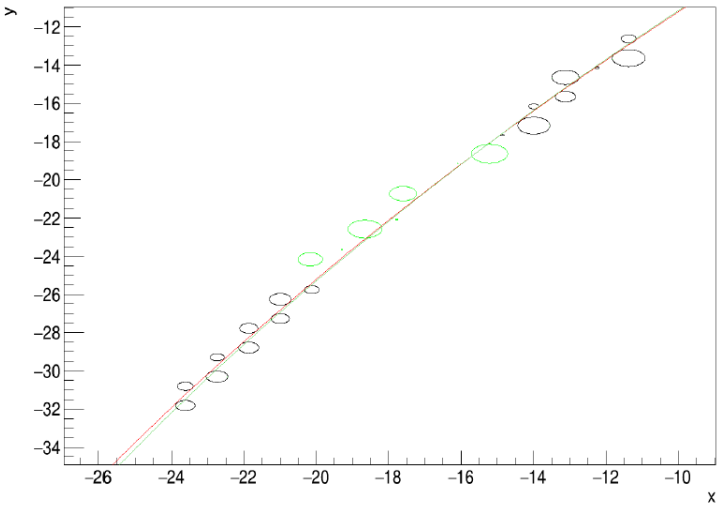

Figure 1: Simulated isochrone data for a track in the STT.

Algorithms based on two or three dimensional hitpoints, usually do not use the additional isochrone information. For the STT, however, a tracking algorithm is needed that finds tracks that are tangential to every isochrone. To deal with this challenge an approach based on the Apollonius problem is developed. The Apollonius problem is a mathematical problem of connecting three circles with a fourth circle that is tangential to the other three circles. At the current state of development, the solutions for the Apollonius problems are calculated for two isochrones and the interaction point. So, at the moment the algorithm can only reconstruct paths of particles originating from the interaction point. In this case for every pair of isochrones four Apollonius solutions exist. This mathematical description is the basis for a Hough transformation to find the track of the charged particle. For the Hough transformation the calculation of the Apollonius circles is done for every pair of isochrones. All centers of calculated Apollonius circles are filled in a histogram. In theory it is expected that one entry in the histogram results in a peak, since every pair of hitpoints should have one Apollonius circle that is also tangential to every other hitpoint. In this way the true track of the charged particle can be found. In reality however, it is not as easy, since for example there are uncertainties in measuring the isochrone radius or the charged particle is not emitted from the interaction point (because of secondary decay vertices). Therefore, no single peak can be found at the momentary point of development. So, the next step is to examine the influence of the uncertainties of measuring the isochrone radius.

In the future the algorithm will be extended to work with three hitpoints. With this extension also secondary decay vertices can be found.

Improvements on the Data Acquisition System of KOALA Experiment at COSY

Yong Zhou and Huagen Xu

An EMS[1]-based data acquisition system has been developed and commissioned for the KOALA beam tests at COSY[2]. Several improvements on the DAQ system have been made in preparation of the new beam test in 2019, in which a newly-built forward detector will be commissioned together with the recoil detector. First, the problem of unsynchronization between different modules in the system[3] is solved. Second, a new design of the decoding procedure is implemented. Last but not least, a refactoring of the DAQ codebase is also carried out for easier maintenance and development in the future. These improvements are presented in this short report.

The DAQ hardware of the KOALA experiment is a VME-based system with multiple digitization modules from Mesytec (TDCs, QDCs and ADCs)[4]. To minimize the deadtime and improve the performance, each module works independently in multi-event mode. Synchronization between the modules is based on a timestamp, which is generated by a common trigger and a common clock distributed to each module. However, in previous tests the timestamps from different modules started to deviate from each other during long runs, as shown in Fig.1a This will cause a serious problem for the coming beam test, because the coincidence between the recoil detector and the forward detector is utilized to remove the large backgroud events in the recoil angle close to 90°. Thorough study and tests on the Mesytec modules have been carried out to solve this problem. As a result, two major modifications are made in the DAQ setup: (i) A new order of the register setting sequence is applied in the initilization of the Mesytec modules, resulting in a well-defined state before resetting the timpestamp counter; (ii) The buffer--full flag signal from each module is integrated into the trigger logic, resulting in a more robust VETO mechanism. After these modifications, the timestamps from different modules perfectly match each other now, as shown in Fig.1b.

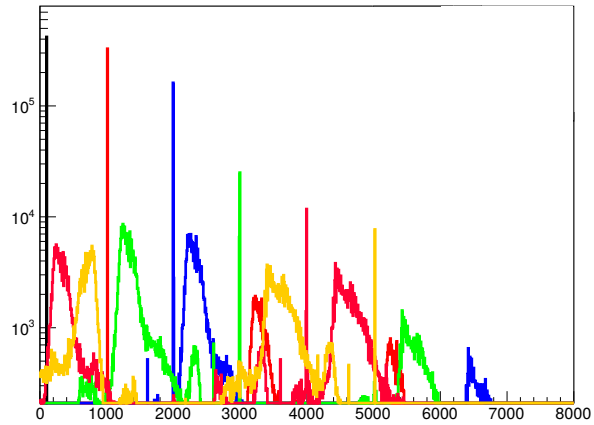

(a) Before modifications

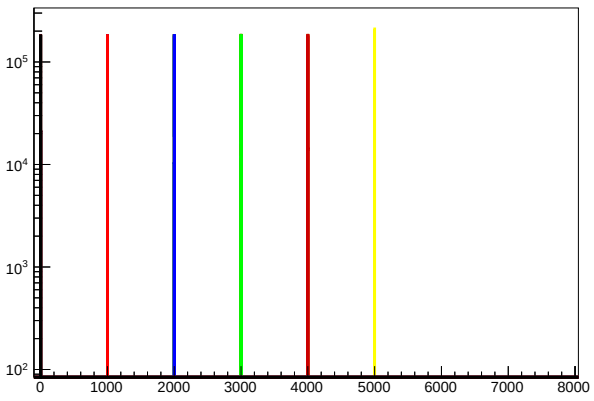

(b) After modifications

Fig. 1: Difference of timestamps between 6 modules in the system (First module as the reference, and a constant gap is inserted for better illustration)

The old decoding algorithm is a single-block program, and does not rely on the timestamp information to assemble the event. To accomodate the new developments of the DAQ system, the decoding mechanism has been redesigned based on object-oriented principle. The decoding is decomposed into three separate steps, which are represented by three abstract classes: **Decoder:** raw binary data is decoded and saved into a FIFO buffer for each module respectively; **Assembler:** data from each module are collected from the FIFO buffers and assembled into a complete event based on the same timestamp; **Analyzer:** electronics-based data is mapped into detector-based data, and user-defined analysis especially the code from simulation package can be integrated seamlessly. The new code is organized as an independent package in the DAQ software.

The EMS architecture was developed more than 20 years ago[1] and was used extensively in experiments commissioned at COSY. In this process, new components related to specific experiments were added into EMS and the result is a large codebase with many functions which are not needed in KOALA. This is a heavy burden for the maintainance, and it also causes confusion for new developers in KOALA. Thus, a refactoring of the EMS codebase has been carried out and the result is a new project called **KoalaEms**. In parallel, the documentation about the DAQ hardware and software is initiated and grows into a separate project. Both projects are managed within a git[5] repository and hosted on `https://pandaatfair.githost.io/KoalaGroup`, which servers as a central hub for KOALA-related development.

References:

[1] K. H. Watzlawik et al. IEEE Transactions on Nuclear Science 43 (1996): 44
[2] Q. Hu, U. Bechstedt, A. Gillitzer et al. Eur. Phys. J. A, 50 10 (2014) 156
[3] P. Wuestner, D. Grzonka, Q. Hu et al. 2016 IEEE-NPSS Real Time Conference (RT). IEEE, 2016 156
[4] `www.mesytec.com`
[5] `https://git-scm.com`

Structural design and realization of the HADES STS1 as a PANDA Phase-0 Experiment

Artur Derichs

Within the Hades experiment setup, the Straw-Tube-Station (STS) is being realized as parth of the PANDA Phase-0 program. The mechanical design, include the construction of the self-supporting straw double-layers and the alignment procedure, which fits into the hexagonal body of the electromagnetic calorimeter has been worked out and coordinated with the project partners. This report shows the project status as well as the scope of the STS1 station, which has been designed and constructed at IKP. The basic layout of the detector has a high similarity to the PANDA STT detector. By realizing this structure, synergetic benefits for PANDA are achieved, such as increasing the general level of detail, improving QM and qualification of the support structure and readout electronic concepts.

The basic structure consists of four double-layers with five modules per double-layer. Each module has 32 straws, except the center-module with 48 straws. In total, the STS1 detector consists of more than 750 straws. For track reconstruction, each double-layer is rotated by 90 degrees. To support the modularity of a double-layer, the modules are designed to be identical, except for the central part with the beam window. This allows for easy exchanging.

On-site, a fully packed double-layer was set up for mechanical test purposes. After prototyping experience and some changes, the final structure was defined together with the involved partners in a design-freeze. This setup will be used for the follow-up tests, first in the COSY-TOF area for functional tests and precision alignment. As part of these measures, the cable management/routing will be further improved concurrently to the preassembly, with the goal of maximum prefabrication of the STS1 detector in the IKP. After the mechanical modifications, the setup is ready to use all modules for the upcoming preassembly tests.

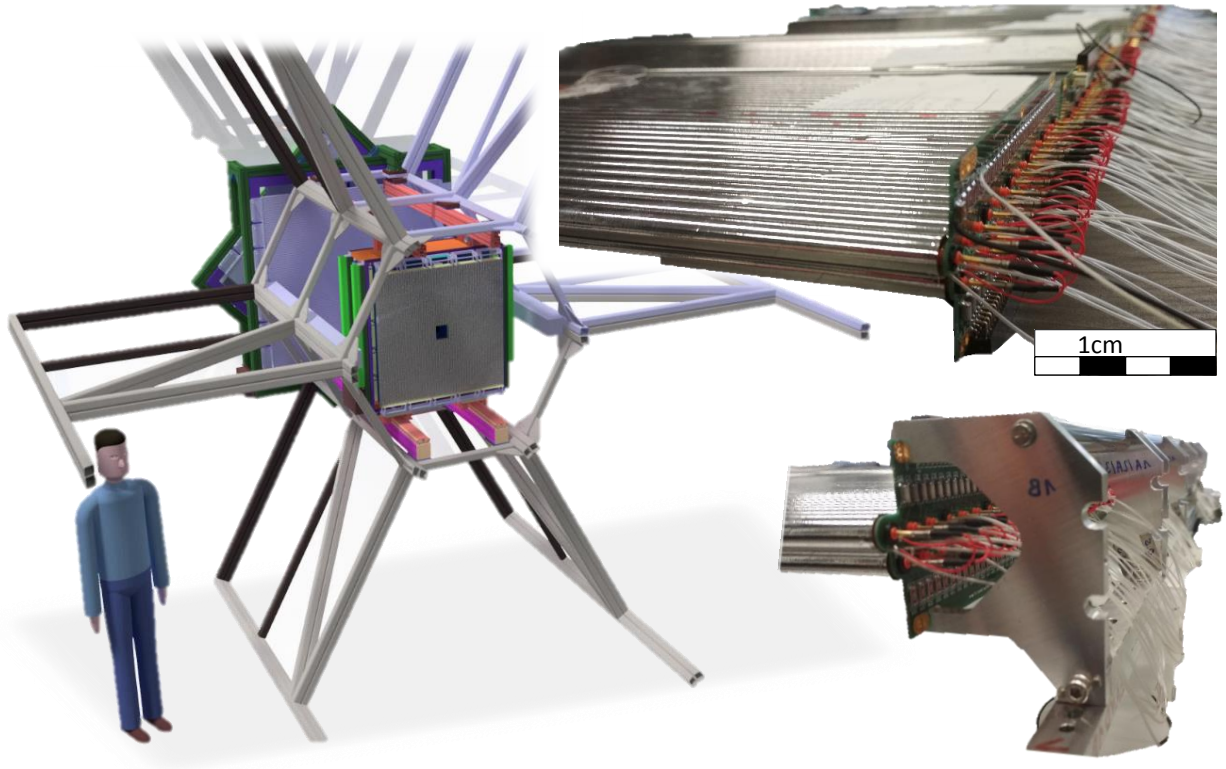

Figure 1: HADES-PANDA Phase-0 setup with IKP-Straws

The PANDA STT prototype with a sampling ADC readout

V. Serdyuk

The Straw Tube Tracker (STT) presents a fundamental component of the PANDA Target Spectrometer. The main task of the STT is the measurement of the charged particle momenta after track reconstruction as well as the identification of low momentum charged particle by specific energy loss measurements (below about $1 GeV/c$).

A digital readout concept based on a multisampling ADC (sADC) is presently under development for the STT detector.

The advantage of the sADC over a discriminator-TDC method is the availability of information on the complete signal waveform. That allows to extract more observables from the recorded pulse shape, for instance pulse trailing edge, peak height, pulse shape integration. In particular this gives a benefit for the signal pile-up detection at high rates and the possibility to suppress afterpulses due to photoeffect on cathodes for events with high ionization depositions.

An additional feature of this approach is the so called 'frontend free readout' where the signal are transferred directly from straws by long (12 meters) high voltage coaxial cables to the decoupling boards with preamplifiers. On the STT itself (inside the PANDA solenoid) simple PCBs were placed which contain only passive components and therefore are less vulnerable to failures. So any defect of individual straws during the data taking can be easily fixed from outside the beam area with no need to switch off big groups of detector channels. The material budget and the space in the upstream region of the STT can be minimized. There is no need for cooling since there is no heat generated at front-end of the detector and no radiation damage of the electronics.

To test this readout concept, a straw tubes prototype containing 16 layers with 24 straws 1.5 meters long in each layer was built in a close packed structure. A care was taken to provide good electrical contact of the aluminium inner surface straw cathode to the PCB ground through the gold plated springs using a conductive paint.

A crate with decoupling boards with 128 channels in total was built in the electronic laboratory of IKP as a first prototype for PANDA. As a first step to make a commissioning of the detector a set of preamplifiers with a gain of 40 was connected through 12 meter cables to the straws. Each bandle of cables was wrapped with shielding jackets to decrease the noise generated by external electromagnetic background. The crate and straw detector were also schielded and properly grounded.

The performance of the detector was tested in March 2018 at COSY with proton and deuteron extracted beams of different momenta using a fast flash ADC (FQDC,

WASA type) with a sampling frequency of 240 MHz.

In addition to the STT prototypes three planar drift chambers and 4 mm straw tubes were installed in the COSY beam area along the beam which gave the possibility to on-line monitor beam shapes, time structures of the beam and control during the beam tuning and the data taking, the position and stability of the beams. During these measurements a spatial resolution better than 150 mkm (sigma) and an energy resolution close to 9% (FWHM) were obtained, which meets the PANDA requirement for the STT.

A prototype of highly integrated ADC compact DAQ system based on a single open VPX-crate for digitisation the signals and analyses of their shapes with FPGA algorithms with a small number of channels (16) was tested in April 2018 beam time at COSY. The analog modules with amplifiers and shapers were inserted from the rear side while sampling and processing from the front side. The connection of the preamplifier from the high voltage decoupling mini-crate was done with ribbon SAMTEC cables. The sampling frequency was about 100 - 150 MHz. Such approach leads to a system with an integration of 2240 channels into a single 19"-crate. This first test in a beam showed a proper performance of the readout. At present the work made in ZEA FZJ with external companies is focused on corrections of minory technical imperfectnessis in the design and the production of a system with 400 channels as a demonstrator for the PANDA STT readout. The functionality is under investigation in running tests with cosmic rays, radioactive sources and will continue in future beam tests at COSY.

SiPM Radiation Hardness Study with COSY

Tamer Tolba

By providing fast timing information for all charged particles reaching the device, the barrel time of flight, barrel ToF, will be an essential part of the particle identification, PID, system of the PANDA at FAIR detector. The barrel ToF concept is a modern version of a ToF wall in which large organic scintillator plates are segmented into small scintillator tiles made out of fast scintillating materials. The optical readout is performed by Silicon Photomultipliers, SiPM, embedded within the gaps between tiles.
The PANDA barrel ToF detector will be located between the barrel-DIRC and the EMC detectors with approximately 50 cm radial distance to the beam axis. This location exposes the barrel TOF to high energy and flux radiation. It is thus imperative to avoid severe degradation of the SiPM's performance due to this exposure.

The expected damage effect from the radiation exposure can be categorized as follows:

1- Ionizing Energy Loss (IEL), usually caused by photons and charged particles, e.g. electrons:
   a- Charge build-up of the surface-protection Oxide layer of the SiPMs.
   b- Increase in the leakage current.

2- Non-Ionizing Energy Loss (NIEL), usually caused by heavier particles, e.g. protons, neutrons and pions:
   a- Crystal defects in the bulk of the Si lattice. This usually generated by the heavy particles that penetrate to the bulk of the SiPM die and cause a displacement in the Si atoms (the Primary Knock-on Atoms (PKA)).
   b- Change of effective doping concentration by producing acceptor like defects which modifies the depletion (breakdown) voltage.
   c- Increase of charge carrier trapping which leads to a loss of charge (signal), and hence gain.
   d- Easier thermal excitement of electrons and holes that causes an increase of the leakage current, hence the dark current noise.

The estimated average equivalent neutron dose on the barrel ToF detector is in order of 9.13×10^9 n_{eq} (1 MeV)/cm^2 a year. This estimated neutron equivalent flux is based on assuming an exposed area of 5 cm^2 of a “full” fused silica material (for the Barrel DIRC detector). Because the exact internal structure and doping concentrations of the SiPMs are not disclosed vendors, it is difficult to accurately estimate/simulate a priori the effect of the radiation damage on the SiPM structure. Thus, the radiation dependence; as a function of energy and flux, of such devices needs to be measured experimentally.

While there are previous radiation-hardness measurements of some SiPMs; at low radiation energy ranges, below 212 MeV, and one measurement at very high energy, 23 GeV, no previous studies of the SiPMs have been performed in the energy region relevant for PANDA, i.e. about 1.5-3.5 GeV. Hence, these measurements will be the first in this energy range.

This project aims at studying the radiation hardness of the SiPMs using the COSY beam. In order to mitigate the effect of the systematic uncertainties, the study will depend on the “relative” measurements of the SiPMs performance under and/or after the exposure to high-energy and high-flux radiation with respect to their performance without such exposure.

Simulation study and prototype tests for the PANDA FToF detector

D. Veretennikov

FToF detector for PANDA PID. Particle identification (PID) in the Forward Spectrometer in the PANDA experiment is realized with the help of the (Forward Time-of-Flight) FToF wall and forward RICH detectors. While the forward RICH provides effective hadron separation for momenta above 2 GeV/c for pions and above 4 GeV/c for protons, the FToF detector could provide hadron ID at particle momenta below 4 GeV/c.

In addition to contributing to the PID of forward going, low momentum particles, the FToF detector will also provide information on the time stamp by using a fast organic scintillator. For a relativistic particle (i.e. hadrons with $\gamma > 3$) this information helps to reconstruct the event start time in the IP with a precision of a few ns. Provided the particle is identified as either a hadron or a charged lepton (muon or electron), this precision could be improved to about 100 ps, which is the planned time resolution of the FToF detector.

The FToF TDR was presented to the collaboration, and after accounting for the comments, the TDR was submitted to FAIR for external review. In November the TDR was approved by the FAIR ECE. In addition to that, many tests and further development was performed at PNPI, mostly with 1 GeV proton beam and optimization of the readout electronics.

Laser test station. Testing prototypes with a proton beam is the best choice because conditions in this case are very close what we will have in PANDA. However, beam tests are expensive and are not convenient for mass production tests. To simplify the testing procedure, we built a laser test station. Laser parameters are presented in Table 1.

Table 1: Parameters of the PDL 800-B laser used for the test station

Wave lengths	371 - 372 nm
Minimum pulse width	48 ps
Time stamp precision	3 ps
Peak power	up to 1 W
Repetition rate	1 Hz - 40 MHz

Measurements with the laser require neither an accelerator nor a radioactive source. At the same time, the flash produced by a real particle in a plastic scintillator is very well reproduced. The ability to control the flash parameters allows to better investigate the characteristics of a photodetector, in particular, the response to very weak low-photon signals and determine important characteristics such as the TTS (Time Transition Spread) - the one-photon response.

Results for the time resolution obtained with the laser tests on a real prototype using the real front-end electronics presented on Fig.1. The time resolution obtained with the laser (87 ps) is slightly better than that measured with beam (92 ps). The main reason is that the energy deposited in the plastic by the laser pulse is fixed and not changed from pulse to pulse. So

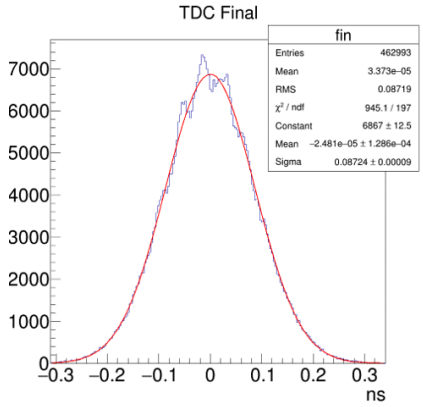

Fig. 1: Time resolution obtained on laser test station

analyzing laser data does not require any correction for the signal amplitude, and thus provides a more precise result.

PID with Cellular Automaton tracking. In September, the first version of the PANDA forward track reconstruction (Cellular Automaton or CAtracking) was included in PANDAROOT. It uses the cellular automaton to build track segments and combine then into a track. The particle mass is reconstructed using the same equation used for the ideal track reconstruction:

$$m = \frac{p}{c}\sqrt{\frac{t^2}{t_c^2} - 1} \tag{1}$$

Here p is the particle momentum, $t_c = L/c$, L is the length of the particle track starting from the IP (start point), or from a decay vertex, to the hit position of a FToF counter, c is the speed of light, t is the measured time of flight, i.e., $t/t_c = c/v$, where v is the particle velocity. Results for $p/\pi/K$ mass reconstruction for different momentum ranges are presented on Fig.2.

A quantitative description of the particle separation is given by the following formula:

$$n_{i,j} = \frac{|m_i - m_j|}{(\sigma_i + \sigma_j)/2} \tag{2}$$

Assuming that the peak can be described by a gaussian, here $n_{i,j}$ is the separation power between particle i and j, m is the mass of particle and σ is the variance of the corresponding gaussian. Two peaks are well separated if $n > 3$, $2 < n < 3$ means that the peaks are still separated but has some overlapping data and $n < 1$ means that the two peaks has a significant fraction of overlapping data which cannot be separated. The separation power for different types of particles is presented in Fig.3. One can see, that in the FToF region below 4 GeV/c all particle are separated with $n > 2$. As expected, the results with the cellular automaton track reconstruction are worse ($n > 2$) than was obtained for the ideal track reconstruction ($n > 2.5$).

Just as for the ideal track reconstruction case, the event start time (T_0) can be calculated by looping through all possible

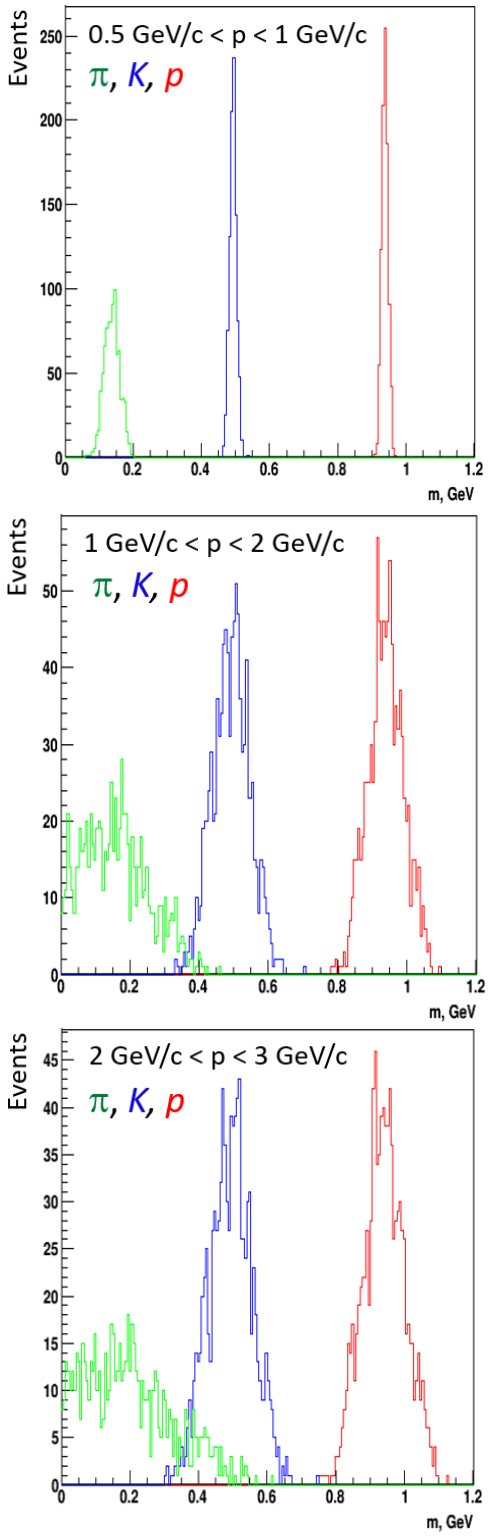

Fig. 2: Reconstructed mass using the CAtracking for π (green), K (blue) and p (red).

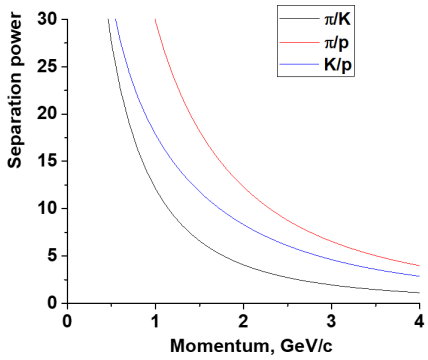

Fig. 3: Separation power n for different pairs of particles, using the CAtracking routine.

combinations of particles for a given number of tracks. This procedure only works when the number of hits are $n > 2$. For a number of hits N, a system of N equations can be formulated:

$$
\begin{aligned}
t_1^{ToF} &= T_0 + \frac{L_1}{c}\frac{\sqrt{p_1^2+m_1^2}}{p_1} \\
t_2^{ToF} &= T_0 + \frac{L_2}{c}\frac{\sqrt{p_2^2+m_2^2}}{p_2} \\
&\cdots\cdots\cdots\cdots\cdots\cdots\cdots\cdots \\
t_N^{ToF} &= T_0 + \frac{L_N}{c}\frac{\sqrt{p_N^2+m_N^2}}{p_N}
\end{aligned}
\tag{3}
$$

Here we have $N+1$ unknown variables $m_1,...,m_N,T_0$ and N equations. This system can be solved by looping through all combinations of $m_i = [m_e, m_\mu, m_\pi, m_K, m_p]$. For each variant of mass combination T_0 is calculated for all equations and combination when T_0 same for all equations are chooses. The number of combinations for N hits is equal to 5^N, so this analysis can only be done offline. The results obtained with CAtracking presented in Fig.4. Here, the value of $T_0 - T_{0,MC}$ presented, where $T_{0,MC}$ is exact and taken from the Monte Carlo simulations. In the ideal case this value should be a delta function at zero. The precision to determine T_0 using the CAtracking algorithm and the same looping algorithm as for the ideal tracking is 90 ps.

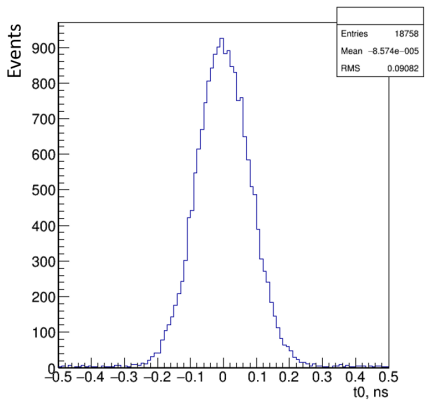

Fig. 4: Precision of the T_0 determination with CAtracking.

Semiconductor detector development for GSI/FAIR

T. Krings

One main focus of the detector lab in 2018 was the work on further developments of semiconductor detector systems with regard to future experiments at GSI/FAIR.

Since almost two decades the atomic physics department of GSI and the detector lab of the IKP have a very successful collaboration on the design and development of structured planar multichannel HPGe- and Si(Li)- detector systems with position-, time-, and energy resolution.

Employing these systems as Compton polarimeters opens a unique insight into the dynamics of atomic processes in highly charged heavy ions by experiments at the accelerator facility GSI and also synchrotron facilities. The continuous technological developments have resulted in detector systems with the ability to determine the linear polarization of an x-ray source, e.g. an ion beam interacting with a target, with high precision covering an energy range from 40 keV up to 400-500 keV.

To cover an energy range from a few keV to ~30 keV we have developed a Compton polarimeter prototype (see Fig. 1) to determine the degree of linear polarization of this radiation. The concept is based on a passive low-Z scatterer (e.g. Be, SiC, PE) in which the emitted x-rays will undergo Compton scattering and in a subsequent step they will be deposited on a ~3.5 mm thick pixelated HPGe detector. The back side contact of this detector is segmented with a structure of 19 hexagonal pixels. The asymmetry of the scattering distribution is a signature of the degree of linear polarization. The detector may be used as a 19-pixel x-ray detector or in combination with a scatterer as Compton polarimeter. The readout stage is split into two parts. The first part is the cryogenically cooled FET input stage and the second stage is built from discrete charge sensitive preamplifiers operating at room temperature.

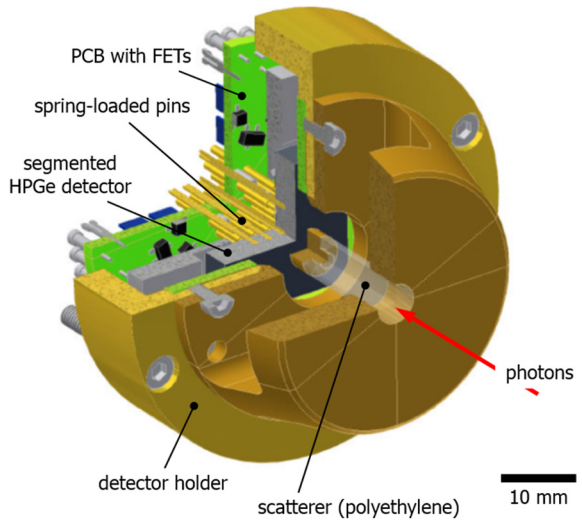

Fig. 1: Sectional view of the detector head with the mounted detector, the PCB with spring-loaded pins and the FETs and the low-Z scatterer in front of the detector.

The detector elements are connected to the FET-input by spring-loaded pins instead of wire-bonds. All 19 pixels show an energy resolution of ~850 eV for the 59.5 keV gamma line of Am-241 at a shaping time of 3 µs (see Fig. 2).

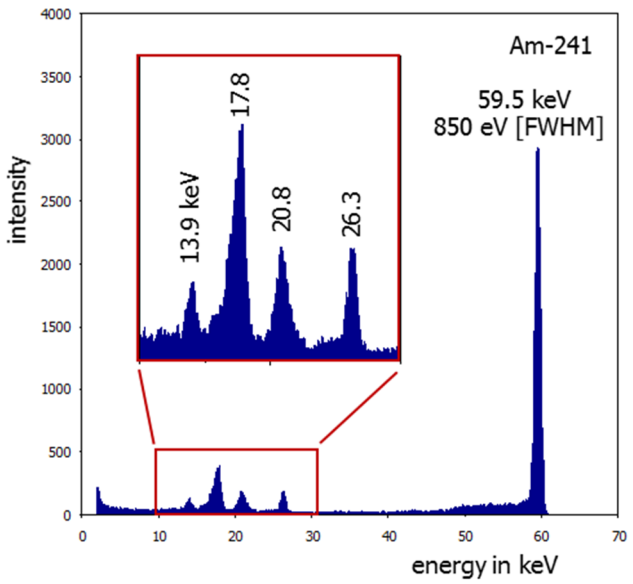

Fig. 2: Spectroscopic result of pixel #4. A spectrum of an Am-241 source with the Np-triplet and the 59.5 keV gamma line indicating an energy resolution of ~850 eV at 59.5 keV measured at a shaping time of 3 µs. [This measurement was taken before mounting the scatterer in front of the detector.]

A second detector system was realized together with GSI, HI-Jena and Friedrich-Schiller-University Jena. It consists of a 16 mm thick HPGe-detector which is segmented into 64 pixels (3.5 mm x 3.5 mm each) arranged in a 8x8 matrix. The main goal of this project is the test of different preamplifiers for the readout of the detector elements to further improve the energy resolution of the detector systems. The PCBs with the cold FETs can be easily replaced without removing the wire-bonds to the pixels.

With the new experimental challenges coming up with the FAIR project, especially the physics program of the SPARC collaboration at HESR, the measurement range for the linear polarization will be extended up to 1 MeV and beyond. For these physics applications the development of a detector system produced from two thick position and energy sensitive planar semiconductor detectors in telescope configuration is planned. The results and experience obtained with the described 19-pixel and the 64-pixel detector systems will be integrated into this development.

The WASA MDC for experiments at FRS in GSI

V. Serdyuk

After the decision to stop the hadron physics experiments at COSY the WASA detector was disassembled and stored in the accelerator building outside the ring. In 2017 it was proposed to reuse the WASA-at-COSY central detector (CD) in GSI for the experiments at the Fragment Separator (FRS). The proposal was quickly endorsed by WASA collaboration.

GSI recently obtained promising results investigating the production of light hypernuclei ${}^{3}_{\Lambda}H$ and ${}^{4}_{\Lambda}H$ with heavy ion beams which however revealed several puzzles related to contradictions in their lifetimes compared to data from other experiments. Also an indication on the existence of a bound state ${}^{3}_{\Lambda}n$ (Λ-hyperon and two neutrons) in HypHI Phase 0 at GSI needs more careful research.

In order to improve the sensitivity and the precision of measurements the WASA CD will be placed in the central focal plane S2 of FRS. In addition to the research program on light Λ-hypernuclei, two other experiments on η'-mesic nuclei and baryon resonances are proposed with the same configuration with only changes of the target position and using proton beam from SIS18. All three experiments were approved by the GSI PAC and planned for beam times in 2019-2020. This gives new opportunities at the border of nuclear and hadron physics.

The WASA CD consists of central tracker mini drift chamber (MDC), a plastic scintillator hodoscope, a solenoid and CsI elctromagnetic calorimeter. On the beggining of 2018 as a first step the MDC and relevant componenets (gas system with slow control, amplifier-discriminators CMP16 together with signal cables and necessary crates) were transported to GSI. The digital part - TDC, were provided from the GSI electronics pool. A special room close to the FRS area was constructed for cabling and commissioning of the MDC. Considering the fragility of the MDC and the fact that it is for the use in a third experiment, a special care was taken to identify and check all potential defect of the detectors and connections. Some problems including irreparable (broken pins, wires) were known already from the first experiment in Uppsala and later in Julich at COSY. All the coaxial cables transferring the analog signals to CMP16 were checked and repaired. The gas tightness was checked for individual layers. The cosmic rays test were done 'layer by layer' in order to have a possibility to fix connection problems online.

Presently the MDC is under long term cosmic test, fully assembled and ready for the installation at FRS. Its performance is acceptable for the proposed experiments.

A Lamb-shift Polarimeter for a Molecular Beam Source in Novosibirsk

L. Huxold[a], M. Büscher[a,b], R. Engels[c], K. Grigoryev[c], D. Toporkov[d], Y. Shestakov[d]

A prototype of a source of polarized hydrogen and deuterium molecules has been developed at the Budker Institute of Nuclear Physics (BINP) in Novosibirsk. The Molecular Beam Source (MBS) is based on the Stern-Gerlach principle. First tests indicate that the separation of $\overrightarrow{H}_2$ and $\overrightarrow{D}_2$ molecules in the different nuclear spin projection states is possible [1]. To verify this, a direct measurement of the nuclear spin polarization is needed. A Lamb-Shift Polarimeter (LSP) is well suited for this purpose [2]. Therefore, an LSP has been built at the Institut für Kernphysik (IKP) of the Forschungszentrum Jülich. It has been shipped to Novosibirsk and first successful tests were performed.

An LSP consists of a Wienfilter, a cesium cell, a Spinfilter, and a quenching chamber. The Wienfilter is able to separate masses in the beam due to their different velocities at the same energy. In the cesium cell metastable hydrogen or deuterium atoms are produced in a charge transfer process with cesium vapor. The most important component is the Spinfilter, which is able to selectively transmit a single hyperfine state of the metastable atoms, while the other are quenched to the ground state. The transmitted metastable atoms are quenched to the ground state inside the quenching chamber and the emitted Lyman-α photons are counted with a photomultiplier. For this LSP an old Wienfilter has been refurbished at the IKP workshop, while the other components were newly constructed according to existing drawings at the central workshop of the Forschungszentrum Jülich.

The Spinfilter essentially consists of a solenoid and a cavity inside. The solenoid provides a magnetic field, which has to be variable between about 53.5 mT and 60.5 mT, while having a homogeneity of 10^{-3} or better, over the length of the cavity, throughout this range. In order to achieve the desired homogeneity several windings were added, where needed. A plot showing the relative deviation from the average magnetic field inside the cavity along the beam axis is given in Fig.1. The cavity has to be tuned to a resonant frequency of 1.60975 GHz and a FWHM of about 1 MHz. Additionally, it provides a static electric field, which couples the two (three for deuterium) $m_J = -1/2$ sub-states of the metastable hydrogen atoms to the short lived $2P_{1/2}$ state. The hyperfine states with total electron angular momentum projection $m_J = 1/2$ are coupled to the $2P_{1/2}$ state with a radio frequency in a cavity. At a magnetic field of 53.5 mT the radio frequency needed to couple the $2S_{1/2}$, $m_J = 1/2$, $m_I = 1/2$ state of the hydrogen atom to the $2P_{1/2}$ state matches the resonant frequency of 1.60975 GHz. Around the resonance the coupling between the two states becomes strong enough, that the atoms are trapped in an oscillation between these states and only a fraction can decay into the ground state.

Therefore, at 53.5 mT the $2S_{1/2}$, $m_J = 1/2$, $m_I = 1/2$ state of the hydrogen atom is transmitted through the Spinfilter while all other states are quenched to the ground state. Likewise the $2S_{1/2}$, $m_J = 1/2$, $m_I = -1/2$ state of the hydrogen atom is transmitted at 60.5 mT. For deuterium atoms $m_I = 1$, $m_I = 0$ and $m_I = -1$ states are transmitted at 56.5 mT, 57.5 mT and 58.5 mT respectively.

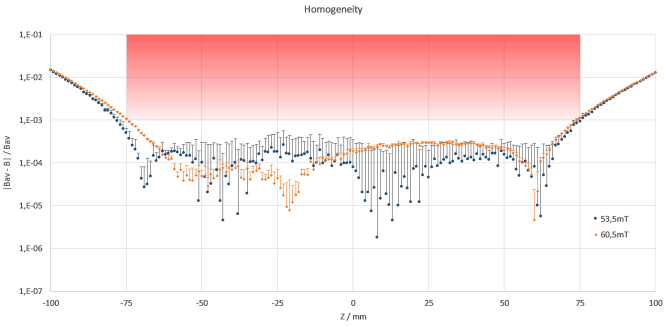

Fig. 1: The relative deviation from the average magnetic field inside the cavity along the beam axis for 53.5 mT and 60.5 mT. The cavity extends 75 mm on both sides of the center. The relative deviation is smaller than 10^{-3} throughout this region.

The LSP was assembled at the IKP in Jülich and then shipped to the BINP in Novosibirsk. In Novosibirsk it was unpacked at the experiment site and connected to an ionizer and the ABS, which is modifiable to the MBS. A picture of the LSP at the BINP is given in Fig. 2. All components of the LSP were tested, indicating, that the LSP is operational. Measurements with the ABS and the LSP started in the end of February 2019.

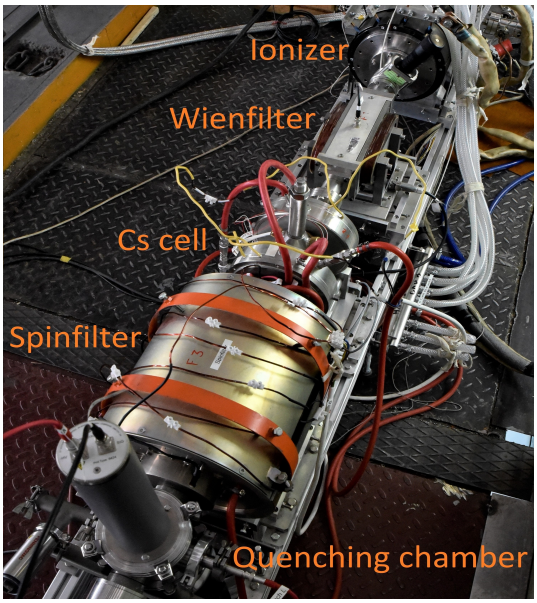

Fig. 2: The LSP at the experiment site in BINP.

References:

[1] D.K. Toporkov et al.; Nucl. Instrum. Meth. A **868** (2017) 15.
[2] R. Engels et al.; Rev. Sci. Instr. **85** (2014) 103505.

This work has been supported by the
DFG-RSF project 309228869,
http://gepris.dfg.de/gepris/projekt/309228869.

[a] Heinrich-Heine University Düsseldorf, Institute for Laser- and Plasma Physics, Germany
[b] Peter Grünberg Institute, Research Center Jülich, Germany
[c] Institute for Nuclear Physics, Research Center Jülich, Germany
[d] Budker Institute of Nuclear Physics, Russia

Status of the Polarized H_2, D_2 and HD molecule production

R. Engels, M. Büscher[a,b], S. Clausen, K. Grigoryev, L. Huxold[b], F. König, L. Kotchenda[c], P. Kravtsov[c], H. Ströher, V. Trofimov[c], and A. Vasilyev[c]

With polarized internal targets at COSY, double-polarized experiments were possible at ANKE and are still foreseen for PAX. The complicated gas target consists of a T-shaped storage cell that is fed with polarized atoms from an atomic beam source (ABS) based on the Stern-Gerlach experiment. The COSY beam can pass such a cell without wall interactions, while the target density is increased by a factor about 100 compared to a jet target. During the wall collisions of the polarized atoms, the polarization should be preserved in such a target. Nevertheless, several effects, e.g. the recombination of the atoms into molecules, can destroy the nuclear polarization and reduce the figure of merit of the scattering experiment. Therefore, in a collaboration of the PNPI[a], the PGI-6[c], and the IKP a setup was built to optimize the nuclear polarization in such a storage cell. For example, if the nuclear polarization would be preserved during the recombination process into molecules, the target density can be increased further. Besides the measurements of the molecular polarization [1, 2], it was observed that even polarized H_3^+ ions could be produced in our gold-coated storage cells (Fig. 1). To produce these ions, polarized H_2 molecules must interact with polarized H_2^+ ions to form the H_3^+ ions. Those ions are accelerated with an electric field of 1-2 keV together with polarized protons and H_2^+ ions into a Lamb-shift polarimeter to measure the nuclear polarization. A Wien filter in between is able to separate the masses due to the different ion velocities. In a Cs cell the ions react with the cesium vapor and produce metastable hydrogen atoms in different hyperfine substates, depending on the nuclear polarization of the incoming ions. Behind, a spinfilter is used to separate the atoms in the metastable substates so that at the end the amount of atoms in the different substates can be determined when the atoms are quenched into the ground state and the produced Lyman-α photons are counted with a photomultiplier. In Fig. 1 a Lyman-spectrum of the H_3^+ ions is shown. The intensity of the first peak corresponds to atoms with proton spin $+1/2$, the second peak to $-1/2$ orientation. From the intensity ratio the nuclear polarization could be determined as $P = -0.23$. This value fits perfectly to the polarization of the molecules that was about $P = -0.25$ during these experiments. Therefore, within the accuracy of our measurements no nuclear polarization was lost during the process $H_2 + H_2^+ \rightarrow H_3^+ + H$.

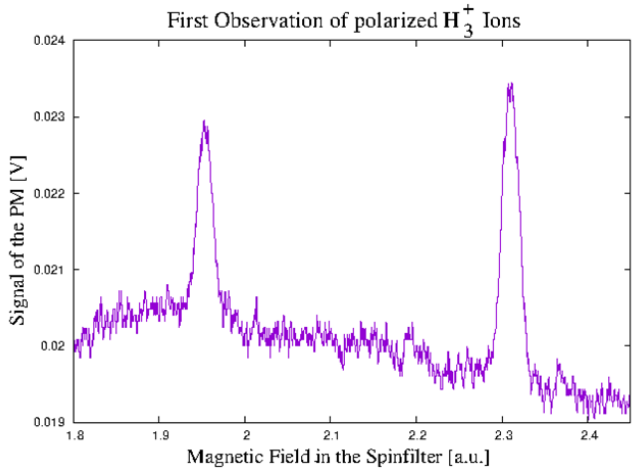

Fig. 1: A Lyman-α spectrum of the Lamb-shift polarimeter for H_3^+ ions. The resulting nuclear polarization was measured to be $P = -0.23$, which corresponds to the polarization of the H_2 molecules during these measurements.

In more recent experiments, the influence of a nickel surface was studied. Due to unexpected amounts of water on the surface, the recombination was suppressed and only atoms could be observed in the storage cells. As a ferromagnetic material, the magnetic domains on the surface may produce large gradients between them, which should destroy the polarization during wall collisions. Only when the nickel would be saturated by an external magnetic field B of about 0.7 T and the surface homogeneously magnetized, the polarization of the atoms should be preserved. Figure 2 shows such a measurement of the absolute nuclear polarization value of the atoms in the hyperfine substates 1 and 3 as a function of the external magnetic field B.

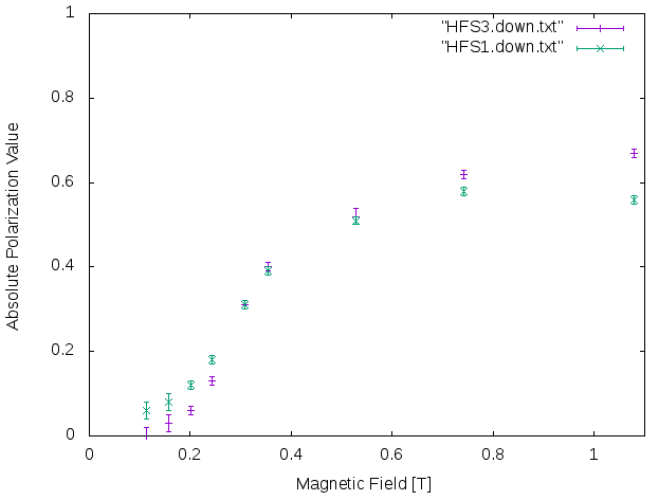

Fig. 2: Measured polarization of hydrogen atoms in the hyperfine substates 1 (green) and 3 (magenta) as function of an external magnetic field in a nickel-coated cell.

References:

[1] R. Engels et al.; Rev. Sci. Instr. **85** (2014) 103505.
[2] R. Engels et al.; Phys. Rev. Lett. **115** (2015) 113007.

[a] Peter-Grünberg Institut (PGI-6), FZ Jülich, Germany
[b] Institut für Laser- und Plasma-Physik, Universität Düsseldorf, Germany
[c] Petersburg Nuclear Physics Institute (PNPI), Gatchina, Russia

A new type of laser-induced polarized proton source

R. Engels, J. Böker, M. Büscher[a,b], I. Engin[a], O. Felden, R. Gebel, K. Grigoryev, A. Hützen[a,b], L. Huxold[b], Chr. Kannis[c], A. Lehrach, P. Rakitzis[c], D. Sofikitis[c], and C. Zheng[d]

The polarized proton/deuteron source at COSY is in use since more than 20 years. It consists of a polarized atomic beam source, based on the Stern-Gerlach effect, that can produce a beam of hydrogen/deuterium atoms with polarization values up to 0.9. But the intensity of such a source is limited to about 10^{17} atoms/s. When these atoms are ionized, either into polarized protons or H^- ions like at COSY, some polarization is lost and the intensity of the ion beams are limited and could not exceed 100 μA for protons up to now. Only with "optically pumped" methods, based on laser-excitation of hydrogen atoms, it was possible to get proton beams with higher intensities and similar polarization. But for deuterons this method did not work up to now.

Meanwhile, P. Rakitzis and his group at the University of Crete proposed another method of optical pumping via non-equilibrium states [1]: An HCl gas is injected into the interaction chamber by a standard gas nozzle with a high-speed short-pulse piezo valve that can be operated at 5 bar inlet-gas pressure to produce a gas density in the range of 10^{19} atoms/cm^3. Few millimeters below the nozzle, the interaction between gas and laser beams takes place (see Fig. 1). The polarizing laser system is a pulsed Nd:YAG laser. Its peculiarity is the quasi-simultaneous output of the fundamental wavelength at 1064 nm and the fifth harmonic (213 nm). The repetition rate of the laser system is 5 Hz and the pulses are of 170 ps duration, which is sufficiently short with regard to the transfer time of the electron spin polarization to the nucleus due to hyperfine interaction ($\sim$ 1 ns). The linearly polarized 1064 nm beam with a pulse energy of 100 mJ is focused with an intensity of $\sim 5\times10^{13}$ W/cm^2 into the interaction chamber to align the HCl bonds. By this, the signal intensity is increased and the amplification factor is calculated to be about 2. At the same time but under a 90 angle, the circularly polarized fifth harmonic with an energy of 20 mJ is also focused at an intensity of 10^{12} W/cm^2 into the vacuum chamber to interact with the HCl gas. The aligned HCl molecules are photo-dissociated by UV excitation via the $A^1\Pi_1$ state, which has a total electronic angular-momentum projection of $\Omega = +1$ along the bond axis. Hence, the resulting H and Cl photofragments conserve this +1 projection of the laser photons, producing H and Cl atoms each with the projections of approximately $m_s = +1/2$ (so that they sum to +1), and thus the H-atom electron spin is fixed to $m_s = +1/2$. In a weak magnetic field (Zeeman region), all H atoms are in a coherent superposition of the total angular momentum states $|F, m_F>$ with the coupling $F = S + I$ of the electron spin S and the nuclear spin I. When the electron spin is fixed due to the polarization of the incident laser beam, e.g., $m_s = +1/2$, then only the spin combinations $|m_s = +1/2, m_I = +1/2>$ and $|+1/2, -1/2>$ can be found in the free hydrogen atoms. The hyperfine state $|+1/2, +1/2> = |F = 1, m_F = +1>$ is an eigenstate and will stay unchanged in time. Since the states $|-1/2, +1/2>$ and $|+1/2, -1/2>$ are not eigenstates, they will be expressed as linear combinations of the eigenstates $|F = 1, m_F = 0>$ and $|F = 0, m_F = 0>$, which have different energies. Therefore, atoms produced in the $|+1/2, -1/2>$ state will oscillate to the $|-1/2, +1/2>$ state and back. If now the electron-polarized hydrogen atoms are produced during a very short time t $<$ 1 ns, they will oscillate in phase. Therefore, after 0.35 ns only the spin combinations $|+1/2, +1/2>$ and $|-1/2, +1/2>$ are found. This means that the electron polarization of the hydrogen atoms, produced by the laser beam, is transferred into a nuclear polarization. If now the hydrogen atoms are ionized and accelerated, the induced protons will remain polarized.

Fig. 1: The experimental setup (from left to right): The Nd:YAG laser inside a shielding box, laser optics, interaction chamber with pulsed nozzle, ionizer, and the components of the Lamb-shift polarimeter.

Within the JuSPARC/ATHENA project a collaboration of the PGI-6, the IKP and the University of Crete is preparing a proof-of principle experiment of this method at IKP [2]. In a first step we will resign the ionization of the polarized atoms in time, i.e. the atoms in the state $|-1/2, +1/2>$ will not oscillate in phase any more after the time of flight from the interaction point to the ionizing volume ($\sim 10^{-5}$ s) inside the electron-impact ionizer. When now these atoms are ionized, the nuclear polarization is about 0. But the polarization of the atoms in the eigenstates $|+1/2, +1/2>$ stay unchanged in time, so that the total expected polarization of the produced protons should be in the ideal case $P = 0.5$. This value and the intensity of the produced proton beam will be measured and optimized with the following Lamb-shift polarimeter [3]. As next, deuterated halides like DI or DBr can be used to produce polarized deuteron beams with the same laser setup. Following, the polarized hydrogen/deuterium atoms can be ionized and ac-

celerated with another intense laser with a short time delay of 0.35 ns. For example, the powerful SULF laser in Shanghai (10 PW) offers the opportunity to get with this method pulsed polarized proton beams in the GeV energy range. If the polarized atoms are just ionized with a much simpler laser system, the produced hyperpolarized proton/deuterons can be collected and accelerated with electrostatic fields. Here, more powerful lasers and more intense gas jets allow to increase the amount of the produced polarized proton beam. A development of such a new type of polarized proton/deuteron source based on our experience is under discussion with the Jefferson Lab.

References:

[1] D. Sofikitis et al.; Phys. Rev. Lett. **121**(2018) 083001.

[2] A. Hützen et al.; High Power Laser Science and Engineering (in print), DOI: 10.1017/hpl.2018.73.

[3] R. Engels et al.; Rev. Sci. Instr. **74**(2003) 4607.

[a] Peter-Grünberg Institut (PGI-6), FZ Jülich, Germany

[b] Institut für Laser-und Plasma Physik, Universität Düsseldorf, Germany

[c] University of Crete, Greece

[d] EMMI at GSI, Darmstadt, Germany

Integration of the COSY 2MeV Electron Cooler into EPICS

P. Niedermayer

1 Abstract

We report on the control system upgrade of the 2MeV electron cooler at the Cooler Synchrotron (COSY) at IKP.

An Input/Output Controller (IOC) was implemented to integrate the cooler into the the Experimental Physics and Industrial Control System (EPICS) based COSY control system, providing 1059 readout parameters of the cooler as EPICS Process Variables (PVs). Thereby archiving of the parameters of the electron cooler was achieved, which is crucial for data analysis and correlation. Furthermore, the status of the magnets of the electron cooler influencing proton orbit as well as the proton beam positions measured by the cooler BPMs were made available to the COSY control system. New GUIs were developed to monitor the cooler and control its magnet power supplies.

2 The 2MeV Electron Cooler

The 2MeV cooler at COSY is an electron cooler operating in the energy range from 0.025 MeV to 2 MeV with an electron current up to 3 A. [1]

A model of the cooler is shown in figure 1. The electron *gun*, *accelerating column* and electron *collector* are located in a SF_6 filled pressure vessel. In the gun, electrons are emitted from the BaO thermionic cathode. The electron current is controlled by a static voltage applied between the cathode and the anode. Electrons are then accelerated to their nominal kinetic energy in the accelerating column. The accelerating potential is thereby defined by 33 high voltage sections.

The magnetic field induced by solenoids and toroids is used to guide the electron beam through the vacuum pipe to the cooling section, where the electrons interact with the protons circulating in the ring. Since the electrons pass the cooling section only once, energy is transferred from "hot" protons to "cold" electrons, thus "cooling" the proton beam by reducing the momentum spread and transverse emittance. [2] After passing the cooling section, the electron beam is transported back to the pressure vessel, where the electrons are decelerated in the same high voltage sections that were previously used for acceleration (recuperation). The slow electrons then pass through a Wien filter and a suppressor module before they are trapped in the collector from where the current is returned to the electron gun.

For control of the electron orbit, 53 individually adjustable corrector coils are installed along the transport channel. 12 BPMs measure the electron orbit and the two in the cooling section additionally measure the proton beam position.

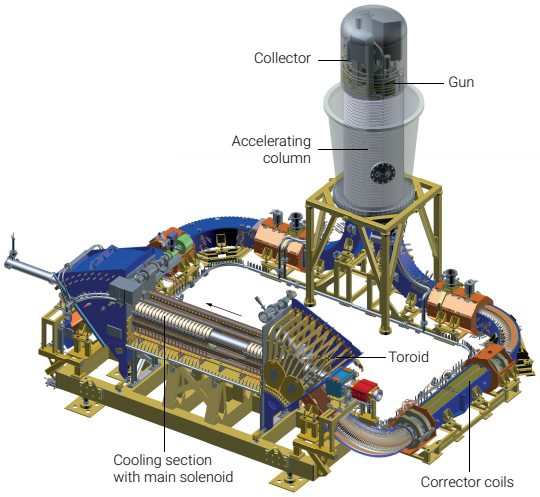

Figure 1: The 2MeV electron cooler at COSY

3 Control Systems of the Cooler

The 2MeV cooler consists of a number of systems for generation, handling and diagnostics of the electron beam as described in 2. Six different servers for control and readout of these systems are in operation:

- The **BPM** server for the 12 Beam Position Monitors along the beamline
- The **MPS** server for the corrector magnet power supplies
- The **PS server** for the main power supplies of the solenoids and toroids that provide the guiding magnetic field
- The **INTERLOCK** server for status bits of the interlock system as well as related analogue readouts
- The **ACC** server for the 33 high voltage sections and their auxiliary systems
- The **SGF** server for systems contained in or powering the the high voltage terminal (cascade transformer, anode, filament, grid, collector, suppressor and Wien filter)

Clients communicate with these servers using a set of SCPI-like commands to read out and set parameters. In addition, the ACC and SGF servers use a streaming mode where they continuously send out ADC data to connected clients.

The control system of the cooler was initially designed as a standalone solution and separated from the COSY control system. The servers are located in an isolated network. A dedicated computer running the graphical user interfaces (GUIs) was used to operate the cooler. Some of these GUIs allow to save the current set-points and restore them later, some parameter logs were saved as text files on the local machine.

4 EPICS IOC Development

The control system of COSY is currently being upgraded to EPICS. EPICS is a widely used and open source standard in the accelerator community, that benefits from good support and dedicated tools e.g. for displaying, archiving, saving and restoring various kinds of data.

Therefore the decision was made to include the cooler into the EPICS control system in order to benefit from these advantages. Access to certain systems of the electron cooler is then also possible from the COSY control system. This is especially helpful for the magnets, which have a direct influence on the proton orbit in COSY. In addition, the proton orbit measured by the cooler BPM can be used in the COSY control system. This improves the orbit correction software, which was previously lacking beam position measurements in this section.

For implementation of these changes, a gateway computer was installed between the isolated electron cooler and the COSY networks. This machine hosts an EPICS IOC that on one side communicates to the servers described above. On the other side the IOC serves EPICS process-variables (PV) to both networks.

The implementation was based on the EPICS modules *Stream* [3] and *AsynDriver* [4]. *AsynDriver* provides asynchronous communication to the servers while *Stream* was used for implementing the server specific protocols.

Each parameter of the electron cooler is represented by a PV with corresponding description, physical unit and range. The ADC and DAC values returned by the servers are converted to the corresponding physical quantity and published to the control system as PVs. Additionally, various status PVs are implemented. All PVs are continuously archived by the central archiving appliance which not only allows live display but also review of their history. Making use of EPICS alarm system, unusual or critical behaviour is alerted and passed to the COSY control system. The PVs for the proton orbit position are also being used by the orbit correction software.

Figure 2 shows an exemplary GUI for the power supplies of the main solenoids and toroids ("PS") and the corrector magnets ("CORRECTOR"). Given the PV prefix in the left column status, voltage and current of the power supplies are displayed. It is possible to switch the devices on or off and adjust nominal currents for multiple devices simultaneously.

5 Conclusion

During the upgrade process an EPICS IOC was implemented that provides most parameters of the 2MeV electron cooler. The following table gives an overview of the implemented process-variables

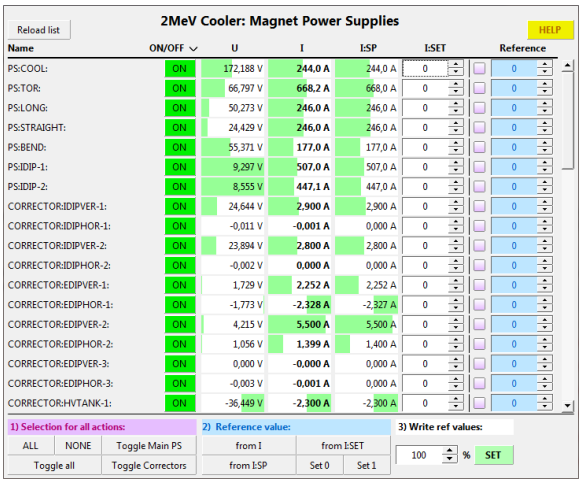

Figure 2: Screenshot of the GUI dedicated to readout and control of the electron cooler power supplies

Set parameters	**121**
Analogue (DAC)	60
Binary status	61
Readout parameters	**1059**
Analogue	632
Set-point (DAC)	70
Measured (ADC)	562
Binary status	368
Other	59
Other (raw values etc.)	887
Total number of PVs	**2067**

Readout of measured as well as set-point values was implemented for all systems of the electron cooler. Setting the parameters is currently implemented for the magnet power supplies only but is planned for all other systems as well.

Furthermore, it is planned to extend the capabilities of the cooler control software by using the newly implemented EPICS system. For example it is desired to automate the start-up-procedure and to have the ability to define arbitrary ramps for the electron current in respect to the COSY timing.

References

[1] **Features of cooling dynamics in a high-voltage electron cooling system of the COSY**, *Bryzgunov, M. I. and Kamerdzhiev, V. S. and Parkhomchuk, V. V. and Reva, V. B.*, 2015. In: Tech. Phys. 60 (8), S. 1227–1233.

[2] **2MeV electron cooler for COSY and HESR – first results**, *Kamerdzhiev, V. et. al.*, 2014. In: Proceedings of the 5th International Particle Accelerator Converence, IPAC2014, Dresden, Germany. DOI: 10.18429/JACoW-IPAC2014-MOPRI070

[3] **EPICS Stream Device**, *Paul Scherrer Institut*, `http://epics.web.psi.ch/software/streamdevice`

[4] **EPICS asynDriver**, *Mark Rivers*, `http://epics.anl.gov/modules/soft/asyn`

Correction of BPM electrical offsets and gain errors.

S. Merzliakov, I. Bekman, C. Böhme, V. Kamerdzhiev, T. Wagner, K. Reimers

Methods used to correct electrical offsets of COSY beam position monitors (BPM) and gain errors of the readout channels are described. The goal is to achieve the accuracy of beam position measurement of 1% or better. The implementation of the method consists of the introduction of additional gain coefficients, which are individual for each channel. These coefficients are used to fine tune the main gain settings. They were obtained by calculation of the influence of parasitic capacitances in the pickup - amplifier- systems. The corrections are implemented in the Libera [1] signal processors and in the accelerator control system.

Method

For beam position measurement at COSY a system of 30 pickups with 4 plates each is used. The position measurement is based on the principle of charge division between the two opposite plates. The simplified block diagram of the DAQ system for one sensor is presented in the fig.1.
The picture shows the pickup with 4 plates, connected to amplifiers; Libera [1] - Hadron Beam Position Processor; Beckhoff [2] – unit for control of amplifiers gain and parameters of the generators. The system includes also a power amplifier and a 1x4 splitter for in-situ tests and calibration. The amplifiers consist of two serially coupled amplifiers, the first has a fixed gain of 20 dB and the second has a variable analog controled gain from 0 to 50 dB.
A calculation of X and Y coordinates of beam center according to the Libera algorithm is carried out by the formulas:

$$X = Kx * \left(\frac{(V_L - V_R)}{(V_L + V_R)} \right) + X_{\text{offset}} \text{ and}$$

$$Y = Ky * \left(\frac{(V_U - V_D)}{(V_U + V_D)} \right) + Y_{\text{offset}}$$

Where V_L, V_R, V_U, V_D, are values of input signals after amplification and digitalization by Libera- ADC; Kx and Ky are geometry factors related to the sensitivity of the sensors (V/mm).
Boundary conditions of those expressions are equal to the transfer coefficients from the charge at the pickups to the digital data from ADCs for Right to Left and Up to Down pairs of channels. The factors determining the equivalence are also presented in the picture. These are Cs-calibration capacitors that transmit a test signal to the amplifier inputs, the Cp - capacitance of the pickups to the ground and the amplifications of the second stage of the amplifiers.
Since the accuracy of the gain setting for the second stage is only 5% and varies from chip to chip, the system uses the procedure of gain calibration by signals from the generator through the calibration capacitance Cs. Frequent repetition of the procedure ensures temperature and long-term stability of the system.
The calibration procedure consists of two steps. The first is to align the gains of horizontal and vertical pickups. The resolution of the system after this step is determined only by the noise parameters of the amplifiers and is close to 20μm. However, the absolute accuracy is determined by differences in the values of the Cs- capacitors. In the worst case, it amounts to ± 2 mm, which results from the fact that for the best capacitors the tolerance is $\pm 0.25\%$.
In order to make the absolute accuracy of measurements better than 1%, the offset correction method was proposed and used. This part of software implemented in the accelerator control system introduces additional gain corrections that are specific to each DAQ channel. These additional parameters included in the final beam coordinates are affected by the capacitors Cs and Cp of each pair plate - amplifier. These coefficients were pre-calculated based on individual measurements of transfer functions of amplifiers connected to pickups during their installation at COSY.
Briefly, the offset correction is done by measuring the transfer function with capacitance between opposite plates (C0_U-D and C0_L-R in fig. 1) as well as the series capacitance in the test signal path included. The serial connection of the generator signal to the pickup on one side and the amplitude measurement from the output "Pout" of the amplifier on the other side allows to carry out the measurement with equal charge at the amplifier inputs. The equality of the test charges simulates the situation of beam passage with zero offset relative to the pickup center.
The method is illustrated by fig. 2, where simplified diagrams are presented for measuring the transmission coefficients from the generator to the output "Pout" of the amplifier between Up and Down plates.
Final coefficients were calculated taking into account the results from precision measurements of transfer coefficients from the input of the 1x4 Splitter to the inputs of the amplifiers (see fig.1), these were calculated as:

$$Ks_i = \frac{U_{\text{Pout}_i}}{(U_{\text{gen}}) * 20dB};$$

Where i=(L,U,R and D);
If set that the additional coefficient K_r ane K_d equals 1 then the final formulas to calculate additional coefficient K_l and K_u are the following:

$$K_l = \left(\frac{Ks_l}{Ks_r} \right) * \left(\frac{Kc_r}{Kc_l} \right) * \left(\frac{(1 - Kc_l)}{(1 - Kc_r)} \right),$$

and

$$K_u = \left(\frac{Ks_u}{Ks_d} \right) * \left(\frac{Kc_d}{Kc_u} \right) * \left(\frac{(1 - Kc_u)}{(1 - Kc_d)} \right),$$

Where:

Ks_l – transfer coefficient from input of Splitter to input of Left-amplifier (see fig. 1);

Ks_r – transfer coefficient from input of Splitter to input of Right-amplifier (see fig. 1);

Kc_u – transfer coefficient from generator to input of Up-amplifier;

Kc_d – transfer coefficient from generator to input of Down-amplifier;

Ks_u – transfer coefficient from input of Splitter to input of Up-amplifier (see fig. 1);

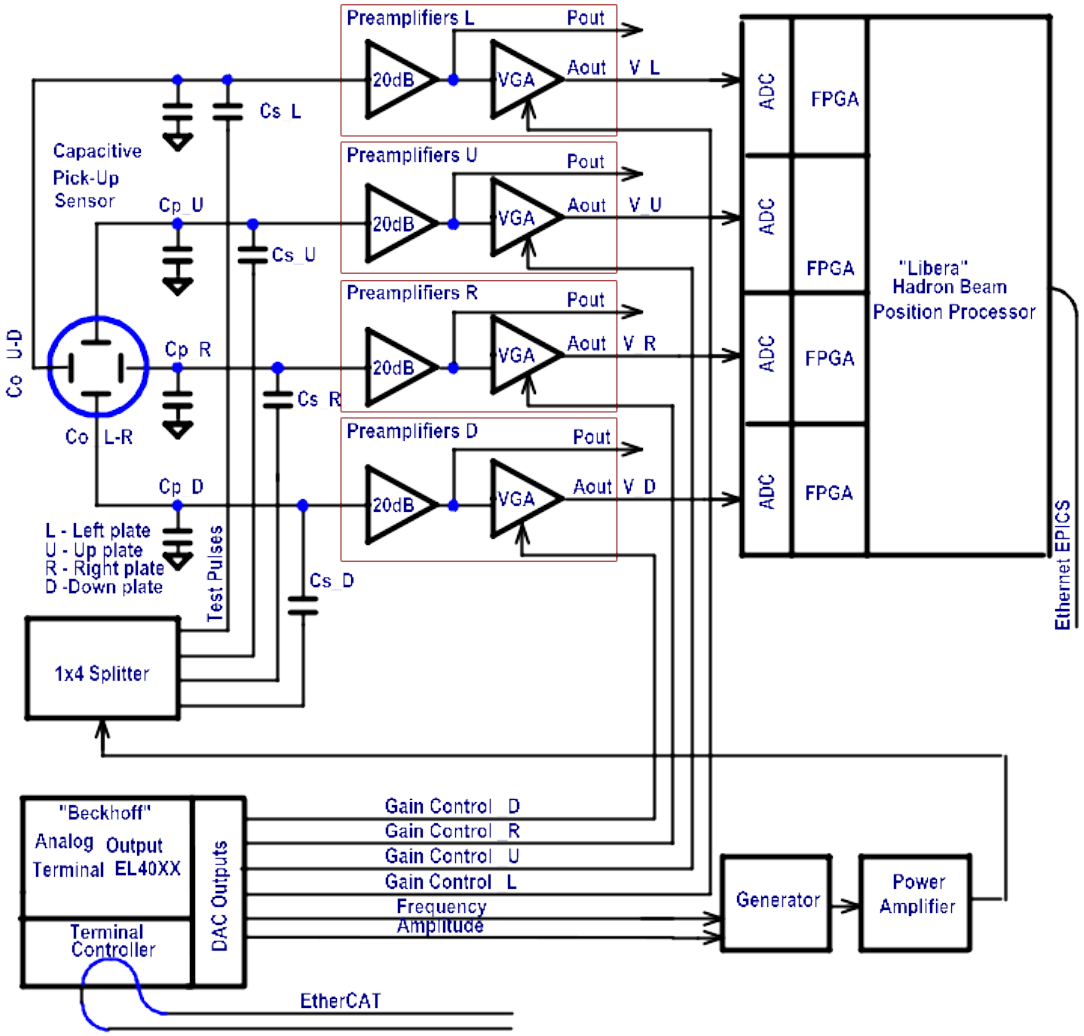

Figure 1: Block diagram of the DAQ of one BPM.

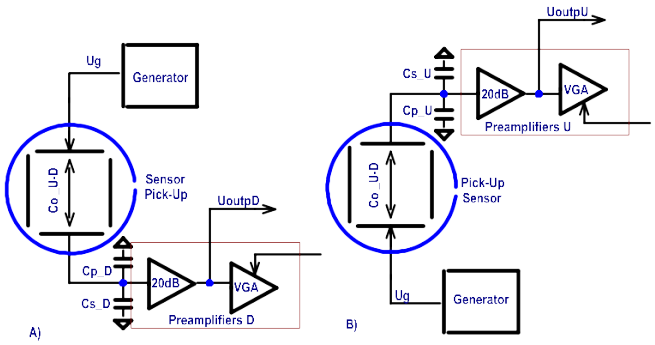

Figure 2: Block diagrams illustrating the measurements of transfer coefficients with capacitance between Up-Down plates of pickup included; a) –from Up to Down plate; b) - from Down to Up plate.

Ks_d – transfer coefficient from input of Splitter to input of Down-amplifier (see fig. 1);

Kc_u – transfer coefficient from generator to input of Up-amplifier, (see fig. 2 B);

Kc_d – transfer coefficient from generator to input of Down-amplifier (see fig. 2 A);

The offset correction method was checked on the test bench [4] and has shown good agreement of measured and calculated values - the center of pickups was determined with precision close 20μm

Software

For the routine BPM offset correction at COSY an Operator Interface (OPI) was developed to automate the process of correcting position bias for the individual gains of the pick-ups - before applicatoin of the factors described in previous section, which are held constant after commissioning.
The calibration routine uses the previously described signal from the generator to the amplifiers and the final position output from the Libera systems which is accessible via EPICS. The algorithm used to find the optimal gain setting for each BPM is a stepwise optimization and works as follows.
At first it turns on the generators in order to obtain a first measurement of the position, which should be optimized to zero. In the first step of the optimization it will compare the measured position to a threshold set by user. In case it is above the threshold it will adjust the gains of the amplifiers for that plane, to move closer to the zero position, by one user defined step. The gains of both amplifiers, up and down or left and right, are adjusted by lowering one and increasing the other by one step. This is done in order to not increase both gains to high values (and thereby increase the noise) in case the measurement is oscillating around zero but still above the

threshold.
This stepwise calibration is done for all BPMs until all of them are below the user defined threshold. In order to prevent an infinite execution, additional safety measures are applied, like not repeating an already used gain setting, as this would lead to an infinite loop. At the end of execution the user is informed which BPMs could be calibrated to zero.
This method of stepwise optimization is robust but rather slow. Thus the user is advised to execute it multiple times with different settings to speed up the calibration. The first execution should be with a larger threshold and larger step size and then reducing the threshold and step size until the desired precision or the noise level of the amplifiers is reached.

References

[1] **Libera Hadron, Hadron Beam Position Processor** , User Manual, Version 1.01. Instrument Technologies Velika Pot 22, SI-5250 Solkan, Slovenia.

[2] **EtherCat standard**, https://www.beckhoff.com/english.asp?fieldbus_components/system_ethernet_ip.htm

[3] **GainZeroSearch**, https://gitlab.cce.kfa-juelich.de/BCC/BPM/GainZeroSearch

[4] **Beam Diagnostics for the High Energy Storage Ring at FAIR**, C. Böhme et al. , DOI:10.18429/JACoW-IBIC2015-MOPB014

Tools for software development at COSY

I. Bekman, C. Böhme, P. Niedermayer, M. Simon, M. Thelen

In 2018 a set of tools was made available at IKP-4 for software development at COSY. The goal is to have a centralized infrastructure to improve collaboration on code development, quality control and integration of software. In addition a central infrastructure for e.g. storage of manuals, decription of practices and conventions needed to be established, as in the past they were scattered over several storage systems or were available on paper only.
The newly established tools are used to improve software work flow, but also for documentation and collaboration on scientific publications, as well as issue tracking for both software and hardware. Another usage case is the continuous integration, testing, and deployment of productive code at COSY. Additionally the development environment training delivered by Cosylab is discussed.

Software for COSY

The core requirements for system and software development were defined as:

- Versioning system
- Documentation system
- Issue tracking system
- Group management system

The existing software infrastructure for COSY was assessed and it was found that there are several tools available:

- `Elog`[1] - Electronic logbooks for operators, groups' and experiments' records, ephemeral data and state of the machine
- Accelerator Wiki - `wiki` [2] containing information relevant for accelerator operation
- Controls Wiki - `wiki` [2] for more technical information with a strong emphasis on controls
- `Internal Web Page` - storage of documentation, minutes etc. Only write accessible to a few staff members
- `Seafile` - cloud server, institute internal
- `Sciebo` - cloud server, federal state wide
- `SVN` server - software versioning

The assessment showed that there is a large number of places where information can be stored making it time consuming to find the required data.
A set of requirements was generated in collaboration with the Cosylab company [3] . As a result the decisive requirements were established:

- modern software versioning system based on `git`[4]
- issue tracking integration with group structure and versioning system
- minimum number of instances to search for information
- clear usage and broad user acceptance
- collaboration with external groups and companies
- integration with `EPICS`[5] control system at COSY, optimally with `CI/CD` principle (Continuous Integration and Continuous Development)

Software Platform

The final toolset includes:

- `GitLab EE` [6], separate instance at IKP4: [9]
  - versioning and collaboration are done in one place
  - reuse of code and solutions is encouraged, independently if for EPICS, GUIs or other
  - documentation is grouped with the code, but can also be linked in a common wiki [**?**]
  - elog is synced regularly to and legacy wikis are transferred to the GitLab
  - issue tracking is performed "close" to the source code
  - collaboration on latex papers
  - search over source code, documentation, wiki pages, elog, issue tracking and discussions is performed in a single instance
  - mirroring of external code allows in-house-hosting of crucial infrastructure
  - CI/CD allows running of processes independently of the user machine, e.g. compiling of cross-platform applications, creating PDFs, running scheduled code execution, delivering binary code to production systems
- `Elog`:
  - Robust and easy to use tool
  - Well known by users
  - Back-end API allows scripting and integration with other tools
- `Redmine` [7]
  - Project management software
  - Suitable for group management tasks
  - Cross-integration with GitLab possible
  - Import and export filters to MS Project available
  - Provided by ITS of FZ-Juelich, therefore limited configuration possibilities by IKP.

Several `CI/CD` tools were written for transition from the original to the final configuration

Development Environment Training

A set of documents [10] was written outlining the processes mentioned in the first chapter, with detailed instructions for best practice in context of software development, production and EPICS integration. In November 2018 a one week training[11] for developers, operators and machine supervisors was successfully held at IKP by Cosylab covering the topics listed above as well as the group management software and EPICS graphical interface [8] development. As the workshop was open for all FZJ members, some colleagues from other institutes joined the event.

References

[1] **ELOG**, S. Ritt, `https://elog.psi.ch/elog`
[2] **MediaWiki**, `https://www.mediawiki.org`
[3] **Cosylab d.d.**, `https://www.cosylab.com`
[4] **git**, `https://git-scm.com`
[5] **"Experimental Physics and Industrial Control System"**, `http://www.aps.anl.gov/epics`
[6] **GitLab**, GitLab Inc., `https://about.gitlab.com`
[7] **Redmine**, `https://www.redmine.org`
[8] **Control System Studio**, `http://controlsystemstudio.org`
[9] **GitLab at IKP**, `https://gitlab.cce.kfa-juelich.de`
[10] **GitLab at IKP: Conventions**, `/Processes/Conventions`
[11] **GitLab at IKP: Training**, `/Processes/trainings/Training`
[12] **GitLab at IKP: wiki**, `/wiki/IKP/`

Track Reconstruction and Particle Identification in the P-349 Antiproton Polarization Experiment

D. Alfs, D. Grzonka, J. Ritman
Institut für Kernphysik, Forschungszentrum Jülich

TOWARDS A POLARIZED ANTIPROTON BEAM

Proposed preparation methods:

- spin filtering - not yet tested for antiprotons
- Λ decay into polarized $\bar{p}$ - high $\bar{p}$ momenta, high emittance

Physics with polarized antiprotons

- $\bar{p}p$ polarized cross section
- QCD proton spin structure
- $\bar{p}p$ annihilation at rest
- antiprotonic atom spectroscopy

POLARIZATION MEASUREMENT

Polarization is going to be determined from left-right asymmetry of scattering on a liquid hydrogen target in the CNI region.

For a transversely polarized beam:

$$\sigma = \sigma_0(1 + A_y P \cos\phi)$$

Expected $A_y = 4.5\%$ for the scattering in the CNI region (θ_{LAB} = 10 - 20 mrad).

⇒ **Track resolution ~1 mrad and reliable PID**

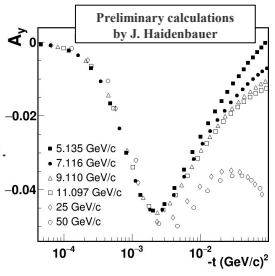

EXPERIMENTAL SETUP

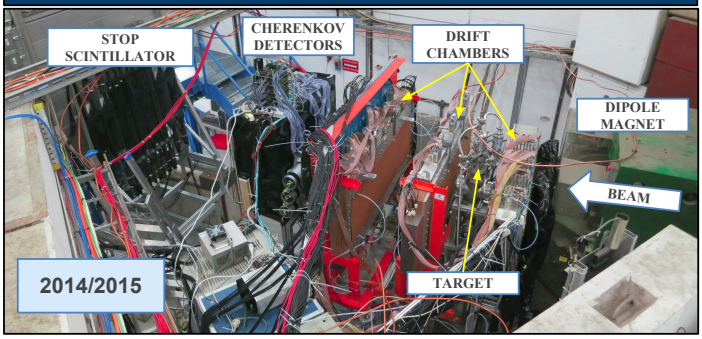

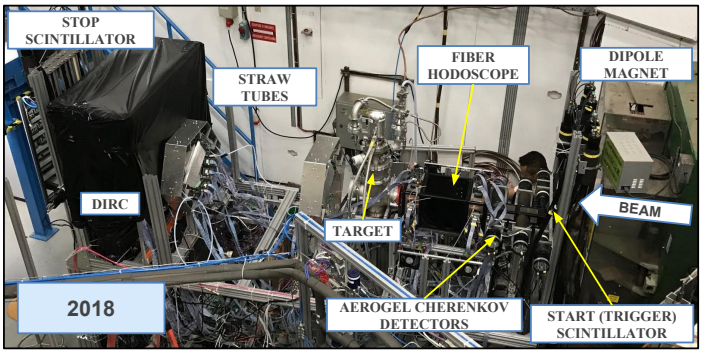

PARTICLE IDENTIFICATION

- **Light propagation in DIRC depends on the track angle and position.**
- **Detailed MC simulations are needed for reliable particle identification.**

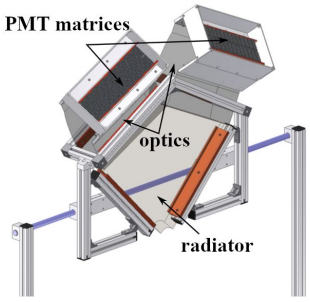

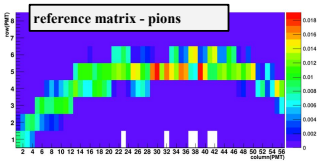

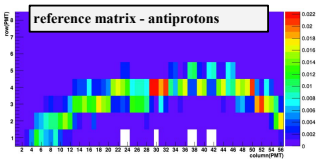

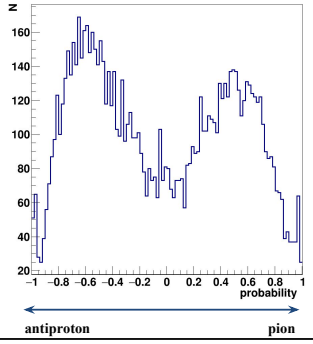

TRACK RECONSTRUCTION (2014/15 setup)

- **drift time - space calibration - $\sigma \sim 150 - 300\ \mu m$**
- **fine tuning of the relative positioning of drift chambers**

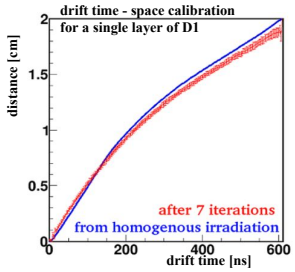

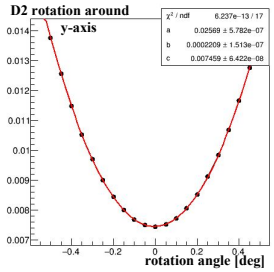

- **track resolution:**
  current upper limit ~5 mrad
  ⇒ improvements possible

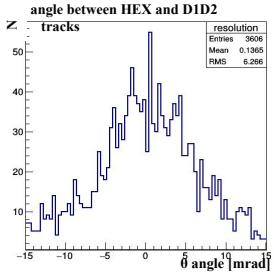

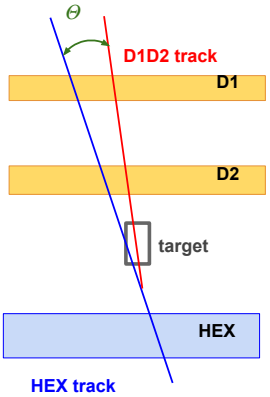

Summary and outlook

- Improvement of the drift time - space calibration for individual cells.
- Event based PID using position and angle dependent reference matrices.
- Analysis of 2018 data (preliminary results show position resolution in the straw tubes < 100 μm).

This work was supported by the Polish Ministry of Science and Higher Education and DAAD from resources of Bundesministerium für Bildung und Forschung (BMBF) and by Marie Sklodowska-Curie Innovative Training Network Fellowship of the European Commission's Horizon 2020 Programme (No. 721559 AVA).

Federal Ministry of Education and Research

DESIGN OF A DETECTOR FOR STUDIES OF S = −2 BARYON INTERACTION INDUCED BY STOPPED ANTIPROTON ANNIHILATION

Dominika Alfs[1,2], Dieter Grzonka[2]

1) Faculty of Physics, Astronomy and Applied Computer Science, Jagiellonian University in Kraków, Poland
2) Institut für Kernphysik, Forschungszentrum Jülich, Germany

JÜLICH Forschungszentrum

JAGIELLONIAN UNIVERSITY IN KRAKÓW

MOTIVATION

➤ **study of Y-N and Y-Y interaction** - database limited [1,2], baryon-baryon interaction of S = −2 system important for better understanding of SU(3) flavor symmetry and **H-Dibaryon search** (H : [uu dd ss]) [3,4]

➤ availability of low energy, phase space cooled antiproton beam with ELENA and FLAIR

PRODUCTION OF S=−2 SYSTEMS VIA DOUBLE STRANGENESS EXCHANGE REACTION

optimum condition for interacting Ξ-N system: **recoil free Ξ production [5,6]**

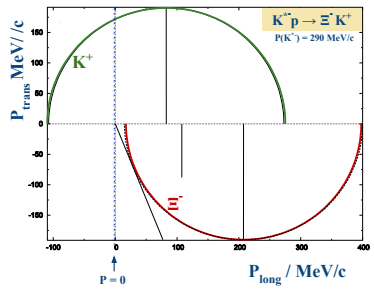

K* from annihilation of stopped antiprotons - well suited for recoil free Ξ production

step 1: $\bar{p}p \rightarrow \bar{K}^{*-}K^{*+}$ (BR: $6\cdot10^{-3}$)

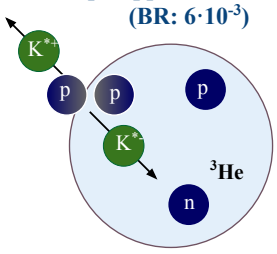

large $\bar{p}$ stop rate on a ^{3}He target

step 2: $K^{*-}n \rightarrow \Xi^- K^0$

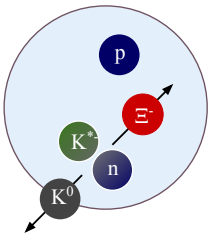

very low recoil on Ξ⁻ (recoil free kinematics)

S = −2 states

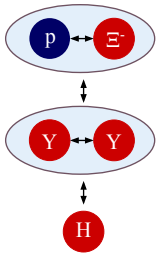

low relative energy

TRIGGERING

primary reaction (step 1 + step 2)

multiplicity of charged particles

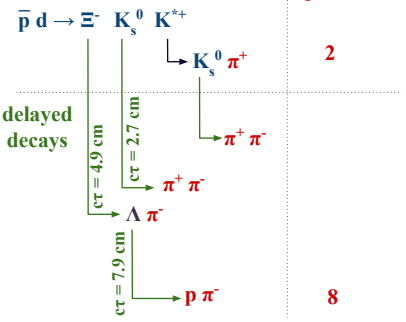

DETECTION PRINCIPLE

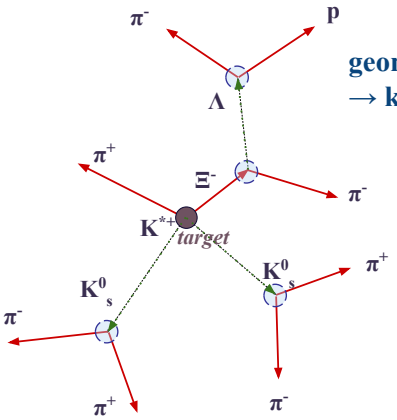

geometry
→ kinematical complete event reconstruction

measurement of charged particle tracks
reconstruction of decay vertices
reconstruction of neutral particle tracks

first step: determination of $\sigma(K^*N \rightarrow K\Xi) / \sigma(K^*N \rightarrow X)$

BASIC DETECTOR DESIGN

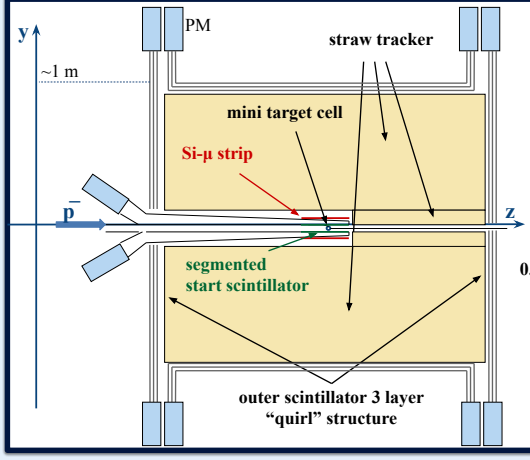

➤ goal: detector geometry close to 4π

➤ vertex and tracking detectors necessary (e.g. Si-μ strip and straw tubes; Ξ detection efficiency at 1cm: ~35%)

➤ antiprotons need to be stopped within a small target volume

➤ low energy (about 1 MeV), low emittance antiproton beam needed

0.01 mm Mylar foil

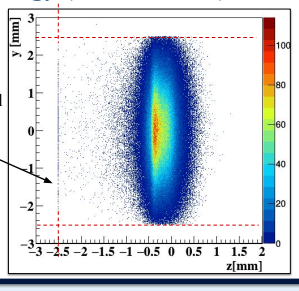

Stopping of 0.7 MeV antiproton beam ($\sigma_{x,y}$=1 mm) in the gaseous ^{3}He target cell (T = 20 K, p = 1 bar, r = 2.5 mm)

GEANT4 simulations (Physics List: QGSP_BERT)

References
1. J.A.Kadyk st al.,
2. Eisele Phys. Lett. 37B, 205 (1971)
3. R.L. Jaffe, PRL 38, 195-198 (1977)
4. T. Sakai et al., Prog.Theor.Phys.Suppl., 137, 121 (2000).
5. D. Grzonka et al., AIP Conf. Proc. 793 (2005) 190.
6. K. Kilian, Proc. 4th LEAR Workshop (1988).

Drift chamber calibration and track reconstruction in the P-349 Antiproton Polarization Experiment

D. Alfs[1,2], D. Grzonka[2], M. Zieliński[1] for the P-349 Collaboration

1) Faculty of Physics, Astronomy and Applied Computer Science, Jagiellonian University in Kraków, Poland
2) Institut für Kernphysik, Forschungszentrum Jülich, Germany

TOWARDS A POLARIZED ANTIPROTON BEAM

Physics with polarized antiprotons

- $\bar{p}p$ polarized cross section
- QCD proton spin structure
- $\bar{p}p$ annihilation at rest
- antiprotonic atom spectroscopy

Proposed preparation methods:

- spin filtering - effortful, not yet tested for antiprotons [1]
- $\bar{\Lambda}$ decay into polarized $\bar{p}$ (45%) - high $\bar{p}$ momenta [2]

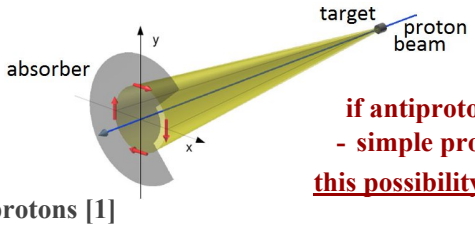

if antiproton production is polarized - simple production method available.

this possibility has never been tested [3,4].

POLARIZATION MEASUREMENT VIA ELASTIC SCATTERING IN THE CNI REGION

Polarization is going to be determined from left-right asymmetry of scattering on a liquid hydrogen target.

For a transversely polarized beam:

$$\sigma = \sigma_0 (1 + A_y P \cos\phi)$$

Expected $A_y = 4.5\%$ for the scattering in the CNI region (θ_{LAB} =10 - 20 mrad).

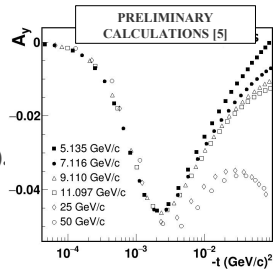

⇒ **Track resolution ~1 mrad and reliable PID needed.**

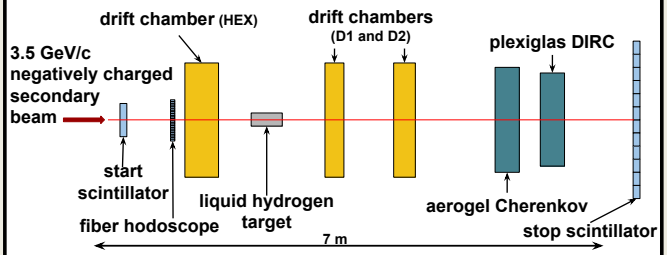

Measurement at the East Area of the CERN/PS.
$\bar{p}$ production: 24 GeV proton beam on a solid target.

PID WITH PLEXIGLASS DIRC

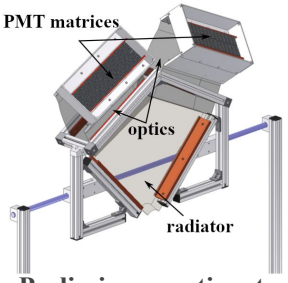

Reconstruction only for a part of the Cherenkov is ring possible.

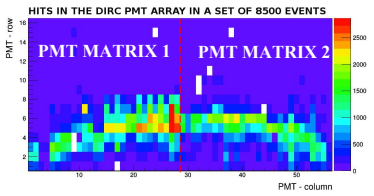

Preliminary antiproton - pion identification with DIRC distribution of Cherenkov arc maxima

triggered event sample

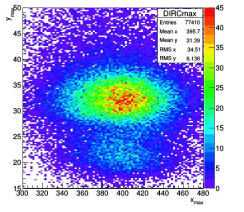

additional cut on aerogel Cherenkov

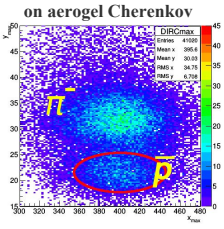

triggered event sample cut on aerogel Cherenkov

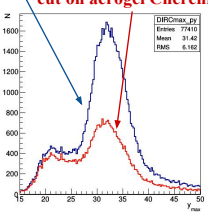

- Light propagation in DIRC depends on the track angle and position.
- Detailed MC simulations are needed for reliable particle identification on an event by event basis.

TRACK RECONSTRUCTION

- drift time - space calibration - position resolution 150 - 300 μm
- fine tuning of the relative positioning of drift chambers

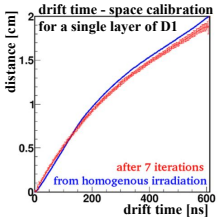

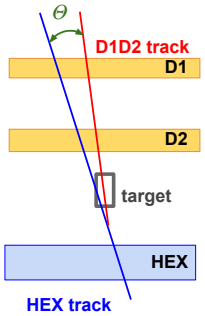

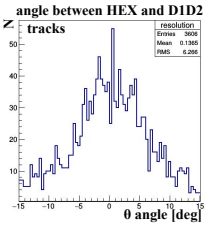

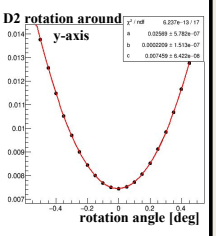

Current track resolution: about 5 mrad (θ)
⇒ improvements still possible

OUTLINE

- Focus of the ongoing analysis: improvement of the track resolution and MC studies for PID in DIRC.
- New measurement scheduled for summer 2018.

References

1. PAX collaboration, arXiv 0904.2325 [nucl-ex] (2009)
2. A. Bravar et al. Phys. Rev. Lett. 77, 2626 (1996)
3. K. Kilian, et al., Int. J. Mod. Phys. A 26 (2011)
4. D. Grzonka, et al., Acta Phys. Polon. B 46 191 (2015)
5. J. Haidenbauer, private communication

ACKNOWLEDGEMENTS

This work was supported by the Polish Ministry of Science and Higher Education and DAAD from resources of Bundesministerium für Bildung und Forschung (BMBF), by Marian Smoluchowski Kraków Research Consortium "Matter–Energy–Future (KNOW) and the Polish Ministry of Science and Higher Education through grant number 7150/E-338/M/2018.

Simulations of Excited Hyperon Production with the PANDA Phase-0 Measurements at HADES

Waleed Esmail and James Ritman for the HADES Collaboration

JÜLICH Forschungszentrum

Motivation

The electromagnetic (EM) decay of bayrons provides detailed information on their underlying structure. **Interactions of real and virtual photons** with electric charges of the quark fields provide unique information about the quark structure of hadrons and about phenomenological parameters describing their form factors.

Comparison of data for the **EM decay** of decuplet hyperons, Σ^*, to the predictions of quark models provides a measure of the importance of meson cloud diagrams in the $\Sigma^* \rightarrow Y\,\gamma$ transition.

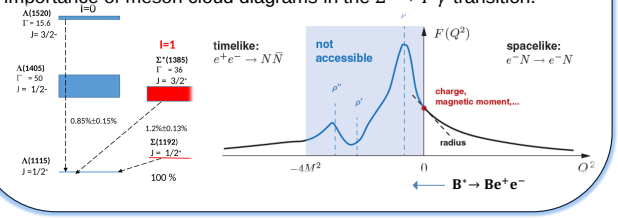

HADES Spectrometer

The **H**igh **A**cceptance **D**i-**E**lectron **S**pectrometer (HADES) is located at GSI Helmholtzzentrum für Schwerionenforschung GmbH in Darmstadt, Germany. It is a fixed target experiment focusing on the measurement of heavy ion reactions and proton and pion induced reactions. The detector has very good performance on the identification of hadrons and electrons, which opens the door to research on strangeness physics and electromagnetic transitions.

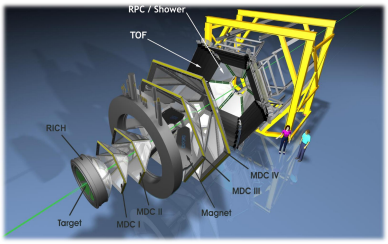

HADES Forward Detector

With the start of FAIR Phase-0 program many of the detector systems will be replaced/upgraded. Of particular importance to hyperon reconstruction is the new **F**orward **D**etector (FD) extending the acceptance to polar angles of 0.5º to 6.5º.

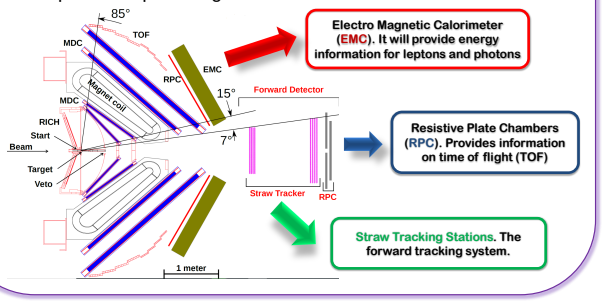

Straw Tracking Stations(STS)

The forward tracking system consist of two stations, each composed of 8 layers of self-supporting straw tubes. They are currently assembled by the Jülich and Krakow groups, based on developments for the PANDA forward tracker. The system consists of two stations STS1 and STS2 each consisting of two double layers.

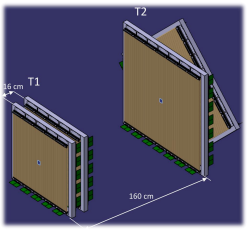

Hyperon Simulation

1. Pluto simulation of the signal

$p(4.5GeV)p \rightarrow \Sigma(1385)K^+p$, with $\Sigma(1385) \rightarrow \Lambda\gamma$.

2. Particle Identification (PID)

- Charged Particle Identification (PID) combines the energy loss or velocity.
- Photons are identified as energy cluster in the EMC with no tracks associated and β close to 1.

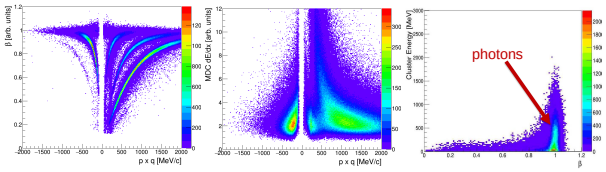

3. Lambda Reconstruction

- Lambdas can be reconstructed in either HADES or the FD.
- Considering energy and momentum conservation protons from Λ decay should fly almost in the same direction as Λ. So the FD will significantly improve the Λ reconstruction.

$\Lambda \rightarrow p\pi^-$

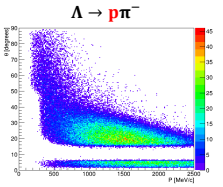

- At HADES Lambdas are reconstructed by adding the four momentum of p and π^-.
- For Lambda reconstruction at the FD, π^- tracks from HADES and p tracks from the FD are combined, the minimum distance between these tracks is calculated, pairs with distance less than 10 mm are considered Lambda candidates.

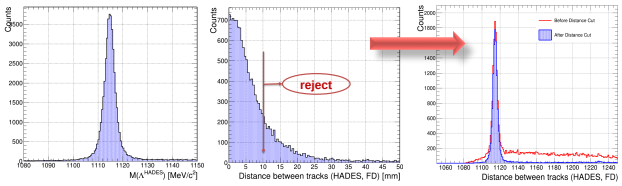

4. Sigma Reconstruction:

- $\Sigma(1385)$ can be reconstructed with efficiency ~ 3%.
- An estimation of the number of reconstructed Σ(1385) for pp at beam kinetic energy E=4.5GeV, 28 days of beam time and instantaneous luminosity $\mathcal{L} = 2 \times 10^{31} cm^2 s^{-1}$ is:

68,000 Σs

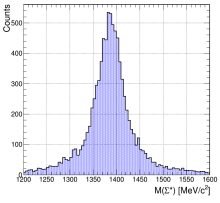

References:

1. CLAS Collaboration. (2011). Physical Review D - PHYS REV D. 83.
2. CLAS Collaboration (2011). 10.1103/PhysRevD.85.059903.
3. HADES Collaboration (2009). European Physical Journal A.
4. HADES Collaboration (2017). Proposal for experiments at SIS18 during FAIR Phase-0.
5. Krzysztof Nowakowski (2018). Simulations for hyperon decays with HADES, Workshop on two-pion and e+e- production in hadronic reactions.

Matter and Universe Days 2019
14-15 February 2019

DESY.

The EDM Polarimeter Development at COSY-Jülich

Fabian Müller
Institut für Kernphysik (IKP), Forschungszentrum Jülich
III. Physikalisches Institut B, RWTH Aachen

Principle / Method

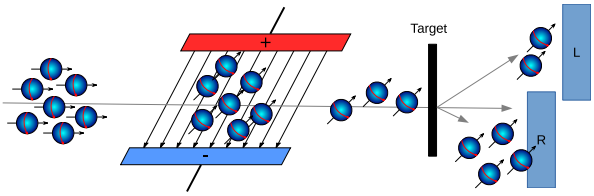

- Apply **electric field** $\vec{E}$ to particles in strorage ring
- Finite EDM $\vec{d}$ **rotates spin** out of horizontal plane
- Measure vertical **polarization build-up** $\frac{d\vec{s}}{dt} \propto \vec{d} \times \vec{E}$

Concept

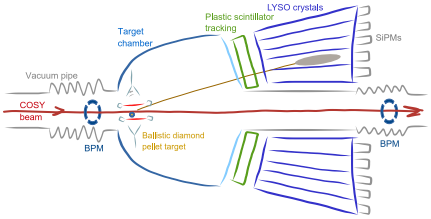

- Energy measurement without magnetic fields
- Continuous on-line operation with high efficiency
- Spin rotation measurement (~ 1 μrad/s for 10^{-26} e·cm)

LYSO Modules

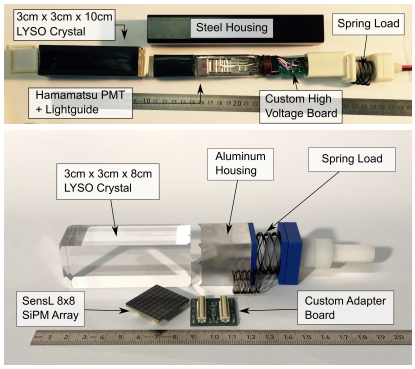

Version I
Hamamatsu PMT
~ 1000 V supply

Version II
Sensl SiPM
~ 29 V supply

Tests at COSY

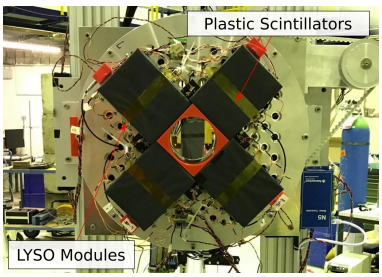

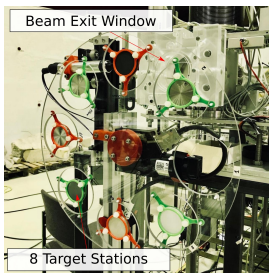

- Detector tests with external beam
- Target materials C, Si, Al, Sn and Mg

Results

- Clean PID using ΔE *vs* E

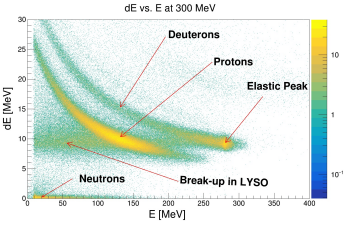

- High energy resolution ~ 1 %

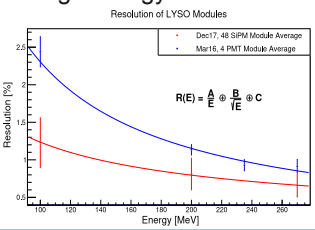

- Bragg-Peak measurement

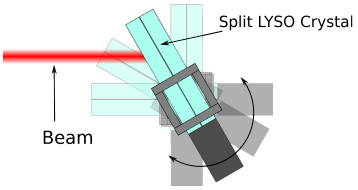

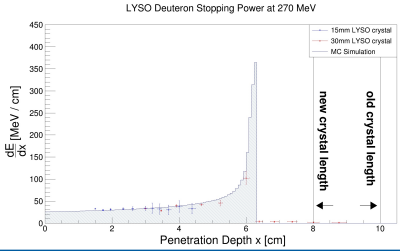

- Triangular ΔE Position Reconstruction

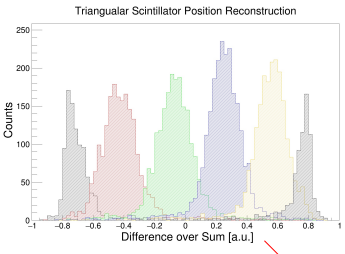

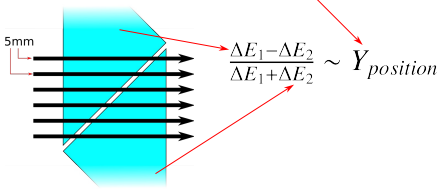

Electrostatic Deflector Development

Dr. Kirill Grigoryev
Institute for Nuclear Physics (IKP)
for JEDI collaboration

MOTIVATION

Precision experiments like, search for the permanent electric dipole moments (EDM) with polarized protons or deuterons, require a dedicated electrostatic or combined electro-magnetic storage ring. High field electrostatic bending elements are necessary to achieve high sensitivity of the beam position.

STORAGE RING EXPERIMENTAL REQUIREMENTS

Particle	p (MeV/c)	E (MV/m)	B (T)
Proton	701	16.79	0.000
Deuteron	1000	-3.98	0.160
^{3}He	1285	17.16	-0.051

SIMULATIONS

SYMMETRIC POWER SUPPLIES OR GROUNDED CASE

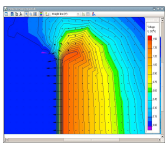
Grounded : U1 = 0, U2 = 2U

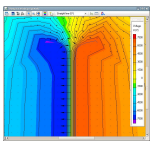
Symmetric : U1 = -U2 = U

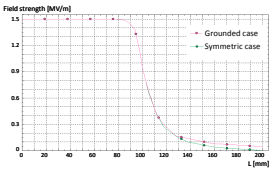

ELECTRONS EMISSION

Electrons initial energy: 50 eV, Voltage: ±100 kV → 4MV/m

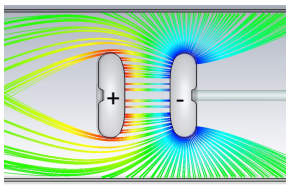

B-field: 0 T

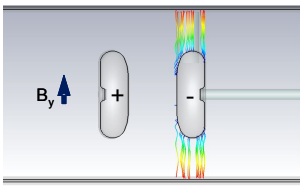

B-field: 0.15 T

SMALL SCALE SETUP

Setup with few centimeters deflectors
- less weight - simplify support;
- easy to machine and prepare the surface;
- conventional high-voltage devises;
- minimal safety restrictions.

LARGE SCALE SETUP

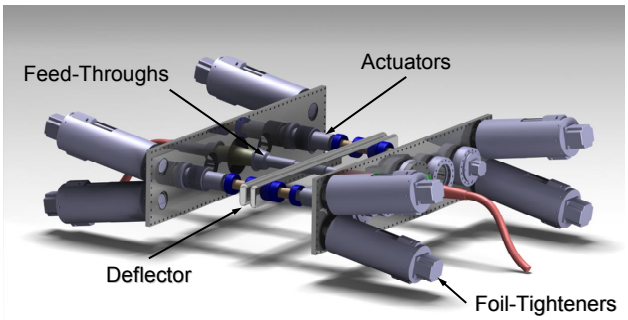

PARAMETERS

Electrode length	=	1020 mm
Electrode height	=	90 mm
Electrode spacing	=	20 – 80 mm
Maximum e-field	=	± 200 MV on each electrode
Material / coating	=	TiN coated Aluminum

RESULTS

DARK CURRENT MEASUREMENTS

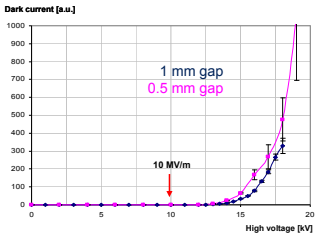

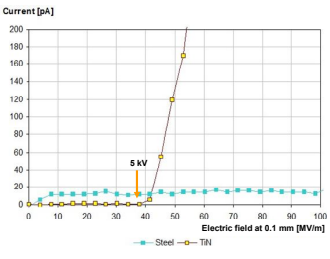

Polished stainless steel
- 240 MV/m measured at 0.05 mm with half-sphere vs. flat surface
- 17 MV/m with 17 kV at 1 mm two small half-spheres

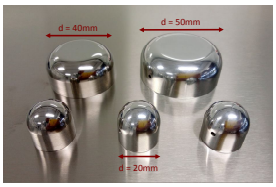

Polished aluminum
- 30 MV/m measured at 0.1 mm two small half-spheres

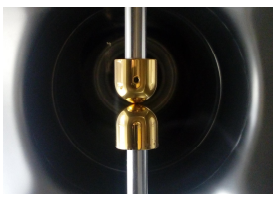

TiN coating
- smaller breakdown voltage
- zero dark current

Beam Based Alignment at the Cooler Synchrotron (COSY)

Tim Wagner for the JEDI Collaboration
RWTH Aachen University & Forschungszentrum Jülich

Motivation

- An Electric Dipole Moment (EDM) d measurement needs the orbit to be as good as possible
- Orbit RMS should be lower than 100 µm

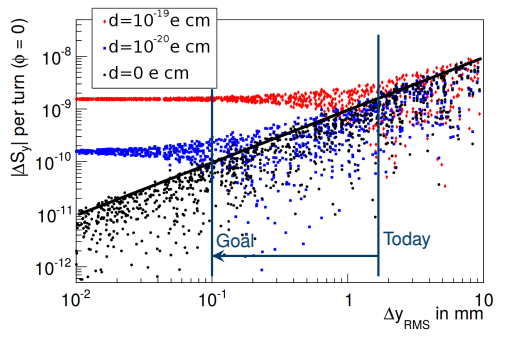

Figure: Spin buildup $|\Delta S_y|$ for different EDM values depending on the orbit RMS Δy_{RMS}[1]. The spin buildup is the measure for the EDM and freezes out at some point. The contribution due to misalignments dominates for large orbit RMS, but keeps decreasing for smaller orbit RMS until the EDM signal becomes visible.

Technique

- Use the beam to optimize the beam position inside quadrupole
- Vary quadrupole strength k, then observe and minimize orbit change
- Orbit change [2] described by:

$$\Delta x(s) = \left(\frac{\Delta k x(s_0)\ell}{B\rho}\right)\left(\frac{1}{1-k\frac{\ell\beta(s_0)}{2B\rho\tan\pi\nu}}\right) \times \frac{\sqrt{\beta(s)}\sqrt{\beta(s_0)}}{2\sin\pi\nu}\cos(\phi(s)-\phi(s_0)-\pi\nu)$$

- Minimized with the following merit function:

$$f = \frac{1}{N_{\mathrm{BPM}}}\sum_{i=1}^{N_{\mathrm{BPM}}}(x_i(+\Delta k)-x_i(-\Delta k))^2$$
$$f \propto (\Delta x(s))^2 \propto (x(s_0))^2$$

- Merit function has the shape of a parabola and the minimum is the optimal position in the quadrupole

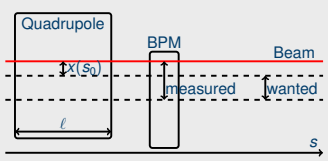

Figure: Sketch of one quadrupole and BPM and some of the parameters in the equation above. In addition the measured position and the wanted position is indicated.

Results

- Quadrupole strength of quadrupole QT12 varied with the use of back leg windings
- Beam moved inside the quadrupole in horizontal and vertical direction

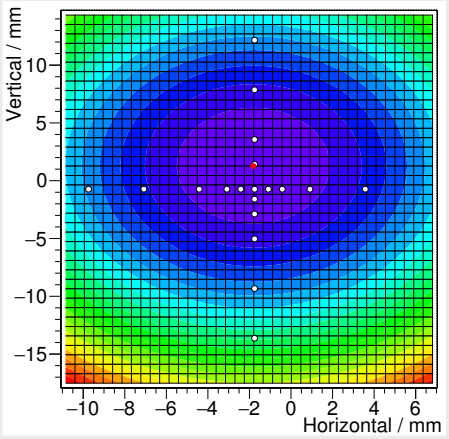

(a) Top view

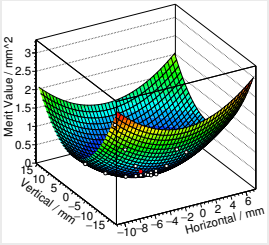

(b) Side view

Figure: Measurement for the beam based alignment. The white dots indicate the measurement points where the merit function was evaluated and the red dot is the minimum, i.e. optimal position, found by the fit. The x- and y-axis are labeled with the corresponding beam offset in mm.

- Optimal position located at (-1.98 ± 0.01) mm horizontally and (1.15 ± 0.01) mm vertically
- Beam Based Alignment with the use of back leg windings works
- Additional quadrupoles have to be made adjustable and the BPM offset has to be measured

References

[1] M. S. Rosenthal. "Experimental Benchmarking of Spin Tracking Algorithms for Electric Dipole Moment Searches at the Cooler Synchrotron COSY". PhD thesis. RWTH Aachen University, 2016.

[2] G. Portmann et al. "Automated beam based alignment of the ALS quadrupoles". In: *Conf. Proc.* C950501 (1996), pp. 2693–2695.

Contact: Tim Wagner - t.wagner@fz-juelich.de

First Commissioning Results of the Waveguide RF Wien Filter

Jamal Slim, Physics Institute III B, RWTH Aachen University

Structure of the waveguide RF Wien filter

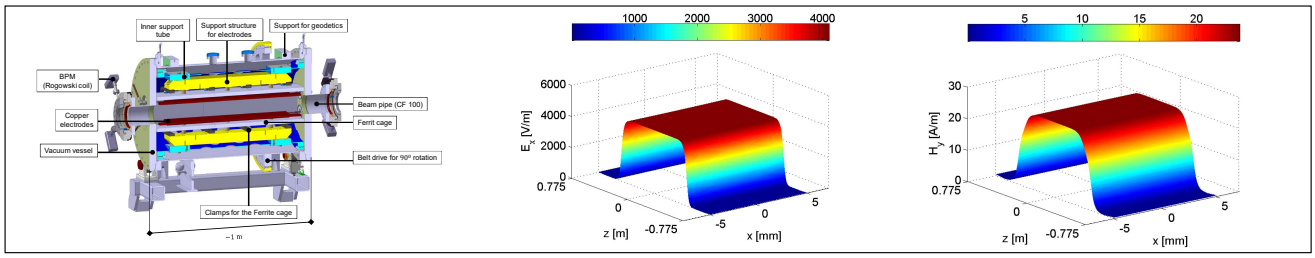

Driving circuit

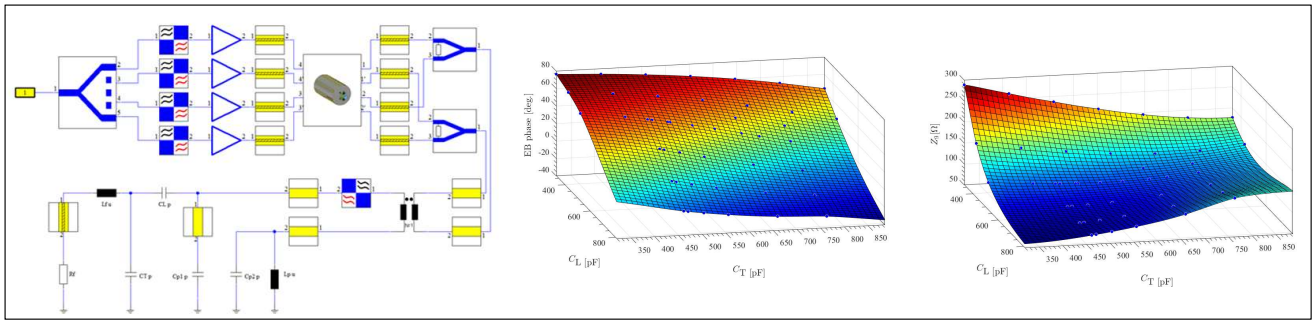

Lorentz Force Measurements

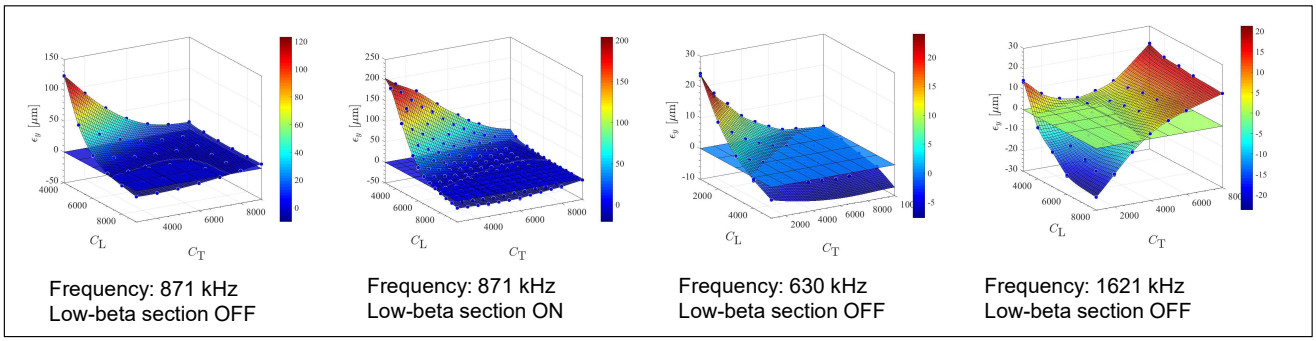

Frequency: 871 kHz
Low-beta section OFF

Frequency: 871 kHz
Low-beta section ON

Frequency: 630 kHz
Low-beta section OFF

Frequency: 1621 kHz
Low-beta section OFF

Spin Response

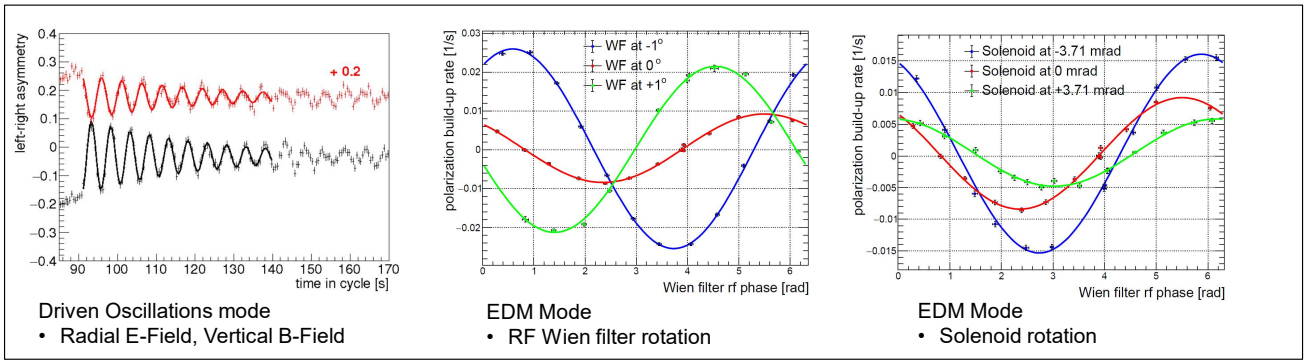

Driven Oscillations mode
- Radial E-Field, Vertical B-Field

EDM Mode
- RF Wien filter rotation

EDM Mode
- Solenoid rotation

- J. Slim et. al. NIM-A 828, 116 (2016)
- J. Slim et. al. NIM-A 859, 52 (2017)
- N. Hempelmann et. al. PRL 119, (2017)

JEDI Collaboration: http://collaborations.fz-juelich.de/ikp/jedi/

Spin tune mapping at COSY

Artem Saleev on behalf of JEDI Collaboration
Institute of Nuclear Physics - Forschungszentrum Jülich

Motivation: Systematics at EDM searches

- Magnetic Dipole Moment of particle is much greater than its Electric Dipole Moment
- High precision spin tune: a tool to quantify the systematic effects due to Magnetic Dipole Moment

Method: Spin tune mapping

- Two solenoids at COSY switched on
- Spin tune map $\Delta\upsilon_s(\chi_+, \chi_-)$ consists of the spin tune measurements $\upsilon_s(\chi_1, \chi_2)$ on the mesh $\chi_1 \times \chi_2$ of solenoid's spin kicks
- Build the map of spin tune shifts $\Delta\upsilon_s$

COSY ring

- Arcs (A_1, A_2)
- Solenoids (S_1, S_2)
- Polarimeter (P)

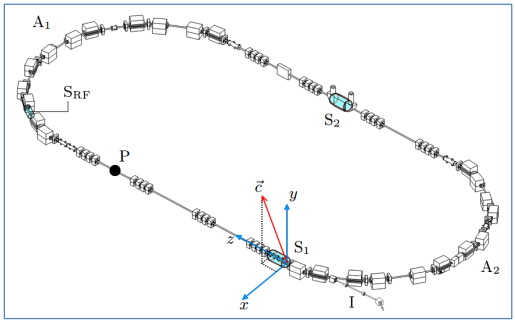

Scheme for experiment

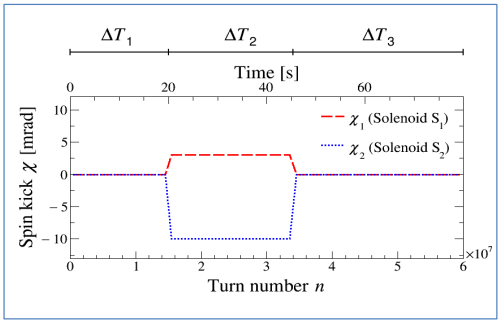

- Solenoids on at ΔT_2
- Solenoids off at ΔT_1, ΔT_3

Results: Spin tune map of COSY

- Spin tune shift $\Delta\upsilon_s$ from nominal value υ_s is resolved **with precision $\delta\upsilon_s = 3.2 \cdot 10^{-9}$**
- Angular precision $\mathbf{2.8}\ \boldsymbol{\mu rad}$ to the direction of stable spin axis $\vec{c}$ achieved – very sensitive probe of systematics!

Spin phase analysis

- Deviation of measured spin phase from assumed value
- Spin tune shift $\Delta\upsilon_s = \frac{1}{2}(\Delta\upsilon_{s_1} + \Delta\upsilon_{s_2})$

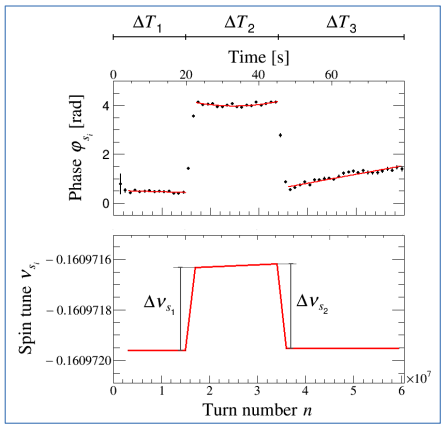

Spin tune map

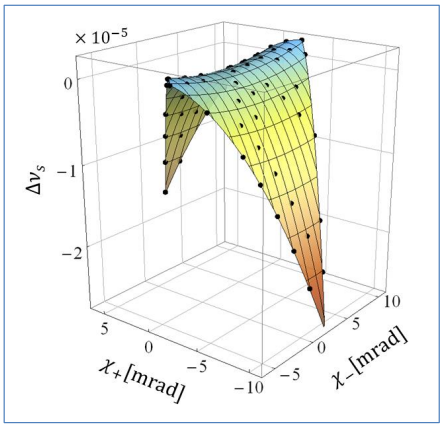

- A feature: saddle point – non-zero location is a sign of systematic effects

$\chi_\pm = \frac{1}{2}(\chi_1 \pm \chi_2)$

Development of compact, highly sensitive beam position monitors for storage rings

Falastine Abusaif*, RWTH Aachen University*, Juelich Forschungszentrum*
On behalf of the JEDI collaboration

Motivation

What makes the EDM so special?

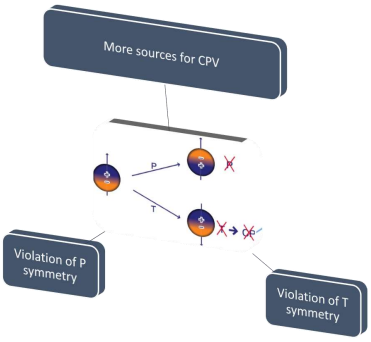

Introduction

The JEDI collaboration is currently preparing for measuring the Deuteron EDM in the COoler SYnchrotron (COSY). One of the major challenges that one needs to worry about is the precise knowledge about the beam position along the ring.

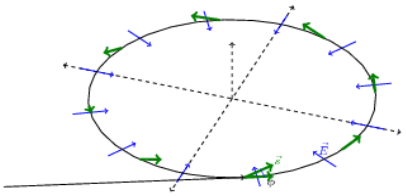

$$\frac{d\vec{s}}{dt} = \vec{s} \times \left(\vec{\Omega}_{MDM} + \vec{\Omega}_{EDM}\right)$$

$$\frac{d\vec{s}}{dt} \propto d.\vec{E} \times \vec{S}$$

Study polarization build-ups due to spin interactions with electric field

Beam position monitors along the ring

- Beam center of mass
- Longitudinal bunch shape
- Beam closed orbit
- True EDM signal

Theoretical background

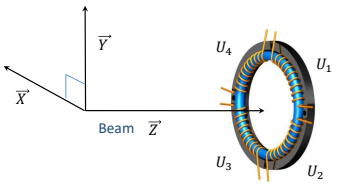

- **A current-carrying wire (to mimic COSY beam)**
- **Faraday's law**
- **Induced voltages**

- $\frac{\Delta U_{hor}}{\sum_{i=1}^{4} U_i} = \frac{(U_1+U_2)-(U_3+U_4)}{\sum_{i=1}^{4} U_i}$

$= c_1 x - c_2(x^3 - 3y^2x) + c_3(x^5 - 10y^2x^3 + 5y^4x) + \ldots$

- $\frac{\Delta U_{ver}}{\sum_{i=1}^{4} U_i} = \frac{(U_1+U_4)-(U_3+U_2)}{\sum_{i=1}^{4} U_i}$

$= c_1 y - c_2(y^3 - 3x^2y) + c_3(y^5 - 10x^2y^3 + 5x^4y) + \ldots$

* C_i : Constants depend on coil parameters

Methodology

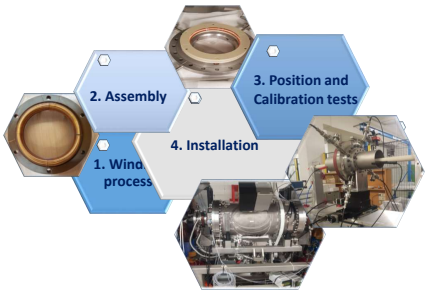

Grid map

In a calibration test :
The coil is moved in a step size of ($\mp some\ range\ mm$) with the help of the stepping motors in both the horizontal and vertical directions. The map yielded should be symmetric .

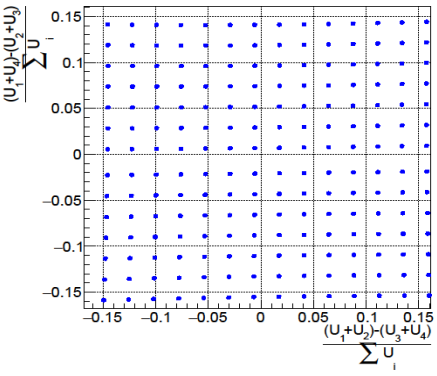

Last beam time Jan/Feb 2018

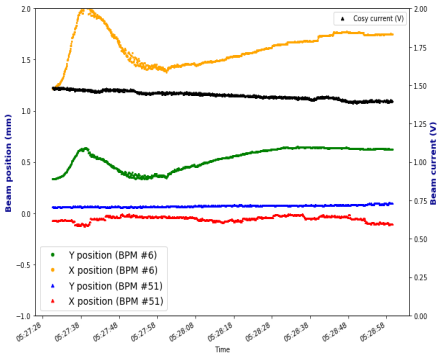

Future upgrades

- Precise positions:
  With knife edge around the wire to eclectically determine the wire positions

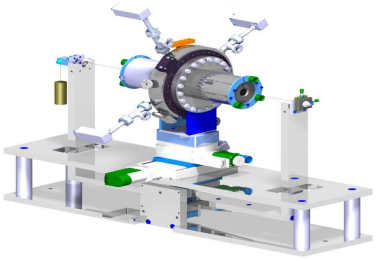

- Controlling potential noise sources

Noise at the input of the lock-in amplifier

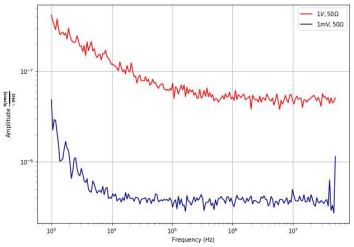

- Use the proper signal pre-amplifier depending on improved SNR values.
- Control the current strength at the test-stand **(0.1 – 1.0 mA)**

Summary

- Rogowski coil BPM's are highly sensitive and compact devices
- Currently, the greatest goal is to have a perfectly produced, tested, and calibrated coils with zero issues
- In the final prototype ring, we would have several of such monitors for distinct experimental purposes

7th International Symposium on Symmetries in Subatomic Physics (SSP2018)

Search for Electric Dipole Moments at COSY in Jülich

Closed-Orbit and Spin Tracking Simulations

V. Schmidt[1], Institut für Kernphysik 4, Forschungszentrum Jülich, 52425 Jülich, Germany,
[1]also at III. Physikalisches Institut B, RWTH Aachen University

Motivation

Basic idea of measuring an EDM:

- Inject particles with $\vec{p} \parallel \vec{S}$
- Apply radial electric field
- For $\vec{d} \neq 0$: spin rotates out of horizontal plane
- Measure: build-up of vertical polarization ($\phi \propto |\vec{d}|$)

$$\frac{d\vec{S}}{dt} = \vec{S} \times \vec{\Omega}_{MDM} + \vec{S} \times \vec{\Omega}_{EDM}$$

$$\vec{\mu} = 2(G+1) \cdot \frac{e}{2m} \vec{S}$$

$$\vec{d} = \eta \cdot \frac{e}{2mc} \vec{S}$$

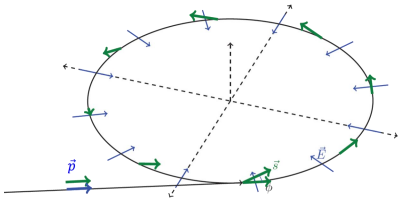

Wien filter method

- Vertical fields
- $\vec{S} \parallel \vec{p}$
- Spin rotates in horizontal plane
- $\vec{d} \neq 0$: vertical spin build-up

without Wien filter: No net EDM effect

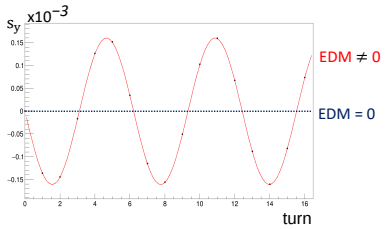

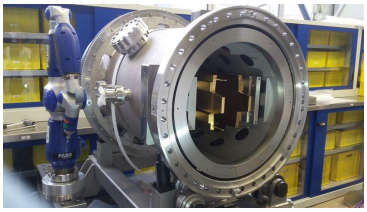

with Wien filter: Net EDM effect

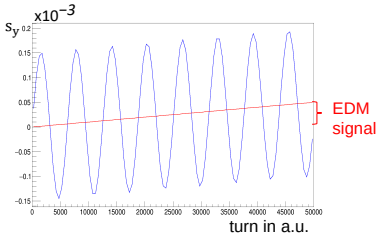

Misalignment of quadrupoles

- Disturbed closed-orbit due to QP misalignment
- Spin sees radial magnetic field
- Radial magnetic fields lead to vertical spin build-up

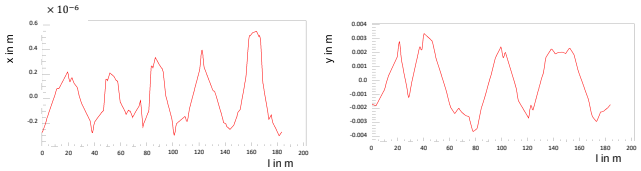

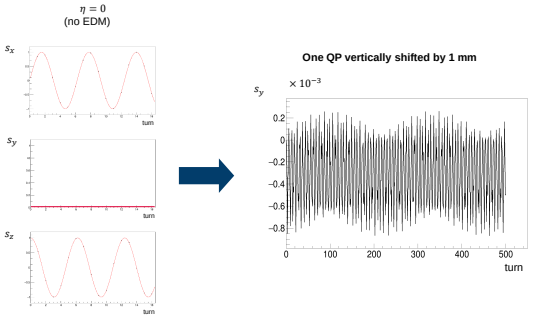

Invariant spin axis

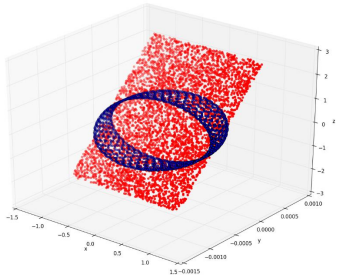

Determine **best-fit plane** and find **average spin rotation axis**

- 300 sets of random quadrupole misalignments
- Calculate invariant spin axis for each setting
- $RMS_{n_z} \approx 0.001$

→ $\sigma_{EDM} = 3 \cdot 10^{-18}\ e \cdot cm$

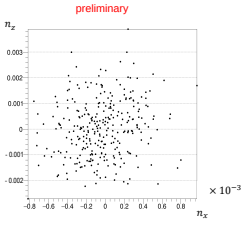

- Horizontal projection of invariant spin vectors
- Vertical component close to 1.0
- Small deviations in horizontal plane

Muon Veto in the JUNO Detector

Christoph Genster
IKP-2, Forschungszentrum Jülich, c.genster@fz-juelich.de

Gefördert durch DFG Deutsche Forschungsgemeinschaft

Cosmogenic Backgrounds in Liquid Scintillator Detectors

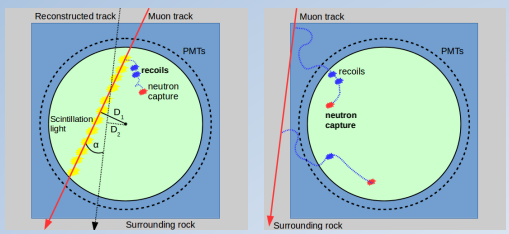

Cosmic muons create instable isotopes and fast neutrons when traversing the detector and surrounding rock

- Mainly due to spallation on nuclei (mostly ^{12}C)
- ^{8}He and ^{9}Li are the most prominent with lifetimes of 172 ms and 256 ms, respectively
- (β^-,n)-decay mimics the IBD signal from neutrino interactions
- Correlated in time and space with parent muon

Situation in JUNO

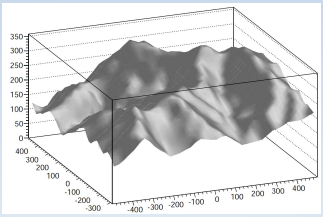

Mountain profile at the experimental site

- 700 m overburden to reduce muon flux
- Modified Gaisser formula for flux simulation at sea level
- Propagation to detecor with the MUSIC package
- Resulting muon flux at detector
  0.003 $s^{-1}m^{-2}$ with E_{mean}= 215 GeV

Veto strategy: Cylindrical volume **r = 3 m** around muon track for **t = 1.2 s**

Process	Rate without veto	Rate with veto
Muon flux in central detector	3.5/s	
Reactor neutrino signal	83/day	60/day
(β^-,n) decay of ^{8}He and ^{9}Li	84/day	1.6/day

Reconstruction Algorithms

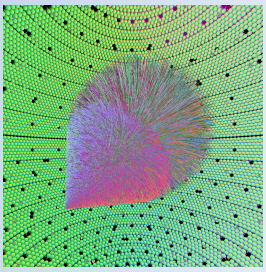

Light propagation simulation for starting muon in the JUNO central detector
https://simoncblyth.bitbucket.io/

Central Detector Reconstruction (ConeReco)

- Based on fastest light information
- Geometrical approach models light cone for forward- and sphere for backward-moving light
- Model includes Cherenkov light from waterbuffer
- Selection of PMTs based on waveform rise time and charge
- Likelihood fit with MINUIT of 5 parameters (entry point, direction, t_0)
- Developed for 20-inch PMT, 3-inch PMT and combination of both systems

Waterpool Reconstruction

- Based on hit charge & time information on waterpool PMTs
- Finds and counts charge clusters for event classification
- Connects two most likely clusters to a track
- Can work as seeding algorithm for the central detector reconstruction

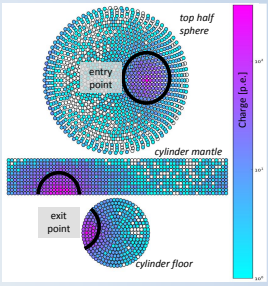

Charge distribution in waterpool PMTs for one muon event

Results

Evaluated with 5900 tracks, displayed in track's distance from the detector center D and angle α between the true and reconstructed track (definition in figure above)

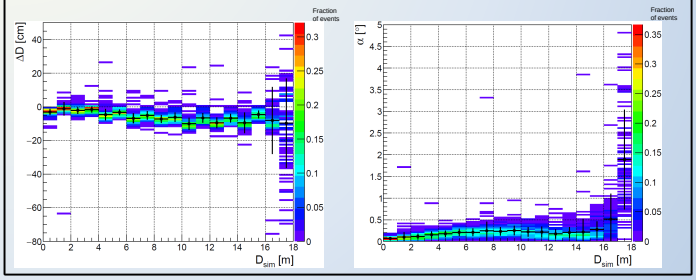

Waveform Simulation and Reconstruction

- Electronics simulation works on single-hit basis
- Most PMT effects included, largest impact by transit time spread (TTS)
- Readout window of 1250 ns samples with 1 GHz
- Waveform sampling simulated with 3x8 bit FADC with dynamic range of 1600 photoelectrons

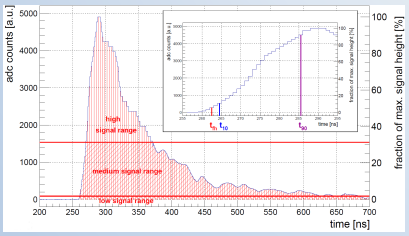

- Recontruction extracts first hit time (fht) from rising edge at 6% threshold of max signal
- Rise time determined as time between 10% and 90% of signal height
- Resolution over all LPMT at 3.5 ns close to TTS

- Full electronics simulation
- Mean position bias better than 30 cm
- Mean direction bias below 1.6°
- Best performance at the detector center
- Stable performance up to a distance from center of 16 m

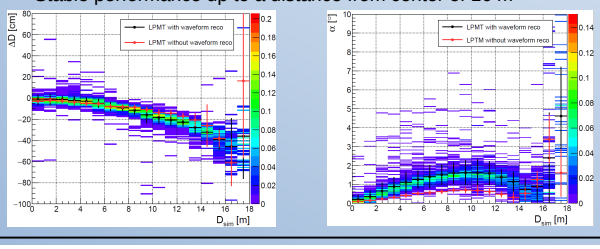

Deadtime Estimation

- ToyMC with realistic energy, angle and multiplicity distributions
- Accounts for various and overlapping veto cylinders
- For imperfect tracking the cylinder radius is increased according to bias in ΔD and α

Veto strategy	Exposure ratio
No veto	100%
Perfect tracking (r=3 m, t=1.2 s)	86%
ConeReco w/ electronics simulation and waveform reco. (r(ΔD,α)>3 m, t=1.2 s)	82%

Conclusion

- Muons can be reconstructed with bias of less than 45 cm in **D**istance from center and 1.5° in **direction**
- The resolution is better than 5 cm and 0.3° in the largest part of the detector, excluding the edge
- Detailed report published as technical paper in JINST in March 2018: **Muon reconstruction with a geometrical model in JUNO** *JINST* **13** T03003

Solar neutrino analysis with the Borexino detector

Mariia Redchuk[1,2]
on behalf of the Borexino collaboration

[1] **Institut für Kernphysik, Forschungszentrum Jülich**, 52425 Jülich, Germany [2] **RWTH Aachen University**, 52062 Aachen, Germany

Solar neutrinos

Neutrinos are the only carriers of the information about **nuclear fusion processes** occuring in the **core of the Sun**

Low (**LZ**) and high (**HZ**) **metallicity models** predict the fluxes of the neutrinos produced

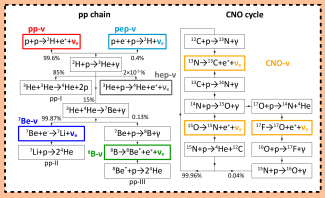

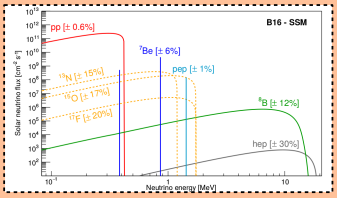

Study the Sun with neutrinos (**solar metallicity**) ⟺ Study neutrinos with the Sun (**neutrino oscillations**)

The Borexino Detector

Buffer
PC + DMP quencher

Nylon Outer Vessel
R = 5.5 m
Barrier for Rn

Nylon Inner Vessel
R = 4.25 m, ~300 t
Liquid scintillator: PC/PPO solution

Fiducial Volume
~70 t
Software cut

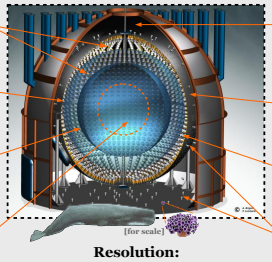

Water tank
R = 9 m, 2.1 kt water
Barrier for γ and *n*
μ Cherenkov detector

Stainless Steel Sphere
R = 6.85 m

Inner detector PMTs
~2000 PMTs
Mounted on SSS

Outer detector PMTs
~200 PMTs
Mounted on SSS, floor

Resolution:
~50 keV & ~10 cm @ 1 MeV

Neutrino detection:
$\nu + e^- \rightarrow \nu + e^-$

Phase II Results

Dataset: December 2011 to May 2016

Exposure: ~1300 days x 70 tons **Energy range:** 0.19 ~ 2.93 MeV

Constraining the rate of **ν(CNO)**
based on Standard Solar Model[1] HZ/LZ:

	Rate [cpd/100t]	Flux [cm^{-2} s^{-1}]
$\nu(pp)$	$134 \pm 10^{+6}_{-10}$	$(6.1 \pm 0.5^{+0.3}_{-0.5}) \times 10^{10}$
$\nu(^7\mathrm{Be})$	$48.3 \pm 1.1^{+0.4}_{-0.7}$	$(4.99 \pm 0.13^{+0.07}_{-0.10}) \times 10^{9}$
$\nu(pep)$ HZ	$2.43 \pm 0.36^{+0.15}_{-0.22}$	$(1.27 \pm 0.19^{+0.08}_{-0.12}) \times 10^{8}$
$\nu(pep)$ LZ	$2.65 \pm 0.36^{+0.15}_{-0.24}$	$(1.39 \pm 0.19^{+0.08}_{-0.13}) \times 10^{8}$

Constraining Rate(*pp*)/Rate(*pep*)
using MSW-LMA[2] + 2.5% error well-known from theory:

	Rate [cpd/100t]	Flux [cm^{-2} s^{-1}]
ν(CNO)	< 8.1 (95% C.L.)	$< 7.9 \times 10^{8}$ (95% C.L.)

Multivariate fit result (example)

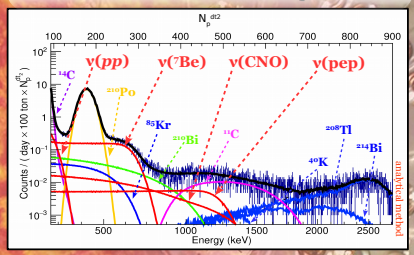

Systematic uncertainties

Source of uncertainty	*pp* −%	*pp* +%	^{7}Be −%	^{7}Be +%	*pep* −%	*pep* +%
Fit method (analytical/MC)	-1.2	1.2	-0.2	0.2	-4.0	4.0
Choice of energy estimator	-2.5	2.5	-0.1	0.1	-2.4	2.4
Pile-up modeling	-2.5	0.5	0	0	0	0
Fit range and binning	-3.0	3.0	-0.1	0.1	1.0	1.0
Fit models (see text)	-4.5	0.5	-1.0	0.2	-6.8	2.8
Inclusion of ^{85}Kr constraint	-2.2	2.2	0	0.4	-3.2	0
Live Time	-0.05	0.05	-0.05	0.05	-0.05	0.05
Scintillator density	-0.05	0.05	-0.05	0.05	-0.05	0.05
Fiducial volume	-1.1	0.6	-1.1	0.6	-1.1	0.6
Total systematics (%)	-7.1	4.7	-1.5	0.8	-9.0	5.6

Highlights of the results

- updated **ν(*pp*)** measurement with **9.5%** precision
- **2.7%** precision measurement of **ν(^{7}Be)**
- **>5σ** discovery of **ν(*pep*)**
- the most stringent upper limit on **ν(CNO)**

Lowest energy region

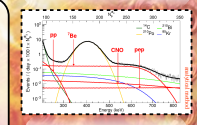

ν(*pep*) shoulder

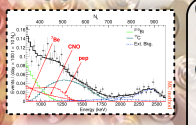

High metallicity hypothesis weak hint

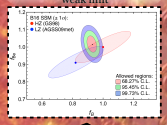

P($\nu_e \rightarrow \nu_e$) from the *pp* chain under HZ assumption

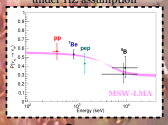

Highlights of the systematics

- Fit procedure done with
  1) **Monte Carlo**
  2) **analytical** approach
- **Pile-up modelling**:
  1) convolution with each species
  2) synthetic pile-up
- **Compatible results** obtained with
  1) different FV and TFC methods
  2) fitting in charge variable

HELMHOLTZ
SPITZENFORSCHUNG FÜR GROSSE HERAUSFORDERUNGEN

RWTH AACHEN UNIVERSITY

Data selection

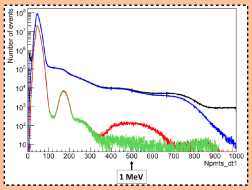

- no cuts
- μ and μ daughter cut
- FV cut
- TFC cut

Three-fold coincidence (TFC)

$$\mu + {}^{12}\mathrm{C} \rightarrow \mu + {}^{11}\mathrm{C} + n$$

(250 μs)

$$n + p \rightarrow D + \gamma$$

(29.4 min)

$${}^{11}\mathrm{C} \rightarrow {}^{11}\mathrm{B} + e^+ + \nu_e$$

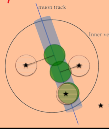

Multivariate Fit

TFC-tagged spectrum with **~90% ^{11}C** and **~40%** exposure

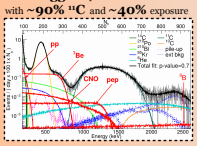

TFC-subtracted spectrum with **~10% ^{11}C** and **~60%** exposure

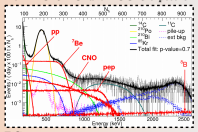

RD (radial distribution)
distinguishing external and uniform components

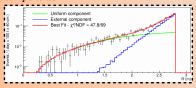

PS (pulse shape variable)
distinguishing e$^-$ and e$^-$
evaluate the remaining ^{11}C in TFC-sub

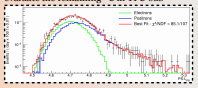

Multivariate likelihood

$$\mathcal{L}_{\mathrm{MV}}(\vec{\theta}) = \mathcal{L}_{\mathrm{TFC\text{-}sub}}(\vec{\theta}) \cdot \mathcal{L}_{\mathrm{TFC\text{-}tagged}}(\vec{\theta}) \cdot \mathcal{L}_{\mathrm{RD}}(\vec{\theta}) \cdot \mathcal{L}_{\mathrm{PS}}(\vec{\theta})$$

Free parameters:
rates of all species, some detector response parameters, synthetic pile-up (optional)

Monte Carlo method ⟷ Analytical method

Detector response

Energy estimators

- N_h Total # of detected **hits** (photons)
- N_{pe} Total # of **photoelectrons** (charge)
- N_p Total # of **triggered PMTs** ...within the first... $N_p^{dt_2}$ 230ns, $N_p^{dt_1}$ 400 ns

Used in the analytical fit:

Analytical model

Deposited energy → photoelectrons

$$N_{pe}(E) = LY \cdot \left(Q(E) \cdot E + f_{Cher} \cdot Ch(E) \right)$$

light yield: energy → photons [# photons/MeV] | quenching: $\frac{1}{E}\int_0^E \frac{dE}{1 + k_B \frac{dE}{dx}}$ | Cherenkov tuning parameter

Photoelectrons → number of PMTs

$$N_p(E) = N_{live}\left(1 - e^{-\frac{N_{pe}}{N_{live}}}\left[1 + p_t \frac{N_{pe}}{N_{live}}\right]\right)\left(1 - g_C \frac{N_{pe}}{N_{live}}\right)$$

average # live PMTs (dataset) | single e$^-$ response (calibrations) | geometric correction (tuned with MC)

References:

[1] N. Vinyoles, A. M. Serenelli, F. L. Villante, S. Basu, J. Bergström, M. C. Gonzalez-Garcia, M. Maltoni, C. Peña-Garay, and N. Song
A New Generation of Standard Solar Models
The Astrophysical Journal 835, 202 (2017)

[2] I.Esteban, M. C. Gonzalez-Garcia, M. Maltoni, I. Martinez-Soler, T. Schwetz
Updated fit to three neutrino mixing: exploring the accelerator-reactor complementarity
Journal of High Energy Physics 01 (2017)

[3] G. Bellini et al. (Borexino Collaboration)
Final results of Borexino Phase-I on low-energy solar neutrino spectroscopy
Physical Review D 89, 112007 (2014)

[4] M. Agostini et al. (Borexino Collaboration)
First Simultaneous Precision Spectroscopy of pp, ^{7}Be, and *pep* Solar Neutrinos with Borexino Phase-II
arXiv: 1707.09279 [hep-ex] (2017)

[5] G. Bellini et al. (Borexino Collaboration)
Precision Measurement of the ^{7}Be Solar Neutrino Interaction Rate in Borexino
Physical Review Letters 107, 141302 (2011).

Waveform Reconstruction of IBD and Muon Events in JUNO

Michaela Schever on behalf of the JUNO collaboration,
PhD student Forschungszentrum Jülich GmbH, RWTH Aachen University,
m.schever@fz-juelich.de

Physics Motivation [1]

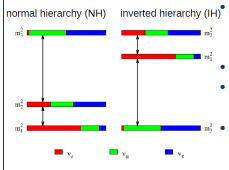

Neutrino mass hierarchy

- Measurement of neutrino mass hierarchy: confirm either normal hierarchy (NH) or inverted hierarchy (IH)
- Phase of oscillation is different for NH and IH
- Requires good energy resolution (design: $3\%/\sqrt{E/MeV}$)
- Discrimination between NH and IH with ~3σ after 6 years with E_{res} = 3% and ~100,000 IBD events

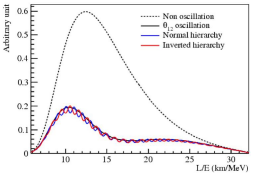

Neutrino reactor spectrum

Experiment [2]

- 20 kton liquid scintillator detector
- Acrylic sphere: 35 m diameter
- 18,000 large PMTs (20" diameter)
  - 5,000 Hamamatsu PMTs
  - 13,000 NNVT PMTs
- 25,000 small PMTs (3" diameter)
- 650 m underground
- 52 km baseline
- Location: Jiangmen in China
- Data-taking will start in 2021

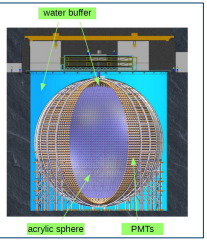

IBD Waveform Reconstruction

Introduction

- Antineutrinos are detected via the Inverse Beta Decay (IBD): $\bar{\nu}_e + p \rightarrow e^+ + n$
- Positron annihilates with electron into 2 photons
- Total visible energy E_{vis} is related to kinetic energy of antineutrino: $E_{vis} \approx E_\nu - 782$ keV
- PMTs convert photons into photo-electrons (PE)
- IBD events have a low occupancy rate (="hit density"), typically ≤ 3 PE per PMT
- Waveform is FADC trace of the PMT read-out electronics
- Sample frequency is 1 GHz
- Waveforms feature PEs as peaks

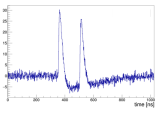
Example of IBD waveform

- IBD waveform reconstruction methods under study:
  - **Deconvolution method**
  - **Waveform template fit**
  - Waveform integration
  - Hit counting

Methods

Deconvolution Method:

- Waveform results from convolution of photon hit distribution with single PE (SPE) response plus noise
- Deconvolution method reconstructs charge and time of each hit based on Discrete Fourier Transforms (DFT) from the integral of the peak area and peak position
- SPE hit reconstruction possible from frequency domain

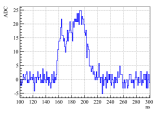
Example of simulated waveform [3]

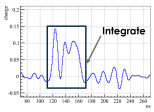

Waveform after deconvolution [3]

Waveform Template Fit:

- Waveform is fitted with template fit
- Template describes SPE response
- Charge and time are reconstructed from fit parameters

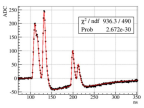
Example of waveform template fit [4]

Results

Deconvolution Method:

- Residual charge non-linearity of 1 %

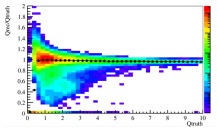
Charge resolution for 0 – 10 PEs per waveform [3]

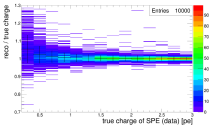
Charge resolution for SPE waveforms

Waveform Template Fit:

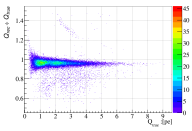
Charge resolution for 0 – 10 PEs per waveform [4]

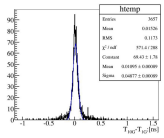
Time resolution [4]

Muon Waveform Reconstruction

Introduction

- Waveforms of muon events feature a high number of PE (NPE), typically 500 – 5000 PE
- Reconstruction of each photon like for IBD events not possible
- First hit time (fht), charge, and rise time are needed to reconstruct muon tracks for muon vetoes [5]

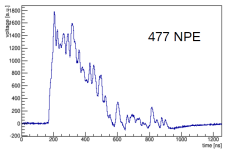

Example of muon waveform

Methods

Time:

- Find fht in typically steeply rising edge of waveform
- Use Constant Fraction Discriminator (CFD) approach:
  - Set fht when waveform passes threshold
  - Set threshold as relative fraction of waveform height

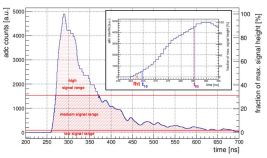

Charge:

- Charge reconstruction done by integrating the entire waveform after baseline correction

Results

Time:

- Best fht resolution for threshold at 4% of signal height
- Fht resolution: 3.4 ns

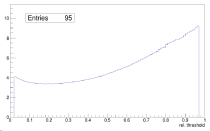
Fht resolution in dependence on relative threshold height

Charge:

- Charge resolution with RMS ≈ 0.17 obtained

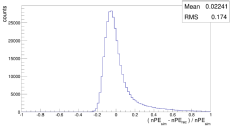
Distribution of true – reconstructed charge relative to true charge

Conclusion & Outlook

IBD Waveform Reconstruction:

- IBD results show a charge non-linearity of 1%
- Further studies are conducted on the time reconstruction for each single PE
- IBD waveform reconstruction by deep learning recently started

Muon Waveform Reconstruction:

- Muon waveform reconstruction allows good muon track reconstruction for muon veto [5]
- Muon waveform reconstruction study continued based on deep learning

References

[1] JUNO collaboration, F. An et al., *Neutrino Physics with JUNO*, 1507.05613.
[2] JUNO collaboration, Z. Djurcic et al., *JUNO Conceptual Design Report*, 1508.07166.
[3] Zeyuan Yu, Institute of High Energy Physics, Beijing
[4] Yaping Cheng, Forschungszentrum Jülich GmbH & Institute of High Energy Physics, Beijing
[5] Christoph Genster et al., *Muon reconstruction with a geometrical model in JUNO*, JINST, 13 (2018) T03003

Gefördert durch
DFG Deutsche Forschungsgemeinschaft

Reduction of the ^{14}C-background

Philipp Kampmann
IKP2 – Forschungszentrum Jülich

Gefördert durch DFG Deutsche Forschungsgemeinschaft
JÜLICH Forschungszentrum

The JUNO mass hierarchy sensitivity

- **Goal of JUNO: Measure the Neutrino Mass Hierarchy (MH)**

Analysis strategy:
- Fit both MH-models to the measured energy spectrum
- Use the difference of the minimized χ^2-values as **discriminator** for an hypothesis test:

$$\Delta\chi^2 = \chi^2(\underbrace{NH}_{\text{Model}};\underbrace{IH}_{\text{Data}}) - \chi^2(IH;IH)$$

- Significance of the discrimination can be estimated via Wilks' Theorem
- JUNO expects to discriminate the false MH with **3-4σ** ($9 < \Delta\chi^2 < 16$)

- MH-models differ in the oscillatory fine structure in the energy spectrum:
  - **Energy resolution is crucial!**

JUNO spectrum (6 years)

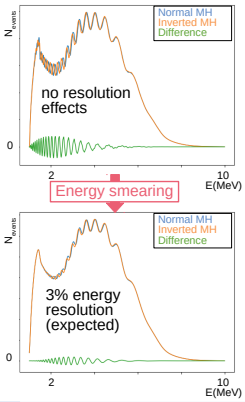

^{14}C-background

- JUNO uses liquid organic scintillator:

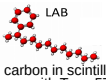

- Much carbon in scintillator → Much ^{14}C
  - β-decay with $T_{1/2} \approx 5700$ y
- Total of 40 kBq in JUNO
  - → 5% pile-up events (1250 ns DAQ window)
  - → Prompt spectrum gets convoluted with ^{14}C-spectrum

Liquid Scintillator in JUNO
- Linear **A**lkyl**B**enzene (**LAB**) - like Daya Bay, SNO+
- 3 g/l PPO as fluor
- 15 mg/l bis-MSB as wavelength shifter

Matter	^{14}C/^{12}C ratio
Atmosphere	10^{-12}
Borexino Scintillator	10^{-18}
JUNO Scintillator	10^{-17}

^{14}C spectrum

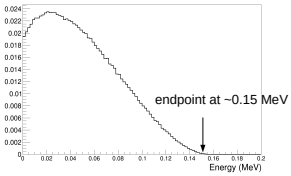

Effect on monoenergetic positrons

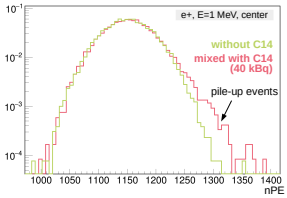

Methods for suppressing the impact of ^{14}C

The clusterization algorithm

Identify multiple event clusters in the hit time distribution:

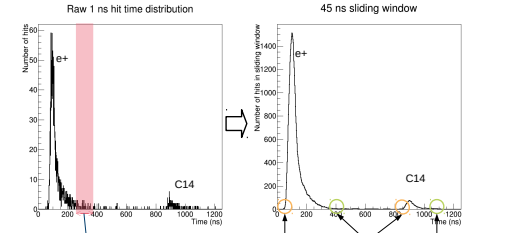

Sliding window:
- Sums up consecutive bins
- Moves in 1 ns steps
- Smoothens curve

Cluster start:
- Signal increases over start threshold

Cluster end:
- Signal falls under end threshold

Optimization of clusterization parameters on MH sensitivity:

- 3 parameters need to be optimized:
  - Threshold of cluster start
  - Threshold of cluster end
  - Size of sliding window
- **Idea: Optimize clusterization to give the best discrimination between different mass hierarchies**
- Included 3 effects on the spectrum in the **G**lobal **N**eutrino **A**nalysis sensitivity tool[1]:
  - Reduction of ^{14}C events
  - Loss of signal events
  - Distortion of effective ^{14}C-spectrum
- Further optimization possible!
- Limited in time: Close clusters get reconstructed as one

[1]http://astronu.jinr.ru/wiki/index.php/GNA

Impact of clusterization on the MH-sensitivity

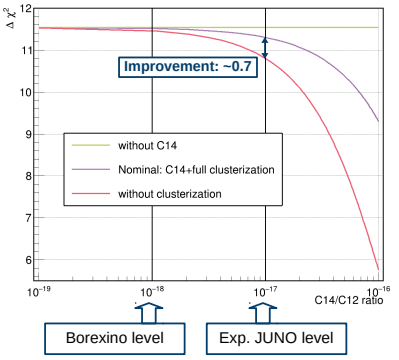

Spherical harmonics

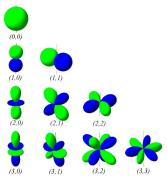

Evaluate the multipole expansion of the signal to find pile-up events

- Evaluation of spherical harmonics shows different contributions of higher order than monopoles
- Point-like events in scintillator should be pure monopoles
- Calculated spherical harmonics from Point-Of-View of the reconstructed vertex
  - Weighted hits with deviation from mean time

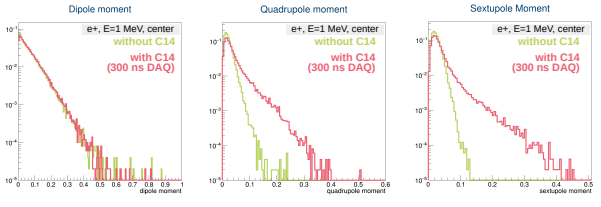

Likelihood of hit pattern

- Obtained likelihood *P(hit time | PMT distance to vertex)* from Monte Carlo simulation
- Find the best fitting position (reconstruct event position)
- Use the absolute likelihood value in the minimum to discriminate pile-up events
- Should also discriminate any other event, which is not point-like/not represented by the LLH model

Absolute likelihood value

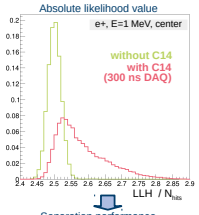

Likelihood of hit times (Input to the analysis)

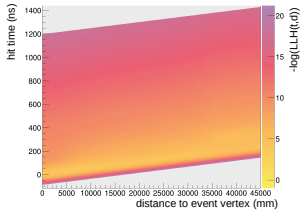

Separation performance

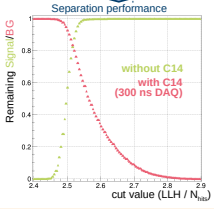

Reduction of the ^{14}C-background in JUNO

Philipp Kampmann, Livia Ludhova
International Neutrino Summer School 2018

p.kampmann@fz-juelich.de

The JUNO experiment

Primary goal : Measure the neutrino mass hierarchy in 6 years with 3-4σ

- Reactor neutrinos from 53 km baseline (83 ν/day)
- Liquid (organic) scintillator
- High PMT coverage
  - Good energy resolution of **3%/MeV**
- ~700 m overburden
- Anti-neutrino detection via **I**nverse **B**eta **D**ecay (IBD):

$$\bar{\nu}_e + p \rightarrow n + e^+$$

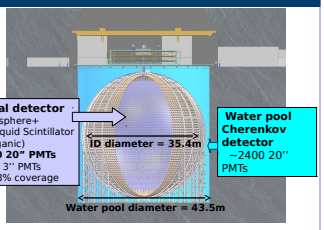

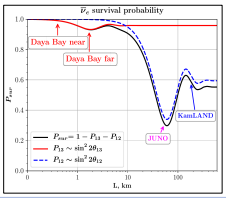

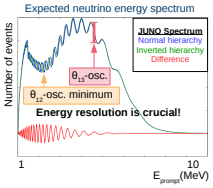

^{14}C-background

- JUNO uses liquid organic scintillator:

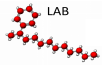

Liquid Scintillator in JUNO
- Linear **A**lkyl**B**enzene (**LAB**) - like Daya Bay, SNO+
- 3 g/l PPO as fluor
- 15 mg/l bis-MSB as wavelength shifter

- Much carbon in scintillator → Much ^{14}C
  - β-decay with $T_{1/2}$ = 5700 y
- Total of 40 kBq in JUNO
  - 5% pile-up events (1250 ns DAQ window)
  - Prompt spectrum gets convoluted with ^{14}C-spectrum

Matter	^{14}C/^{12}C ratio
Atmosphere	10^{-12}
Borexino Scintillator	10^{-18}
JUNO Scintillator	10^{-17}

^{14}C spectrum

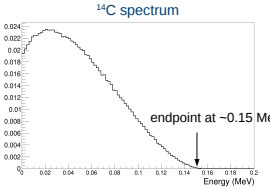

Effect on monoenergetic positrons

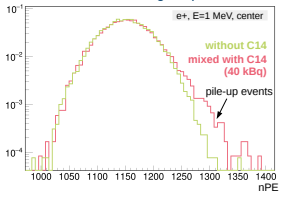

Methods for suppressing the impact of ^{14}C

The clusterization algorithm

Identify multiple event clusters in the hit time distribution:

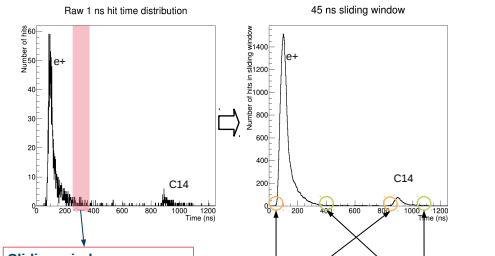

Sliding window:
- Sums up consecutive bins
- Moves in 1 ns steps
- Smoothens curve

Cluster start:
- Signal increases over start threshold

Cluster end:
- Signal falls under end threshold

Optimization of clusterization parameters on MH sensitivity:

- 3 parameters need to be optimized:
  - Threshold of cluster start
  - Threshold of cluster end
  - Size of sliding window
- **Idea: Optimize clusterization to give the best discrimination between different mass hierarchies:**

$$\Delta\chi^2 = \chi^2(NH;IH) - \chi^2(IH;IH)$$

- Included 3 effects on the spectrum in the **G**lobal **N**eutrino **A**nalysis sensitivity tool[1]:
  - Reduction of ^{14}C events
  - Loss of signal events
  - Distortion of effective ^{14}C-spectrum
- Further optimization possible!

[1]http://astronu.jinr.ru/wiki/index.php/GNA

Impact of clusterization on the MH-sensitivity

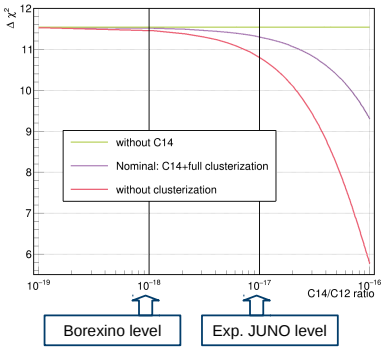

Spherical harmonics

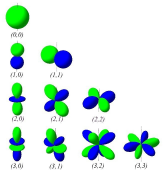

Evaluate the multipole expansion of the signal to find pile-up events

- Evaluation of spherical harmonics shows different contributions of higher order than monopoles
- Point-like events in scintillator should be pure monopoles
- Calculated spherical harmonics from Point-Of-View of the reconstructed vertex
  - Weighted hits with deviation from mean time

Dipole moment

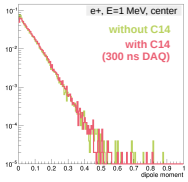

Quadrupole moment

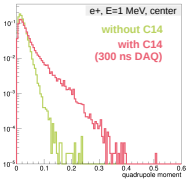

Sextupole Moment

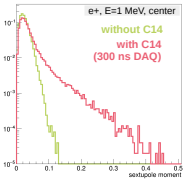

Likelihood of hit pattern

- Obtained likelihood *P(hit time | PMT distance)* from Monte Carlo simulation
- Find the best fitting position (reconstruct event position)
- Use the absoute likelihood value in the minimum to discriminate pile-up events
- Should also discriminate any other event, which is not point-like/not represented by the LLH model

Likelihood of hit times (Input to the analysis)

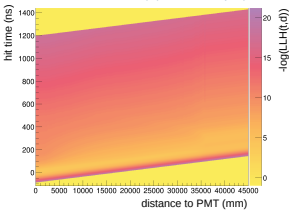

Absolute likelihood value

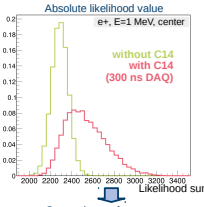

Separation performance

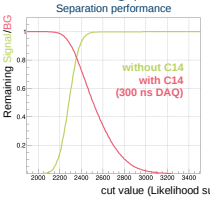

Reduction of the ^{14}C-background in JUNO

Philipp Kampmann and Livia Ludhova

p.kampmann@fz-juelich.de

The JUNO experiment

Primary goal : Measure the neutrino mass hierarchy in 6 years with 3-4σ

- Reactor neutrinos from 53 km baseline (83 ν̄/day)
- Liquid (organic) scintillator
- High PMT coverage
  - ➔ Good energy resolution of **3%/MeV**
- ~700 m overburden
- Anti-neutrino detection via **I**nverse **B**eta **D**ecay (IBD):

$$\bar{\nu}_e + p \rightarrow n + e^+$$

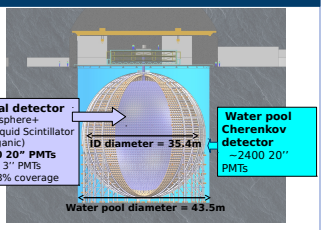

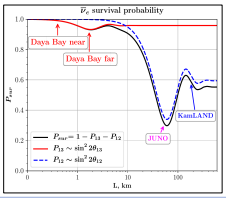

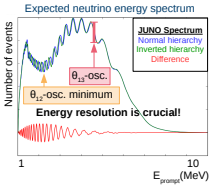

^{14}C-background

- JUNO uses liquid organic scintillator:

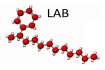

Liquid Scintillator in JUNO
- Linear **A**lkyl**B**enzene (**LAB**) - like Daya Bay, SNO+
- 3 g/l PPO as fluor
- 15 mg/l bis-MSB as wavelength shifter

- Much carbon in scintillator → Much ^{14}C
  - β-decay with $T_{1/2}$ = 5700 y
- Total of 40 kBq in JUNO
  - ➔ 5% pile-up events (1250 ns DAQ window)
  - ➔ Prompt spectrum gets convoluted with ^{14}C-spectrum

Matter	^{14}C/^{12}C ratio
Atmosphere	10^{-12}
Borexino Scintillator	10^{-18}
JUNO Scintillator	10^{-17}

^{14}C spectrum

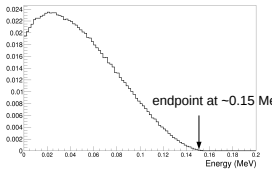

Effect on monoenergetic positrons

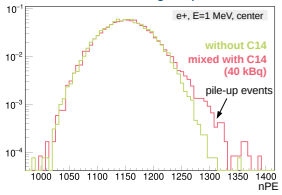

Methods for suppressing the impact of ^{14}C

The clusterization algorithm

Identify multiple event clusters in the hit time distribution:

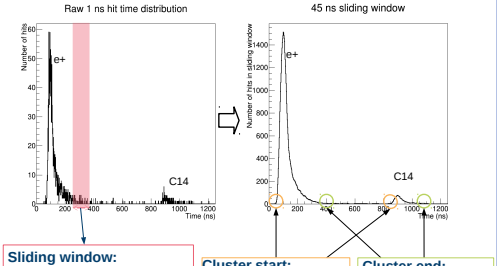

Sliding window:
- Sums up consecutive bins
- Moves in 1 ns steps
- Smoothens curve

Cluster start:
- Signal increases over start threshold

Cluster end:
- Signal falls under end threshold

Optimization of clusterization parameters on MH sensitivity:

- 3 parameters need to be optimized:
  - Threshold of cluster start
  - Threshold of cluster end
  - Size of sliding window
- **Idea: Optimize clusterization to give the best discrimination between different mass hierarchies:**

$$\Delta\chi^2 = \chi^2(NH;IH) - \chi^2(IH;IH)$$

- Included 3 effects on the spectrum in the **G**lobal **N**eutrino **A**nalysis sensitivity tool[1]:
  - Reduction of ^{14}C events
  - Loss of signal events
  - Distortion of effective ^{14}C-spectrum
- Further optimization possible!

[1] http://astronu.jinr.ru/wiki/index.php/GNA

Impact of clusterization on the MH-sensitivity

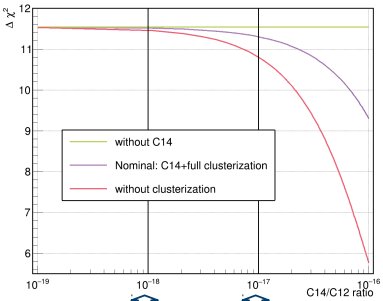

Spherical harmonics

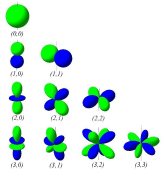

Evaluate the multipole expansion of the signal to find pile-up events

- Evaluation of spherical harmonics shows different contributions of higher order than monopoles
- Point-like events in scintillator should be pure monopoles
- Calculated spherical harmonics from Point-Of-View of the reconstructed vertex
  - Weighted hits with deviation from mean time

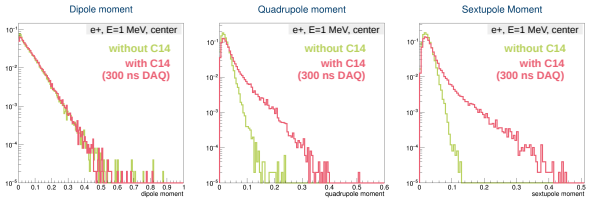

Likelihood of hit pattern

- Obtained likelihood *P(hit time | PMT distance)* from Monte Carlo simulation
- Find the best fitting position (reconstruct event position)
- Use the absoute likelihood value in the minimum to discriminate pile-up events
- Should also discriminate any other event, which is not point-like/not represented by the LLH model

Likelihood of hit times (Input to the analysis)

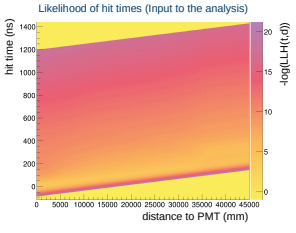

Absolute likelihood value

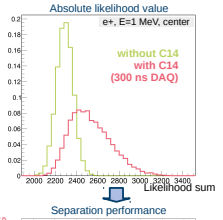

Separation performance

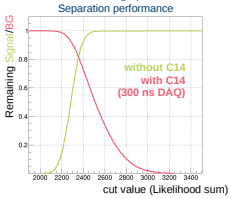

GNA fitter and detector response impact on JUNO mass hierarchy sensitivity

Yaping Cheng[1], Anna Fatkina[2], Maxim Gonchar[2], Livia Ludhova[1,3], Dmitry Naumov[2]
Konstantin Treskov[2]
1 IKP-2 Forschungszentrum Jülich, Germany 2 Joint Institute for Nuclear Research, Dubna, Russia
3 RWTH Aachen University, Germany

Introduction

The Jiangmen Underground Neutrino Observatory (JUNO) is a 20 kt liquid scintillator detector that will be located at Kaiping, Jiangmen city in South China. An energy resolution of 3% at 1 MeV is required to determine the neutrino mass hierarchy (MH) by spectral analysis. In this world largest liquid scintillator detector, a good understanding of the energy response is essential for MH determination.

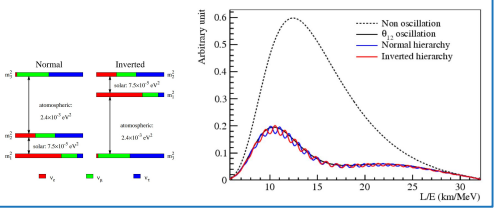

Statistical method

The χ^2 is constructed the following way:

$$\chi^2 = (x-\mu(\theta,\eta))^T V_{stat}^{-1}(x-\mu(\theta,\eta)) + (\eta-\eta_0)^T V_\eta^{-1}(\eta-\eta_0)$$

where:

- x, μ — vectors with data and model prediction.
- θ — vector with free parameters.
- η — vector with uncertainties, propagated via penalty terms.
- η_0 — default values of η.
- V_η — error matrix for η.

LS NL measurement

Several groups from Prague, TUM, Milan are working on LS non-linearity (NL) measurement now. The basic principle is compton coincidence technique.

$$E_{vis}^{e^+} = E_{vis}^{e^-} + 2 * E_{vis}^{\gamma(0.511MeV)}$$

$$E_{vis}^{\gamma} = \int E_{vis}^{e} * \frac{dN}{dE}(E_{true}^{e}) * dE_{true}^{e}$$

The method to propagate LS response from e^- to e^+ is based on the assumption that e^- and e^+ have identical behaviour while depositing kinetic energy in LS and then the gamma NL can be deduced from e^-/e^+.

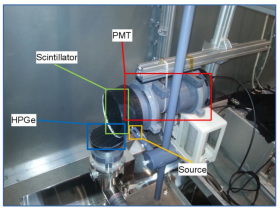

GNA features and JUNO calculation scheme

- GNA — a fitter for comprehensive physical models with large number of parameters.
- Design is based on the Daya Bay experience.
- Dataflow programming paradigm: model is built as directed lazily-evaluated graph that operates on vectors.
- Implementation: C++ (core), Python (interface).
- Built on top of: Eigen (linalg), ROOT (minimization), boost.
- Transparent multicore/GPGPU computations are on the way.
- Statistical approaches implemented:
  - χ^2 and Poisson test statistics.
  - Feldman-Cousins approach.
  - Likelihood profiling.
  - Propagation of systematics via pull term and covariance matrix.

http://astronu.jinr.ru/wiki/index.php/GNA

The energy spectra prediction is done in this way:

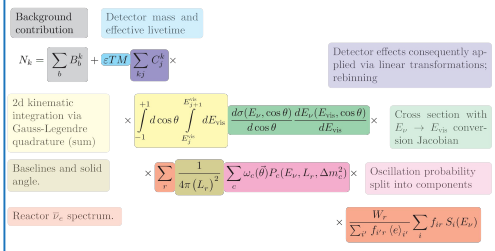

- Detector effects: energy scale nonlinearity, resolution.
- Huber-Muller antineutrino spectra for isotopes.
- SNF/off-equilibrium are not considered for sensitivity.

Non-linearity study based on DYB model

The Daya Bay (DYB) non-linearity (NL) curve is tuned based on various DYB gamma calibration sources and the continuous beta spectrum of ^{12}B is also used (Ref. [1]).
The Daya Bay energy nonlinearity is parametrized in this way:

$$\frac{E_{rec}}{E_{true}} = f_0(E) + \sum a_i(f_i(E) - f_0(E))$$

Function $f_0(E)$ is the nominal model. The functions $f_i(E)$ represent the alternative curves chosen in order to parametrize $f_0(E)$ uncertainty with parameters a_i=0±1. From the NL curve, we can get NL response matrix.

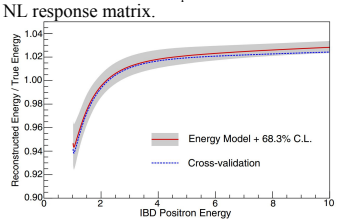

Change the uncertainty of NL curve by changing the sigma value of a_i. Adding pull terms for a_i, and use the measured spectrum itself to calibrate the NL model. Varying the uncertainty of the NL curve and studying its impact by inspecting the $\Delta\chi^2$ between False MH and true MH. **From the left plot, we can see the overall change in $\Delta\chi^2$ is less than 1.**
The right plot is the scan result for sigma(a_i)=1.

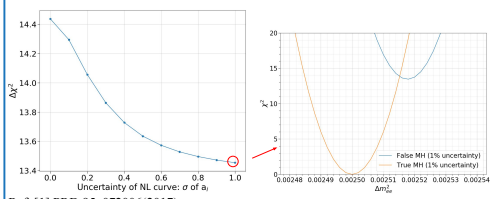

Ref. [1] PRD 95, 072006(2017)

Non-linearity study based on analytical model

Assume after the energy non-linearity correction, we have a residual nonlinearity with the form like this (Ref. [2]):

$$\frac{E_{rec}}{E_{true}} = \frac{1+p_0}{1+p_1 * exp(-p_2 E_{true})}$$

Here p2 = 0.2/MeV, we studied p0 and p1 with combinations like (p0, p1)=(0.5%, 1%) (1%, 2%) (1.5%, 3%)
If p0=1% and p1=2%, we will have a residual NL like this:

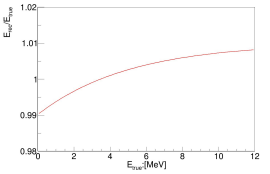

According to Ref. [2], we can measure this residual nonlinearity to some extent by the spectrum itself, based on the multiple peaks induced by Δm^2_{ee} oscillation.
A test quadratic nonlinear function can be used in the prediction, pull terms are added, here we consider the sigma of q1, q2, and q3 are 0.02.

$$E_{rec} = q_0 + (1+q_1) * E_{true} + q_2 * E_{true}^2$$

The best fit results for p0=1% , p1=2% is:

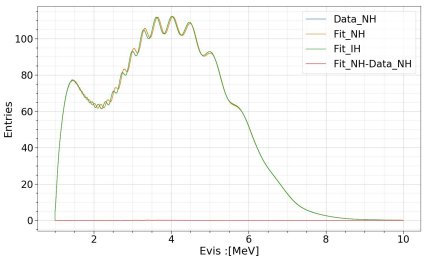

Assume that the true MH is normal, then with different intensities of residual NL (represented by p0 and p1), using the quadratic NL function in two prediction scenarios NH (true MH) and IH (false MH), the results are as follows, the $\Delta\chi2$ is quite stable inside this residual NL range

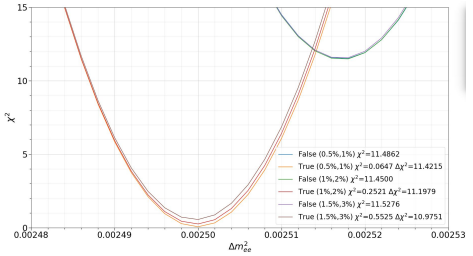

Ref. [2] PRD 88, 013008 (2013)

Non-Uniformity study

From detector center to edge, we can see clear change in the number of photoelectrons (nPE) per MeV wrt radius. Since b in the energy resolution parametrization

$$\frac{\sigma}{E} = \sqrt{a^2 + \left(\frac{b}{\sqrt{E}}\right)^2 + \left(\frac{c}{E}\right)^2}$$

is related to photon fluctuation, we can use different energy resolution at different radius. Coefficient b can be updated as the reciprocal of the square root of mean nPE/MeV at the certain radius.

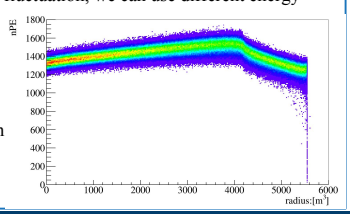

How many layers is enough to catch the structure in nPE/MeV curve? A scan results is shown below.
Divide the whole LS region into equal-volumed shells, apply different energy resolution in each shell.
From this plot, we can see that small improvements can be made, $\Delta\chi^2$ increase ~0.25. From 10 layers on, the $\Delta\chi^2$ is almost stable.

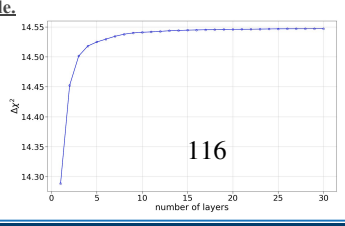

Event Reconstruction with Machine Learning in JUNO

Yu Xu
IKP2 Forschungszentrum Jülich

Gefördert durch DFG Deutsche Forschungsgemeinschaft

Motivation

- The Jiangmen Underground Neutrino Observatory (JUNO) has a large and complex detector with tens of thousands electronics channels, producing 2 PB raw data per year.
- We require $3\%/\sqrt{E}$ energy resolution so as to meet the requirement of the experiment.
- It's a big challenge to deal with such a large amount of data, thus new ideas is needed. Machine learning method is a good choice.

- Machine Learning techniques help a lot in high energy physics experiments for long time ago
- Better performance with the same amount of data, including the discovery of Higgs boson.
- Deep Learning Methods are on the rise, and naturally applicable in the area of neutrino physics

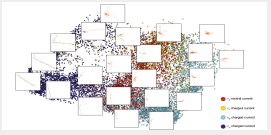

particle identification with CNN in NOvA

Reference: *Nature* **volume 560**, pages 41–48 (2018)

Pulse Shape Discrimination (PSD)

Principle

- PSD is an useful method to discriminate different kinds of particles, based on different time constant of light emission of different particles

$$P(t) = \sum_{i=1}^{3} \frac{w_i}{\tau_i} \exp\left(\frac{-t}{\tau_i}\right)$$

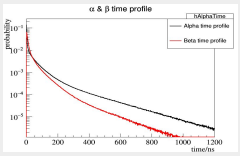

- Generally, the particles can be classified into two categories:
  - alpha like: with larger slower component
  - beta like: with smaller slower component

Particles	Fast(ns)/fraction	Slow(ns)/fraction	Slower(ns)/fraction
e^-, e^+, γ	4.93/79.9%	20.6/17.1%	190/3.0%
n, p	4.93/65%	34.0/23.1%	220/11.9%
α	4.93/65%	35.0/22.8%	220/12.2%

Network structure

- Input: the bin contents of the pulse shape histograms, [400, 1] array
- Simple structure: one hidden layer with 20 neurons

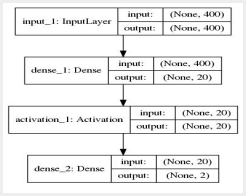

Alpha/beta discrimination:

- Application:
  - solar neutrino analysis, to reject alpha backgrounds
- Alpha and beta is 100% separated, even with large transfer time spread (TTS)

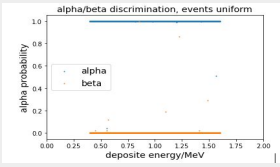

e/p discrimination:

- Application:
  - Diffused Supernova Neutrino Background (DSNB): to reject fast neutron and Atmosphere NC background
  - Supernova: separate v-e scattering and v-p scattering in ES channel
- Positron and proton are totally separated in DSNB energy range
- The accuracy is larger than 99.9% even with 12 ns TTS

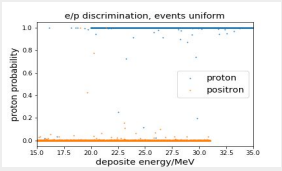

e+/e- discrimination

- Application:
  - Li9/He8 background rejection
  - Supernova: C12-CC channel separation
- Positronium considered: part of positron compose o-Ps with electron and decay after 3 ns
- Have some ability to separate e+ and e-
- Performance depends heavily on TTS
- juno tts: 28% PMT with 3ns TTS, 72% PMT with 12ns TTS

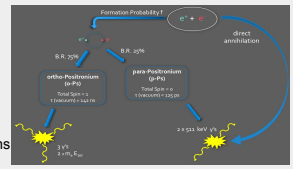

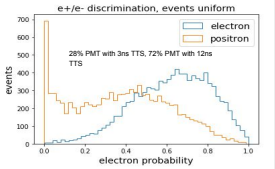

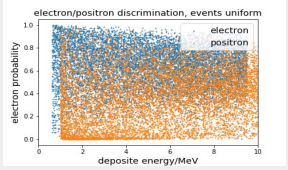

cut value	0.1		0.3		0.5	
	e+ survive	e- remain	e+ survive	e- remain	e+ survive	e- remain
TTS=3ns	41.51%	1.86%	64.11%	7.57%	78.7%	16.87%
juno tts	17.47%	0.63%	39.01%	5.18%	67.79%	25.9%

Waveform Reconstruction & Electronics Non-linearity

Motivation

- The performance of waveform reconstruction determine the performance of energy and vertex reconstruction.
- About 20, 000 PMT channels in JUNO
- Fast and accurate waveform reconstruction algorithm is needed.

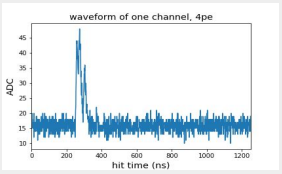

Network structure

- Here we use RNN to do the reconstruction
- Input: the bin contents of the waveform histograms, and transfer to RNN-required format
- Simple structure: one hidden LSTM layer

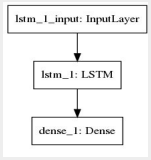

Charge reconstruction

- With neural networks, we can achieve high accuracy at low pe level
- The accuracy is 95%, 90%, 81% at 1 pe, 2 pe, 3 pe, respectively
- Cannot reconstruct time information by now
- High pe part is not important at IBD energy range
- Reconstruction speed is fast, about 0.1 ms per channel

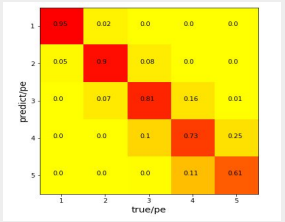

$$f_{electronics-nonlinearity} = \frac{E_{rec}}{E_{vis}}$$

electronics non-linearity

- Good performance on electronics non-linearity. It's small and easy to characterize
- Uncertainty of non-linearity less than 1%

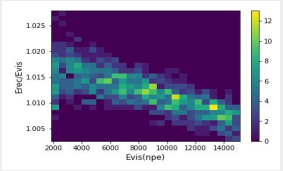

Conclusion

- We have achieved some good results with neural networks in some fields
- With the new results got by neural networks, we can improve the sensitivity for some physics problems, like DSNB
- It remains a big issue to apply the method with real data

- Find some new ideas to improve the networks
- Apply new result in different physics topics
- In the future, maybe we can build a framework with neural networks, from detector simulation to final event reconstruction

Jül-4418 • Mai 2019
ISSN 0944-2952

Mitglied der Helmholtz-Gemeinschaft